New experimental techniques for studying:

(i) Trace element substitution in minerals, and

(ii) Determining S-L-V relationships in silicate-H_2O systems at high pressure

by

Nicholas David Tailby

A thesis submitted for the degree of

Doctor of Philosophy

of the Australian National University

Research School of Earth Sciences
Australian National University
Canberra, ACT
Australia

July, 2009

The experimental techniques, analytical data, interpretations and conclusions presented in this thesis are my own unless otherwise acknowledged in the text.

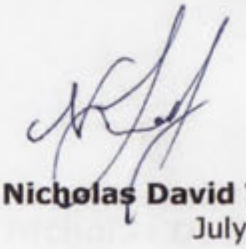

Nicholas David Tailby
July, 2009

"For my family, because they are the source of so much happiness in my life."

"For my family, because so much that is good in my life comes from you. I love you all so very much."

Acknowledgements

I would like to start by thanking the Research School of Earth Sciences and the Australian National University for providing me with the opportunity to undertake this PhD. I would also like to thank the Federal Government for funding me under an Australian Postgraduate Award, and the Australian Synchrotron Research Program for providing funds to carry out experiments at the Advanced Photon Source in Chicago.

To all my friends at the RSES and within experimental petrology, you've made coming to work an absolute pleasure every day. I'd like to say special thanks to Istvan (my fellow factory worker), Carl and Hack (my mentors), Guil, Cassian, Anja, Tegan, Joe, Gisi, Sparky, Jeremy, Oliver, Charlotte and Ash. I'd also like to single out Frances Jenner, for providing endless professional help and being such an amazing friend over the last few years. Nicole Keller deserves special mention for making every day hilarious, no matter how tough or boring our lives seemed. I would also like to thank my good mate Duck, who is a brilliant scientist, but an even greater mate.

There are a number of people who have taught me a great deal in the lab, including Dean and Hibbo, and especially David Clark. Dave and I found ourselves learning the ins-and-outs of the lab at the same time, and his contributions were central to the realisation of this thesis. I don't know how Dave put up with me, but I cannot thank him enough for all his technical support and all the giggles we've had.

I'd also like to thank Frank Brink for all his support on the SEM and Robert Rapp for everything related to the microprobe. Thanks should also go to Andrew Walker and Andrew Berry for contributing their time and expertise to zircon studies.

To my family - particularly the unflagging support and guidance of my amazing parents, Margaret and Gary - I can never, EVER, repay everything you've done for me. I'd also like to thank Beck and Chris for always taking time for me and making sure I was on the right path. You, my family, have made the last 29 years so much fun and so beautiful, I hope the coming decades are even better!

To my various housemates (Wazza, Hawesy, Jess and Gina), I thank you all for putting up with a nerdy, bad-dancing, and late-working housemate. It's been way too much fun and full of great memories. Particular thanks has to go to my great friend and housemate Dan, you've always gone out of your way to take care of me, you've been through every up and down, all I can do is say thank you for who you are.

To all my mates here in Canberra, including the baseball and cricket lads, I'd just like to say a big thanks for making life outside of uni a real pleasure.

Finally, and most importantly, I'd like to thank my supervisors and advisors John Mavrogenes, Jörg Hermann, Hugh O'Neill, Katy Evans and Daniela Rubatto. I am continually amazed that a group comprising such different personalities and skills can work together in such a positive and supportive fashion. You kept all the doors open for me, spent a considerable amount of time teaching me new skills and ideas, offered me financial support when research or personal circumstances required, and instilled in me an insatiable fascination for research. I cannot thank you enough for all the guidance, support and good times you've all shown me. I will miss working with you and within a research group that functions so well as a team and as friends. As I progress into the next chapter of my life and career, I hope that I can emulate the same level of guidance and professionalism you've shown. I cannot thank you all enough, and I hope this thesis and research does you proud.

Table of Contents

Chapter 1. General Introduction 1

PART 1: Ti Site Occupancy in Zircon 5

Abstract 6

Chapter 2. Introduction 7

Chapter 3. Literature Review – Zircon Thermometry 11

3.1 Overview 13

3.2: The zircon thermometer hypothesis (Watson and Harrison, 2005; Watson et al., 2006) 13

3.3: Early studies of Ti-in-zircon thermometry 24

3.4: Development of the zircon thermometer (Ferry and Watson, 2007) 26

3.5: Previous experimental research in the TiO_2-ZrO_2-SiO_2 system 29

3.6: Summary 32

3.7: Thesis overview – aims and rationale 32

Chapter 4. Experimental Strategy 33

4.1: Starting material 35

4.2: Experimental setup 35

4.3: Synchrotron standards 37

Chapter 5. Analytical Techniques 39

5.1: Scanning Electron Microscopy (EDS) 41

5.2: Electron Probe Microanalysis (WDS) 41

5.3: Synchrotron Techniques 42

5.4: Scanning Electron Microscopy Cathode Luminescence (SEM-CL) 43

5.5: Laser-Ablation ICP-MS analyses 43

5.6: Density Functional Theory (DFT) modelling 43

5.7: XANES Modelling 45

Chapter 6. Results 47

6.1 TiO_2-ZrO_2-SiO_2 experimental petrography 49

6.2: EMPA and EDS results: with a focus on synthetic zircons 55

6.3: Ti K_α x-ray maps from synthetic zircons 62
6.4: XANES Spectroscopy 63
6.5: Density Functional Theory Calculations 71
6.6: XANES Modelling 72
6.7: SEM-CL imaging, LA-ICP-MS analyses and X-ray maps 74

Chapter 7. Discussion **79**
7.1 The zircon structure 81
7.2: Ti site occupancy in zircon 85
7.3: Synchrotron Techniques: XANES 89
7.4: Comments on the Effect of Pressure on Ti-in-Zircon 90
7.5: Summary 92

Chapter 8. Conclusions **97**

PART 2: The Pelite-H_2O System at 25-35 kbar **101**

Abstract **102**

Chapter 9. Introduction **103**

Chapter 10. Literature Review **107**
10.1: Overview 109
10.2: Mineral/rock-H_2O studies at high pressures 109
10.3: Pelitic sediments and arc lavas: tracking geochemical cycles 121
10.4: Oxygen buffer and H-sensor techniques in hydrothermal experiments 129
10.5: Sliding metal-metal oxide (MMO) sensors 134
10.6: Relating oxygen buffers and sliding sensors 137
10.7: Summary 138

Chapter 11. Experimental Design **139**
11.1: Experimental rationale 141
11.2: Experimental design 144
11.3: Experimental tests 147
11.4: Summary 163

Chapter 12. Analytical Techniques **165**
12.1: Scanning Electron Microscopy (SEM-EDS) 167

12.2: Electron Probe Microanalysis (EPMA-WDS) 169
12.3: X-ray diffraction (XRD) 169
12.4: Laser ablation inductively coupled mass spectrometry (LA-ICP-MS) 169

Chapter 13. Experimental Technique 171
13.1: The inner H-sensor capsule 173
13.2: Ag-capsule and starting material 174
13.3: The final assembly and starting mixtures 180
13.4: Summary 183

Chapter 14. Results **185**
14.1: General summary of experimental run products 187
14.2: Textures: Oxygen buffers, solid phases, glass and vapour bubbles 195
14.3: Major element EDS results from the pelite-H_2O system 198
14.4: H-sensors: WDS results and experimental observations 209

Chapter 15. Discussion **217**
15.1: The wet solidus, melting reaction and starting H_2O content 219
15.2: Textural interpretation of the L-V solvus 222
15.3: H-sensors 224
15.4: The pelite-H_2O critical curve and wet solidus 230
15.5: Potential of the experimental technique 232
15.6: Problems and limitations of the experimental technique 233

Chapter 16. Conclusions **235**

References **239**

Appendix 1 **257**

Appendix 2 **265**

Appendix 3

Appendix 4 **271**

List of Figures

Part 1

Chapter 3: Literature Review-Zircon Thermometry

Figure 3.1: *Photomicrographs of experimental run products (from Watson et al., 2006).* 15

Figure 3.2: *Ti content of synthetic and natural zircon from Watson et al. (2006).* 16

Figure 3.3: *Starting composition of hydrothermal silicate melt experiments in terms of TiO_2-ZrO_2-SiO_2.* 18

Figure 3.4: *Linear goodness of fit trends for natural and synthetic zircons.* 19

Figure 3.5: *Natural zircons from Stillup Tal (ST) and Bishop tuff (BT).* 20

Figure 3.6: *P-T position of experimental and natural zircons.* 22

Figure 3.7: *Calculated 2σ, assuming a normal (Gaussian)* distribution from standard error and averages *reported by Watson et al. (2006).* 23

Figure 3.8: *Natural metamorphic zircon showing fir-tree zonation (Holden et al., 2006).* 25

Figure 3.9: *Zircon thermometry and analytical spots (SHRIMP) of Temora zircons.* 25

Figure 3.10: *Recalibration of the zircon thermometer.* 28

Figure 3.11: *TiO_2-ZrO_2-SiO_2 system (wt%) at 1 atm/1400 °C* 30

Figure 3.12: *ZrO_2-TiO_2 binary system and phase analyses at 1 atm.* 31

Figure 3.13: *Binary ZrO_2-TiO_2 system as a function of different pressures* 32

Chapter 4: Experimental Strategy

Figure 4.1: *Experimental starting compositions in the ZrO_2-TiO_2-SiO_2 system* 37

Chapter 6: Results

Figure 6.1: *BSE image of unleached experiment 1200-b showing immiscibility of silicate and tungstate flux.* 50

Figure 6.2: *Internal zonation in 1200-u srilankite imaged with BSE.* 51

Figure 6.3: *Electron back scatter images of 1,200 °C experiments.* 52

Figure 6.4: *Electron back scatter images of 1,200 °C experiments* 53

Figure 6.5: *Electron back scatter images of 1,300 °C experiments.* 54

Figure 6.6: *Electron back scatter image of 1,400 °C experiments.* 54

Figure 6.7: *Ti distribution histogram from experiment 1,300-S as determined from EPMA.* 59

Figure 6.8: *Ti distribution histograms for 1,300 °C experiments as determined from EPMA.* 60

Figure 6.9: *Ti distribution histogram from 1,100 °C experiments as determined from EPMA.* 61

Figure 6.10: *Ti distribution histogram from experiment 1400.* 61

Figure 6.11: *False colour image of Ti x-ray maps from 1300-U synthetic zircons.* 62

Figure 6.12: *SEM-BSE images of standard cristobalite and tetragonal zirconia.* 63

Figure 6.13: *XRD pattern for cristobalite standard powder.* 63

Figure 6.14: *Normalized Ti K-α XANES spectra for zircon, cristobalite, tetragonal zirconia and rutile.* 64

Figure 6.15: *Normalized Ti K-α XANES spectra of rutile, cristobalite and zircon.* 65

Figure 6.16: *Energy and normalized peak height of the Ti K-α XANES 1s-3d pre-edge feature of various Ti-bearing minerals.* 66

Figure 6.17: *Normalised Ti K-edge XANES pre-edge spectra of 45 randomly orientated zircon grains measured in fluorescence mode.* 67

Figure 6.18: *Normalized Ti K-edge XANES pre-edge spectra of zircon at different orientations..* 68

Figure 6.19: *Un-normalized XANES pre-edge spectra across Ti sectors in synthetic 1300-U zircon.* 69

Figure 6.20: *Normalized Ti K-edge XANES spectra of sodic glass from experiment 1300-S and 12 zircon analyses from 1300-S zircons at random orientation.* 70

Figure 6.21: *Observed and calculated Ti K-edge FT EXAFS spectra of Ti in zircon.* 71

Figure 6.22: *Comparison of measured and modelled Ti Kα XANES spectra for $^{[4]}$Ti in zircon at x-, y- and z-polarization.* 73

Figure 6.23: *Model Ti Kα spectra for zircon with changing $^{[4]}$Ti:$^{[8]}$Ti* 74

Figure 6.24: *Sector zoning in natural and synthetic zircons.* 75

Figure 6.25: *Comparison of SEM-CL and trace element distribution in natural zircon.* 76

Chapter 7: Discussion

Figure 7.1: *3-D projection of the zircon (ATO4) structure.* 81

Figure 7.2: *Simplified zircon projection along <100>.* 82

Figure 7.3: *Model isothermal ternary diagram for TiO_2-ZrO_2-SiO_2 system.* 84

Figure 7.4: *Ti content of synthetic zircons from fully buffered zircon experiments.* 85

Figure 7.5: *Composition of tetragonal zirconia, srilankite and rutile from 1 atmosphere experiments relative to the ZrO_2-TiO_2 binary phase diagram.* 87

Figure 7.6: *Ti content of synthetic zircons from fully buffered and unbuffered zircon experiments .* 88

Figure 7.7: *Figure 7.7: LA-ICP-MS ablation of synthetic 1300-U zircon.* 89

Figure 7.8: *Locus of silica buffer reactions plotted against log a_{SiO_2} - temperature.* 93

Part 2

Chapter 10: Literature Review

Figure 10.1: *P-T projection of wet and dry solidi for various silicate-H_2O systems.* 110

Figure 10.2: *Model $NaAlSi_3O_8$-H_2O P-T projection.* 111

Figure 10.3: *Various P-T-X schematics required illustrating phase relationships in the $NaAlSi_3O_8$-H_2O system.* 113

Figure 10.4: *Theoretical P-T-X relations in silicate-H_2O system.* 114

Figure 10.5: *Experimentally determined phase relations in the albite-H_2O system.* 116

Figure 10.6: *Experimentally based P-T projections of the $NaAlSi_2O_6$-SiO_2-H_2O system.* 118

Figure 10.7: *Experimentally determined critical curve P-T projections for various binary systems, modified after Bureau and Keppler (1999).* 119

Figure 10.8: *Simplified polythermal, isobaric ternary sections.* 120

Figure 10.9: *Extended trace element spidergram for Mariana arc basalts.* 121

Figure 10.10: *Comparison of oxygen fugacity estimates made from MORB and island arc basalts reported in the literature (after Mallman and O'Neill, 2007).* 122

Figure 10.11: *Experimentally determined pelite-H_2O wet solidus from existing literature.* 124

Figure 10.12: *Top slab P-T paths predicted from numerical and analogue models at different subduction angles, convergence rates and slab ages compared to the preferred wet solidus.* 125

Figure 10.13: *Temperature-f_{O_2} curves at 1 atmosphere for various solid media oxygen buffers.* 130

Figure 10.14: *Simplified experiment arrangements for hydrogen sensors described by Chou and Cygan (1990).* 133

Figure 10.15: *Schematic diagram demonstrating the relationship between membrane thickness and f_{H_2} gradient.* 134

Figure 10.16: *Binary alloy systems at 1 atmosphere (atm) and 700 °C (modified from Taylor et al., 1992).* 136

Figure 10.17: *Working range of the NiO-Ni-Pd and CoO-Co-Pd H-sensors relative to some MMO oxygen buffers at 1 atmosphere/900 °C.* 138

Chapter 11: Experimental Design: Rationale, Calibrations and Tests

Figure 11.1: *Experimentally determined pelite-H_2O wet solidus.* 141

Figure 11.2: *P-T range of various experimental apparatuses (figure modified after Holloway and Wood, 1988).* 142

Figure 11.3: *Cross-sectional schematic of the piston cylinder apparatus.* 143

Figure 11.4: *Experimental pressure calibrations.* 145

Figure 11.5: *Front cross-sectional view of the un-swaged Ag capsule.* 146

Figure 11.6: *Schematic of the brass swaging tool.* 146

Figure 11.7: *Schematics of the 1/2" assembly.* 150

Figure 11.8: *3-dimensional cross-section of the 1/2" assembly produced with CAD software.* 151

Figure 11.9: *Heating experiment of 20 kbar/800 °C synthetic fluid inclusions.* 152

Figure 11.10: *Silica species from experiments at different pressure-temperature conditions.* 153

Figure 11.11: *Representative piston travel measurements made from 35 kbar experiments as a function of time.* 154

Figure 11.12: *Covariation diagram of piston travel vs. time.* 155

Figure 11.13: *Photomicrograph of thermal gradient experiment, from run D-1077.* 156

Figure 11.14: *Temperature gradient measured from two experiments in the Ø 6 mm Ag capsule at different temperatures.* 156

Figure 11.15: *Photomicrograph of deformed capsule from experiment D-1079.* 157

Figure 11.16: *Phase transitions and physical properties of experimental components in the 1/2" assembly.* 161

Figure 11.17: *Extrapolated hydrogen permeability constants for precious metals at 2 kbar (after Chou, 1986).* 162

Figure 11.18: *Fe-FeO and Fe-Ir sensor experiment.* 163

Chapter 12: Analytical Techniques

Figure 12.1: *Representative time series analysis from experiment C-3130 at 10x10 µm defocused beam.* 168

Chapter 13: Experimental Technique

Figure 13.1: *H-sensor from layered Ni-Pd test experiment.* 174

Figure 13.2: *Simplified geological map of the Pam Peninsula, New Caledonia.* 176

Figure 13.3: *BSE images of pelite 1008-1 glass chips after 90 hours at 1,400 °C in the box furnace.* 176

Figure 13.4: *Major element comparison of pelite 1008-4 and GLOSS (Plank and Langmuir, 1998).* 177

Figure 13.5: *Minor and trace element comparison of pelite 1008-4 and GLOSS (Plank and Langmuir (1998) without the addition of 6 wt% SiO_2.* 178

Figure 13.6: *Ternary projection of pelite 1008-4 experimental starting material compared to GLOSS (Plank and Langmuir, 1998).* 179

Figure 13.7: *General schematic of the final Ø 6.0 mm Ag capsule after swaging.* 180

Figure 13.8: *P-T-X locus (relative to H_2O-content) of individual pelite experiments.* 183

Chapter 14: Results

Figure 14.1: *T-X stability fields and wet solidus as 35 kbar.* 189

Figure 14.2: *FE-SEM secondary electron (SE) photomicrograph of experiment C-3128.* 190

Figure 14.3: *SEM SE photomicrographs of 750°C/35 kbar experiments at variable H_2O contents.* 191

Figure 14.4: *SEM SE photomicrographs from 800°C/35 kbar experiments at variable H_2O contents.* 192

Figure 14.5: *SEM SE photomicrographs from 900°C/35 kbar experiments at variable H_2O contents.* 193

Figure 14.6: *SEM SE photomicrographs from 900°C/25 kbar experiments at variable H_2O contents.* 194

Figure 14.7: *SEM Se photomicrographs of Re-ReO_2 buffer assemblages from experiment D-1017.* 195

Figure 14.8: *Photomicrographs of vapour bubble-glass relationships from experiments C-3150 and D-1022.* 196

Figure 14.9: *Photomicrographs of experimental garnet and rutile textures.* 196

Figure 14.10: *Photomicrographs of experimental quartz and coesite textures.* 197

Figure 14.11: *Photomicrographs of experimental phengite-dominated domains.* 198

Figure 14.12: *Glass analyses from experiments plotted into the total alkali-silica (TAS) diagram.* 202

Figure 14.13: *Major element covariation diagrams of scanning (raster) beam analyses of experimental glasses.* 203

Figure 14.14: *Energy dispersive x-ray maps over a vapour bubble rich domain from experiment D-1022.* 204

Figure 14.15: *X-rays maps over vapour-bubble rich domain in experiment C-3127 (35 kbar).* 205
Figure 14.16: *Analyses of 35 kbar experimental garnets projected into garnet end-member diagrams.* 207
Figure 14.17: *Phengite compositions: Si (pfu) and TiO2 content.* 209
Figure 14.18: *Optical micrograph of experiment D-1017 showing NiO and Ni-Pd alloy, zirconia tubing and Pt-capsule.* 210
Figure 14.19: *Photomicrographs of failed sensors.* 210
Figure 14.20: *X-ray maps of Ni and Pd concentrations in experiment C-3119.* 211
Figure 14.21: *Covariation diagrams of Ni vs. Pd from 35 kbar/900°C experiments.* 213
Figure 14.22: *H-sensor alloy compositions from experiments at 35 kbar/900°C and 25 kbar/900°C.* 214
Figure 14.23: *H-sensor alloy compositions from experiments at 35 kbar/800°C.* 215
Figure 14.24: *H-sensor alloy compositions from glass-absent experiments at 35 kbar/700-750°C.* 215

Chapter 15: Discussion

Figure 15.1: *The pelite wet solidus using data from this study and previous research.* 220
Figure 15.2: *Modal proportions (% estimates) of phases vs. starting H_2O (wt.%) for 35 kbar runs.* 221
Figure 15.3: *Textural observations from experiment C-3127 and theoretical pseudo-binary projection.* 223
Figure 15.4: *Schematic of the pelite-H_2O experimental arrangement and diagram showing MMO buffer and H-sensor working range.* 225
Figure 15.5: *Hypothetical pelite H_2O binary schematic and activity relationships.* 227
Figure 15.6: *H-sensor results interpreted in terms of the pelite-H_2O L-V solvus and supercriticality.* 228
Figure 15.7: *Three dimensional schematic showing different quench regimes for an experiment at supercritical conditions.* 229
Figure 15.8: *The pelite-H_2O wet solidus and critical curve as indicated by this research.* 231

Chapter 1

General Introduction

The field of experimental petrology is by nature derivative, in that it simulates processes seen in nature. Accordingly, experimental petrology must evolve in order to remain at the forefront of science. As the broader scientific community moves into new areas, experimental petrologists must not simply follow, but also pave the way for new avenues of research.

In recent years new analytical techniques have enabled geologists to measure trace elements at incredibly low levels – our challenge in experimental petrology is to explain the processes that control trace element distributions.

Two questions lie at the heart of any experimental campaign:

(1) What problem am I trying to solve?
(2) What experimental technique/s can be used to solve this problem?

This thesis describes two new research methods (combining experimental and analytical techniques) that can be used to study a range of systems or mineral assemblages over a range of P-T-*X* conditions. In essence, this research aims to describe two new means of addressing a number of important questions within the Earth Science community.
As these two techniques are completely different, they are presented as two individual research projects (Part 1 and Part 2 of this thesis).

Part 1 of this thesis describes a new method for determining how trace element substitution and saturation occurs within minerals. The method combines different analytical techniques and phase assemblages in order to determine substitution mechanisms within minerals. These substitution mechanisms can be isovalent and isostructural, or they can be polyvalent (i.e., trace element substitution that occurs with changing oxidation state), and they can involve multiple or changing site occupancy in complex minerals (i.e., phases that consist of multiple sites and complex substitution mechanisms).

In order to test the new method, this research focused on studying Ti-in-zircon thermometry. The technique described here demonstrates how the use of experiments buffered by appropriate mineral species and utilizing multiple, independent analytical techniques – particularly the use of modelling and analytical techniques that fingerprint site occupancy and oxidation state – can constrain site occupancy of trace elements within minerals. Such techniques are crucial to establishing accurate thermodynamic models that can be applied to the study of natural systems.

Part 2 of this thesis presents a new experimental technique for studying silicate-H_2O systems at high pressure conditions (i.e., >20 kbar). This technique is different from conventional silicate-H_2O experiments because it does not require capsule welding in order to seal experiments, and does not employ capsule freezing or fluid traps in order to

analyse solutes within the vapour phase. The new technique is largely based on thermodynamic principles (focussing on changes in the f_{H_2} and the f_{O_2}), rather than textural observations, in order to determine solubility relationships among silicate (solid and melt phases) and hydrous species (the vapour phase) at experimental conditions. More importantly, the technique can be used to assess how accurately textural observations predict phase relationships at experimental conditions (i.e., assess previous studies).

In order to test the experimental method, results described and presented in Part 2 of this thesis focus on the pelite-H_2O system. As discussed in later sections of the thesis, results reported within the literature show notably different mineral stability (based on textural interpretation), wet solidi and supercriticality in the pelite-H_2O system.

Part 1

Ti Site Occupancy in Zircon

ABSTRACT

Ti site occupancy in zircon ($ZrSiO_4$) is fundamental to thermobarometry because substitution mechanisms control Ti content-temperature relations. Described here are the results of three independent methods used to demonstrate that Ti predominately substitutes for Si and not Zr in zircon.

Zircons were synthesized from oxide powders held in a Na_2WO_4 flux at 1 bar and 1,100-1,400 °C. Fully buffered experiments run at 1,300 °C show zircons equilibrated with rutile + cristobalite have Ti contents (1201 ppm) nearly half that of zircons equilibrated with srilankite + tetragonal zirconia (2640 ppm). The lower Ti content of zircons produced under silica-saturated conditions indicates that Ti substitution predominately occurs on the Si site. Moreover, the higher Ti contents of silica-saturated experiments at 1 bar (1201 ppm), relative to those at 10 kbar (457 ppm, Ferry and Watson, 2007), indicate a substantial pressure effect on Ti solubility in zircon (correcting for different silica species present).

Measured Ti K-α edge X-ray Absorption Near Edge Structure (XANES) spectra of synthetic zircons show energies and normalized intensities akin to those seen among tetrahedrally coordinated Ti-bearing standard minerals, strongly suggesting that Ti occupies the Si site. Density functional theory (DFT) calculations confirm that Ti substitution is most likely to occur on the Si site and predict a Ti-O bond length of 1.797 Å (compared to an average of 2.160 Å for substitution on the Zr site), in excellent agreement with X-ray Absorption Fine Structure (EXAFS) spectra of experimentally grown zircons which indicate a value of 1.76(1) Å. The software FEFF8.4 was used to simulate XANES spectra from the defect structures determined by DFT for Ti substituting on both the Si and Zr sites. The predicted spectrum for Ti on the Si site reproduces all the key features of the experimental zircon spectra, whereas Ti on the Zr site is markedly different. All applied methods confirm that Ti predominately substitutes for Si in zircon. Consequently, the Ti content of zircon is not only a function of temperature, but increases with decreasing silica activity. Because elements that activate or quench cathodoluminescence (CL) in zircon are incorporated into the Zr site, a decoupling of CL signal and Ti distribution (which occurs on the Si site in zircon) is expected. This hypothesis has been verified by a systematic CL-trace element study of natural and experimental zircon.

Chapter 2

Zircon Introduction

2.1: Zircon introduction

It is difficult to overstate the importance of zircon to the broader Earth Science community. The unique properties of zircon make it one of the most intensively studied minerals within the Earth's crust. These properties include: physical and chemical durability; the ability to incorporate a variety of radioactive and non-radioactive elements and the mineral's resistance to diffusive re-equilibration (Hanchar and Watson, 2003; Cherniak and Watson, 2007). From a practical or applied geology perspective, these properties make zircon the undisputed champion of geochronology (e.g., Hermann et al, 2001; Hiess et al., 2008); virtually the only record of conditions that existed during the early earth (Haedean zircons – e.g., Watson and Harrison, 2005; Maas et al, 1992) and a trace element host that can be used to track mantle/crust evolution (e.g., Lu-Hf – Amelin et al., 2000; Harrison et al., 2005, 2008).

Recent hypotheses suggest that the Ti content of zircon can be used to calculate a crystallization temperature (Watson and Harrison, 2005; Watson et al., 2006; Ferry and Watson, 2007). Such a geothermometer represents a potentially powerful geological indicator in that temperature estimates can be combined with additional information preserved in isotopic systems of interest (e.g., U-Th-Pb systems – Hermann et al., 2001; Hiess et al., 2008, and; Lu-Hf – Amelin et al., 2000; Harrison et al., 2005).

The main aim of this research is to determine Ti site occupancy in zircon. The details of this research are primarily concerned with how the zircon thermometer functions over a range of pressure-temperature-composition (P-T-*X*) conditions applicable to natural zircon-bearing rocks. This aim differs from previous research and discussion (e.g., Watson et al., 2006; Glikson, 2006; Nutman, 2006) in that it is not concerned with what a given temperature estimate represents, but how Ti site occupancy may influence the accuracy of a given temperature estimate. In addition to calibration and application of the zircon thermometer, Ti site occupancy can also be used to assess the relationship between Ti distribution and petrographic techniques applied to zircon (e.g., scanning electron microscopy cathodoluminescence and electron back scatter imagery).

Chapter 3

Literature Review – Zircon Thermometry

3.1 Overview

This review begins by discussing the original zircon thermometer hypothesis presented by Watson et al. (2006). Particular focus is placed on the strengths and weaknesses associated with the key experimental and theoretical principles of this hypothesis. This discussion then leads into various thermometry studies of natural zircon populations and how they provide insight into factors that may contribute to zircon thermometry. The final sections of this review focus on recent recalibrations of the zircon thermometer (Ferry and Watson, 2008) and previous experimental work in the TiO_2-ZrO_2-SiO_2 system. With these concepts in place, attention is then turned to outstanding issues surrounding zircon thermometry and how these relate to the aims of this thesis.

3.2: The zircon thermometer hypothesis (Watson and Harrison, 2005; Watson et al., 2006)

The zircon thermometer hypothesis was introduced by Watson and Harrison (2005), who used the Ti content of Jack Hills zircons to hypothesize magmatic and tectonic conditions that existed during the Hadean (4.35-4.00 Ga). Later work by Watson et al. (2006) provided details surrounding how the calibration was obtained and conditions over which the thermometer is broadly applicable.

Thermodynamic basis of the original hypothesis

The underlying concept behind the zircon thermometer (Watson and Harrison, 2005; Watson et al., 2006) is that the Ti content of zircon, in a rutile saturated system (a_{TiO_2} =1), varies systematically as a function of crystallization temperature. As discussed by Watson and co-authors (2005, 2006), the hypothesis assumes that Ti^{4+} enters the zircon lattice via isostructural substitution for either Zr^{4+} or Si^{4+}. The hypothesis also assumes that Ti incorporation is unaffected by the substitution of other elements – i.e., Ti substitution does not require charge balance and is not diluted by the substitution of other elements into the zircon structure.

The thermometric reaction on which the Watson et al. (2006) calibration was based is expressed:

$$TiO_{2(rutile)} = TiO_{2(zircon)} \qquad (\textbf{\textit{eq. 3.1}})$$

such that the equilibrium constant can be expressed:

$$k = \frac{a_{TiO_2}^{zircon}}{a_{TiO_2}^{rutile}} \qquad (\textbf{\textit{eq. 3.2}})$$

If $a_{TiO_2}^{rutile} \sim 1$ (assuming pure rutile saturation), then $k \cong a_{TiO_2}^{zircon}$ such that:

$$a_{TiO_2}^{zircon} = \gamma_{TiO_2}^{zircon} X_{TiO_2}^{zircon} = \exp\left[\frac{-\Delta G^o}{RT}\right] \qquad \textbf{(eq. 3.3)}$$

If $\gamma_{TiO_2}^{zircon}$ is assumed to be constant, then the Ti-content of zircon can be said to be linearly related to 1/T.

The zircon thermometer calibration was obtained from Ti analyses of zircons experimentally grown at high temperatures (1,025-1,450 °C) and natural zircons equilibrated at lower temperatures (580-1,070 °C). As these two zircon populations are vastly different, they will be discussed independently:

Synthetic zircons

Experimental zircons were synthesized from mixes and experimental techniques that can be separated into two groups:

1) Systems where zircon was grown in the presence of a fluid phase (H_2O and/or 1 M HF solution). This experimental method involved a nested capsule in capsule assembly, where zircon was grown by nucleation on crystal seeds[1] or by reacting ZrO_2 and SiO_2 in the presence of the fluid.
2) Systems where zircon was grown from oxide dissolved in a hydrous silicate melt (Table 3.1).

The discussion, representative photomicrographs and associated figure captions show rutile and zircon as the only two minerals within (and considered fundamental to the success of) experimental charges (see Figure 3.1). The only other species within experiments reported by Watson et al. (2006) were hydrous silicate melt, fluid quench or inclusions (residual starting oxide material within zircon). It is worth noting that later information presented by Ferry and Watson (2007) indicates that one experiment (run 66 - 1,050 °C) contained coexisting zircon-rutile-β quartz; one experiment (run 57 - 1,400 °C) contained coexisting zircon-rutile-zirconia; and all other twelve experiments lacked a third buffering phase.

[1] Zircon seeds were grown from ZrO_2 and SiO_2 pre-dissolved at 1,500 °C

Table 3.1: Experimental starting compositions of "hydrothermal melt" grown zircons (in wt% oxide, after Watson et al., 2006)

Exp. #	67	70	71	73	81	82b	91	95
T (°C)/ P (kb)	1,225 10 kb	1,280 10 kb	1,350 10 kb	1,450 10 kb	1,450 10 kb	1,100 10 kb	1,025 20 kb	1,225 10 kb
SiO_2	70.0	60.0	60.0	84.5	70.0	80.5	58.0	58.0
TiO_2	7.9	10.2	10.2	6.2	6.4	4.0	4.0	4.0
Al_2O_3	6.8	6.9	6.9	-	-	-	18.0	18.0
FeO	0.4	0.4	0.4	-	-	0.2	-	-
MgO	0.1	0.1	0.1	-	-	-	5.0	5.0
CaO	0.3	0.3	0.3	-	-	0.1	5.0	5.0
Na_2O	1.9	2.0	2.0	-	-	1.0	4.0	4.0
K_2O	10.7	10.0	10.0	-	-	5.4	4.0	4.0
ZrO_2	11.0	10.1	10.1	-	-	5.5	2.0	2.0
zircon[a]	-	-	-	9.3	23.6	-	-	-
H_2O[b]	19.4	18.4	19.1	5.4	20.3	6.9	24.5	19.3

[a] zircon seeds added to the starting oxide mix
[b] $(H_2O)/(oxides + H_2O)$ in wt%

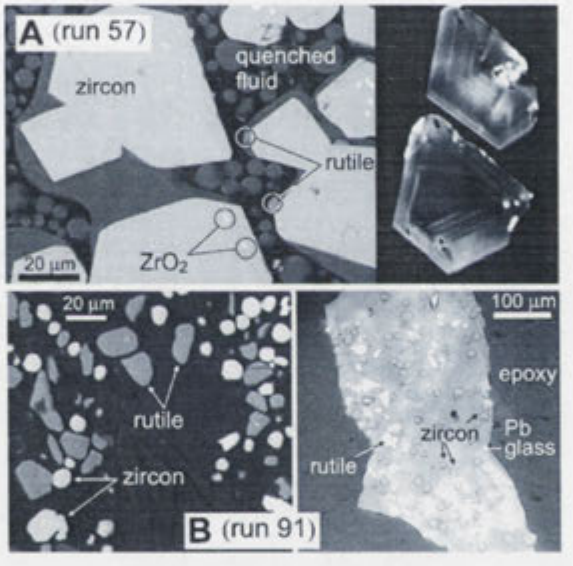

***Figure 3.1**: Representative photomicrographs of experimental run products of Watson et al. (2006).*

Natural zircons

Natural zircon samples were selected from rocks for which temperature estimates already existed, as determined by other geothermometers (e.g., the two-pyroxene or garnet-omphacite exchange thermometers). The common characteristic of natural zircons, was co-existence with rutile (with the exception of the Bishop Tuff zircons). The five natural zircon populations not only span a broad temperature range (580-1,070 °C), but also a broad pressure range (1 bar-30 kbar) and chemical/mineral compositions. Comparison of zircons from the Labait Harzburgite (a metasomatized peridotitic mantle xenolith) and the Bishop Tuff (an unaltered rhyolitic rock) highlight variability among natural samples (Table 3.2).

Table 3.2: Sample descriptions of zircon-bearing natural samples (after Watson et al., 2006 and references therein)

	Labait harzburgite	Bishop tuff rhyolite
Pressure	30 kbar	1.0-2.3 kbar
Temperature	1,070 °C	725 °C
Mineral paragenesis	Phologopite, orthopyroxene, olivine, chromite, sulphides, rutile and zircon	Quartz, sanidine, plagioclase, biotite, magnetite and zircon
log(a_{SiO_2})	-0.21[a]	0
log (a_{TiO_2})	0	-0.22[b]

[a] silica activity estimates based on reaction buffer at 1 bar (En = Ol, see Figure 7.8). This estimate does not take into account any pressure effect on the buffer reaction.

[b] a_{TiO_2} for the Bishop tuff is likely buffered by ilmenite or titanite. Watson et al. (2006) inferred a_{TiO_2} from experimental research into rutile saturation in silicate melt by Hayden and Watson (2007) and Ryerson and Watson (1987).

The calibration

The Ti content of 17 zircon populations, 12 synthetic and 5 natural, was used to calibrate the zircon thermometer (Figure 3.2):

$$T(°C)_{zircon} = \frac{5080 \pm 30}{(6.01 \pm 0.03) - \log(Ti)} - 273 \qquad \textit{(eq. 3.4)}$$

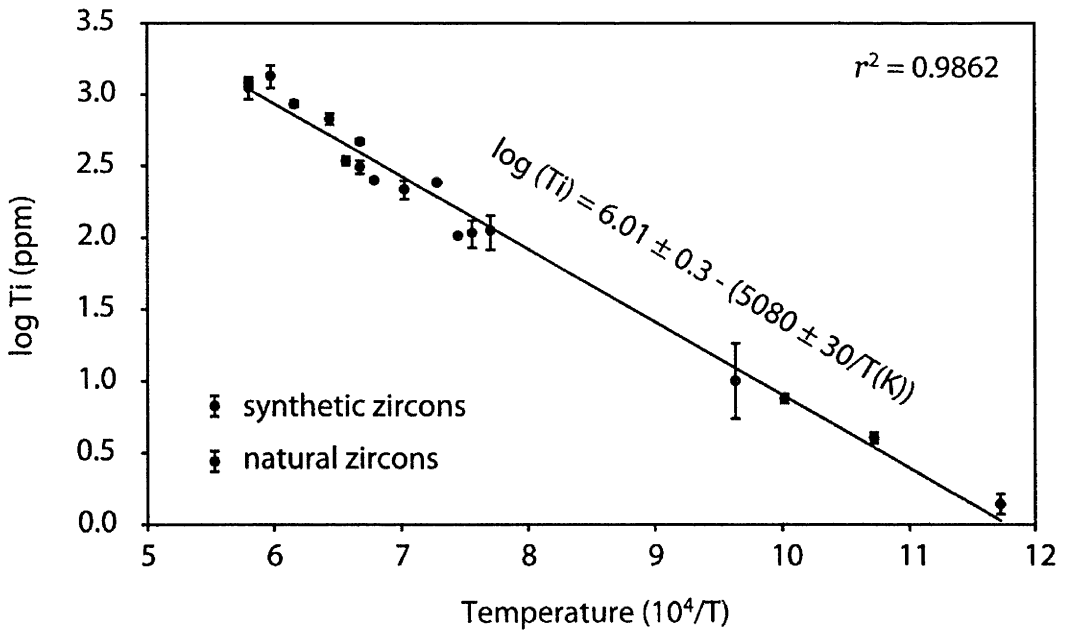

Figure 3.2: *Ti content of synthetic (black circles) and natural zircon (red circles) from Watson et al. (2006). All synthetic experiments report two standard errors (with the exception of run 57 – $10^4/T$=5.98, which shows two standard deviations). Error associated with natural zircon populations is shown in two standard deviations (calculated from data presented by Watson et al., 2006).*

Key concepts and ideas regarding the Ti-in-zircon hypothesis

Data presented by Watson et al. (2006) clearly demonstrates a temperature dependence on the Ti-content of zircon. The authors discuss factors that have potential to influence the accuracy of a given temperature estimate. The presence of rutile is considered particularly important, such that a rock or experiment lacking rutile (i.e., a_{TiO_2} <1) requires an a_{TiO_2} estimate to make an appropriate temperature correction. Isotopic interference ($^{96}Zr^{2+}$) during ion microprobe (IMP) analyses, secondary fluorescence from Ti-rich phases during electron microprobe microanalyses (EPMA), and the introduction of Ti to surfaces or cracks during zircon alteration/transportation/lithification can all result in inaccurate temperature estimates.

Watson et al. (2006) used variation in equilibration pressure of synthetic and natural zircons to indicate that pressure has negligible effect on the thermometer. In particular, this assumption is based on the fact that all zircon populations show Ti contents falling at or around the calibration curve, yet span pressures from 2.6 to 30 kbar.

Previous concerns with the Watson et al (2006) Ti-in-zircon hypothesis

Introduction of the zircon thermometer (Watson and Harrison, 2005; Watson et al., 2006) was rapidly followed by comments on the original manuscript (Glikson, 2006; Nutman, 2006) and application to natural zircons (e.g., Harrison et al., 2005; Holden et al., 2005; Claiborne et al., 2006; Baldwin et al., 2007; Bea et al., 2007; Harrison et al., 2007; Harrison and Schmitt, 2007; Fu et al., 2008; Heiss et al., 2008). Here it is essential to set out that this discussion focuses on potential problems with the thermometer hypothesis and are in no way concerned with what a given temperature estimate represents.

a_{SiO_2} and Ti-saturation in zircon

The most fundamental concern with the work of Watson et al. (2006) is that the exchange reaction $TiO_{2(rutile)}$ = $TiO_{2(zircon)}$ (equation 1) inadequately describes the Ti substitution mechanism in zircon. Many theoretical substitution mechanisms (or combinations thereof) exist for Ti in zircon, including: isostructural replacement of Zr^{4+} and/or Si^{4+}; substitution on interstitial sites, and substitution associated with specific crystal defects (e.g., vacancies, dislocations, etc). Equally important, potential exists for the dominant Ti substitution mechanism to vary as a function of P-T-*X*. In short, the substitution reaction presented by Watson et al. (2006) is an oversimplification that does not fully address Ti site occupancy and the influence this may have on the accuracy of zircon thermometry.

The main weakness here is that the original hypothesis not only oversimplifies the exchange reaction, but that the experiments show no direct mineral assemblage on which a_{SiO_2} can be estimated. Experimental run products reported by Watson et al. (2006) indicate that

experiments lacked quartz and/or primary zirconia[2] (e.g., a silica buffer). The most basic Ti-in-zircon experiment requires three starting components (or compounds) – TiO_2, ZrO_2 and SiO_2 in order to produce rutile and zircon. As dictated by the Gibbs' phase rule, any experiment consisting of three components, at a fixed pressure (P) and temperature (T), requires three phases in order to be fully buffered (invariant). As experiments presented by Watson et al. (2006) only contain rutile and zircon, silica activity (a_{SiO_2}) is unconstrained for the Ti exchange reaction in zircon.

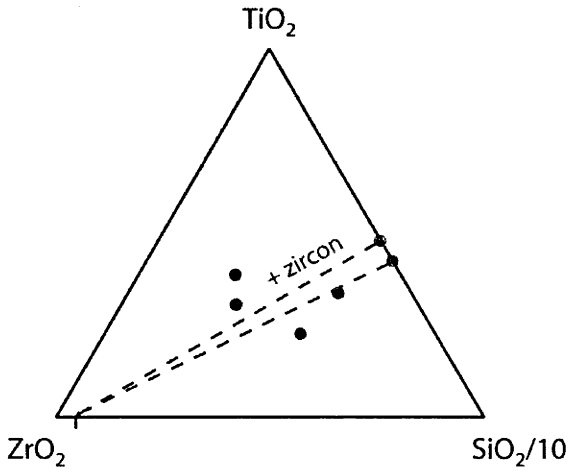

***Figure 3.3**: Starting composition of hydrous silicate melt experiments of Watson et al. (2006) in terms of TiO_2-ZrO_2-SiO_2. Black circles represent un-seeded experiments, red circles represent seeded experiments with mixing lines towards zircon (dashed red line).*

As shown in Table 3.1 and Figure 3.3, the various experiments of Watson et al. (2006) employed different starting compositions (*X*) and were run at different pressures (P) and temperatures (T). In this sense, the a_{SiO_2} of experiments used in the original calibration is not only unconstrained, but likely to vary according to the different P-T-*X* of each experiment.

Comparison of natural and synthetic zircons

There is no doubting that data presented by Watson et al. (2006) show a temperature dependence of Ti content in zircon. Closer inspection of the raw data shows lines of best fit for synthetic zircons (where a_{SiO_2} is unconstrained) and natural zircons (most of which existed at a a_{SiO_2} of unity) separately (Figure 3.4). Analyses from the Labait harzburgite were excluded from Figure 3.4 as this sample is both silica and titania undersaturated. If the two zircon populations represent a continuum Ti-temperature space they should overlap. Divergence between these two zircon suites, as shown in Figure 3.4, indicates that some factor or process separates natural and synthetic zircon. That natural zircons contain quartz,

[2] recognizing that later reports by Ferry and Watson (2007) indicate one experiment contained β quartz and one experiment contained zirconia.

while synthetic populations lack a silica buffer, tentatively suggests that a_{SiO_2} may influence Ti saturation in zircon.

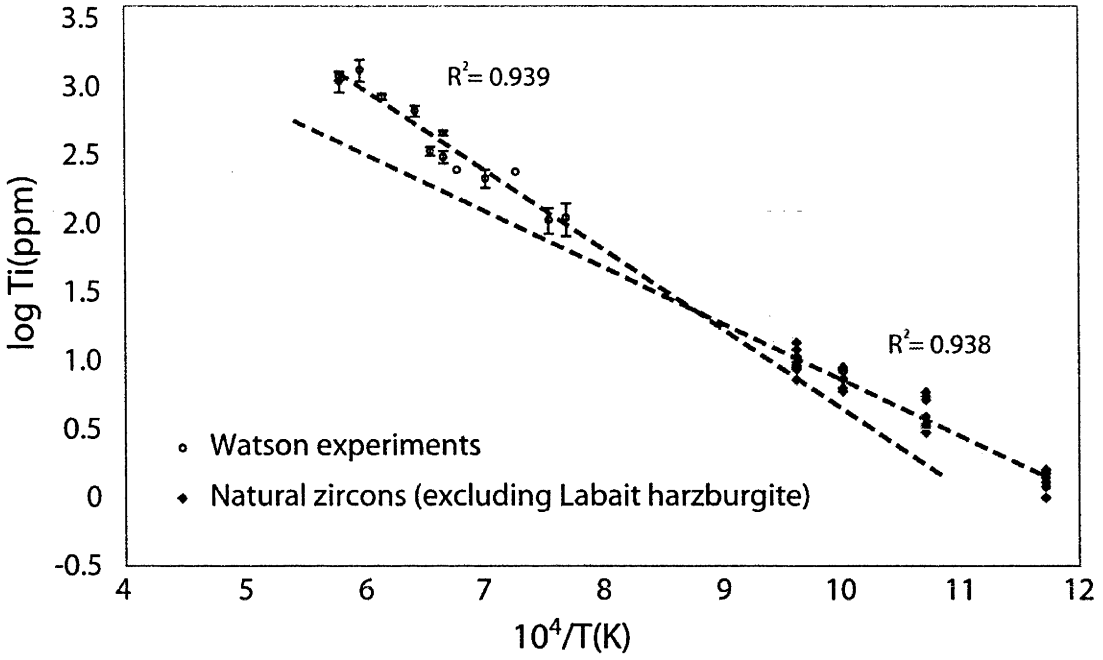

***Figure 3.4**: Linear goodness of fit trends for natural (red) and synthetic (black) zircons (figure constructed by data presented in the original work of Watson et al. (2006)).*

Internal zonation and Ti distribution in zircon

The use of natural zircons for calibration purposes (Watson et al., 2006), while permitting studies at lower temperatures than possible via experimentation, introduces concerns regarding the conditions under which any given zircon grain crystallized. Representative scanning electron microscope cathodoluminescence (SEM-CL) images presented by Watson et al. (2006) show sector and oscillatory zoning in natural zircon grains (Figure 3.5). The development of sector zoning implicitly indicates disequilibrium during zircon growth (e.g., Watson and Liang, 1995), while the calibration assumes that measured Ti contents represent crystallization temperatures. Similarly, temperature estimates made from oscillatory zoned zircons imply that there is no corollary zonation in Ti or that Ti diffusion can re-equilibrate Ti contents from core to rim of a given zircon grain.

Ti analyses of natural zircons show small to notable Ti variation, with measured standard deviations (σ) falling between 8.8-25.8% of the mean of individual populations. Given the variable statistics among natural zircons and the lack of discussion regarding the relationship between various types of zonation observed in SEM-CL and Ti distribution, several questions persist:

Can SEM-CL or BSE imaging be used as a guide for Ti distribution in zircon?

Is the Ti content of a sector zoned zircon reliable for thermometry purposes?

Can Ti show zoning in zircon (oscillatory, sector, fir tree) in the absence of corollary SEM-CL or BSE sector zoning? In other words, is there a general and consistent relationship between CL/BSE and Ti distribution?

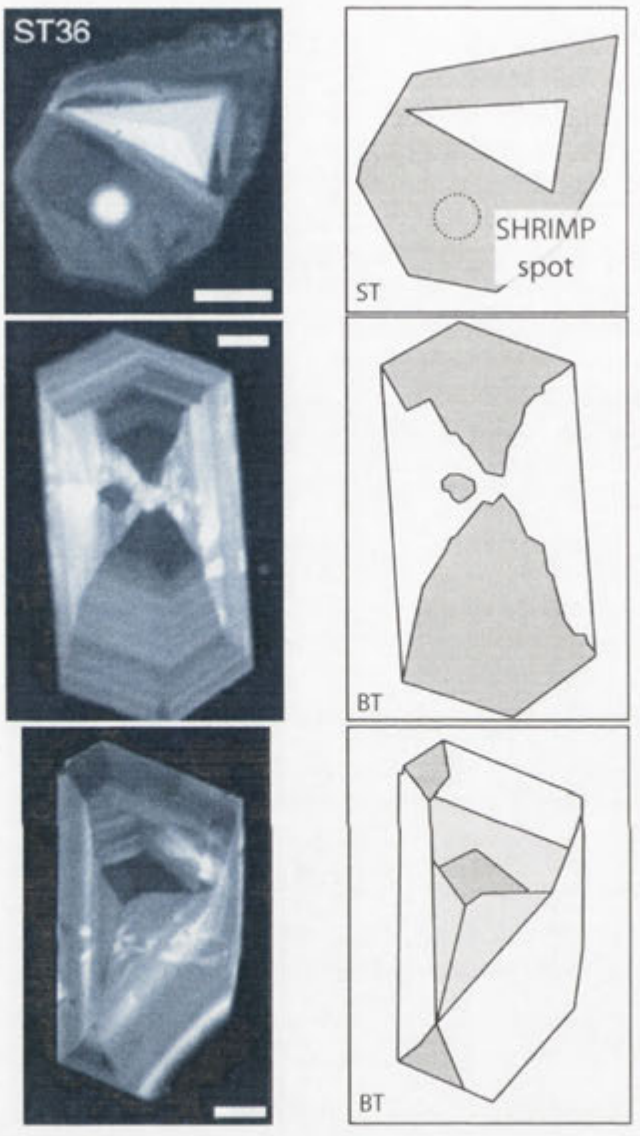

***Figure 3.5**: Natural zircons from Stillup Tal (ST) and Bishop tuff (BT). Note that BT zircons show components of both oscillatory and sector zoning, while ST zircons only show sector zoning. White scale bars represet 30 μm in all SEM photomicrographs.*

The pressure effect

As previously discussed, Watson et al (2006) used pressure variability among zircon populations to suggest that the pressure effect on the zircon thermometer is negligible. The samples used in the original calibration (both natural and synthetic) were equilibrated over a broad pressure range (2.6-30 kbar) and appear to define a consistent trend (Watson et al., 2006). With the exception of two natural samples (Bishop tuff and Labait harzburgite), natural zircons used for calibration purposes crystallized at pressures close to 10 kbar: Adirondack migmatite – 7-9 kbar, Stillup tal – 7-8 kbar, and Santa Catalina migmatite – 8-11 kbar. The two natural zircon populations at pressure extremes of the calibration: the

Bishop tuff (maximum pressure of 2.6 kbar – Anderson et al., 2000) and the Labait hazburgite (~30 kbar – Lee and Rudnick, 1999), show mineral assemblages that differ significantly from those of synthetic zircons of Watson et al. (2006). The Labait harzburgite is silica-undersaturated (with a_{SiO_2} <<1 and likely buffered by co-existing orthopyroxene and olivine), while the Bishop tuff is titania-undersaturated (with a_{TiO_2} <1 and likely buffered by ilmenite, titanite or magnetite – see Table 3.2).

Using the natural samples in the Watson et al. calibration (2006) to suggest a negligible pressure effect on Ti-in-zircon assumes that a_{SiO_2} does not influence Ti saturation in zircon and an appropriate correction can be made where a_{TiO_2} <1. It should be noted that the a_{TiO_2} correction applied to Bishop tuff zircons is based on Ti-in-quartz measurements (Wark and Watson, 2006) and Ti saturation models of Ryerson and Watson (1987). Ti-in-quartz correction for the Bishop Tuff is based on the Wark and Watson calibration (2006) which was calculated on experiments run at 10 kbar. The pressure estimate of Bishop tuff (Anderson et al., 2000) is 8 kbar lower than the calibration of Wark and Watson (2006) and there is no research into the pressure effect on Ti in zircon. Similarly, rutile saturation models of Ryerson and Watson (1987) are based on experiments with CaO, MgO, FeO and ZrO_2 contents that significantly differ (in terms of both the compositional parameter and ZrO_2 content) from experimental starting compositions of Watson et al. (2006). While such corrections and assumptions represent the best estimates on current information it is unclear if they provide an accurate estimate of a_{TiO_2}.

Another concern with the original calibration is that the assumed pressure of the Bishop Tuff zircons (1-2.6 kbar) is based on the H_2O- and CO_2- content of sanidine hosted melt inclusions and calculated maximum gas-saturation pressures (Anderson et al., 2000). In order to apply the pressure estimate of Anderson et al. (2000), zircon had to co-crystallize with or re-equilibrate with the melt at the time of sanidine crystallization. It should be noted that while melt inclusions from late eruptives of the Bishop Tuff estimate pressures of 1–2.6 kbar, melt inclusions from early eruptives estimate pressures of 1–30 kbar. The work of Anderson et al. (2000) represents the most up-to-date pressure estimates of the pre-eruptive melt/s from Bishop tuff sample locality, but there is no direct evidence to suggest that zircons from the late eruptives crystallized at the same pressure as sanidine, quartz or any other pressure (1–30 kbar) or temperature recorded by inclusions from the various units of the intrusion. In short, while the Bishop Tuff zircon required an a_{TiO_2} correction to account for the lack of rutile, it is unclear if the pressure estimate is representative of zircon crystallization.

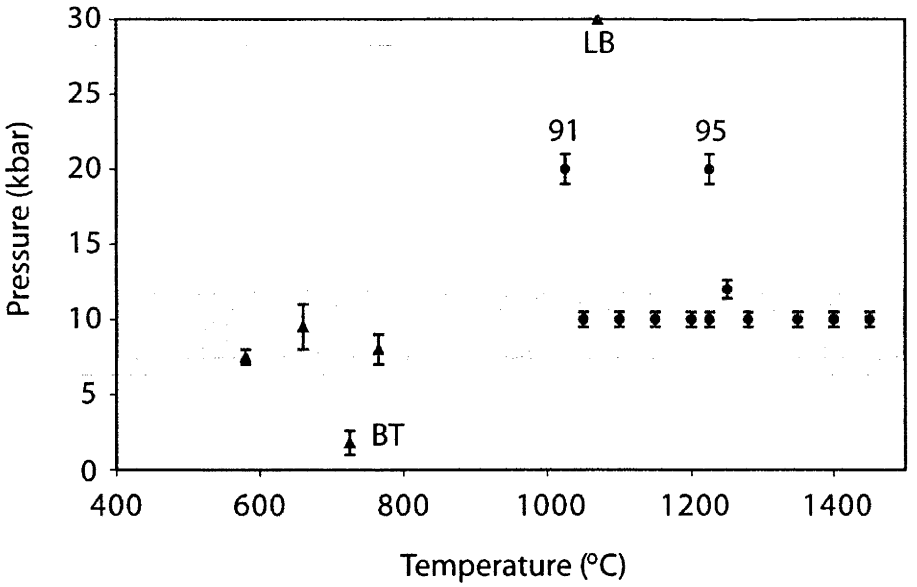

***Figure 3.6**: P-T position of experimental (black circles – error bars assume 5% uncertainty) and natural (red triangles with reported uncertainty) zircons. Shaded region represents the P-T field over which most zircons equilibrated. BT = Bishop tuff, LB = Labait Harzburgite, 91 and 95 refer to experiments from Watson et al. (2006).*

Additional concerns surrounding the pressure effect assumptions of Watson et al. (2006) relate to synthetic zircons. The majority of synthetic zircons were equilibrated at ~10 kbar, with 11 experiments run at 10 kbar, one at 12 kbar, and two at 20 kbar. As demonstrated in Table 3.1, experiments run at 20 kbar (runs 91 and 95) have lower SiO_2 contents and higher Al_2O_3 contents than all other experiments. While these two experiments appear to show Ti content-temperature trends consistent with other zircon populations (and the calibration curve), decreased a_{SiO_2} and different starting compositions in these experiments may compensate for the influence of pressure.

In summary, the pressure effect conclusions of Watson et al. (2006) are based on two unbuffered synthetic zircon populations at 20 kbar, Bishop tuff zircons where a_{TiO_2} <1 and where crystallization pressure estimates range from 1.1-30 kbar, and Labait Harzburgite zircons where a_{SiO_2} <1. As there is no systematic study of Ti content at various pressures and the majority of experimental and natural zircons used to calibrate the thermometer (13/17 or 76%) were equilibrated at pressures close to 10 kb, there is insufficient information to elucidate the influence of pressure on Ti saturation in zircon. It is interesting to note that the only two experiments run at constant temperature and variable pressure (exp. 95 - 1,225 °C/20 kbar and exp. 67 - 1,225 °C/10 kbar) show a 49.8% increase in Ti content (311 ± 32 to 466 ± 19 ppm) of as pressure decreases by 10 kbar. Experiments 95 and 67 have different starting compositions (and likely different a_{SiO_2} - see Figure 3.3) and while the change in Ti content appears visually subtle on a log scale plot (Figure 3.4), it is statistically important in terms of determining a pressure effect and calculating calibration uncertainties.

Statistical concerns

The overall calibration reported in the original work of Watson et al. (2006) has a 2σ uncertainty. The lack of statistical information about the Ti distribution in different synthetic zircon populations (other than 2σ uncertainty associated with the overall calibration) poses a minor concern regarding the original work of Watson et al. (2006). It is important to note that the zircon thermometer calibration is based on the incorporation of a trace element into a mineral that is notoriously difficult to nucleate and equilibrate. Similarly, zircon is a mineral known to exhibit a broad range of internal zonation (sector, fir tree, oscillatory, etc – e.g., Hanchar and Miller, 1993) and such zonation can be difficult to detect among small grains or using analytical techniques that require minimum spot size (e.g., ion microprobe). In order to demonstrate equilibrium within the Watson et al. (2006) experiments, and to ensure that the use of standard error and average is an accurate representation of Ti content in a given zircon population, it is essential to establish that measured Ti contents involved a normal (Gaussian) distribution about the mean. Information to establish a statistical distribution about the mean requires (at best) a frequency distribution histogram for Ti measurements of a given experiment, or (at least), a record of the number of analyses (both included and excluded).

Recognizing that journal articles are necessarily succinct, it is likely that detailed discussion regarding Ti data distribution represented an excessively long addition to the original Watson et al. (2006) manuscript. The standard errors reported by Watson et al. (2006) are used to calculate standard deviations as a function of number of analyses (which was not reported in the original publication). As shown in Figure 3.7, error bars expand significantly with the use of standard deviation, and so provide a different representation of statistics surrounding the calibration. The use of standard deviation will not change the calibration or the error associated with it (as both are based around the mean of analyses), but it does allow some guide as to what sort of statistical distribution one may expect for Ti contents in a natural zircon population.

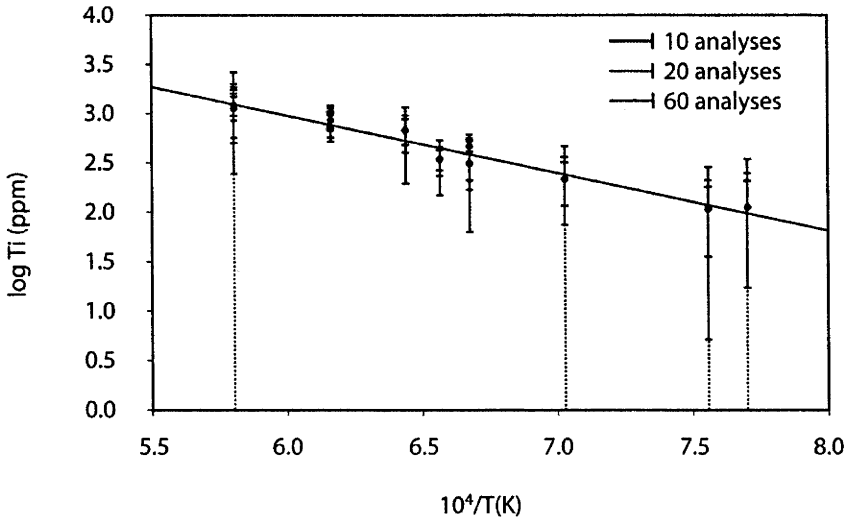

***Figure 3.7**: Calculated 2σ, assuming a normal (Gaussian) distribution from standard error and averages reported by Watson et al. (2006).*

3.3: Early studies of Ti-in-zircon thermometry

The work of Watson and Harrison (2005) was rapidly followed by a number of conference abstracts (with results not reported elsewhere) and publications that are important contributions to zircon thermometry.

Results presented by Harrison et al. (2005 AGU abstract) report model energies associated with isostructural substitution for Zr^{4+} and Si^{4+} in zircon, calculated by SIESTA implementation of density functional theory (DFT). Direct substitution of Ti for the two cation sites in zircon cannot be directly compared in DFT because the two simulations contain different atoms (*pers. comms.* Andrew Walker, 2007). As with research presented later in this thesis, calculations presented by Harrison et al. (2005) were presumably based on evaluating the energy of a reaction that results in Ti changing site. The work of Harrison et al. (2006) indicates that substitution modelled in their research favours the Si^{4+} site by ~0.3 eV. This value was later used by Ferry and Watson (2008) to indicate that ≈95 % of all Ti in zircon substitutes on the tetrahedral site.

Detailed chemistry (i.e., the chemical reaction) of the simulation box used by Harrison et al. (2005) was not presented in the abstract, nor was it published, presented or described elsewhere. The lack of information surrounding DFT simulations makes it difficult to asses the validity of preferential site occupancy, namely because energy differences associated with different substitution mechanisms will vary depending on what minerals coexist with zircon (i.e., how the reaction is described).

Holden et al. (2005 AGU poster) presented sensitive high resolution ion microprobe (SHRIMP-RG) analyses from natural metamorphic and igneous zircons. Metamorphic zircons from this work show average Ti contents and associated temperature estimates consistent with other geothermometers (garnet-omphacite). This being the case, light and dark CL domains in zircon (fir tree zones shown in Figure 3.8), show different Ti contents (640±20 °C and 586±24 °C). This observation suggests that while temperature is the major control on Ti-in-zircon, factors such as internal zonation and disequilibrium can contribute Ti variation.

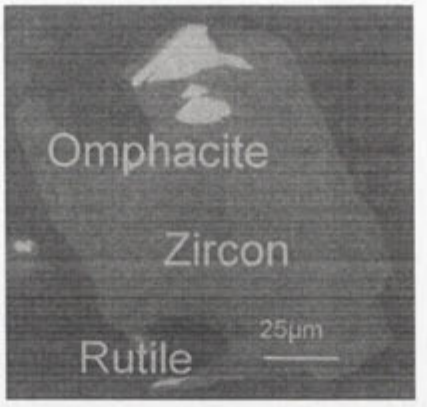

***Figure 3.8**: Natural metamorphic zircon showing fir-tree zonation from Holden et al. (2006).*

Igneous zircons from the Temora gabbroic diorite show various types of zoning as imaged in CL. Figure 3.9 shows a sector zoned Temora zircon with Ti thermometry indicating different crystallization temperatures across each domain (with the darkest CL domain showing the highest Ti content). By contrast, an oscillatory zoned Temora zircon taken from the same sample (with the same U-Pb age) shows core to rim thermometry more consistent with a cooling trend. Dark and light CL domains from these two zircons show antithetic trends with regard to Ti content. The work of Holden et al. (2005) indicates that while zircon thermometry appears to accurately record crystallization temperature in the majority of cases, it also demonstrates that additional factors (e.g., sector zoning) may influence the accuracy of a given temperature estimate. It is interesting to note that the Temora zircons are used as SHRIMP standards for U-Pb dating because the mineral is homogenous (with regard to U-Pb isotopes) at all analytical scales.

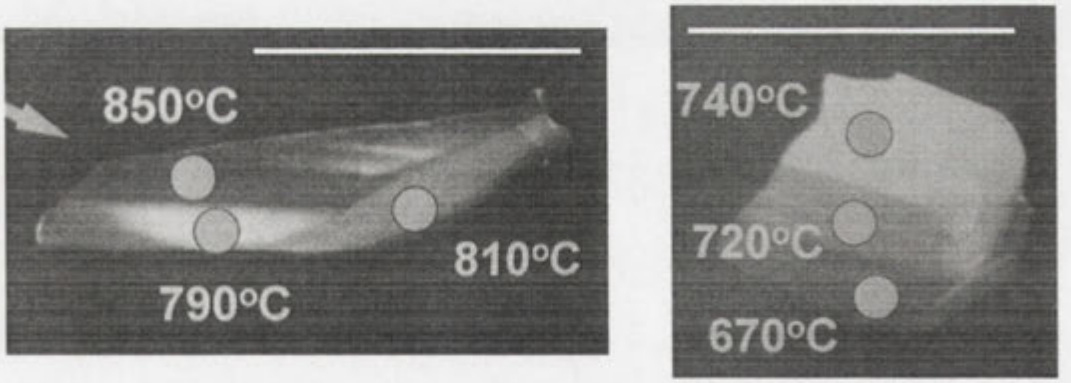

***Figure 3.9**: Zircon thermometry and analytical spots of Temora zircons. SHRIMP analyses indicated by circles, scale bars = 200 µm.*

Additional discussion regarding zircon thermometry was presented by Hermann et al. (2006) who studied zircons from a garnet peridotite lens from Monte Duria, Central Alps. Although crystallization temperature was not focal to this research, theoretical discussion within this manuscript represents the first reconsideration of the factors controlling Ti saturation in zircon. Hermann et al. (2006) suggest that Ti substitution in zircon occurs according to the reaction:

$ZrTiO_4 + SiO_2 = ZrSiO_4 + TiO_2$

such that a_{SiO_2} and a_{TiO_2} both influence Ti-in-zircon thermometry. This was the first publication that recognized a_{SiO_2} as important to zircon thermometry.

3.4: Development of the zircon thermometer (Ferry and Watson, 2007)

A recent refinement of the zircon thermometer, published at an intermediate stage of this PhD project, was presented by Ferry and Watson (2007). This work recognized that Ti saturation in zircon depends on both a_{TiO_2} and a_{SiO_2}, such that the thermometer calibration requires an appreciation of Ti site occupancy and recalibration.

Ferry and Watson (2007) describe the equilibrium reaction controlling Ti saturation in zircon as two theoretical reactions.
The first reaction involves Ti substitution on the zircon tetrahedral site, such that:

$ZrSiO_4 + TiO_2 = ZrTiO_4 + SiO_2$ (***eq. 3.5***)

Where the equilibrium constant can be expressed:

$$k = \frac{a_{ZrTiO_4}^{zircon} a_{SiO_2}}{a_{ZrSiO_4}^{zircon} a_{TiO_2}} \quad (\textit{eq. 3.6})$$

and assuming equilibrium,

$$\Delta H^0 - T\Delta S^0 + P\Delta V^0 + RT \ln a_{ZrTiO_4} + RT \ln a_{SiO_2} - RT \ln a_{ZrSiO_4} - RT \ln a_{TiO_2} = 0 \quad (\textit{eq. 3.7})$$

The second reaction involves Ti substitution on the zircon dodecahedral site, such that:

$TiO_2 + SiO_2 = TiSiO_4$ (***eq. 3.8***)

Where the equilibrium constant can be expressed:

$$k = \frac{a_{TiSiO_4}^{zircon}}{a_{TiO_2} a_{SiO_2}} \quad (\textit{eq. 3.9})$$

and assuming equilibrium,

$$\Delta H^0 - T\Delta S^0 + P\Delta V^0 + RT \ln a_{TiSiO_4} + RT \ln a_{SiO_2} - RT \ln a_{TiO_2} = 0 \quad (\textit{eq. 3.10})$$

The key observation from equations 3.5 and 3.8 is that both reactions include a silica term, such that a_{SiO_2} is pertinent to zircon thermometry. When Ti occupies the tetrahedral site in zircon (equation 3.6), the equilibrium constant is proportional to a_{SiO_2} (such that decreasing a_{SiO_2} results in increasing zircon Ti content). When Ti occupies the dodecahedral site in zircon (equations 3.8 and 3.9), the equilibrium constant is inversely proportional to a_{SiO_2} (such that decreasing a_{SiO_2} results in decreasing zircon Ti content).

Experimental approach

Ferry and Watson (2007) recognized that nearly all experiments of Watson et al (2006) lacked either zirconia or quartz[3] such that a_{SiO_2} (and a_{ZrO_2}) was unconstrained in the original zircon calibration. Ferry and Watson (2007) carried out five additional experiments in order to recalibrate the zircon (and rutile) thermometer. Descriptions of these experiments, in the absence of representative photomicrographs, indicate that runs contained one of two mineral assemblages – zircon + rutile + β-quartz, and, zircon + rutile + zirconia. Ferry and Watson (2007) considered these two mineral assemblages to define the maximum and minimum a_{SiO_2} at which zircon is stable. By defining zircon Ti saturation at these conditions, Ferry and Watson established a new calibration that took into account both a_{TiO_2} and a_{SiO_2}.

Results and discussion

In order to fingerprint Ti site occupancy in zircon, Ferry and Watson (2007) used observations made in previous research and new experimental results to demonstrate that Ti predominately substitutes for the Si site in zircon. The authors cited research into Ti-in-quartz (Wark and Watson, 2006) to show that Ti is known to occupy tetrahedral sites in other minerals, while no known mineral contains 8-coordinated Ti. Ferry and Watson (2007) also cited the already mentioned conference abstract of Harrison et al (2005) to "strongly suggest" that Ti substitution occurs on the zircon Si site. The most convincing evidence for Ti site occupancy comes from comparative results of Watson et al. (2006) and Ferry and Watson (2007) from experiments at 10 kbar/1,050 °C. The zircon-rutile-quartz assemblage (i.e., a_{SiO_2} =1) shows significantly lower zircon Ti contents (108 ± 23 ppm, Watson et al., 2006) than the zircon-rutile-zirconia assemblage (368 ± 28 ppm, where a_{SiO_2} =0.34 – Ferry and Watson, 2007).

[3] Representative photomicrographs and experimental descriptions of Watson et al (2006) make no mention of quartz, while reports from Ferry and Watson (2007) indicate that only one experiment of the original experiments contained quartz. This indicates that a_{SiO_2} was unconstrained in nearly all of the original calibration experiments.

Direct recalibration of the zircon thermometer was based on one experiment of Ferry and Watson[4] (2007 – containing β-quartz-zircon-rutile), while all other datum points were based on corrections made on the original work of Watson et al. (2006). Two datum points were taken from Watson et al. (2006) experiments, which report zircon-rutile-zirconia. Another four datum points were taken from zircon-rutile experiments of Watson et al (2006), with a_{SiO_2} estimated on the basis of Zr-in-rutile. A final four datum points were based on natural zircon populations containing β-quartz-rutile-zircon.

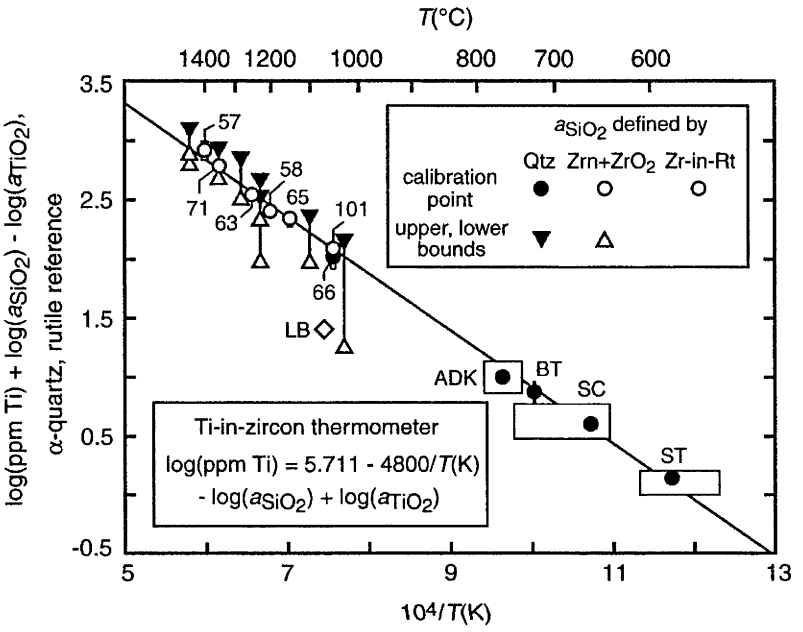

***Figure 3.10**: Recalibration of the zircon thermometer. Black circles with rectangles represent natural assemblages consisting of β-quartz-zircon-rutile, grey circles represent rutile-zircon assemblages where a_{SiO_2} is estimated from Zr-in rutile, open circles represent two Watson et al. (2006) experiments containing zircon-rutile-zirconia, open and black triangles represent 11 Watson et al. (2006) experiments where no Zr-in-rutile measurements were made and average Ti-in-zircon was used to calculate equilibrium with a fictive quartz (dark triangles) or zirconia (open triangles) buffer.*

Problems and concerns

In order to fingerprint Ti site occupancy in zircon, Ferry and Watson (2008) cited the work of Wark and Watson (2006) to indicate that Ti is known to substitute for the Si site in quartz. That such a substitution mechanism occurs in quartz is not surprising as there is no other available substitution site (of different or higher coordination), other than vacancies, defects or interstitial sites in which Ti may substitute. As demonstrated by Farges et al. (1996), most Ti in natural minerals is found in 4-, 5-, or 6-coordination (in terms of oxygen neighbours). As in the Watson et al. (2006) and Ferry and Watson (2007) hypothesis, this observation may be used to suggest that Ti substitution is more likely to occur on the Si site than the Zr

[4] It should be noted that a_{SiO_2} estimates of four synthetic zircon calibration points were calculation on Zr-in-rutile calibrations of Ferry and Watson (2007). This calibration is, in turn, based on natural and synthetic rutile studies from Watson et al. (2006) and Ferry and Watson (2007).

site in zircon. This being the case, comparison of ionic radii for cations at 4- and 8-coordination suggest that substitution is more likely to occur on the Zr site ($^{[8]}$Ti-0.74, $^{[8]}$Zr-0.84) than on the Si site ($^{[4]}$Ti-0.42, $^{[4]}$Si-0.26). If a phase other than zircon consisting of an 8-coordinated Zr site (or another cation of similar ionic radii and charge) and a 4-coordinated Si site existed, and contained trace Ti, this would represent a sound argument for Ti site preference in zircon. In short, 8-coordinated sites are rare while 4-coordinated Si sites dominate natural minerals. To demonstrate site preference in zircon it is necessary to compare Ti substitution in minerals of analogous structure.

Excluding reference to Harrison et al. (2005 –discussed in Section 3.3), the most convincing argument for site preference in zircon comes from experiments equilibrated within different mineral assemblages. As Ferry and Watson point out, zircon (at a_{TiO_2} =1) equilibrated with zirconia shows higher Ti content (368 ± 28) than zircon equilibrated with quartz (108 ± 23) at 1,050°C, which indicate that Ti substitutes on the zircon Si site. The greatest concern surrounding this observation (and the recalibration in general) is that it assumes zircon-rutile-zirconia is an equilibrium assemblage. Various studies into the ZrO_2-TiO_2±SiO_2 system (see Section 3.5) indicate that srilankite is an equilibrium phase at silica undersaturated conditions. Moreover, previous research indicates that zirconia and rutile are separated by the reaction:

$$ZrO_2 + TiO_2 = (Zr,Ti)_2O_4 \qquad (\textbf{\textit{eq. 3.11}})$$

The absence or instability of srilankite at silica undersaturated conditions can, to some extent, be assessed if zirconia and rutile analyses are compared with previous research (particularly the various works of Troitzsch and coauthors, 2004, 2005a, 2005b). This being the case, 4 of 5 experiments of Ferry and Watson (2007) assume Ti content of zirconia based on experiments of Troitzch and Ellis (2004), rather than presenting direct analyses from their own experiments. The absence of representative photomicrographs and Ti measurements of zirconia[5] or quartz makes it impossible to determine if such phases are primary, quench products or residual starting oxides. The absence of such analyses is unusual, as the TiO_2 and ZrO_2 content of both zirconia and rutile are expected to be at the wt% level (Troitzsch and Ellis, 2004, 2005a, 2005b; Wark and Watson, 2006) and easily determined by WDS or EDS.

The question of equilibration is not only pertinent to Ti site occupancy, but it also brings into question the accuracy of estimates surrounding the general calibration. Given that the revised zircon calibration was also based on the Zr-in-rutile correction of Ferry and Watson (2007), it is essential to demonstrate experiments attained equilibrium.

[5] Only one analysis has ever been reported from a third buffering phase, which was from experiment 101 (Ferry and Watson, 2007). Unfortunately these analyses were obtained from a zirconia population that has no previous research equivalent P-T in the ZrO_2-TiO_2 system.

3.5: Previous experimental research in the TiO_2-ZrO_2-SiO_2 system

The earliest research into phase relationships in the TiO_2-ZrO_2-SiO_2 system is found in material science literature. *Phase diagrams for Ceramists* (Levin et al., 1969), and references therein (Taggart and Andrews, 1957; Coughanour et al., 1954) provide a good overview of the system. Figure 3.11 shows the proposed isothermal section at 1atm/1400°C and indicates that five buffering phases exist in this system: rutile (TiO_2), tridymite (SiO_2), zircon ($ZrSiO_4$), tetragonal zirconia (ZrO_2) and srilankite[6] [$(Zr,Ti)_2O_4$].

Figure 3.11 demonstrates that the composition of rutile, srilankite and zirconia is dependent on the presence (or absence) of additional buffering phases within the system. Thus, Zr-solubility in rutile and Ti-solubility in zirconia, for example, appear to be dependent on the activity of ZrO_2, TiO_2 and SiO_2.

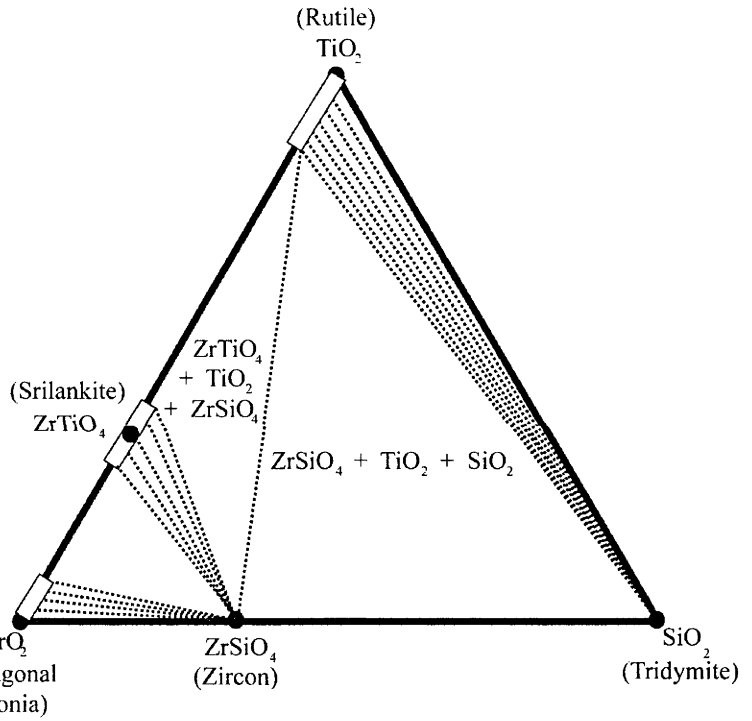

Figure 3.11: *TiO_2-ZrO_2-SiO_2 system (wt%) at 1 atm/1400 °C after Phase Diagrams for Ceramists (1997).*

A considerable amount of material science literature has focussed on the composition and physical properties of srilankite (e.g., Brown and Duwez, 1954; Taggart and Andrews, 1957; Coughanour et al, 1954; Newnham, 1967; Noguchi and Mizuno, 1968; Sugai and Hasegawa, 1968; Ono, 1972; Shevchenko et al., 1980; Willgallis et al., 1983; Bordet et al., 1986; McHale and Roth, 1983, 1986; Wllgallis et al., 1987; Buhl and Willgallis, 1989; Azough et al., 1996; Bianco et al., 1998; Troitzsch and Ellis, 2004, 2005; Troitzsch et al., 2005). On the basis of these 20 references and research presented in this thesis, there is a considerable body of research constraining the stability and composition of srilankite.

[6] Noting that the term srilankite only received IMA approval in 1983, and as such, was not used in the original publication.

Troitzsch and Ellis (2004, 2005a, 2005b) and the TiO_2-ZrO_2 binary

The most recent and up-to-date research on srilankite and the ZrO_2-TiO_2 system was presented by Troitszch and co-authors (2004, with additional data presented in 2005a, 2005b). The results of this research are consistent with previous research in the ZrO_2-TiO_2 system, cover a broad P-T range, and as their experiments contain reversal runs, are the most robust and thorough research.

The work of Troitzsch and co-authors (2004, 2005a, 2005b) demonstrates that a number of phase transitions and compositional shifts occur among ZrO_2-TiO_2 phases in response to ΔT and ΔP. Such changes are demonstrated in 1 atm experimental results (Figure 3.12), where zirconia and srilankite undergo distinct structural changes as a function of temperature.

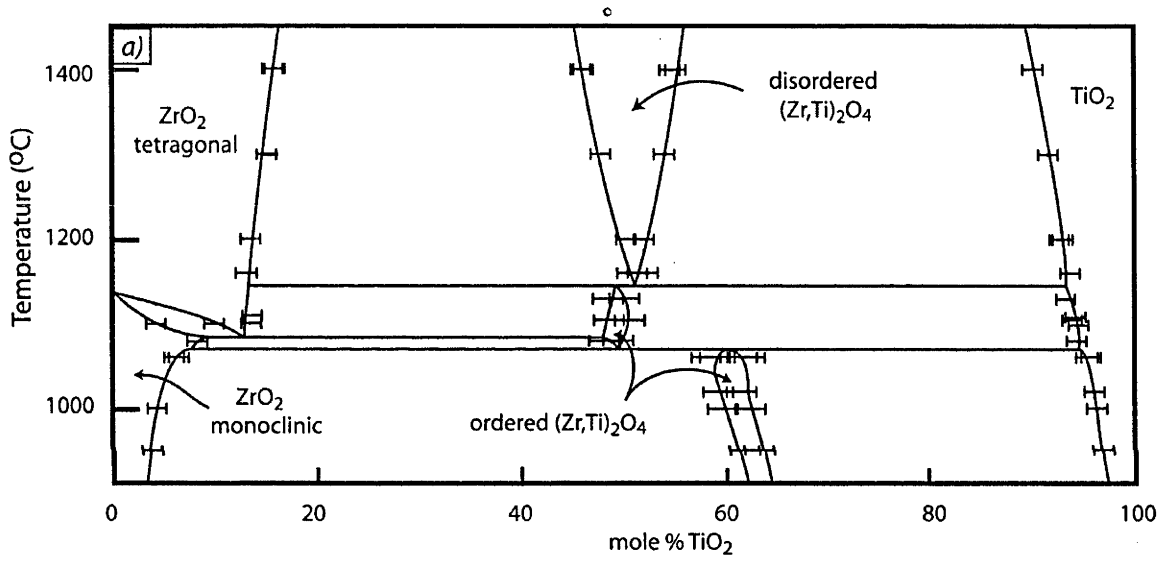

***Figure 3.12**: ZrO_2-TiO_2 binary system and phase analyses at 1 atm (after Troitzsch and Ellis, 2005a)*

The effect of pressure is shown in Figure 3.13, with all minerals in the ZrO_2-TiO_2 system shifting to higher Ti contents with increasing pressure.

The work of Troitzsch and co-authors (2004, 2005a, 2005b) also demonstrates that srilankite is a stable phase at temperatures between 950-1,400 °C and pressures between 0.001-28 kbar (noting that these conditions represent the P-T conditions of experiments and srilankite may be stable over a broader range).

3.6: Summary

The theme which emerges from zircon thermometer studies is that there is a clear temperature dependence on Ti-in-zircon, while some uncertainty exists on how various factors contribute to the accuracy of a given temperature estimate. In order to address the influence of both a_{SiO_2} and a pressure effect on zircon thermometry, it is essential to

conduct experiments in which a_{SiO_2}, a_{TiO_2} and a_{ZrO_2} are constrained by coexisting (buffering) mineral assemblage.

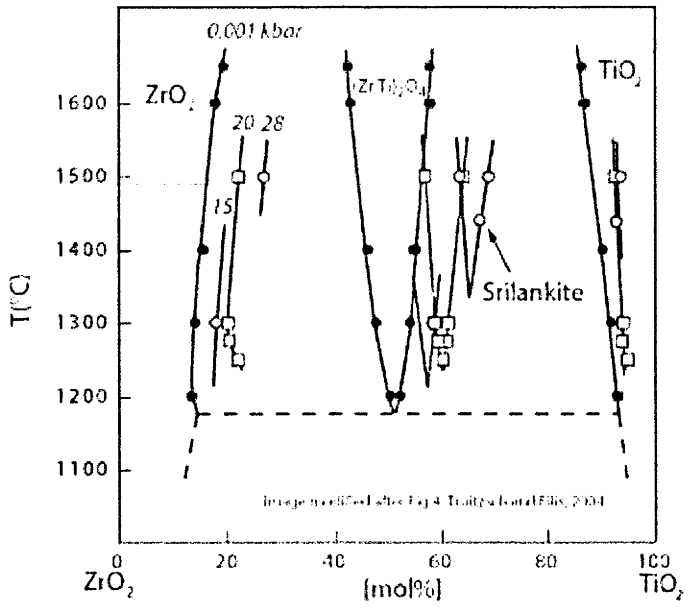

***Figure 3.13**: Binary ZrO_2-TiO_2 system as a function of pressure. Italic numbers refer to experimental pressure in kbar (image reproduced after Troitzsch and Ellis, 2004).*

3.7: Thesis overview – aims and rationale

The main aim of this research is to determine Ti site occupancy in zircon. The details of this research are primarily concerned with how the zircon thermometer functions over a range of pressure-temperature-composition (P-T-*X*) conditions applicable to natural zircon-bearing rocks. As such, this aim differs from previous research and discussion (e.g., Watson et al., 2006; Glikson, 2006; Nutman, 2006) in that it is not concerned with what a given temperature estimate represents, but how Ti site occupancy may influence the accuracy of a given temperature estimate. In addition to calibration of the zircon thermometer, Ti site occupancy can also be used to assess the relationship between Ti distribution and petrographic techniques applied to zircon (e.g., scanning electron microscopy cathodoluminescence and electron back scatter imagery).

Chapter 4

Experimental Strategy

The aim of this experimental study was to synthesize un-seeded zircon grains, equilibrated under varying bulk compositions, mineral assemblages and temperatures in order to investigate Ti site occupancy in zircon. Considerable focus was place on crystallizing zircons of sufficient size for XANES, EPMA and LA-ICP-MS analyses.

Synthesizing phases of the TiO_2-ZrO_2-SiO_2 system presents an experimental challenge, particularly at conditions relevant to geothermometry. Sluggish kinetics surrounding the nucleation of zircon and srilankite poses particular difficulties. In order to circumvent the "metastability" problem inherent to experiments within the TiO_2-ZrO_2-SiO_2 system, a flux-type method was used in this study (previous examples analogous to this method include Ballman and Laudise, 1965; Hanchar et al., 2001; Troitzsch and Ellis, 2004, 2005a; Troitzsch et al., 2005b). The greatest difficulty surrounding flux-based experiments is maintaining the buffered mineral assemblage. If too much flux is added to the experimental charge, it is possible to completely dissolve one or more phase. Further, selective dissolution of various oxide components (or reactants) – relative to other starting oxide components – within the flux has the ability to significantly modify a given TiO_2-ZrO_2-SiO_2 starting composition such that it no longer belongs to the buffering field to which it was intended.

The fluxing method involves the application of low melting point compounds, in this case Na_2WO_4 ± WO_3 (melting temperature 698 °C), within which the experimental reactants (TiO_2, ZrO_2 and SiO_2) are soluble. As experimental temperatures of this study are >400 °C above the melting point of the Na_2WO_4, the flux melt acts as a transport medium that permits faster diffusion of experimental reactants. It is the ability of fluxing agents to decrease the amount of time required for an experiment to attain equilibrium, without influencing phase relationships/reactions, which makes them useful in the study of systems containing zircon and srilankite.

The use of Na_2WO_4 has the added advantage that the flux is water soluble. Experimental run products, including phases and glass, can be separated from Na_2WO_4 by washing pierced/exposed capsules with warm deionized H_2O post quench. In this manner, the flux technique does not require extensive acid etching treatment (e.g., HF) in order to isolate individual phases for analysis.

4.1: Starting material

Oxide starting mixtures of reagent grade powders of TiO_2 (Ventron – 99.8 % purity), ZrO_2 (Hopkins and Williams – 99.9 % purity), and SiO_2 (Aldrich – 99.995 % purity) were ground under acetone in an agate mortar and dried for 2 hours at 200 °C. $Na_2WO_4.H_2O$ (Aldrich – 99.0 % purity) ± WO_3 (Strem – 99.8 % purity) flux mixtures were dehydrated at 400 °C for 24 hours prior to all experiments.

4.2: Experimental setup

Experimental flux and oxide powder mixtures are shown in Table 4.1. Starting mixes were pressed into 2 mm (outer diameter) Pt capsules welded at one end and crimped at the other.

Crimped capsules were suspended using Pt wire attached to a Pt chandelier in a one atmosphere gas mixing vertical furnace (O'Neill and Mavrogenes, 2002). Experiments were run in air, with temperature controlled via a type B thermocouple held immediately adjacent to the experimental charge.

Table 4.1: Experimental starting compositions

Run #	Temperature (°C)	Run time (hours)	TiO_2 (wt %)	SiO_2 (wt %)	ZrO_2 (wt %)	Na_2WO_4 (wt %)	WO_3 (wt %)
1100-*l*	1,100	216	6.60	6.60	6.60	80.00	-
1100-*p*	1,100	216	1.99	2.01	16.00	80.00	-
1100-*c*	1,100	216	4.98	4.01	11.02	79.99	-
1200-s	1,200	168					-
1200-u	1,200	168					-
1200-b	1,200	168	6.05	11.94	12.01	70.00	-
1300-U	1,300	168	5.02	4.06	11.03	79.89	-
1300-S	1,300	168	6.66	6.64	6.65	80.05	-
1300-SF-1.1†	1,300	168	19.75	19.75	19.75	40.15	-
1300-BF-1.2†	1,300	168	6.00	6.00	48.00	40.00	
1300-UF-1.2†	1,300	168	15.06	12.05	33.13	60.24	-
1300-SF-1.2†	1,300	168	19.75	19.75	19.75	26.76	13.38
1400+	1,400	168					

†pre-sintered oxide powders

All experiments were rapid quenched in water and pierced with a stainless steel drill bit or tungsten carbide tool. Pierced capsules were leached on a hotplate for 2-6 hours with de-ionized H_2O at ~40 °C. Leached capsules were impregnated with EPO-FIX epoxy resin and, if residual tungstate flux was still present, the mounted capsule was treated with 1M nitric acid.

Starting mixtures for experiments run at temperatures between 1,100 and 1,300 °C (Table 4.1) utilized TiO_2:ZrO_2:SiO_2 compositions designed to correspond to the three mineral buffered fields shown in Figure 4.1: zircon-cristobalite-rutile, zircon- srilankite-tetragonal zirconia and zircon-srilankite-rutile. Table 4.1 also demonstrates that two types of experiment were employed for this study: 1) oxide mixes pre-sintered at the experimental conditions, and 2) oxide mixes not pre-sintered. Pre-sintering an oxide mix at experimental conditions stimulates nucleation of TiO_2-ZrO_2-SiO_2 phases at the temperature of interest. In this manner pre-sintered oxides operate as crystal seeds in the subsequent flux-bearing experiment, with seeds having a composition appropriate for the run conditions (rather than arbitrary crystal seeds).WO_3 was added to some pre-sintering experiments to limit the amount of alkalis available to produce "Na_2O-SiO_2" melt, while all other experiments contained only Na_2WO_4.

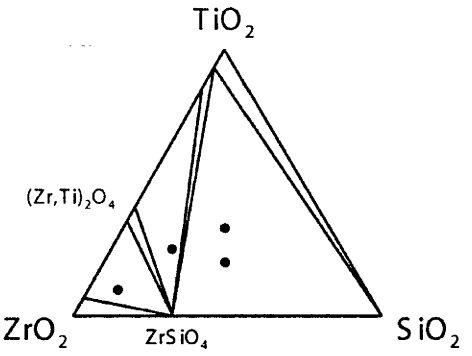

***Figure 4.1**: Experimental starting compositions in the ZrO_2-TiO_2-SiO_2 system.*

4.3: Synchrotron standards

Synchrotron standards of Ti-doped SiO_2 and ZrO_2 were made from gels of $Si(OC_2H_5)_4$, $Ti(OC_2H_5)_4$ and $ZrO(NO_3)_2.xH_2O$ mixtures. Dehydration-weight loss techniques were used to calibrate the water content of zirconyl nitrate.

The sol-gel technique ensures a homogeneous distribution of Ti in the sample, with compounds mixed in ratios to give $Si_{0.992}Ti_{0.008}O_2$ (0.59 wt% TiO_2) and $Zr_{0.993}Ti_{0.007}O_2$ (0.99 wt% TiO_2). Starting materials were pressed into pellets and fired in air at 1,400 °C for 168 hours. In order to monitor sample homogeneity, synchrotron standards were imaged by SEM-BSE, analyzed by EPMA and phase identified by XRD.

Chapter 5

Analytical Techniques

The various analytical techniques used in this research range from general phase analysis to methods to determine Ti site occupancy in zircon. These techniques include scanning electron microscopy (SEM-EDS), electron probe microanalysis (WDS), laser ablation mass spectrometry (LA-ICP-MS), x-ray absorption near edge structures (XANES), x-ray absorption fine structures (XAFS) and cathodoluminescence (SEM-CL). The various analytical spectrographic techniques employed here were accompanied by density functional techniques (SIESTA modelling) and XANES modelling (FEFF8.4 software).

5.1: Scanning Electron Microscopy (SEM-EDS)

Phase identification and petrography were determined by scanning electron microscopy (SEM). Quantitative analysis of experimental run products, with the exception of Ti-in-zircon, was obtained by energy dispersive x-ray spectroscopy (EDS) on a JEOL JSM6400 instrument housed at the Research School of Biological Sciences, ANU.

Beam conditions were set at an accelerating voltage of 15 kV and a beam current of 1 nA. Mineral analyses incorporated a focused beam, with spectra collected over a 120 second counting period. Glass analyses, which involved quantification of a potentially volatile sample medium, were undertaken with a broad scanning beam. Spectrum acquisition time for glass analyses varied from 60-120 seconds, while time series analyses of glass show that Na loss never exceeded 5% over the counting period. SEM-EDS standards included albite (Na and Al), sanidine (Si), rutile (Ti), zirconolite (Zr and Ti), hematite (Fe), pure hafnium (Hf), pure tungsten (W) and zircon (Zr and Si). All spectra were processed with LINK ISIS-SEMIQUANT, employing full ZAF (2 or 3 iterations).

5.2: Electron Probe Microanalysis (WDS)

Electron microprobe analyses used a Cameca SX100 in the wavelength dispersive mode. All analyses used a beam current ranging from 20-40 nA, an accelerating voltage of 15 KeV, and a ~1x1 μm focused beam. The Ti counts were measured simultaneously on two LPET spectrometers, calibrated against natural rutile, zircon (19500) and zirconalite (Phalabowra). Counting times for both spectrometers on the Ti peaks were set to 60 s with the SX100 EPMA software indicating a detection limit of 2 ppm and a 3σ precision of 0.14.

The Ti concentrations of zircons synthesized in this research were several orders of magnitude above the detection limit. Care was taken to avoid problems from stray electrons (e.g., Hermann et al., 2005) by ensuring that the beam was focused away from inclusion-rich domains or edges shared with other (Ti- or Zr-rich) phases. The transparency of synthetic zircons made it possible to target regions within grains devoid of inclusions as determined optically. Similarly, cathodoluminescence under the electron beam made it possible to track beam position relative to the presence of inclusions. Synthetic zircon produces a bright turquoise-blue cathodoluminescence under the electron beam, while zirconia produces a bright green signal and all other phases/species show no CL activation. Phase transparency, optical microscopy, BSE imagery and CL observations can collectively be

combined to optimally target zircon domains (on the surface, at depth and within the electron beam excitation volume).

Ti K-α, Si K-α and Hf L-β X-ray maps were recorded for the largest zircon grains produced in this study, from experiment 1300-U. Analytical polygons were designed to correspond to the size of each zircon grain – ranging from ~80x80 μm to ~300x3000 μm grains. Column conditions were set at 15 KeV and 200 nA, with each analysis (pixel) incorporating a 0.5 second dwell time and separated by a 2 μm step.

5.3: Synchrotron Techniques

Ti K-α edge XANES spectra were collected at Beamline 13-ID-C (GSECARS), at the 7 GeV Advanced Photon Source, Argonne National Laboratory (IL, USA). All $ZrSiO_4$ (zircon), tetragonal zirconia, and SiO_2 (cristobalite) spectra were collected in fluorescence mode, while TiO_2 (rutile) spectra were collected in transmission mode.

Spectra were recorded from individual grains of zircon synthesized in the 1 bar/1,300 °C experiments described in Chapter 4 of this thesis, and embedded in epoxy mounts. Standards of tetragonal zirconia containing ~10,000 ppm Ti and cristobalite with ~5,000 ppm Ti were synthesized from oxide powders (1 bar/1,400 °C/168 hour runtime), with XANES analyses carried out on powders mounted in epoxy mounts. Scanning electron microscopy and x-ray diffraction confirmed that the cristobalite and tetragonal zirconia in the standard mounts consisted of homogenous single-phase material. The in-house (GSECARS) rutile standard consisted of a fine powder mounted between two sheets of kapton film.

The incident photon energy was selected via a cryogenically-cooled Si-(111) double crystal monochromator. The energy resolution for measurements made at the Ti K-edge is ~0.5 eV. Energy calibration of the monochromator on the Ti K-edge was carried out by defining the first derivative peak of the spectrum of Ti metal foil to be 4966 eV. The beam was located and focused to a 2 μm x 2 μm spot using Kirkpatrick-Baez (KB) mirrors by imaging on a Ce-doped YAG phosphor. The critical angle cut-offs of the mirrors provide excellent rejection of high energy harmonics. Absorption spectra were recorded from 4816-4976 eV, with steps of 5 (<4957 eV), 0.25 (4957-4992 eV), and 3 eV (4922-5348 eV; k = 10). Fluorescence was recorded at 45° to the sample and perpendicular to the incident x-ray beam using a Vortex-EX silicon drift detector (SII NanoTechnology Inc.) with digital signal processing electronics from which the Ti K-α integrated intensity was extracted and recorded digitally. Bragg diffraction peaks from the zircon host were rarely observed.

Spectra were recorded for 45 randomly orientated, synthetic zircon crystals. An additional four synthetic zircons were selected for measurement as a function of orientation, for which spectra were recorded at 90° rotations of the crystal. Attempts to acquire spectra from natural zircons were thwarted by their low Ti content (i.e., <20 ppm).

Scans were also carried out on the pre-edge region (4916-4976 eV) for sector-zoned synthetic zircons from experiment 1300-U. While such scans cannot be normalized against the main absorption edge (i.e., pre-edge intensity is unconstrained), they can be used to determine relative energy shifts in the 1*s*-3*d* Ti K-α pre-edge feature as a function of position within the zoned zircon.

Spectra normalization was performed with Athena software (version 0.8.050, Ravel and Newville, 2005). Background subtraction over the pre-edge energy range employed a line function regressed to the raw spectra, while the post-edge region involved regression with a quadratic polynomial. Visual inspection of the pre-edge and post-edge lines ensured that the energy range (or input parameters in Athena) of pre-edge and post-edge lines were optimal for normalization. Extended X-ray Absorption Fine Structure (EXAFS) spectra were modelled using the XFIT software package (Ellis and Freeman 1995) and FEFF 6.01 (de Leon et al. 1991). The EXAFS were fit with a single-scattering shell model using a Levenberg-Marquardt algorithm within XFIT.

5.4: Scanning Electron Microscopy Cathode Luminescence (SEM-CL)

SEM-CL imaging was carried out on polished grain mounts using a conventional low-vacuum Hitatchi S2250-N SEM located at the Research School of Earth Science, ANU. The beam current was set at 40 μA and accelerating voltage of 15 KeV. Slow-scan CL imaging was carried out on natural igneous zircons from Northern Queensland, natural metamorphic zircons from Monviso (Alps), and synthetic grains produced in this study.

5.5: Laser-Ablation ICP-MS analyses

LA-ICP-MS analyses were carried out using an Agilent 7500S, coupled to an ANU HelEX ArF laser system (193 nm wavelength). Two LA-ICP-MS techniques were employed in order to determine the Ti distribution in natural zircons: 1) 25x125 μm slit scan traverse analyses were used to establish the relative distribution of trace elements in the different domains imaged by cathode luminescence, and 2) 80 μm spot analyses, to quantify trace element contents within individual domains.

Slit scan analyses involved the analysis of mass numbers corresponding to ^{89}Y, ^{31}P, ^{238}U, ^{232}Th, ^{172}Yb, and ^{49}Ti. Spot scans incorporated a broader array of trace elements, including ^{238}U, ^{232}Th, $^{208, 207, 206}Pb$, ^{181}Ta, ^{97}Mo, ^{49}Ti, ^{31}P, ^{91}Zr, ^{177}Hf, ^{93}Nb, ^{89}Y, ^{55}Mn and most of the REEs. ^{97}Mo counts were collected in order to establish the potential isobaric interference of doubly charged ^{98}Mo on the ^{49}Ti signal. Standard glass NIST612 was used for calibration while ^{177}Hf was used as the internal standard for spot analyses and was measured by EPMA. Data reduction was performed using an in-house data reduction program based on the method outlined in Longerich et al. (1996).

5.6: Density Functional Theory (DFT) modelling

The structure and energies of various hypothetical Ti incorporation mechanisms were investigated by Dr. Andrew Walker (University College London) using computational

simulation techniques making use of DFT (Hohenberg and Kohn, 1964; Kohn and Sham, 1965).

The SIESTA methodology and code (Soler et al., 2002) is used to examine Ti incorporation by direct substitution for Zr and Si in zircon, and at various potential interstitial sites. The approach is similar to that used to study Ti incorporation in olivine (Berry et al., 2007; Walker et al., 2007) and the thermodynamics of Mg_2TiO_4 spinel (Palin et al., 2008). Briefly, the calculations are performed using a pseudoatomic basis for the valence electrons and pseudopotentials for the atomic cores. Pseudopotentials are fitted to all-electron calculations using the scheme of Troullier and Martins (1991). The basis functions are of double-zeta polarised quality and consist of atomic orbitals confined within a smooth potential that becomes asymptotic to infinity at a chosen radius (Junquera et al., 2001). Along with the pseudopotentials, parameters defining the shape of the basis functions are taken from previous calculations (Junquera et al., 2001; Gale, 2006). The generalised gradient approximation (GGA) with the functional of Perdew et al. (1996) was used with an auxiliary basis consisting of a uniform real space grid defined by a cut-off energy of 250 Ry supplemented by 2x2x2 grid cell sampling.

For the defect cells, the periodic simulation box was a 2x2x2 supercell of the zircon unit cell containing 192 atoms (32 formula units of $ZrSiO_4$). One of the Zr or Si atoms was replaced with a Ti impurity atom. The impurities were therefore separated by >12 Å, enough to minimise defect–defect interactions and allow the simulation of incorporation in the dilute limit. For these calculations the cell parameters were held fixed and the relative positions of the atoms in the simulation cell were allowed to vary in order to minimise the energy. A total of 15 different ways to include Ti in the zircon supercell were considered. First was the direct substitution for Si or Zr with the Ti impurity occupying the centre of each cation site. An additional two initial configurations had Ti substituting for Zr but with Ti located away from the centre of the coordination sphere to consider the possibility of distorted, lower coordination sites. The other initial configurations considered two plausible sites for interstitial Ti located in the channels containing the four-fold screw axis, parallel to the crystallographic *c* direction. On the basis of the distance from coordinating oxygen atoms two sites were located, one a distorted tetrahedron displaced from the screw axis and the other a distorted octahedron with a centre on the screw axis. In each case the impurity was charge balanced by an adjacent Si or Ti vacancy. For the interstitial tetrahedron there are three adjacent Zr and two adjacent Si sites that could host the vacancy while for the interstitial octahedron there are four Zr and two Si sites that could host the vacancy. Because of the low-symmetry nature of the distorted interstitial sites, the 11 ways of charge balancing the interstitial are in-equivalent.

In addition to the zircon supercell, the cohesive energy for a number of other phases was calculated. Data for α-quartz and rutile were taken from calculations described in Berry et al. (2007), while the fully optimised structure and energy of baddeleyite was calculated using the same methodology and a 5x5x5 Monkhorst–Pack mesh (Table 3). For computational

efficiency, the 2x2x2 supercell reciprocal space was only sampled at the gamma point and although this is not completely converged with respect to total energy, the error introduced is less then 0.01 eV.

5.7: XANES Modelling

The Ti K-edge XANES spectra of Ti occupying both the Si and Zr sites in zircon were simulated by Dr. I. Rodina and Dr. A. Soldatov (Southern Federal University) for the defect structures predicted by DFT using a self-consistent full multiple-scattering method (Rehr and Ankudinov, 2005) within FEFF8.4. The spectra were calculated for non-local Dirac-Fock, Hedin-Lundqvist, and Dirac-Hara exchange potentials. The spectral dependence on polarisation, electronic relaxation in the presence of the core-hole, and the cluster size around the absorbing atom were all investigated.

Chapter 6

Results

The results of this research have been derived from a number of analytical and modelling techniques used to fingerprint Ti site occupancy in zircon. As each technique is based on fundamentally different methods, this chapter separates results based on different methods into the following order:

1. Results obtained from TiO_2-ZrO_2-SiO_2 experiments, including experimental petrography and phase analyses.
2. Density functional theory (DFT) calculations based on SIESTA simulations.
3. Synchrotron methods, including measured and modelled XANES spectra.
4. SEM-CL imagery of natural and synthetic zircon with associated trace element analyses.

6.1 TiO_2-ZrO_2-SiO_2 experimental petrography

Representative BSE images of zircon experimental runs are presented in Figures 6.1-6.6 and described in Table 6.1. Experiments produced assemblages consisting of two or three mineral species (with the exception of 1200-b and 1400+), a sodic glass and tungstate flux.

Table 6.1: Summary of experimental run products

Run #	Run products†
1100-l	rutile, zircon, Na-melt
1100-p	rutile, zircon, Na-melt
1100-s	rutile, zircon, Na-melt
1200-s	srilankite, tetragonal zirconia, Na-melt
1200-u	srilankite, tetragonal zirconia, Na-melt
1200-b	tetragonal zirconia, Na-melt
1300-U	rutile, zircon, srilankite, Na-melt
1300-S	rutile, zircon, Na-melt
1300-SF-1.1	rutile, zircon, cristobalite, Na-melt
1300-BF-1.2	tetragonal zirconia, Na-melt
1300-UF-1.1	srilankite, tetragonal zirconia, zircon, Na-melt
1300-SF-1.2	rutile, zircon, cristobalite, Na-melt
1400+	zircon, zirconia, Na-melt

†Note that all experiments contain tungstate flux

Na_2WO_4 flux

Na_2WO_4 flux is not shown in the majority of photomicrographs as the compound was removed via acid or water leaching of capsules after quench (see Chapter 4). Photomicrographs from experiment 1200-b, an unleached experiment, indicates immiscibility between sodic "silicate" melt and tungstate melt (noting that experimental glasses contain measurable WO_3 contents, suggesting some mutual solubility). The texture seen in experiment 1200-B (Figure 6.1) shows that silicate and tungstate domains are clearly defined with very little intergrowth. This observation suggests that the two melts are immiscible at experimental temperatures and are not quench products.

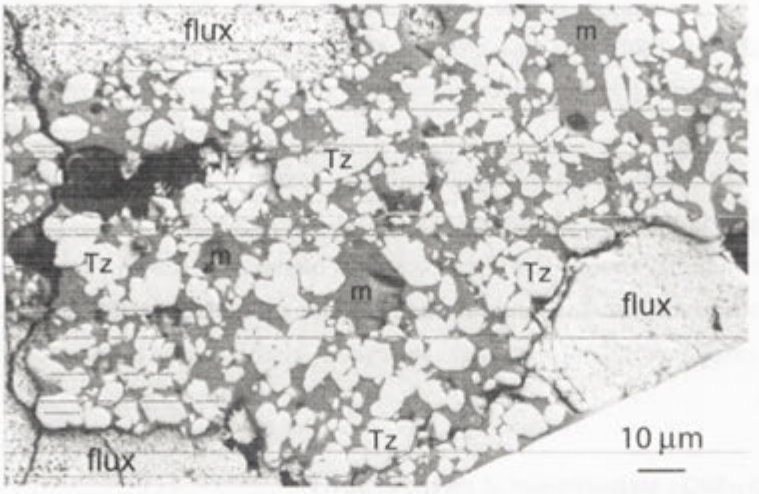

***Figure 6.1**: BSE image of unleached experiment 1200-b showing immiscibility of silicate and tungstate flux. Horizontal 'streaks' in the image are related to charging on the sample surface (progressive beam damage to the volatile flux disrupts the carbon coat). Abbreviations, flux = Na_2WO_4, m = sodic melt and Tz = tetragonal zirconia.*

Sodic melt

Sodic melt was developed in all experiments, with analyses (Table 6.2) showing that melt composition varies significantly with starting composition (particularly TiO_2:ZrO_2:SiO_2) and temperature. Glass analyses are not reported from experiment 1100-*s* because the sodic glass (and tungstate flux) was removed by treatment with 1M nitric acid prior to analyses. It is also worth noting that some glasses show minor Al_2O_3 and/or FeO* contents, components not included in the starting composition, as determined by EDS. The minor introduction of such components is likely related to contamination from the 1 atmosphere furnace (as capsules are crimped and not welded).

Zircon

Experimental zircons produced in this research show angular and well-defined crystal margins, with most grains showing euhedral habit. Zircon grain size is consistent within individual experiments, but varies from 5-600 µm (measured on the crystal long axis) across different experimental runs. Zircons commonly contain a variety of mineral and melt inclusions. Those phases present in the overall groundmass (e.g., rutile, srilankite, zirconia, etc) and residual oxide starting material (particularly ZrO_2) are also included within minerals.

Rutile

Experimental rutiles generally form large (10-200 µm across the long axis), euhedral and elongate grains within experiments. Rutile rarely contains mineral inclusions but can contain rare melt inclusions.

Srilankite

SEM imagery indicates that srilankite petrography varies between experiments. Experiment 1200-u shows euhedral and homogenous srilankite needles (as observed in electron back scatter and analyses), while experiments 1200-s, 1300-U and 1300-UF-1.1 show more subhedral and rounded srilankite grains. As shown in Figure 6.2, srilankite grains from 1200-s show internal compositional zonation (which is reflected in the large σ in Table 6.3). Srilankite grain size is similar among all experiments, with grains generally 10-25 μm in length and 5-10 μm in width.

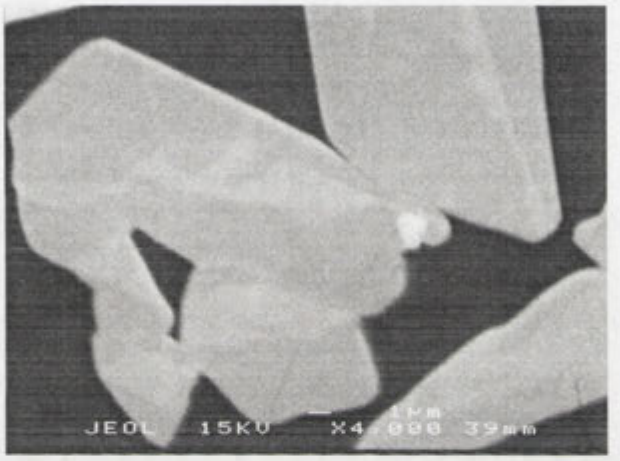

***Figure 6.2**: Internal zonation in 1200-u srilankite imaged with BSE.*

Tetragonal zirconia

Experimental zirconia grains range from 10-40 μm in length (measured across the long axis) and generally exhibit short prismatic to slightly rounded crystal habits. SEM observations indicate that tetragonal zirconia grains are homogeneous (confirmed by the particularly low standard deviation of analyses) and contain almost no inclusions.

General petrography

The various experiments in this research show that all phases within the TiO_2-ZrO_2-SiO_2 system (see Section 3.5 and Figure 3.11) are readily synthesized by the experimental technique. More importantly, grains produced in this research are of sufficient size to permit analysis using various techniques.

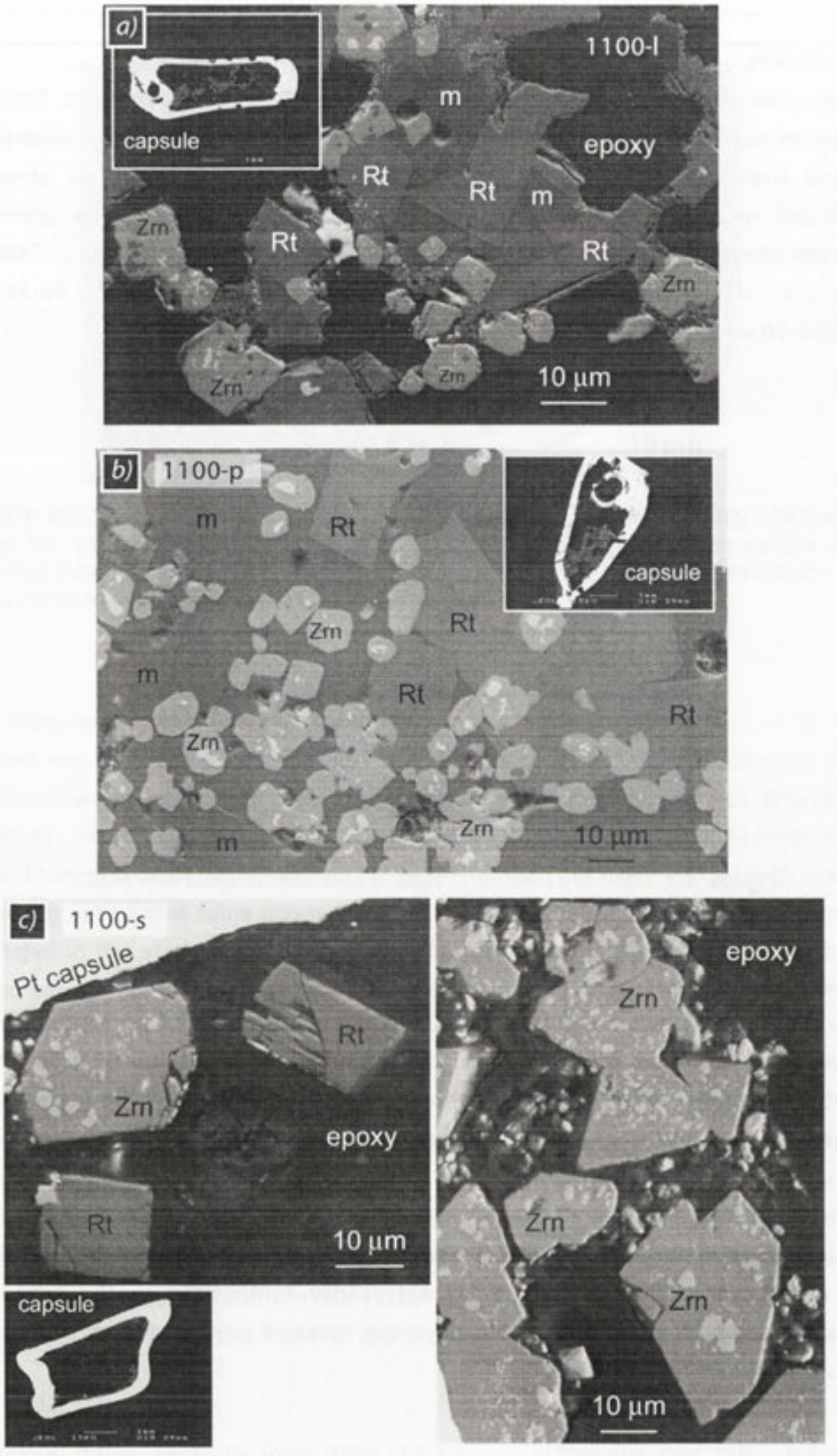

***Figure 6.3**: Representative electron back scatter images of 1,200 °C experiments. Abbreviations – Zrn = zircon, Rt = rutile and m = sodic melt. "Circular" voids in capsules shown in a) and b) represent the locus of capsule piercing. Sodic melt is absent from experiment 1100-s because the experiment was treated with 1 M nitric acid.*

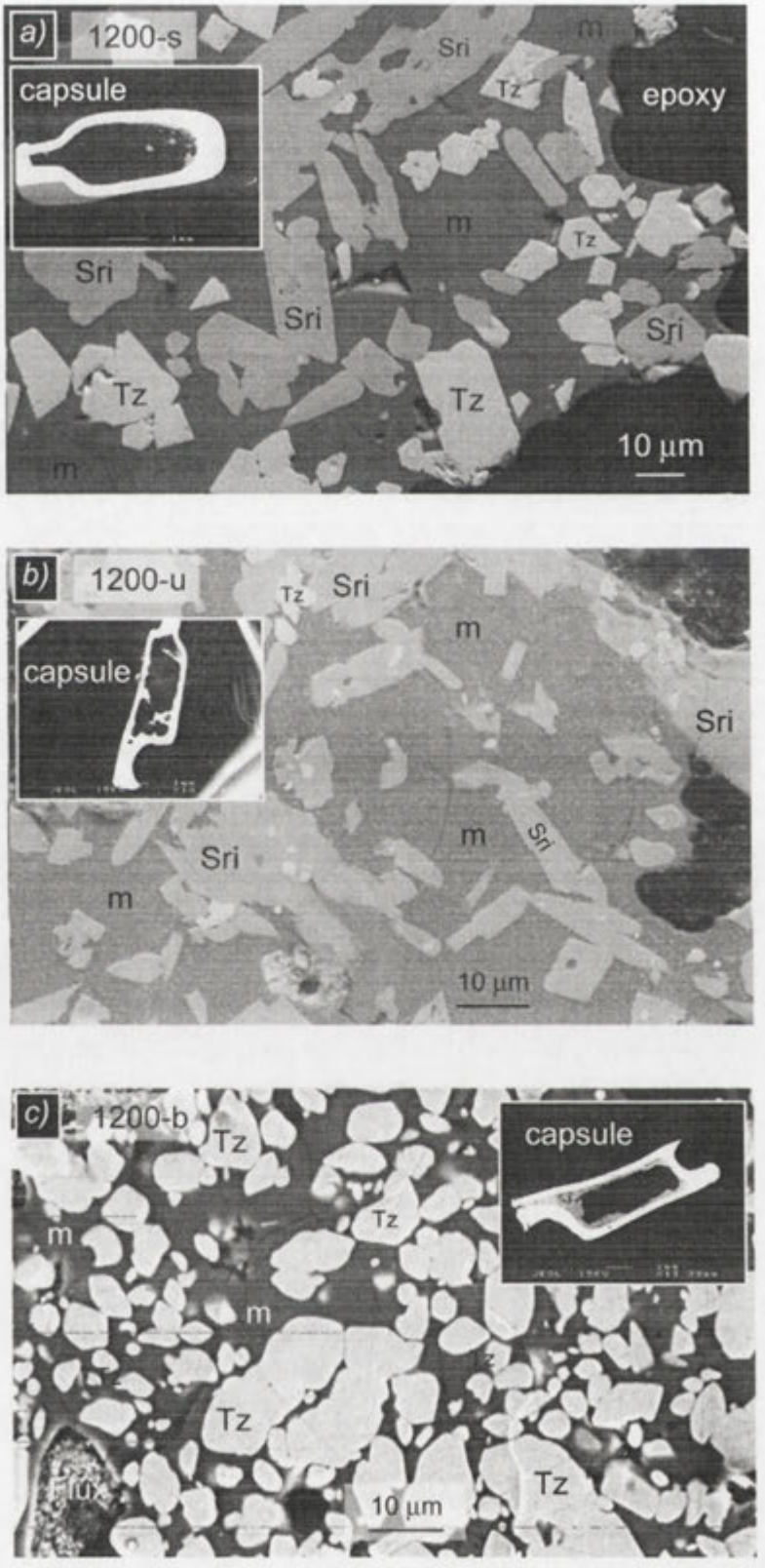

***Figure 6.4**: Representative electron back scatter images of 1,200 °C experiments. Abbreviations – Tz = tetragonal zirconia, Sri = srilankite. All other abbreviations as in previous figures.*

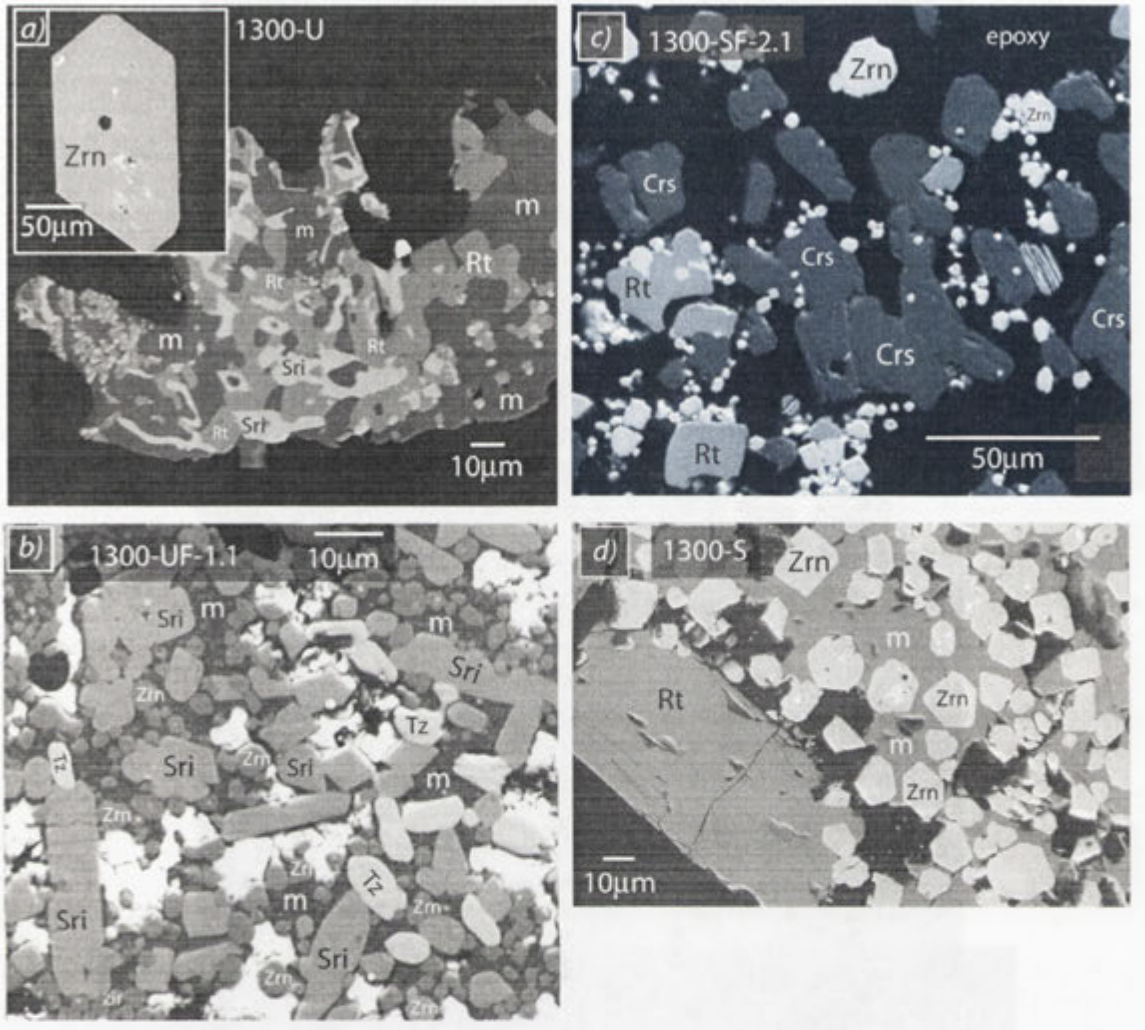

***Figure 6.5**: Representative electron back scatter images of 1,300 °C experiments. Abbreviations as in previous figures.*

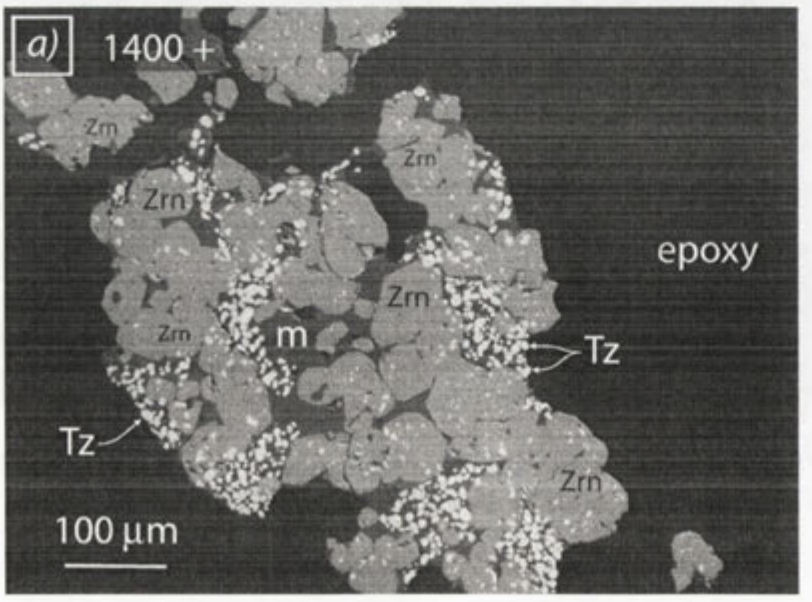

***Figure 6.6**: Representative electron back scatter image of 1,400 °C experiments.*

6.2: EMPA and EDS results: with a focus on synthetic zircons

Experimental melt and phase compositions are presented in Table 6.2 and Table 6.3. Broad, scanning beam analyses of glass show variable Na_2O concentrations from different experiments (with the greatest variation showing 2σ falling within 31% of the mean). This variability likely results from varying degrees of volatilization under the electron beam. It is interesting to note that glasses showing the least statistical variation in Na_2O are from experiments of the lowest alkali content and glasses with the highest TiO_2 content.

Mineral analyses from experiments (Table 6.3) indicate that most minor element substitutions exist at the wt% scale, with all analyses showing notably small statistical variation. Zircon is the only phase among experiments that requires special statistical consideration, as Ti solubility is limited and statistical/analytical distribution is particularly relevant to the accuracy of data interpretation.

Pre-sintered experiments, despite having the smallest grain size and being most susceptible to signal interference via secondary x-ray fluorescence, show zircons with the lowest standard deviations about the mean Ti content. Pre-sintered zircons show measured zircon Ti contents with 2σ falling within ~20 % of the mean. Analytical traverses of pre-sintered experiments show no core-rim or any other form of internal zonation within synthetic zircon grains.

Table 6.2: Melt composition

Run #	1100-*l*	1100-*p*	1200-s	1200-u	1300-U	1300-S	1300-BF-1.2	1300-UF-2.1	1400+
Analyses	8	8	8	5	6	7	7	8	7
Na_2O (σ)	9.49 (1.47)	15.52 (1.41)	15.24 (0.14)	15.06 (0.19)	2.55 (0.25)	4.62 (0.46)	12.13 (1.40)	9.81 (0.99)	10.53 (0.60)
Al_2O_3 (σ)	0.81 (0.07)	bd	bd	0.17 (0.05)	6.80 (0.40)	bd	0.32 (0.05)	0.57 (0.07)	0.12 (0.06)
SiO_2 (σ)	54.34 (1.68)	44.19 (0.95)	29.42 (0.19)	25.47 (0.25)	72.66 (2.19)	61.48 (0.93)	34.11 (0.18)	38.88 (1.64)	60.02 (0.17)
TiO_2 (σ)	16.63 (0.85)	24.35 (1.30)	37.26 (0.27)	37.32 (0.29)	5.07 (0.23)	14.98 (0.56)	28.22 (0.26)	23.88 (3.08)	2.78 (0.15)
FeO (σ)	1.63 (0.10)	bd	0.19 (0.08)	0.83 (0.08)	bd	bd	1.60 (0.07)	bd	0.83 (0.06)
ZrO_2 (σ)	10.78 (0.26)	10.36 (0.36)	9.12 (0.13)	7.82 (0.07)	1.26 (0.17)	9.99 (0.44)	10.67 (0.12)	10.34 (3.99)	21.98 (0.24)
WO_3 (σ)	6.32 (0.43)	5.58 (0.38)	9.41 (0.17)	12.59 (0.47)	9.51 (0.45)	9.40 (0.35)	10.48 (0.24)	15.88 (4.43)	1.43 (0.32)
Total	98.41 (3.20)	98.15 (0.92)	100.64 (0.48)	99.25 (0.62)	97.84 (0.62)	100.48 (0.86)	98.20 (1.23)	98.86 (1.33)	98.41 (0.84)

Note that acid treatment of experiments 1100-s and 1300-SF-2.1 resulted in the complete digestion of sodic glass. Abbreviations – bd = below detection limit.

Table 6.3: Phase analyses

Experiment	Temperature (°C)	Phase	Analyses	SiO_2 (σ)	TiO_2 (σ)	ZrO_2 (σ)	HfO_2 (σ)	Ti-in-zircon ppm (σ)
1100-*l*	1,100							
		rutile	10	bd	93.46 (0.44)	8.30 (0.12)	bd	
		zircon*		35.83 (0.24)		61.76 (0.50)	1.14 (0.08)	3789 (1161)
1100-*s*	1,100							
		rutile	7	0.15 (0.03)	93.04 (0.73)	7.62 (0.27)	bd	
		zircon*	21	35.50 (0.38)	0.57 (0.09)	61.94 (0.34)	1.21 (0.12)	3363 (623)
1100-*p*	1,100							
		rutile	9	bd	93.18 (1.10)	7.11 (1.05)	bd	
		zircon	-	-	-	-	-	-
1200-u	1,200							
		srilankite	5	bd	43.21 (0.55)	55.89 (0.75)	1.45 (0.16)	
		zirconia	4	bd	7.57 (0.75)	87.94 (0.27)	2.11 (0.06)	
1200-s	1,200							
		srilankite	9	bd	46.22 (1.44)	53.33 (1.28)	bd	
		zirconia	8	bd	9.69 (0.36)	86.55 (0.29)	2.01 (0.11)	
1300-UF-1.1	1,300							
		zirconia	23	0.09 (0.07)	10.54 (0.55)	87.88 (0.54)	1.49 (0.12)	
		srilankite	17	0.06 (0.03)	38.09 (1.09)	60.18 (2.17)	1.22 (0.14)	
		zircon	20	35.95 (2.20)	0.44 (0.04)	62.32 (0.39)	1.33 (0.07)	2714 (515)
1300-SF-1.2	1,300							
		cristobalite*	27	98.48 (0.63)	1.63 (0.10)	bd	bd	
		rutile*	44	0.17 (0.15)	92.58 (0.93)	7.06 (0.36)	bd	
		zircon*	22	36.00 (0.28)	0.20 (0.02)	62.22 (0.26)	1.31 (0.12)	1501 (372)
1300-BF-1.2	1,300							
		zirconia	12	bd	1.26 (1.31)	97.14 (1.14)	2.49 (0.20)	

Table 6.3 continued: Phase analyses

Experiment	Temperature (°C)	Phase	Analyses	SiO_2 (σ)	TiO_2 (σ)	ZrO_2 (σ)	HfO_2 (σ)	Ti-in-zircon ppm (σ)
1300-U	1,300							
		srilankite	16	0.16 (0.28)	44.67 (0.82)	53.84 (2.04)	bd	
		rutile*	23	0.27 (0.52)	88.49 (1.33)	10.12 (1.16)	bd	
		zircon*#	59 (EPMA)/ 10 (ICP)	36.16 (0.17)	0.51 (0.14)	63.20 (0.38)	1.08 (0.05)	3168 (931)/ 3051 (778)
1300-S	1,300							
		rutile*	36	0.21 (0.10)	86.26 (1.09)	13.12 (1.07)	na	
		zircon*	42	31.28 ((0.71)	2.76 (0.45)	64.39 (0.70)	0.92 (0.14)	16517 (2678)
1400+	1,400	zirconia	10	bd	bd	97.59 (0.22)	2.41 (0.22)	
		zircon*	14	36.35 (0.16)	0.022 (0.004)	62.27 (0.20)	1.36 (0.07)	132 (26)

Zircon grains from experiments that were not pre-sintered, such as 1300-U, show greater statistical variability in Ti content relative to pre-sintered counterparts (e.g., 1300-UF-2.1 or 1300-SF-2.1). The Ti contents of 1300-U zircons show 2σ values within ~55 % of the mean (Table 6.3). As shown in Figure 6.5a, large (between 100-400 µm), euhedral zircon grains from this experiment were removed from the sample charge to avoid secondary fluorescence or stray electron effects that may occur from Ti-rich glass or co-existing Ti-rich phases during EPMA. The transparency of synthetic 1300-U zircons, coupled with BSE-techniques on mounted grains, can be used to identify inclusions (melt or crystalline). The measured variation of Ti within the 1300-U zircons is likely to be a true measurement of compositional heterogeneity in this experiment, rather than being related to secondary fluorescence.

Ti frequency distribution histograms shown in Figures 6.7 through 6.10 show the statistical variation associated with analyses from zircons of individual experiments. While most experiments show analyses that broadly demonstrate a normal distribution about the mean, experiment 1300-U shows a bimodal distribution (with peaks at 2642 and 4277 ppm).

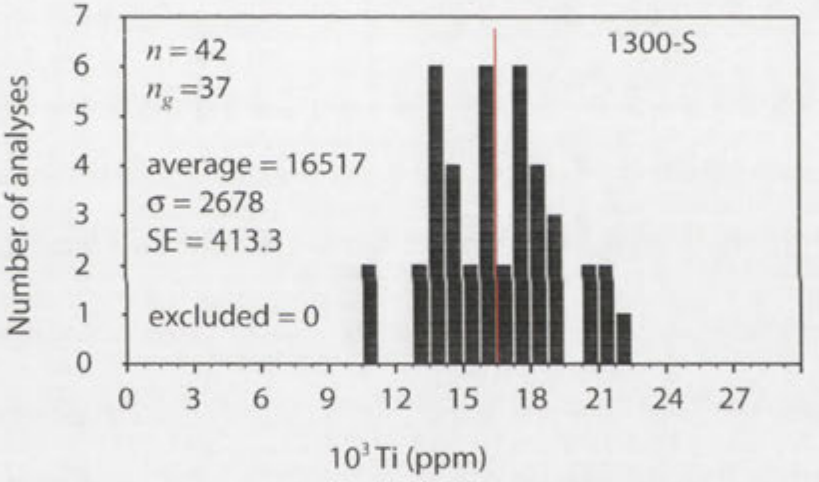

***Figure 6.7**: Ti distribution histogram from experiment 1300-S as determined from EPMA. Abbreviations – n = number of analyses, n_g = number of grains analysed, σ = standard deviation, SE = standard error, excluded = number of analyses excluded (based on low analytical totals or analyses showing ZrO_2, TiO_2 or SiO_2 contents indicative of secondary fluorescence). Red line represents the mean value reported from analyses.*

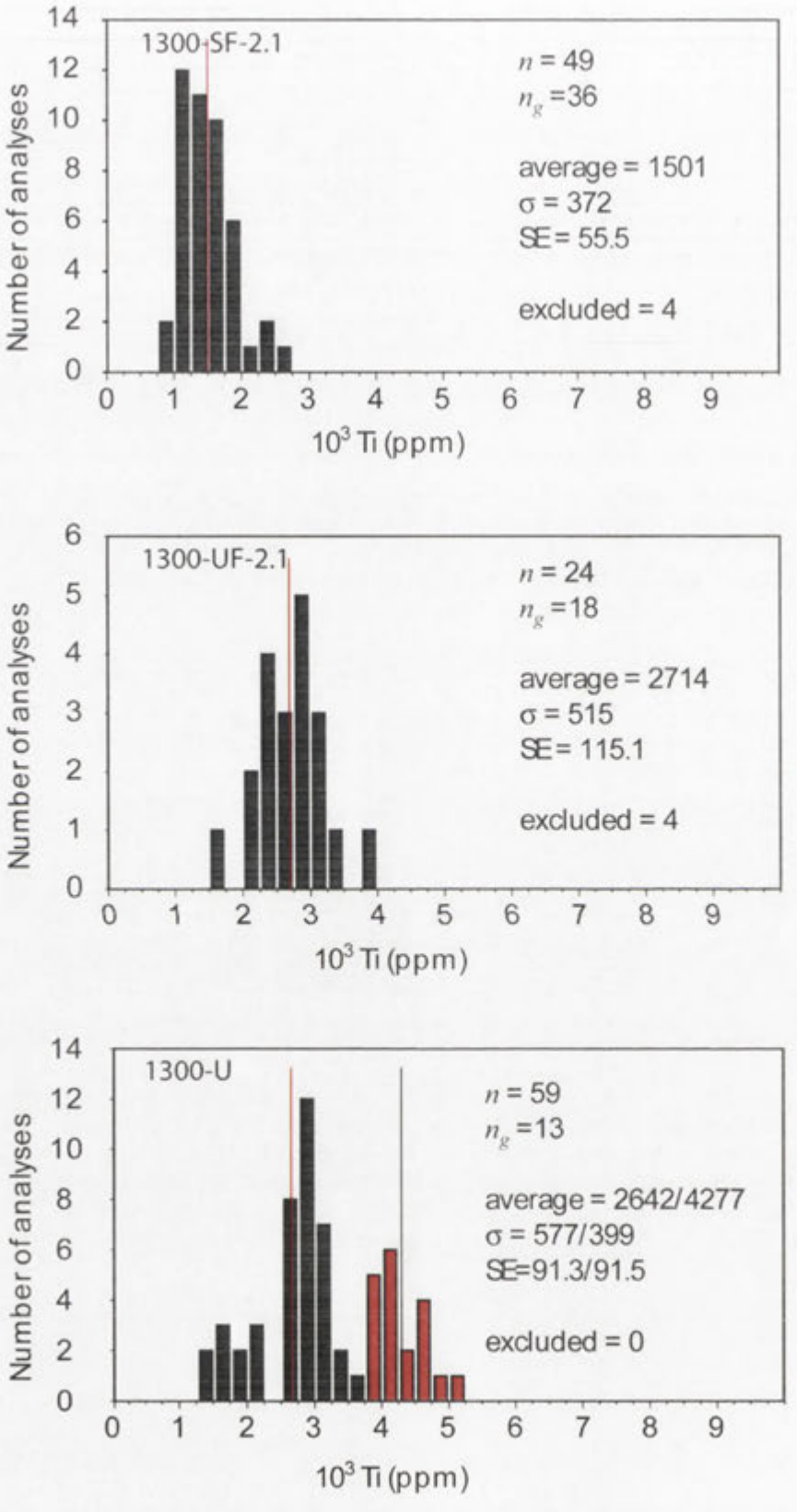

***Figure 6.8**: Ti distribution histograms for 1,300 °C experiments as determined from EPMA. Abbreviations as in Figure 6.7. 1300-U analyses show bimodal distribution with averages and error reported for the two different populations. Note that experiments 1300-SF-2.1 and 1300-UF-2.1 were pre-sintered.*

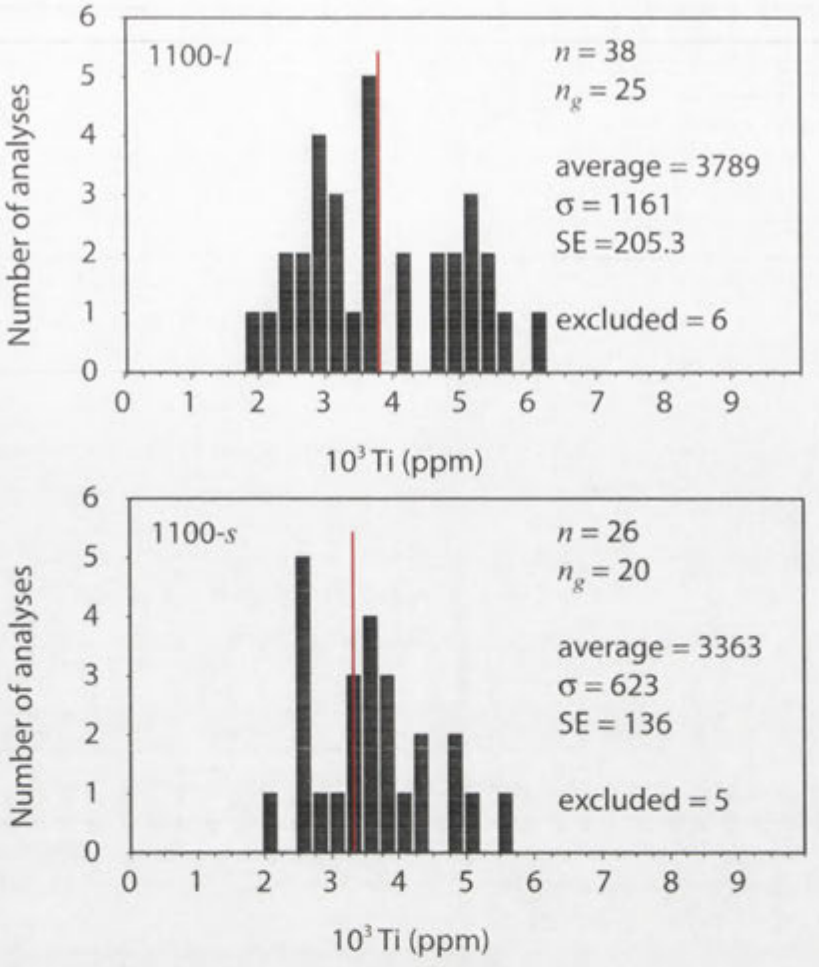

Figure 6.9: *Ti distribution histogram from 1,100 °C experiments as determined from EPMA. Abbreviations as in Figure 6.7.*

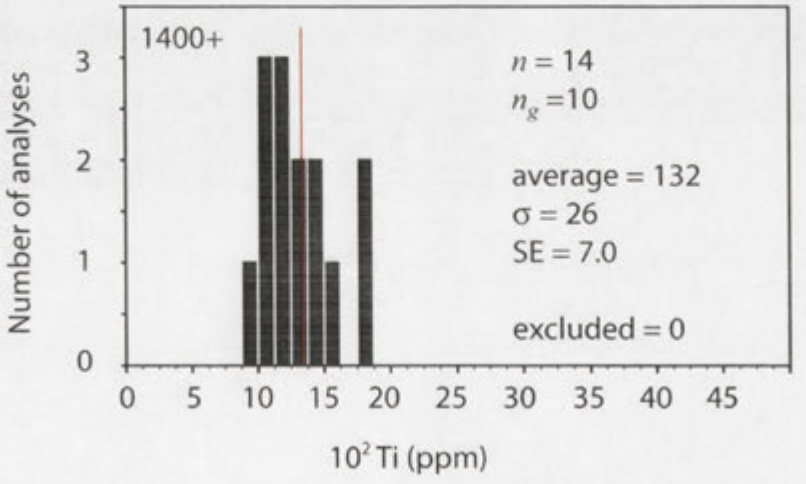

Figure 6.10: *Ti distribution histogram from experiment 1400+. Abbreviations as in Figure 6.7*

Zircon grains synthesized at 1,300 °C show an increasing average Ti content from 1501 ppm at silica-saturated conditions (experiment 1300-SF-2.1) to ~2700 ppm in silica-undersaturated conditions (1300-UF-2.1 and 1300-U).

6.3: Ti K_α x-ray maps from synthetic zircons

Ti x-ray maps were made from zircon grains that show large statistical variation as determined by EPMA. Maps from experiment 1300-U (Figure 6.11) demonstrate that synthetic zircons show various forms of "oscillatory" and sector zoning.

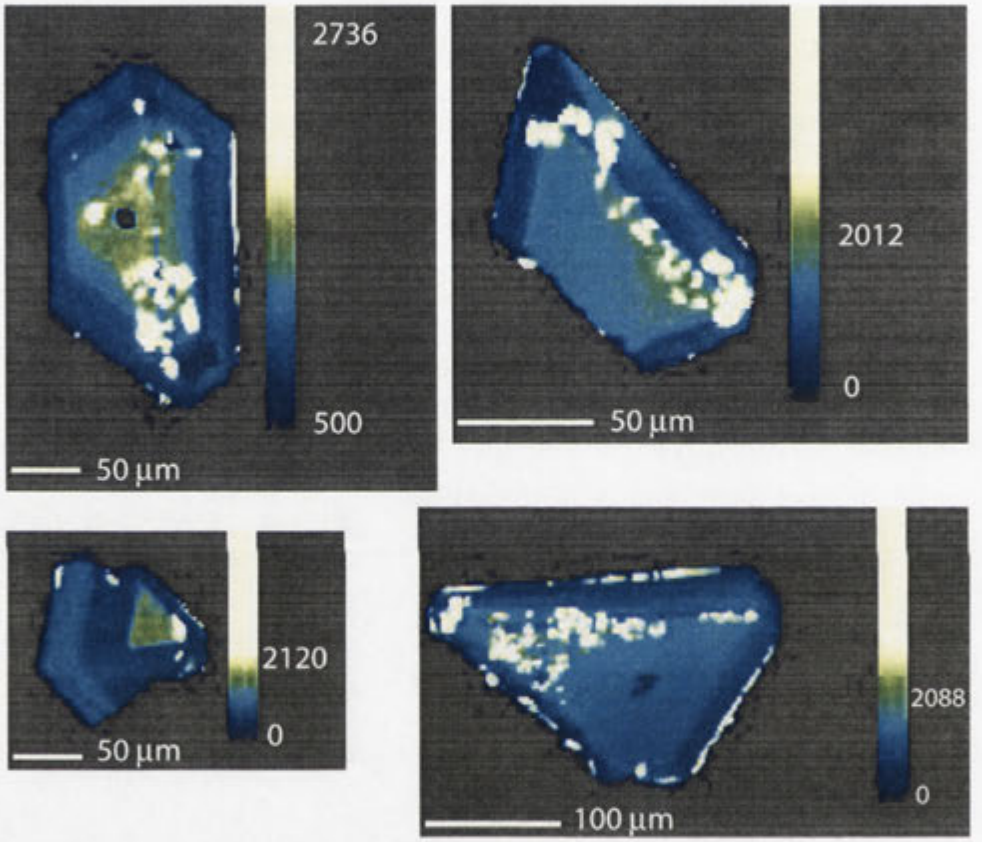

***Figure 6.11**: False colour image of Ti x-ray maps from 1300-U synthetic zircons. Colour scale bar represents Ti counts over the analytical time period. Bright white domains represent mineral inclusions of srilankite and/or rutile.*

6.4: XANES Spectroscopy

Standards

SEM-BSE imagery of synthetic cristobalite and tetragonal zirconia powders (Figure 6.12) show that synchrotron standards consist of a fine-grained, single phase powder. Sharp angular triple point margins indicate equilibrium was achieved during synthesis.

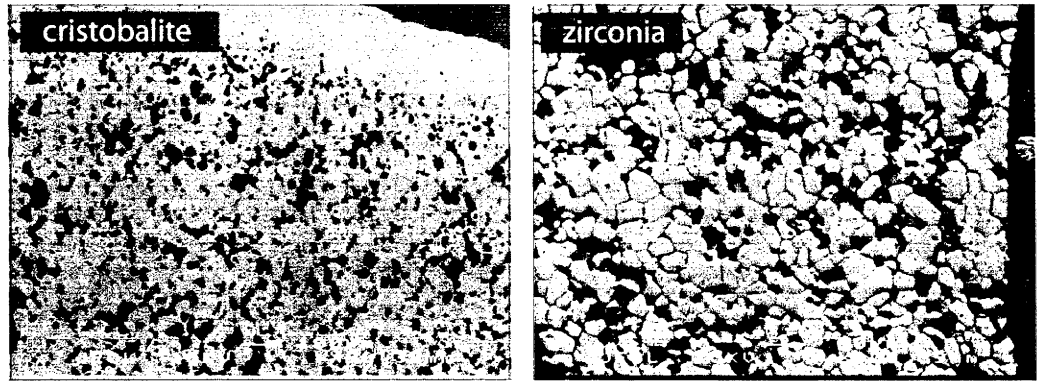

***Figure 6.12**: Representative SEM-BSE images of standard cristobalite and tetragonal zirconia.*

XRD analyses from cristobalite and tetragonal zirconia powders confirm mineral speciation of synthetic standards and indicate that no other phase(s) are present (within the limit of detection limit for the technique).

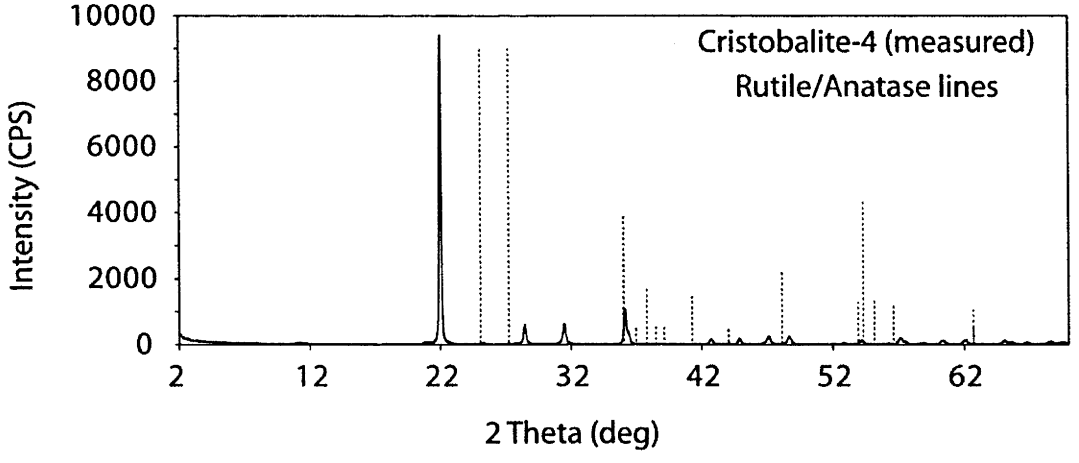

***Figure 6.13**: Representative XRD pattern for cristobalite standard powder. Note that the spectrum shows no measurable signal from any TiO_2-bearing phase (rutile and anatase peaks are shown in red and green lines respectively).*

EPMA of synthetic standards also indicate homogeneity. The Ti content of cristobalite shows 2σ falling within 34.6 % of the mean (1.52 ± 0.17 wt% TiO_2 as determined by 17 analyses). The Ti content of tetragonal zirconia shows 2σ falling within 21.2 % of the mean (1.32 ± 0.14 wt% TiO2 as determined by 9 analyses).

Ti K-edge XANES spectra provide a direct structural probe of the Ti coordination environment. In particular, the 1*s*-3*d* pre-edge transition has been shown for Ti-bearing compounds to vary in energy and intensity with the Ti coordination number (Waychunas, 1987; Farges et al., 1996a, 1996b, 1997a, 1997b; Berry et al., 2007). Farges et al. (1996a, 1996b, 1997b) have shown that increasing Ti coordination (from four to five to six nearest oxygen neighbours) is associated with a decrease in peak height intensity and an increase in energy of the pre-edge feature (see Farges et al., 1996a for detailed discussion).

The synthetic standards studied were: rutile, tetragonal zirconia, and cristobalite. These samples contain Ti at varying concentrations (from trace element to site-forming cation), at different coordinations ([4] and [6]), and varying local O-M-O/O-O bond lengths/angles.

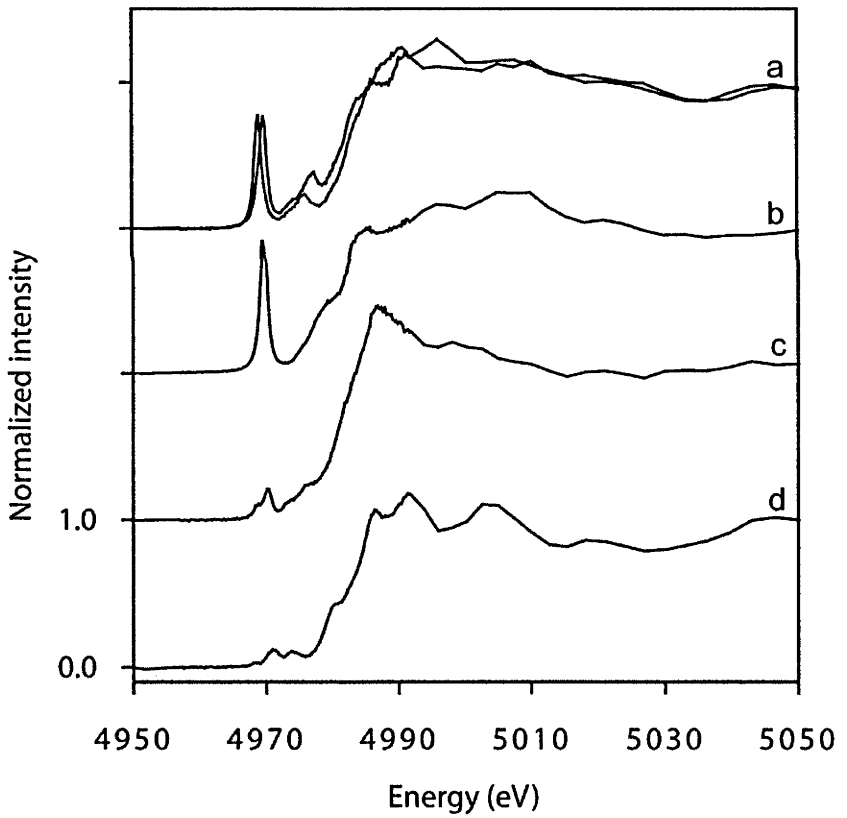

***Figure 6.14**: normalized Ti K-α XANES spectra of: (a) representative zircon crystals, (b) cristobalite, (c) tetragonal zirconia, and (d) rutile.*

Comparison of standards and fully buffered zircons

In order to fingerprint Ti site occupancy in zircon by XANES spectroscopy it is essential that analyses are made on zircon grains of sufficient size and spatial resolution to ensure the incident synchrotron beam can be accurately positioned on zircon and away from any other Ti-rich phase. For this reason, the majority of synchrotron analyses were made from 1300-U

experimental zircons. Additional analyses were made from zircons and glass from experiment 1300-S, but as this experiment lacked an appropriate silica buffer, these analyses will be discussed separately.

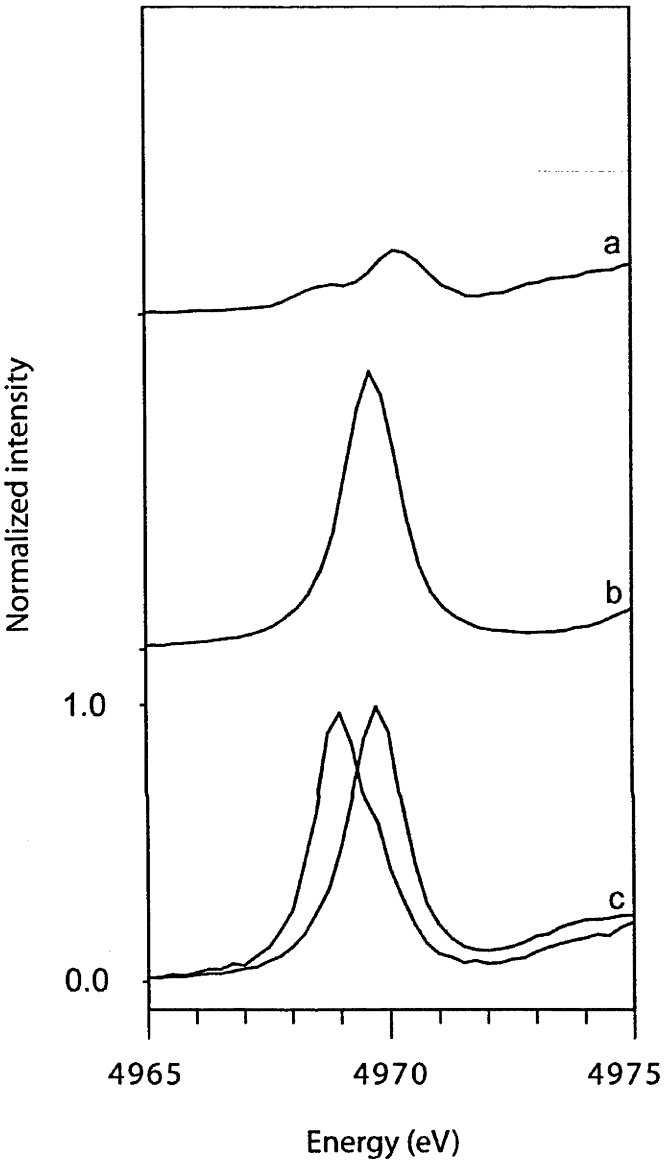

***Figure 6.15**: Normalized Ti K-α XANES spectra of: (a) rutile, (b) cristobalite, and (c) representative zircon crystals.*

Normalized Ti K-edge x-ray absorption spectra (XAS) and x-ray absorption near-edge structures (XANES) spectra for the standards and synthetic 1300-U zircons are shown in Figures 6.14 and 6.15. Ti standards presented here have spectra consistent with previous literature reports (e.g., Waychunas, 1987; Farges et al., 1997b; Berry et al., 2007). As shown in Figures 6.15 and 6.16 the pre-edge region of 4-coordinated Ti in cristobalite has a high normalized peak height (0.91) at lower energy (4969.6 eV) relative to Ti at a 6-coordinated site in rutile where the normalized peak intensity is lower (< 0.21) but shifted to higher energy (4971 eV). The comparison of intensities between studies, however, must be done with caution due to differences in spectral resolution arising from the divergence of

the photon source and choice of monochromator. In this case the resolution of 1.0 eV is comparable to that of the literature data (1.2 eV), allowing direct comparison of results. The peak energies are not affected by the characteristics of the beamline.

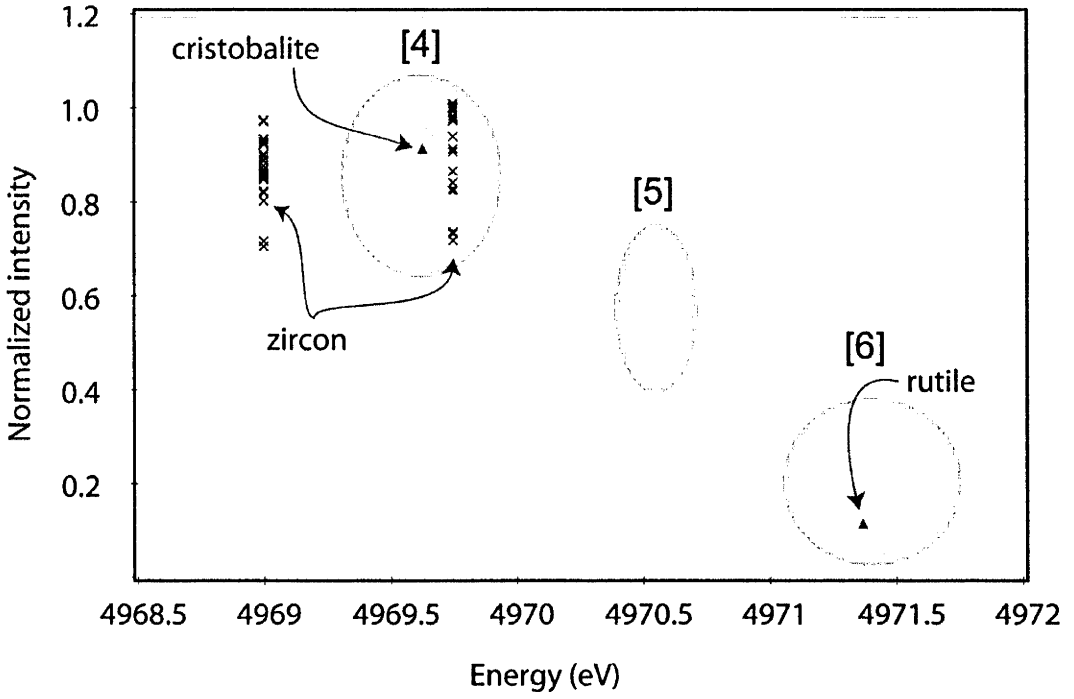

***Figure 6.16**: Energy and normalized peak height of the Ti K-α XANES 1s-3d pre-edge feature of various Ti-bearing minerals, including: zircon (crosses), cristobalite (triangle) and rutile (triangle). Shaded regions correspond to domains of [4], [5], and [6] coordinated Ti (Farges et al, 1996a).*

Normalized peak-heights and energies of 45 individual, randomly orientated zircon Ti K-α 1*s*-3*d* XANES pre-edge features also show excellent correlation (in terms of both energy and intensity) between the 4-coordinated (cristobalite) standard shown here and those presented in previous studies (Farges et al., 1996a; Berry et al., 2007). The most notable deviation from Ti 4-coordinated standards (reported here and elsewhere) and the zircon pre-edge feature is the presence of absorption peaks of equal intensity at two distinct energies (4969.0 and 4969.7 eV) in zircon spectra (see Figures 6.15, 6.17 and 6.18).

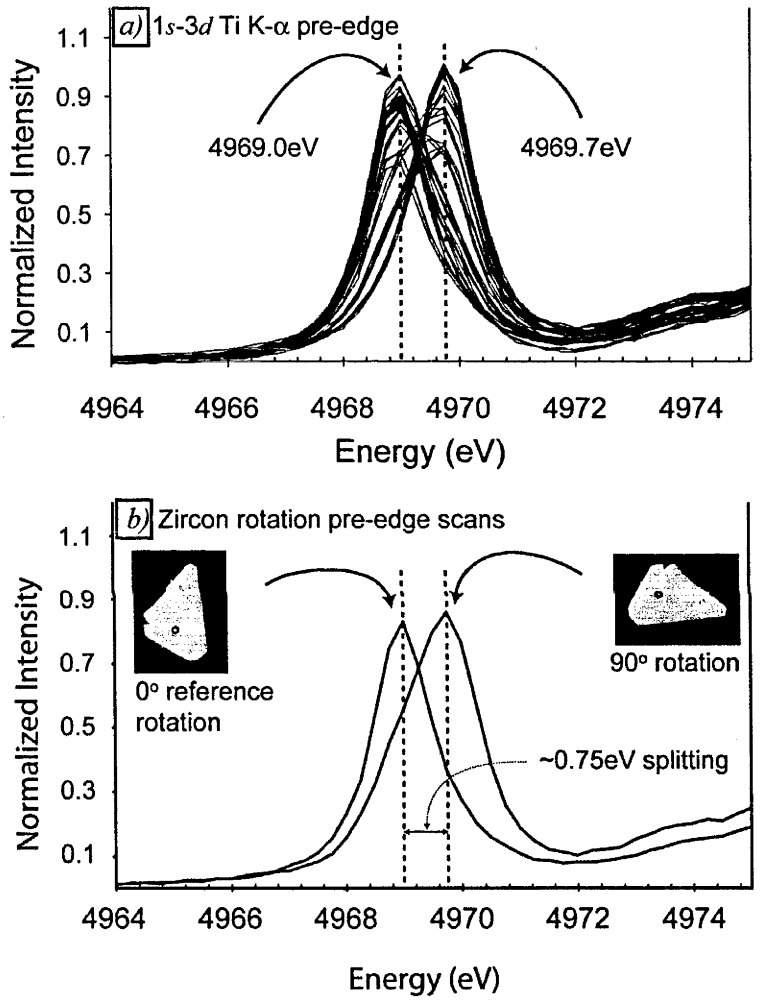

***Figure 6.17**: Normalised Ti K-edge XANES pre-edge spectra of (a) 45 randomly orientated zircon grains measured in fluorescence mode. Spectra show two distinct peaks at 4969.0 eV and 4969.7 eV; (b) an individual zircon grain at reference orientation and with 90° rotation (BSE images for reference). The energy splitting (~0.75 eV) is identical to that seen in the randomly orientated zircon population.*

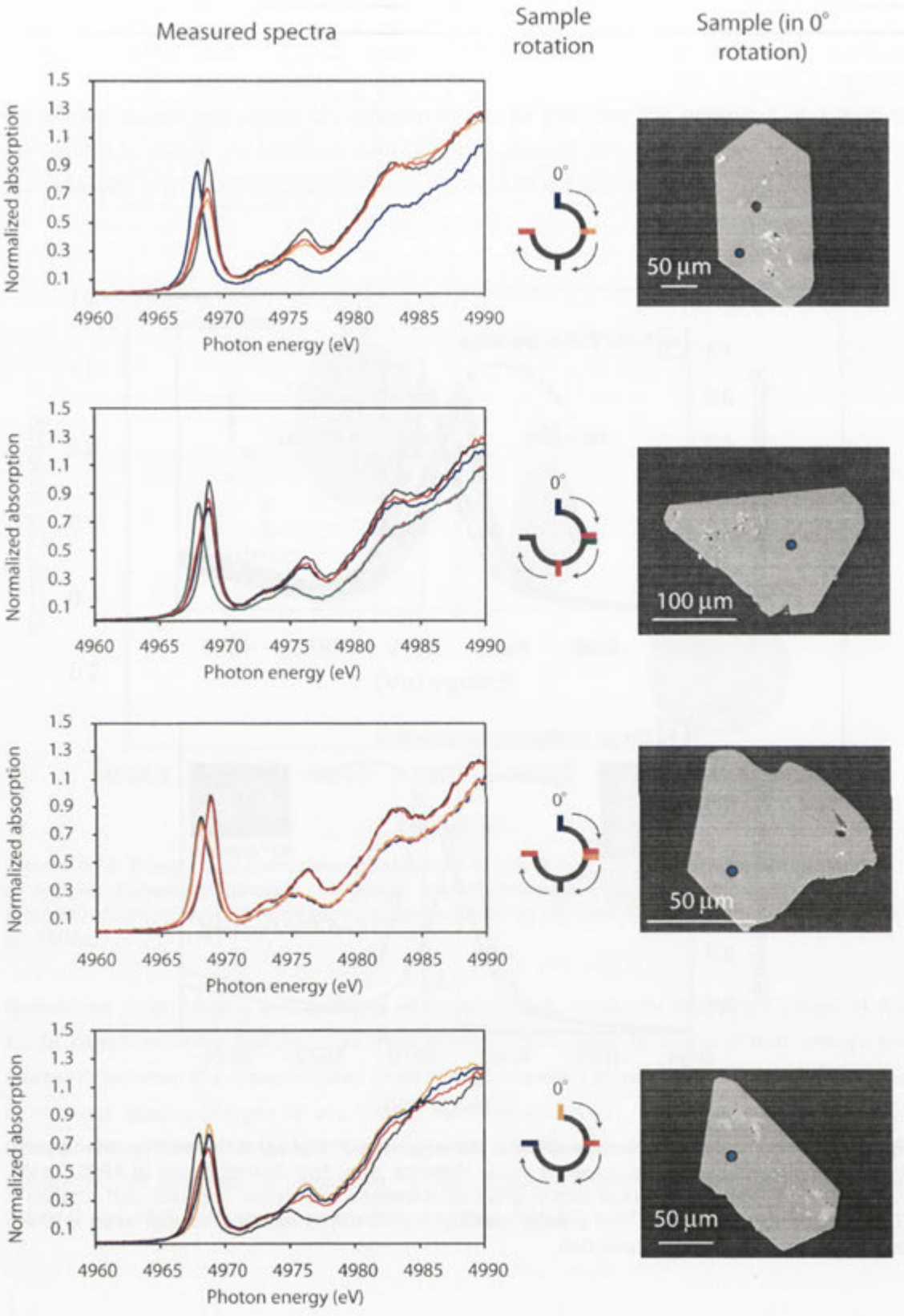

***Figure 6.18**: Normalized Ti K-edge XANES pre-edge spectra of 4 zircon grains at 90° rotation intervals over 360° measured in fluorescence mode. BSE images and incident beam spot shown for reference.*

Orientation scans of individual zircons show that the energy splitting (see Figures 6.17 and 6.18) appear to vary as a function of crystal orientation. A zircon crystal at one orientation exhibits a single pre-edge peak, while a 90° rotation of the crystal can result in a peak of near-equal intensity but shifted in energy by 0.75 eV.

XANES spectra across sector zones

Scans were also carried out in the pre-edge region for sector zoned synthetic zircons from experiment 1300-U. Given the time restrictions associated with each analysis, pre-edge scans were carried out at energies ranging from 4916-4976 eV. While such scans cannot be normalized against the main absorption edge (i.e., pre-edge intensity is unconstrained), they can be used to determine relative energy shifts in the 1*s*-3*d* Ti K-α pre-edge feature as a function of position within the zoned zircon. Figure 6.19 shows that there is no change in energy associated with Ti K-α pre-edge feature across different sectors.

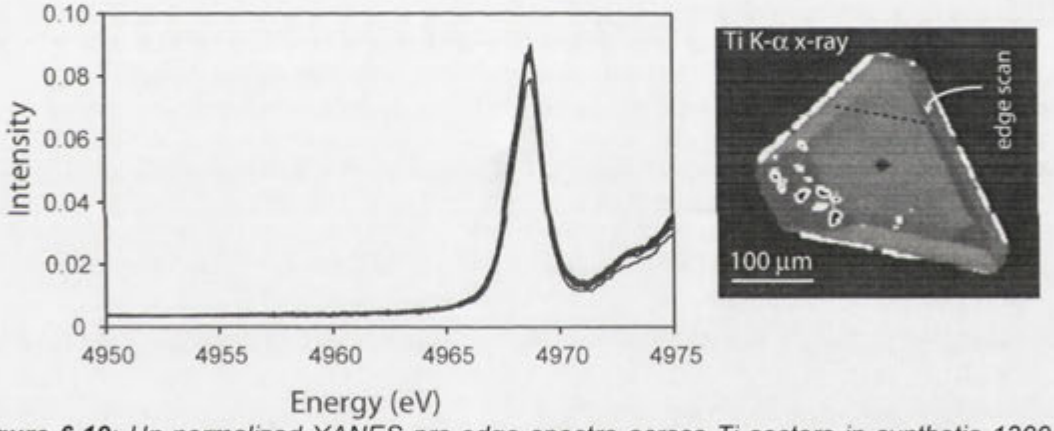

***Figure 6.19**: Un-normalized XANES pre-edge spectra across Ti sectors in synthetic 1300-U zircon. Absorption energy is constrained, while intensity is raw detector counts (i.e., i/i0).*

XANES analyses from 1300-S zircons and glass

Normalised Ti K-edge XANES pre-edge spectra were also collected from zircons and glass from experiment 1300-S. Pre-edge, main edge and fine structures from these analyses show markedly different spectra to mineral buffered zircons of experiment 1300-U and synthetic standards or glasses presented here and elsewhere.

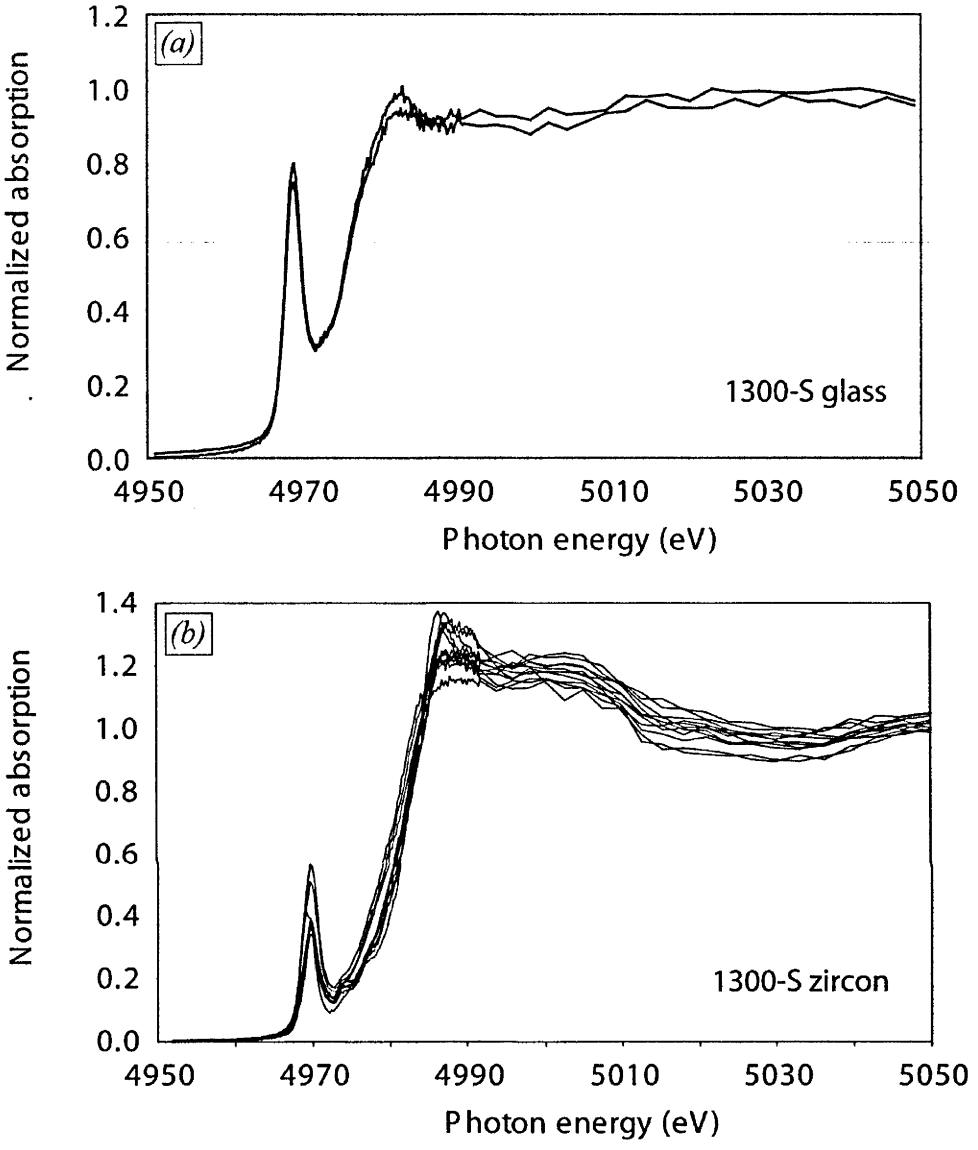

***Figure 6.20**: Normalized Ti K-edge XANES spectra of (a) sodic glass from experiment 1300-S, (b) 12 individual zircon analyses from 1300-S zircons at random orientation.*

Glass analyses show a pre-edge peak situated at 4969 eV and an intensity of between 0.75 and 0.8 eV. The post-edge oscillation pattern is also unlike previous glass spectra reported within the literature, with the closest spectra coming from the work of Farges et al. (1996b – see experiment NTS2).

EXAFS from 1300-U

EXAFS spectra for a random crystallographic orientation of a 1300-U zircon crystal were modelled to give a Ti-O bond length of 1.76(1) Å. The fit to the Fourier transform (FT) of the EXAFS is shown in Figure 6.21.

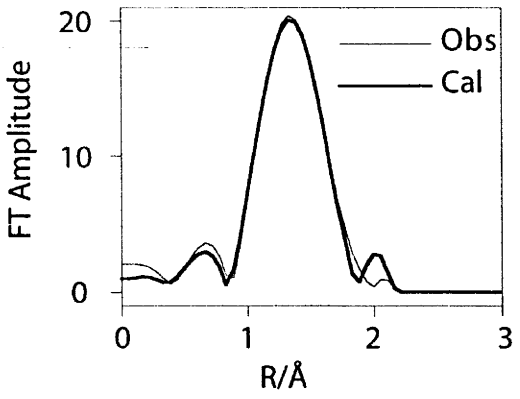

***Figure 6.21**: Observed and calculated Ti K-edge FT EXAFS spectra of Ti in zircon.*

6.5: Density Functional Theory Calculations

DFT calculations were undertaken for 15 different initial defect geometries. After energy minimisation only three different geometries were apparent. In all but one case the Ti atom moved to the centre of the Si or Zr site destroying any vacancy in the simulation cell. One calculation did preserve a Zr vacancy and interstitial Ti, but the final energy was 8.8 eV higher than that of direct substitution of Ti for Zr, so this structure is not considered further.

The simulated bulk zircon contains two unique sets of four identical Zr–O bond lengths, one being 2.167 Å and the other being 2.284 Å. When Ti substitutes for Zr, the site symmetry remains the same but both short and long bonds shorten to 2.085 and 2.234 Å respectively. Ti on the Si site also preserves the point symmetry with Ti–O bonds lengthening to 1.797 Å compared to the original Si–O bond length of 1.648 Å in simulated bulk zircon.

As well as providing detailed structures of the two substitution mechanisms, the DFT calculations also provide the energies of the two systems. However, the energies cannot be directly compared because the content of the two simulation cells is different. In order to compare the stability of the two defects, a source or sink for Si and Zr atoms is needed. For example, if we assume α-quartz and baddeleyite act as the source/sink we can write the equation:

$$Ti_{Zr}^{\times} + Si_{Si}^{\times} + ZrO_2 \rightarrow Zr_{Zr}^{\times} + Ti_{Si}^{\times} + SiO_2, \qquad \textbf{(eq. 6.1)}$$

where, Kröger-Vink notation is used to represent substitutional impurities in zircon. Using the energies reported in Table 3 yields an energy of -0.34 eV, suggesting that Ti is more stable on the Si site then the Zr site. But, there are other sources of Si and Zr. For example we could consider the Si activity to be set by a reaction with forsterite to form enstatite:

$$Ti_{Zr}^{\times} + Si_{Si}^{\times} + ZrO_2 + Mg_2SiO_4 \rightarrow Zr_{Zr}^{\times} + Ti_{Si}^{\times} + 2MgSiO_3, \qquad \textbf{(eq. 6.2)}$$

which yields an energy of -0.05 eV, suggesting that Ti could be found on both sites in zircon under certain chemical conditions.

Table 6.4: DFT energies after geometry optimisation calculated using the SIESTA methodology.

Cell content	Formation energy (eV p.f.u.)
ZrO_2 (baddeleyite)	-2162.21
TiO_2 (rutile)	-1641.39
SiO_2 (α-quartz)	-982.77
$ZrSiO_4$ (zircon)	-3145.12
$TiSiO_4$.31$ZrSiO_4$ (Ti on Zr site in zircon)	-100942.30
$ZrTiO_4$.31$ZrSiO_4$ (Ti on Si site in zircon)	-102122.07

6.6: XANES Modelling

Simulated spectra for Ti occupying the Si and Zr sites are shown in Figure 6.22. Spectra are given for x-rays polarized parallel to the a-, b- and c- crystallographic directions. The modelled spectra for Ti on the Si site reproduce the intense pre-edge feature and its splitting, together with structure on the absorption edge. The polarized spectra for Ti on the Zr site, however, bear little resemblance to the experimental data. All the spectra were calculated using the Hedin-Lundqvist potential in a presence of core-hole and a large cluster of atoms (150-200) around the photoabsorbing Ti ion.

Mixed site occupancy can be modelled at specific crystal orientations or, as in Figure 6.23, $^{[4]}$Ti:$^{[8]}$Ti can be modelled on averages across all 3 crystal orientations (i.e., spectra expected from a homogenous single phase powder). The modelled 1*s*-3*d* Ti K-α pre-edge feature for $^{[8]}$Ti in zircon is so small (and absent at certain crystallographic orientations) that mixed site occupancy results in negligible energy shifts but notable intensity shifts. Other differences between $^{[4]}$Ti and $^{[8]}$Ti spectra include a subtle change in the slope of the main edge and distinct changes in the EXAFS region of the absorption spectrum.

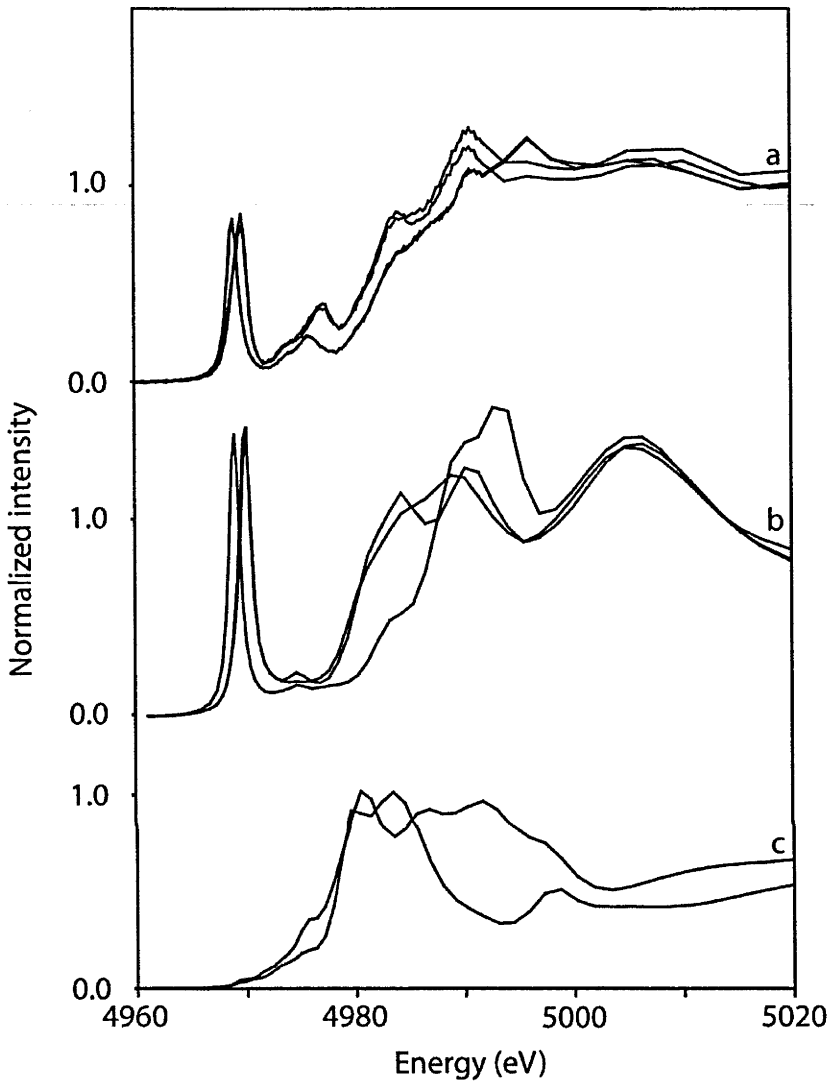

***Figure 6.22**: (a) Representative measured Ti Kα spectra for zircon; (b) model Ti Kα XANES spectra for $^{[4]}$Ti in zircon at x-, y- and z-polarization, and; (c) model Ti Kα XANES spectra for $^{[8]}$Ti in zircon at x-, y- and z-polarization.*

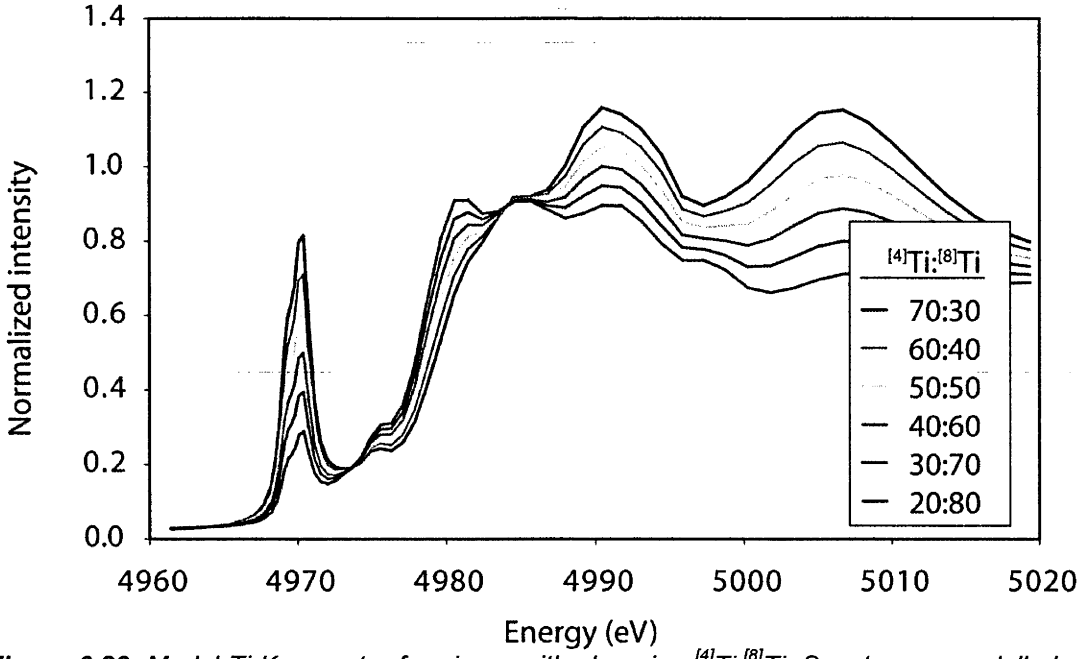

***Figure 6.23**: Model Ti Kα spectra for zircon with changing $^{[4]}Ti:^{[8]}Ti$. Spectra are modelled on average spectral signal for $^{[4]}Ti$ and $^{[8]}Ti$ across a-, b- and c-axis orientations.*

6.7: SEM-CL imaging, LA-ICP-MS analyses and X-ray maps

SEM-CL images and Ti analyses (LA-ICP-MS and x-ray maps) were combined to investigate if correlation between cathodoluminescence and Ti distribution.

Figures 6.24 and 6.25 show SEM-CL images and Ti content measurements from a variety of zoned zircon grains – incorporating both natural and synthetic samples. For the purpose of this research, natural zircon grains displaying the development of distinct SEM-CL domains (e.g., sector or "fir-tree" zonation) were targeted .

Ti K-α x-ray maps of some zircon grains from experiment 1300-U show notable sector zonation with regard to Ti (Figure 6.11). While Ti x-ray maps show heterogeneous distribution within some zircons from this synthetic zircon population (see Figures 6.11 and 6.24), x-ray maps of Si and Hf show no detectable elemental variability. More importantly, SEM-CL images from this experiment (Figure 6.24b) show little or no correlation with Ti-distribution in zircon.

In contrast to 1300-U zircons, a euhedral zircon grain from Monviso (M4, Rubatto and Hermann, 2003) shows the presence of "fir-tree" zonation in SEM-CL. As shown in Figure 6.24a, LA-ICP-MS analyses from this grain show that lighter SEM-CL domains have half the Ti content (0.6 ppm) of darker domains (1.2 ppm).

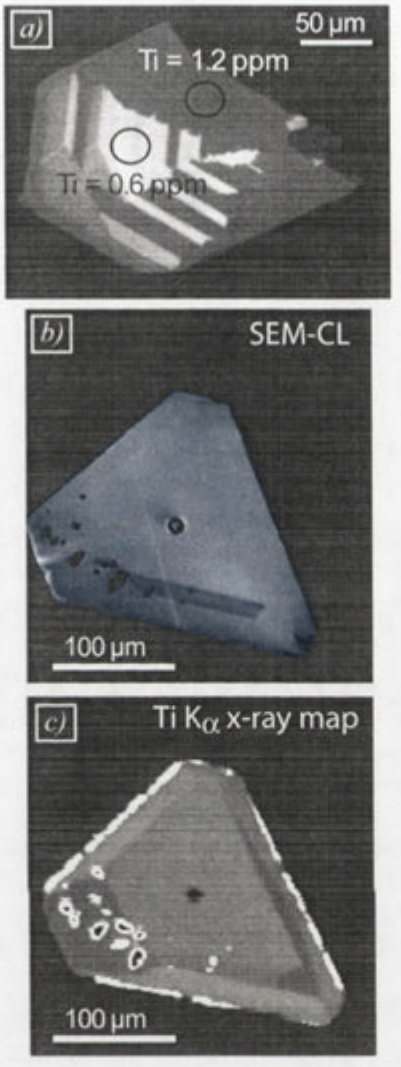

***Figure 6.24**: Sector zoning in natural and synthetic zircons: a) SEM-CL photomicrograph of "fir-tree" zonation in zircon from Monviso (Rubatto and Hermann, 2003) with analytical spots and Ti concentrations; b) SEM-CL image of synthetic 1300-U zircon (with laser ablation pit); c) Ti Kα x-ray map of the same 1300-U zircon.*

Natural zircon samples from northern Queensland (NQ-1) show the clear development of internal zonation in SEM-CL. LA-ICP-MS scan analyses across SEM-CL interfaces reveal that CL activation is correlated to large changes in REE, P, Th and U content (see Figure 6.25 and Table 6.5). Ti analyses from slit scans show that ^{49}Ti counts are very similar across the two SEM-CL domains, with the two populations falling within error of one another. It should be noted that the concentration of Ti is considerably lower than other trace elements (Y, P, U and Yb). Consequently, the pulse nature of the LA-ICP-MS technique limits the sensitivity of this technique at low concentrations (sub-ppm) because the signal tends to introduce spikes with each pulse. It is possible that some subtle variation exists across the two zircons domains, but Ti concentrations are too low to distinguish them.

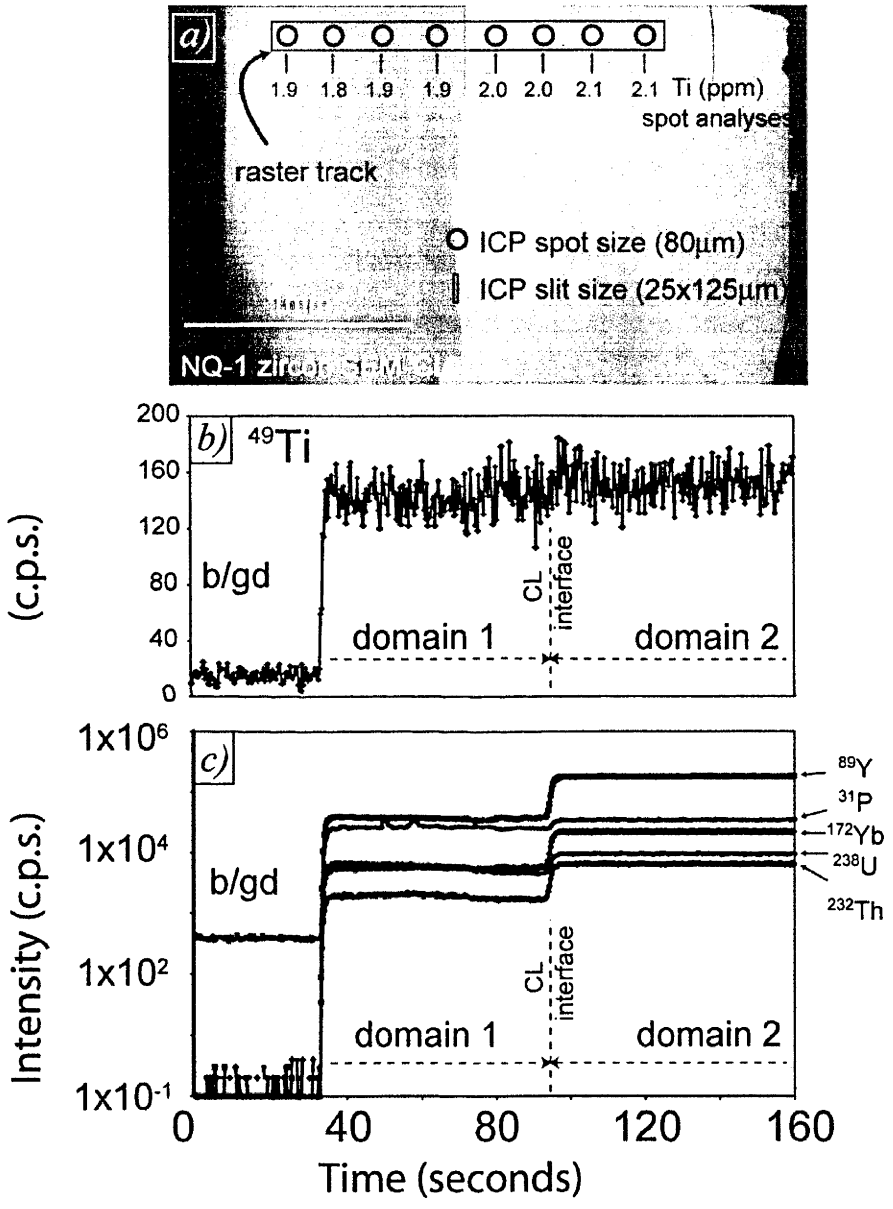

Figure 6.25: *Comparison of SEM-CL and trace element distribution in natural zircon (sample NQ-1): a) SEM-CL photomicrograph with location and size of LA-ICP-MS slit scan traverse and spot analyses (with corresponding Ti concentration); b) intensity-time ablation profile of ^{49}Ti for slit scan traverse across SEM-CL interface; c) Intensity-time profile of trace elements - Y, P, Yb, U and Th – for slit scan traverse across SEM-CL interface.*

Table 6.5: a) Trace element concentrations of sector zoned zircon grain NQ-1 from LA-ICP-MS analyses (see text and Figure 6.25 for analytical details); b) primitive mantle normalized REE profiles of the two domains (McDonough and Frey, 1989).

a)	SECTOR 1				SECTOR 2			
EPMA analyses (wt %)								
	A	B	C	D	E	F	G	H
SiO_2	36.6	36.9	36.6	36.4	37.0	36.8	36.8	36.8
ZrO_2	63.9	63.4	63.5	63.2	63.9	63.3	63.5	63.8
HfO_2	0.7	0.6	0.6	0.6	0.7	0.7	0.7	0.7
LA-ICP-MS analyses (ppm)								
Ti	2.1	2.1	2.0	2.0	1.9	1.9	1.8	1.9
P	270.2	262.5	253.4	253.3	196.2	205.2	190.7	193.0
Y	292.1	279.4	272.1	271.0	57.2	57.7	57.0	58.8
Dy	29.7	28.2	27.2	27.3	5.1	5.1	5.0	5.2
Er	45.0	43.0	41.8	41.4	9.4	9.5	9.5	9.8
Yb	97.8	93.2	90.4	90.1	23.9	24.7	25.4	25.8
Th	25.1	23.9	23.4	23.2	6.4	7.5	7.2	6.8
U	28.7	27.4	26.4	26.6	13.5	16.2	15.1	14.2
Mo	0.3	0.2	0.2	0.2	0.2	0.2	0.2	0.2

b)

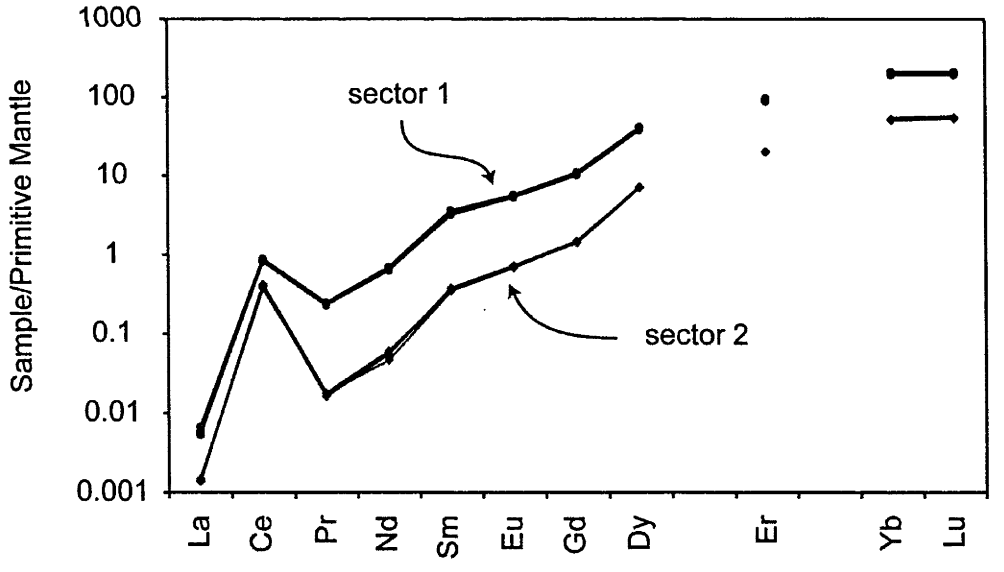

Chapter 7

Discussion

This chapter discusses results from research presented here and within the literature in order to determine how Ti substitutes into zircon and the implications this has for thermometry. Introductory sections focus on the zircon structure and theoretical Ti substitution mechanisms. These discussions lead to interpretation of results presented in the previous chapter and how they pertain to site occupancy and thermometry. The final sections of this chapter focus on how results provide insights into the effect of pressure on zircon thermometry and how Ti distribution can be related to imaging techniques used to monitor zircon zonation.

7.1: The zircon structure

In order to appreciate the various chemical and physical properties of zircon, many of which are important for later discussion, the following section outlines the structure of the mineral. Zircon and related minerals are generally expressed by the formula ATO_4, where the *A*-site cations occupy a large 8-coordinated octahedral site and the *T*-site is occupied by smaller tetrahedral 4-coordinated cations (Finch and Hanchar, 2003). As shown in Figure 7.1 the zircon *T*-site is occupied by SiO_4 tetrahedra and the *A*-site is occupied ZrO_8 dodecahedra. As these two sites are vastly different, with the A-site being particularly unusual among common rock-forming minerals, they are discussed separately.

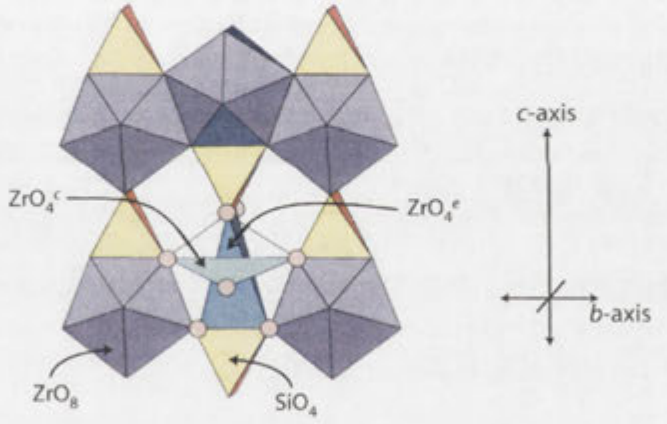

***Figure 7.1**: 3-D projection of the zircon (ATO_4) structure, with axes as indicated. Note the SiO_4 tetrahedra (shown in yellow hues) share edges with two adjacent ZrO_8 dodecahedra and corners with four ZrO_8 dodecahedra).*

SiO_4 tetrahedra (disphenoids)

Zircon SiO_4 tetrahedra consist of tetragonal disphenoids (see Figures 7.1 and 7.2) that are elongated parallel to <001>. As discussed by Speer (1982), distortion of the SiO_4 tetrahedra is thought to result from repulsion between Si^{4+} and Zr^{4+} cations that share common edges along their respective polyhedra. Inter-atomic angles within the zircon tetrahedra show some distortion that is manifested in two sets of O-Si-O bonds, one that exists at 97° the other at 116° (Finch et al, 2001a). Tetrahedral distortion is also shown by variations in O-O bond length, with tetrahedral edges shared with ZrO_8 dodecahedra being 11.6% shorter (2.43 Å – which is opposite the smaller O-Si-O angle) than O-O bonds that only share corners with ZrO_8 dodecahedra (2.75 Å – which is opposite the larger O-Si-O angle) (Finch and Hanchar,

2003). Thus, the SiO_4 tetrahedra, or $^{[4]}Si^{4+}$, in zircon shows notable elongation and distortion relative to an ideal SiO_4 tetrahedron.

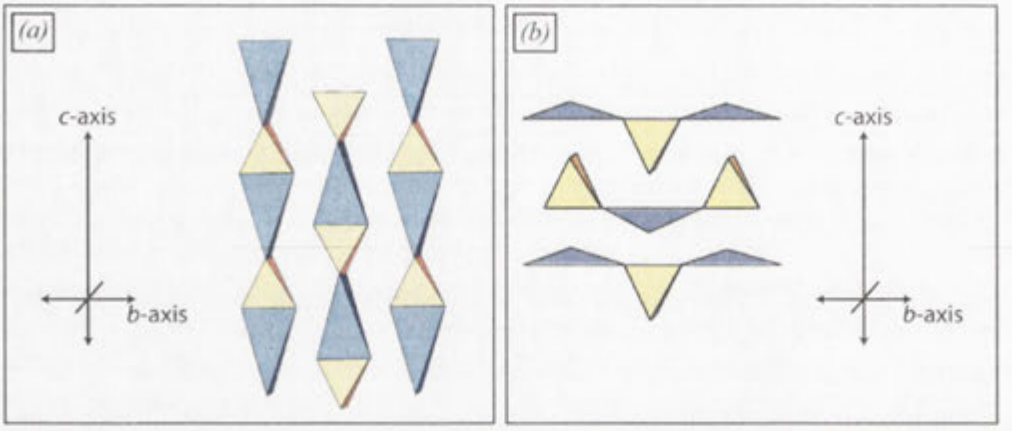

***Figure 7.2**: (a) Simplified zircon projection along <100> demonstrating the isolated chains formed by alternating, edge-sharing tetragonal disphenoids of SiO_4 (in yellow hues) and ZrO_4^e (in light blue hues). Both ZrO_4^e and SiO_4 polyhedra show elongation along <001>. (b) Simplified zircon projection along <100> demonstrating the isolated chains formed by alternating, corner-sharing tetragonal disphenoids of SiO_4 (in yellow hues) and ZrO_4^c (in dark blue hues). Projection modified after Finch and Hanchar (2003).*

ZrO_8 snub dodecahedra (the interpenetrating ZrO_4 model)

The dodecahedral site in zircon also shows some distortion about perfect symmetry. Each Zr^{4+} cation is coordinated with eight oxygen atoms that collectively form a distorted triangular dodecahedron. The $^{[8]}Zr$ dodecahedron in zircon is often described as two interpenetrating ZrO_4 tetrahedra that share a common cation (e.g., Nyman et al., 1984; Finch and Hanchar, 2003). By visualizing the two hypothetical tetrahedra along <100>, the first tetrahedron (commonly referred to as ZrO_4^e) is elongated while the second tetrahedron (commonly referred to as ZrO_4^c) is compressed about the axis. In the absence of this elongation and compression of respective ZrO_4 tetrahedra the $^{[8]}Zr^{4+}$ would result in cubic rather than the observed dodecahedral arrangement.

Elongation and compression of the theoretical ZrO_4 tetrahedra is also expressed in terms of Zr-O bond lengths. Elongated ZrO_4^e polyhedral units comprise four long Zr-O bonds (at 2.27 Å), while compressed ZrO_4^c units comprise four short Zr-O bonds (2.13 Å). As shown in Figures 7.1 and 7.2, each elongated ZrO_4^e polyhedron shares edges with SiO_4 tetrahedra that form chains of polyhedra that are elongated parallel to <001>. Each ZrO_4^c polyhedron shares corners with four SiO_4 tetrahedra forming a tetrahedral array parallel to <010>.

Theoretical Ti substitution in zircon

There are many possible substitution mechanisms for Ti in zircon. These include substitution on crystal defects (e.g., vacancies, dislocations, etc) and isovalent substitution for either the *A*- or *T*- site in zircon. It is also possible for Ti to substitute on multiple sites or different sites under different P-T-*X* conditions. For Ti to substitute on a specific crystal defect and still show a clear temperature dependence (Watson et al., 2006; Ferry and Watson, 2007) would be both unlikely and unprecedented in the field of geochemistry. The systematic substitution

of 10^4 ppm Ti in zircon (as shown by Watson et al., 2006) requires such a significant and proportional number of crystal defects with increasing temperature that it would likely disrupt the zircon structure and so is an unrealistic substitution mechanism.

The substitution of Ti for either $^{[4]}Si^{4+}$ or $^{[8]}Zr^{4+}$ likely requires no charge balance from additional cations because Ti almost exclusively occurs in the tetravalent state within crustal systems (Waychunas, 1987; Watson and Harrison, 2005; Watson et al., 2006). As discussed in previous chapters, most natural Ti-bearing minerals contain Ti in a 6-coordinated octahedral arrangement with surrounding oxygen atoms (Waychunas, 1987; Farges et al., 1996b; Berry et al., 2007). This being the case, recent studies have shown that Ti in both olivine and β-quartz substitutes on the $^{[4]}$Si-site (Hermann et al., 2005; Wark and Watson; 2006; Berry et al., 2007). Dodecahedral sites, relative to tetra- and octahedral sites, are rare among the common Earth minerals. Garnet is the only other common mineral to have a dodecahedral site and, while $^{[8]}$Ti in garnet is thought to be rare, the mixed valence (including di-, tri- and tetravalent) and mixed site (including tetra-, octa- and dodecahedral) of the mineral makes direct comparison to zircon impossible. On the basis of these observations there is no *prima facie* observation that can be used to suggest preferential Ti site occupancy.

As indicated by Ferry and Watson (2007), two end-member reactions are possible for Ti^{4+} substitution in zircon (for further discussion regarding the Ti-in-zircon reaction see Appendix 1):

$$\underset{\text{zircon}}{ZrSiO_4} + TiO_2 = \underset{\text{zircon}}{Zr^{[4]}TiO_4} + SiO_2, \qquad (+\Delta V) \qquad \textbf{(eq. 7.1)}$$

where Ti occupies the 4-coordinated (tetrahedral) Si-site. On the other hand, where Ti occupies the dodecahedral site:

$$TiO_2 + SiO_2 = \underset{\text{zircon}}{^{[8]}TiSiO_4}, \qquad \textbf{(eq. 7.2)}$$

If the mole fraction of the Ti component in zircon exists at the trace element level, zircon activity can be said to approximate unity ($a_{ZrSiO_4} \approx 1$).

If Ti occupies the tetrahedral site in zircon, the equilibrium constant (for equation 6.1) is:

$$K(7.1) = \frac{a^{zircon}_{ZrTiO_4} a_{SiO_2}}{a_{TiO_2}}, \qquad \textbf{(eq. 7.3)}$$

and decreasing silica activity would result in increasing Ti in zircon.

If Ti occupies the dodecahedral site in zircon, the equilibrium constant (for equation 7.2) is:

$$K(7.2) = \frac{a_{TiSiO_4}^{zircon}}{a_{TiO_2} a_{SiO_2}}, \qquad \textit{(eq. 7.4)}$$

and decreasing silica activity would result in decreasing Ti concentration in zircon.

Comparison of equations 7.3 and 7.4 shows that silica activity has opposing effects in the scenarios represented by these equations. That is, when Ti occupies the tetrahedral site, the equilibrium constant is directly proportional to the silica activity, whereas when Ti occupies the dodecahedral site the equilibrium constant is inversely proportional to silica activity. Titania (TiO_2) activity (i.e., where a system is not rutile-buffered) influences Ti-in-zircon thermometry in both substitution scenarios in the same manner. These hypothetical considerations may be combined (in conjunction with previous experimental work discussed in Section 2.5) to construct a theoretical TiO_2-ZrO_2-SiO_2 isothermal diagram (Figure 7.3) that describes how substitution mechanisms differ.

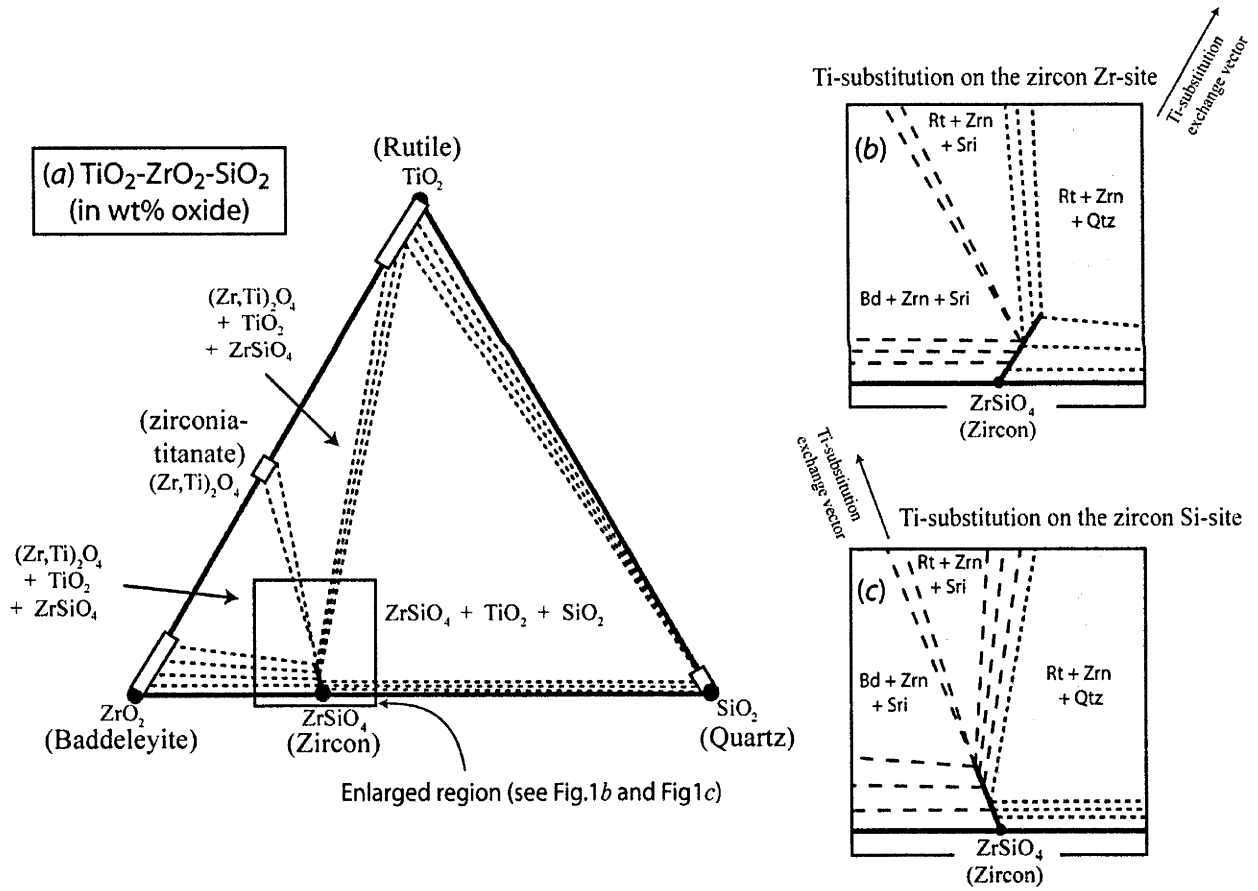

Figure 7.3: *(a) Model isothermal ternary diagram for TiO_2-ZrO_2-SiO_2 system (based on previous reports from: Pena and DeAza, 1976; Troitzsch and Ellis, 2004, 2005a, 2005b; Zack et al., 2004; Tomkins et al., 2007). Solid solution tie-lines are exaggerated to demonstrate exchange vectors between co-existing phases. Srilankite compositions are constructed from disordered composition at 1 bar/1,300 °C reported by Troitzsch and Ellis, 2004. (b) Enlarged and exaggerated region over zircon where Ti-substitution occurs on the Zr-dodecahedral site such that Ti-exchange occurs along a vector towards a hypothetical $TiSiO_4$ composition (c) Enlarged and exaggerated region over zircon where Ti-substitution occurs on the Si-tetrahedral site such that Ti-exchange occurs along a vector towards a pseudo-srinlankite composition. Many phases in this model diagram undergo phase transitions with changing P-T conditions, such that this diagram should only be considered a model chemograph. Abbreviations: Sri = srilankite, Bd = baddeleyite, Zrn = zircon, Rt = rutile, Qtz = quartz.*

These basic considerations show that Ti-site occupancy is crucial to thermometry among phases of the TiO_2-ZrO_2-SiO_2 (TZS) system and that the original equilibrium hypothesis presented by Watson and Harrison (2005) and Watson et al. (2006) needs to be modified, as pointed out by Ferry and Watson (2007). However, it should also be noted that equations 7.1 and 7.2 represent 'end-member' isostructural substitution mechanisms, where Ti occupies one of the two possible sites. In the absence of definitive information regarding site occupancy, it is also possible that Ti occupies both sites in zircon, occupies different sites under different conditions, and/or occupies interstitial/vacancy sites within the mineral.

7.2: Ti site occupancy in zircon

Chemography

EPMA results from fully buffered experimental zircon populations demonstrate that grains produced in silica-undersaturated conditions (e.g., 1300-UF-2.1, 2638 ± 240 ppm Ti) show significantly higher Ti contents than those at silica saturation at the same temperature (e.g., 1300-SF-2.1, 1200 ± 127 ppm Ti, see Table 6.3 and Figure 7.4). This observation supports the findings of Ferry and Watson (2007) that Ti substitutes on the Si site. This is true of systems where a_{TiO_2} is unity (rutile-buffered, e.g. experiment 1300-U) and where a_{TiO_2} <1 (srilankite-buffered, e.g. 1300-UF-2.1). These EPMA results suggest that Ti^{4+} predominantly occupies the Si^{4+} tetrahedral site within the zircon structure according to the substitution represented by equation 7.1.

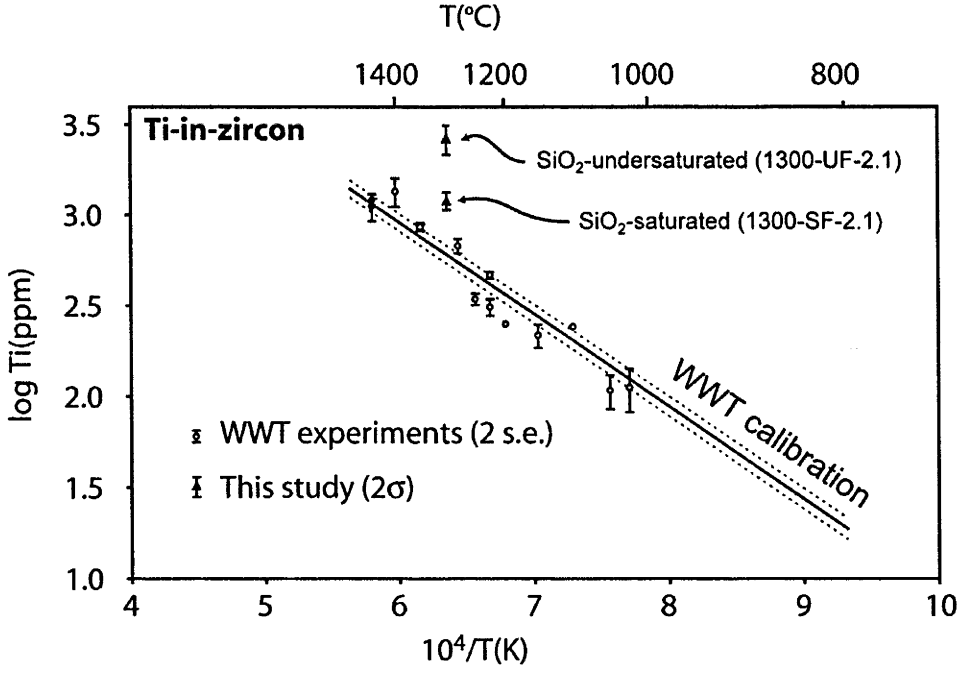

***Figure 7.4**:Ti content of synthetic zircons from fully buffered zircon experiments from this work (triangles), and in Watson et al. experiments relative to the original calibration (WWT = Watson et al., 2006). Dashed lines represent uncertainties associated with the original calibration. Error bars for results from this study are 2σ.*

The composition of zircon should also be considered in the context of other TiO_2-ZrO_2-SiO_2 buffering phases present within experiments. Silica-saturated experiment 1300-SF-2.1, run at 1 bar/1,300 °C, produced an assemblage consisting of co-existing rutile, cristobalite and zircon. Rutile analyses from this experiment show zirconia contents (7.1 ± 0.4 wt% ZrO_2) in agreement with previous 1 bar experiments of Degeling (2003) and Troitzsch and Ellis (2004, 2005). The Ti content of cristobalite (1.63 ± 0.10 wt% TiO_2) is significantly higher than expected for quartz (Wark and Watson, 2006), indicating that Ti is much more soluble in the low-density cristobalite structure than in quartz. The Ti content of zircon in this silica-saturated experiment (1201 ± 127 ppm Ti), is almost double the 606 ppm predicted by Watson et al. (2006) and more than double the 457 ppm predicted by Ferry and Watson (2007). As the 1300-SF-2.1 assemblage is titania- and silica-buffered, the experimental result presented here shows the solubility of Ti in zircon diverging from the equation of Watson et al. (2006).

Srilankite composition changes significantly as a function of mineral assemblage, with rutile-buffered systems showing higher Ti content in srilankite than zirconia-buffered experiments (Table 5.3). All srilankite[1], rutile and zirconia compositions presented here are in excellent agreement with previous 1 bar experiments in the TiO_2-ZrO_2 binary system (Troitzsch and Ellis, 2004, 2005; Troitzsch et al., 2005). Evidence for the attainment of equilibrium includes: the consistency of phase compositions presented here with previous 1 atmosphere experiments (Figure 7.5); the lack of zonation in pre-sintered zircon experiments; and, the low statistical variability among individual phases.

One difference between experiments presented here and those of Watson et al. (2006) and Ferry and Watson (2007) is the presence of srilankite. Troitzsch and Ellis (2004) and Ferry and Watson (2007) both hypothesized that redox conditions may play an important role in the stability of srilankite. This would require the presence or influence of a polyvalent element within the srilankite structure. While redox may be important in the stability of srilankite in natural systems (as discussed by Troitzsch and Ellis, 2004: Fe is known from natural srilankites), it is unlikely to be important in experiments that lack a polyvalent element (e.g., Fe, Cr, V, S, etc). The only manner in which redox conditions can influence srilankite stability within a pure TiO_2-ZrO_2-SiO_2 synthetic system is via the reduction of Ti (from tetravalent to trivalent states) at very low f_{O_2}. As Ti^{3+} is extremely rare at crustal conditions, any experiment containing trivalent titanium should not be used for thermometry calibration. An experiment consisting of rutile and tetragonal zirconia, similar to those reported by Ferry and Watson (2007), is likely to be either too reduced for calibration purposes or represents a metastable mineral assemblage. If an experiment does not attain equilibrium, then the metastable assemblage cannot be said to buffer the chemical potential of reaction components. In other words, the a_{TiO_2} and a_{SiO_2} for the Ferry and Watson (2007) experiments may not be fully constrained.

[1] Srilankite from experiment 1200-u shows some minor compositional variation compared to the original work of Troitzsch and Ellis (2004), but grains from this experiment show notable internal zonation (see Figure 5.2).

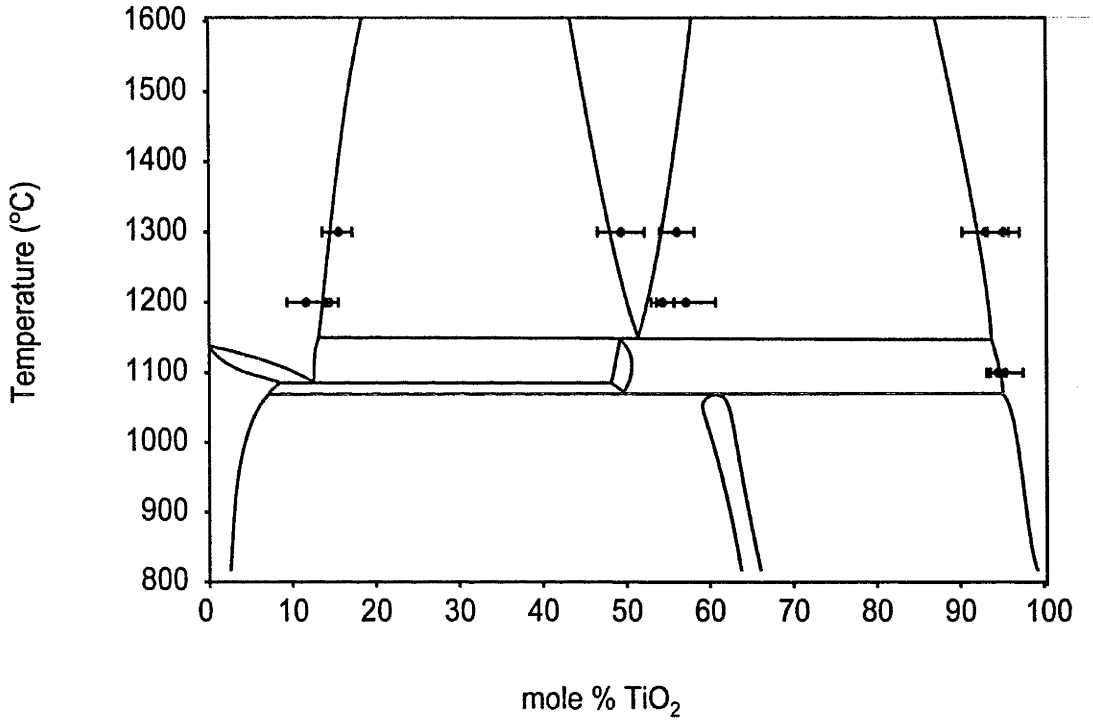

***Figure 7.5**: Composition of tetragonal zirconia, srilankite and rutile from 1 atmosphere experiments presented here (filled circles with 2σ error bars) relative to the ZrO_2-TiO_2 binary phase diagram presented by Troitzsch and Ellis (2005a). Figure after Troitzsch and Ellis (2005a).*

Unbuffered zircon experiments

A significant number of Ti in zircon analyses reported in this research come from experiments where an appropriate silica buffer is not present (neither srilankite nor zirconia). These analyses include zircons from experiments 1300-S, 1100-l and 1100-s where assemblages consist of zircon + rutile + melt. These experiments lack a silica buffer because the Na melt formed from the flux dissolved all the SiO_2. Such assemblages are similar to reports of Watson et al. (2006) and require special consideration. The Ti content of unbuffered zircons shows Ti contents an order of magnitude higher than buffered experiments (see Figure 7.6). It is tempting to assume that the high Ti content of unbuffered experiments is directly related to depressed silica activity. The zircon-zirconia-srilankite assemblage represents the lowest silica activity at which zircon is stable, such that it should define the highest possible Ti content (if Ti partitioning is solely dependent on a_{SiO_2} and a_{TiO_2}). That unbuffered experiments contain significantly higher Ti contents than buffered

experiments indicates that some other process or substitution mechanism is driving Ti solubility.

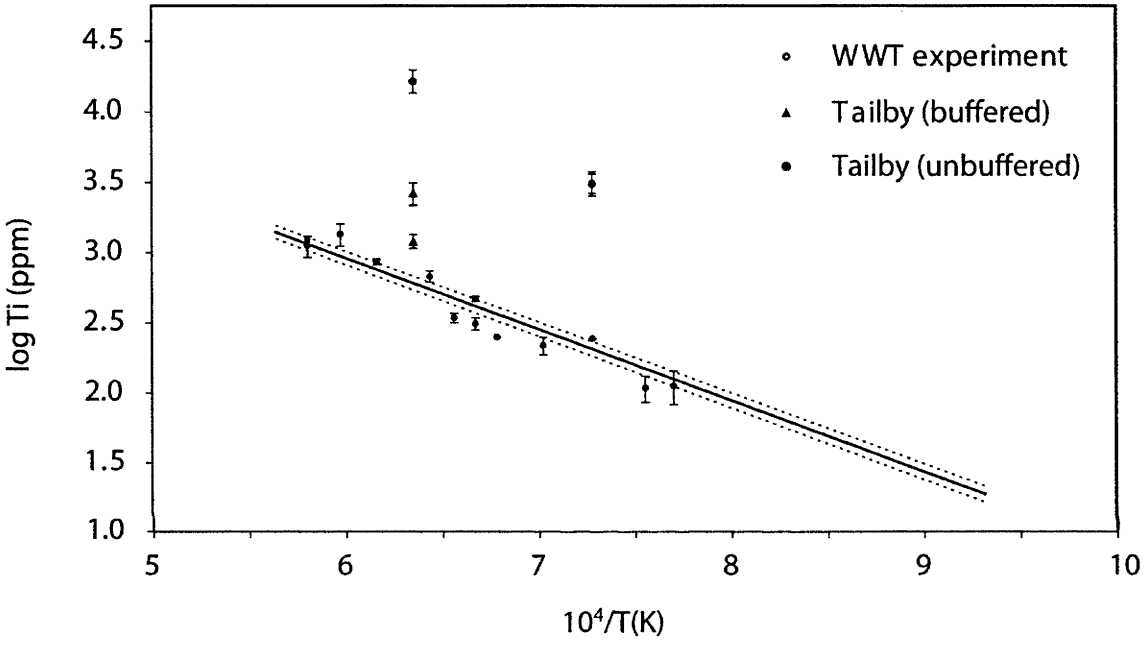

***Figure 7.6**: Ti content of synthetic zircons from fully buffered zircon experiments (black triangles), unbuffered zircons (red circles) from this work and zircons from Watson et al. experiments (black circles) relative to the original calibration (Watson et al., 2006). Dashed lines represent uncertainties associated with the original calibration. Error bars for results from this study are 2σ.*

"Excess" Ti in unbuffered zircons may be related to disequilibrium growth, where zircon cores show high Ti (at the wt% scale), while only the crystal rim is equilibrated (noting that crystal rims are deliberately avoided to limit secondary fluorescence effects).

Another possible cause for "excess" Ti may be related to combined substitution of $^{[8]}Ti^{4+}$ and $^{[4]}W^{6+}$ via scheelite[2]-type substitution ($CaWO_4$). The incorporation of Ti via this type of substitution, while undocumented/unstudied, would result in Ti occupying the zircon *A*- or dodecahedral site. Equally important, this type of substitution would provide another factor contributing to Ti-saturation in zircon and the same process could be true where other large cations that substitute on the tetrahedral site in zircon are involved (e.g., Ge, Mo, V, Cr and As). LA-ICP-MS analyses of buffered zircon grains from 1300-U (the only grains of sufficient

[2] noting that the scheelite structure is a zircon-group mineral and shares a number of structural similarities to zircon.

size for ICP analyses) show no detectable W (Figure 7.7). Unfortunately no LA-ICP-MS or WDS incorporating W analyses were made from unbuffered zircons, so it remains unclear if such combined substitution is possible.

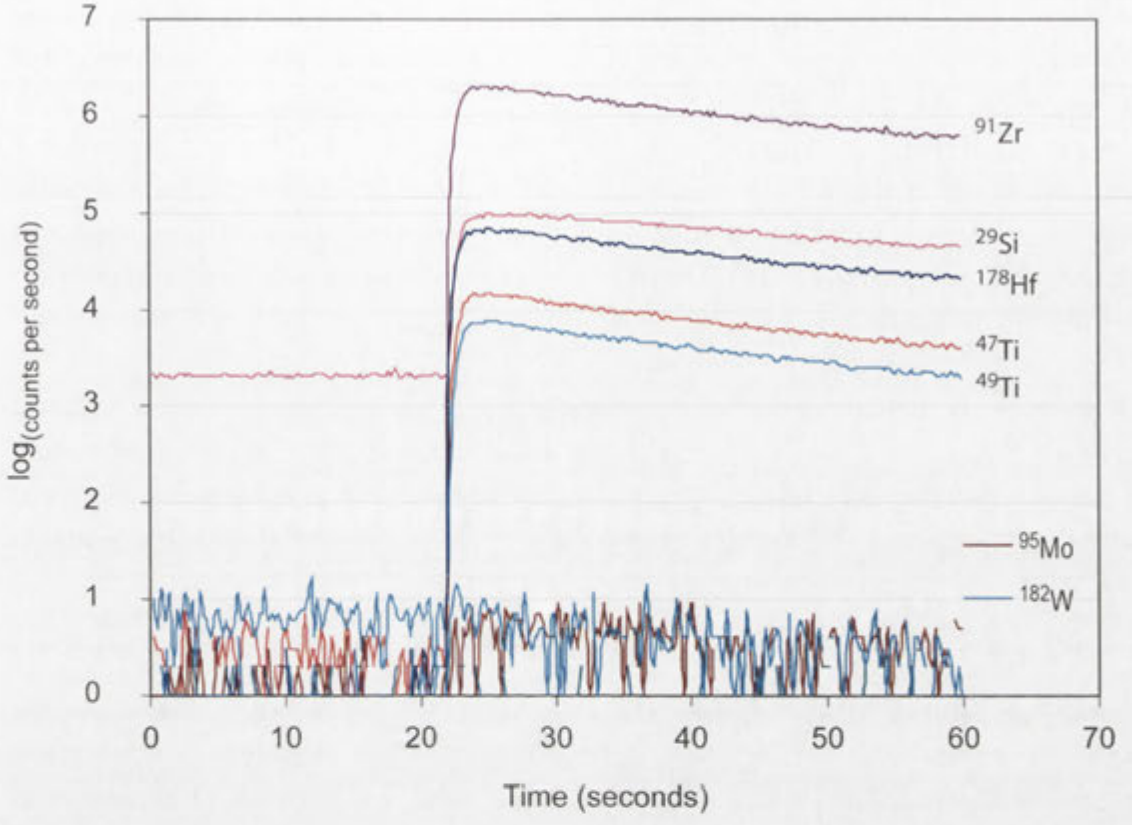

***Figure 7.7**: LA-ICP-MS ablation of synthetic 1300-U zircon.*

7.3: Synchrotron Techniques: XANES

Ti XANES spectra provide a direct probe of the local Ti-bonding environment. In this regard, zircon XANES spectra can be compared with Ti-bearing standards to fingerprint the Ti site in the zircon structure. XANES pre-edge spectra for 1300-U zircons show striking similarities with 4-coordinated Ti-bearing standards (presented here and elsewhere). In particular, the intensity and energy of the 1*s*-3*d* pre-edge energy feature indicate that Ti occupies the tetrahedral site in zircon (Figures 6.14-6.16).

The pre-edge comprises two peaks of approximately equal intensity separated by ~0.75 eV. The peaks vary in energy with the orientation of the horizontally polarised x-ray beam relative to the zircon crystal (Figures 6.17 and 6.18). Such a splitting has not been reported previously for [4]-coordinated Ti in other materials, even though the resolution would have been sufficient to resolve the two components in a powdered sample (e.g. Farges et al. 1996a). In particular, no splitting or broadening was observed for Ti occupying the Si site in forsterite (Berry et al. 2007). The split pre-edge components are, however, reproduced by the XANES modelling of Ti on the Si site. Similar modelling of Ti on the Si site in forsterite indicates an insignificant pre-edge splitting that would not be resolved experimentally. The orientation dependence of the 1*s*-3*d* pre-edge components suggests that they derive from transitions to 3*d* orbitals of different energies arising from the crystal field. The pre-edge has

a high intensity in low symmetry (tetrahedral) environments due to mixing with *p* states. The *p* orbitals are oriented at 90° to each other, as opposed to the 45° relationship between the t_2 and *e* crystal field sets of the *d* orbitals, and electric dipole transitions to states with a significant contribution from these *p* levels would be consistent with the observed angular dependence. At this time the physical explanation for the pre-edge splitting remains unclear and is the subject of ongoing computational work. The existing simulations do confirm that both pre-edge components relate to a single Ti site, which is Ti substituting for Si.

The notable shift in XANES pre-edge energy and intensity with increasing Ti-coordination (e.g., rutile relative to cristobalite), coupled with the general overlap of cristobalite and zircon spectra indicates that Ti predominantly occupies the tetrahedral Si^{4+} site in zircon.

XANES spectra and sector zoning

XANES pre-edge spectra of sector zoned synthetic zircon grains from experiment 1300-U (Figure 6.19) show no detectable shift in the peak energy of the 1*s*-3*d* pre-edge feature across Ti-sectors. This observation suggests that the development of sector zoning in 1300-U zircons (with regard to Ti-distribution) is accompanied by little or no change in the Ti site. Ti appears to occupy the tetrahedral site across all sectors of the 1300-U zircons.

XANES spectra and unbuffered zircons

XANES spectra from 1300-S zircons show distinctly different pre-edge and main-edge spectra from those of 1300-U zircons. The depressed normalized intensity seen in the Ti K-α pre-edge feature in 1300-S indicates that Ti is not tetrahedrally arranged or existed in number of different coordinations (Figure 6.20). Comparison of 1300-S spectra and model mixed Ti site occupancy spectra show some similarities, where the pre-edge peak shows depressed normalized intensity. This could be used to suggest that 1300-S zircons contain Ti in both tetrahedral and dodecahedral arrangement. This being the case, main-edge and post-edge spectra from model spectra show very little correlation to measured spectra from 1300-S, so there is no clear indication as to how or why 1300-S zircons show such high Ti contents or such different Ti XANES pre-edge spectra.

EXAFS from 1300-U zircons

The Ti-O bond length of 1.76(1) Å determined by EXFAS is in excellent agreement with that calculated by DFT for Ti substituting on the Si site (1.797 Å), especially noting that these calculations are often found to overestimate bond lengths by around 1% (Berry et al., 2007). In comparison, the average bond length calculated for Ti substituting on the Zr site was 2.160 Å.

7.4: Comments on the Effect of Pressure on Ti-in-Zircon

Comparison of results presented here (equilibrated at 1 bar) with those of Watson et al. (2006), most at 10 kb, and Ferry and Watson (2007) at 10 kb provide direct experimental evidence for the pressure effect on zircon thermometry. The Ti content of zircons at 1 bar and 1,300 °C (1201 ± 127 ppm) are more than double that predicted by the Ferry and

Watson recalibration (457 ppm) and higher than experiments of Watson et al. (1,350°C/10 kbar/ $a_{SiO_2} \leq 1$, 860 ± 22 ppm). This variability among experiments at a constant temperature and variable pressure can be used to quantify the pressure effect (in a silica- and titania-saturated system).

Calculations based on the different experimental zircon populations must take into account the different silica species present in the various experiments. Experiments of Watson et al. (2006) generally lacked a silica species, meaning $a_{SiO_2} \leq 1$. The zircon thermometer recalibration of Ferry and Watson (2007) was buffered by quartz, while experiments presented here are buffered by cristobalite. As such, the calculated pressure effect needs to be normalized to a standard state of silica (in this case cristobalite).

The experimental work of O'Neill (1987) calculated the free energy difference of the quartz-cristobalite transition, whereby:

$$\Delta G^0_{Q-C} = 2292 - 1.705T \quad \text{(J/mol)} \qquad \textbf{(eq. 7.5)}$$

On the basis of equation 7.5, at 1,300 °C, the free energy difference of quartz and cristobalite is -390 J/mol. The experimental recalibration of Ferry and Watson (2007), relative to the standard state of cristobalite at the temperature of interest and 1 bar, was therefore at $a_{SiO_2} = 0.97$. Assuming that Ti substitution occurs predominately for Si^{4+} over the pressure range of interest, then the pressure effect can be related to equation 7.5, such that:

$$RT \ln a^{zircon}_{ZrTiO_4}(P) = RT \ln a^{zircon}_{ZrTiO_4}(P_i) + \int_{1\,\text{bar}}^{P} \Delta V dP \qquad \textbf{(eq. 7.6)}$$

such that:

$$\ln \frac{a^{zircon}_{ZrTiO_4}(P)}{a^{zircon}_{ZrTiO_4}(1\,\text{bar})} = \overline{\Delta V}(P-1) \qquad \textbf{(eq. 7.7)}$$

where $\overline{\Delta V}$ is an averaged volume change for equation 7.5.

Combining equation 7.5 and equation 7.7, and employing Ti-in-zircon values of Ferry and Watson (2007) and those reported here (Table 5.3):

$$RT\left(\ln \frac{457 \times 0.97}{1201}\right)/9999 = \overline{\Delta V} \qquad \textbf{(eq. 7.8)}$$

such that:

$$\overline{\Delta V} = -1.304\ (\pm\ 0.27)\ \text{J/mol or } -13.04\ (\pm\ 2.7)\ \text{cm}^3$$

These calculations, based on experiments equilibrated at 1,300 °C, a_{SiO_2} = 1 and a_{TiO_2} = 1, demonstrate a substantial effect of pressure on the Ti-in-zircon thermometer.

7.5: Summary

The Gibb's phase rule dictates that any experiment within the TiO_2-ZrO_2-SiO_2 system requires three phases in order to be fully buffered (invariant). The formation of srilankite is of particular importance in demonstrating equilibrium in silica-undersaturated systems. In some cases, the use of pre-synthesized zircon grains can remove the necessity for crystal seeds that introduce analytical uncertainties. Analysis of zircon grains (synthetic and natural) needs to take account of stray electron effects, the influence of inclusion phases, heterogeneous cation distribution and secondary alteration.

The three independent techniques presented here – (1) experimental synthesis, (2) direct structural probes (XANES), and (3) DFT calculations, collectively indicate that Ti preferentially substitutes on the tetrahedral site in zircon. This leads to the conclusion that equation 7.1 represents the appropriate thermometric substitution mechanism. None of the techniques employed here indicate that Ti solely occupies the tetrahedral site, but that Ti substitution mechanism is likely dominated on the zircon Si^{4+} tetrahedral site.

Silica activity and implications for natural zircons

Results presented earlier in this paper establish that Ti predominantly occupies the tetrahedral site in zircon, replacing Si^{4+} according to equation 7.1. This means that increasing a_{SiO_2} decreases the concentration of Ti in zircon at a given temperature, thus requiring an estimate for silica activity during zircon crystallization (as addressed by Ferry and Watson, 2007). Equally important, though beyond the scope of this thesis and addressed by Watson et al. (2006) and Ferry and Watson (2007), is the necessity for an estimate of titania activity during zircon crystallization.

The range of silica activities over which zircon may crystallize is bound by the presence of silica (quartz and its polymorphs, where a_{SiO_2} = 1) and the zircon ↔ baddeleyite + quartz buffer (which defines the minimum a_{SiO_2} stability limit of zircon, see Figure 7.8). The locus of several a_{SiO_2}-buffers has been constructed from the thermodynamic properties of the various reaction phases in question (Holland and Powell, 1998). The maximum range of silica activities over which zircon may crystallize is ~1.3 log units (Figure 7.8 – shaded region).

The zircon stability field in a_{SiO_2} -T space shows that the Δa_{SiO_2} -range between end-member buffer assemblages decreases with increasing temperature.

The 1,300 °C experiments presented here correspond to the two end-member a_{SiO_2} -buffers (quartz-saturated and co-existing baddeleyite-zircon). As such, these experiments may be used to demonstrate the influence of a_{SiO_2} on zircon Ti-saturation. Although a_{TiO_2} of the 1,300 °C silica-undersaturated experiment is less than unity (i.e., not rutile buffered), and the Δa_{SiO_2} between the two buffers is 0.32 log units (see Figure 7.8), the respective experiments show a doubling in Ti content [or ΔTi (ppm) = 0.34 log units] from silica-saturated to silica-undersaturated conditions. Hence, although Ti exists at trace levels, a_{SiO_2} has the capacity to dramatically change the Ti-saturation in zircon.

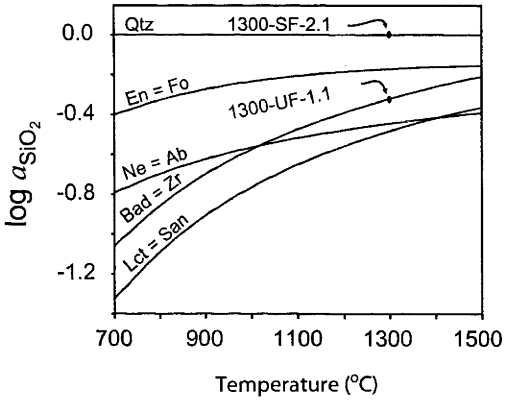

***Figure 7.8**: Locus of silica buffer reactions plotted against log a_{SiO_2} -temperature. Stability range of zircon corresponds to the shaded region, while a system containing quartz (or polymorph thereof) is assumed to be silica buffered (a_{SiO_2} =1). Silica activity for zircon-bearing experiments 1300-SF-2.1 and 1300-UF-2.1 are shown by filled circles. Abbreviations: Qtz = quartz, En = enstatite, Fo = forsterite, Bad = baddeleyite, Ne = nepheline, Alb = albite, Lct = leucite, and San = sanidine.*

Given that silica activity changes can have a significant influence on Ti-saturation in zircon, it is important to consider how such changes may present themselves in natural zircons. In a system that is quartz-undersaturated at the initiation of zircon growth/overgrowth, metamorphic or igneous, it is entirely plausible that a_{SiO_2} would continuously change as the system evolves (be it via assimilation-fractional crystallization processes, metamorphic reactions, etc). Unless Ti-diffusion in zircon can maintain equilibrium between the zircon "core" and the melt/bulk rock, which seems unlikely from Ti diffusion rates (Cherniak and Watson, 2007), it is possible that a continuously crystallizing zircon grain will show Ti content that preserves a_{SiO_2} changes as the system evolves. In such a scenario it would be difficult to distinguish between temperature-driven or a_{SiO_2} -driven Ti-variation. Moreover, where

a_{SiO_2}, a_{TiO_2} and temperature all change during zircon growth, it would be difficult to distinguish the influence of each variable on Ti-saturation.

This begs the question, how does one determine a_{SiO_2} at the time of zircon growth and distinguish between chemically-driven and temperature-driven Ti-variations? As shown in Figure 7.8, the a_{SiO_2} range over which zircon is stable is defined by two end-member buffers. Where quartz is present, the a_{SiO_2} of the melt or mineral assemblage is unity (a_{SiO_2} = 1), and where zircon and baddeleyite coexist ($ZrO_2 + SiO_2 \leftrightarrow ZrSiO_4$) the melt/system is at the minimum a_{SiO_2} of zircon stability. Only the forsterite + enstatite ($Mg_2SiO_4 + SiO_2 \leftrightarrow 2MgSiO_3$) and nepheline + albite ($NaAlSiO_4 + 2SiO_2 \leftrightarrow NaAlSi_3O_8$) buffer reactions exist between these two end-member buffers. Even where zircon co-exists with [enstatite + forsterite], [nepheline +albite] or baddeleyite, the a_{SiO_2} of the buffer reaction is dependent on temperature and pressure. Hence, even where such a buffer assemblage exists, a zircon crystallization temperature estimate can only be bracketed by the a_{SiO_2}-range of the relevant reaction. In such a scenario (recognizing that zircon + enstatite + forsterite, zircon + nepheline + albite or zircon + baddeleyite assemblages are uncommon), zircon temperature estimates can be made and uncertainties estimated accordingly.

These hypothetical examples are introduced to demonstrate some of the considerations, based on Ti occupying the zircon tetrahedral site, which should be made when applying zircon thermometry. This is particularly true of grains that are "out of context", like detrital or porphyroblast-hosted zircons. Accurate temperature estimates based on Ti-variation from core-to-rim, or across various zircon domains, require an appreciation/estimate of what is driving Ti-variation (a_{SiO_2}, a_{TiO_2}, temperature, etc).

SEM-CL, BSE and Ti-distribution

The two techniques typically applied to determine internal zonation in zircon are SEM-CL and BSE imaging (Corfu et al., 2003). The usefulness of both techniques in identifying internal zonation within zircon (see Hanchar and Miller, 1993; Hanchar and Rudnick, 1995; Corfu et al., 2003 for examples) is without question, but the relevance of such imaging to Ti-distribution in zircon has not been established.

The most common form of CL imagery involves measurements from a CL detector fixed to a scanning electron microscope (SEM-CL). Such imagery is panchromatic in nature, thus involving "bulk" or "wholesale" detection of emission spectra. As such, SEM-CL imaging (typically presented in the form of greyscale imaging) provides good CL spatial resolution but presents no information regarding the source of such signal. This is important for zircon thermometry purposes because while CL zonation clearly corresponds to the relative distribution of trace elements within different domains of a given zircon crystal, discussion

still persists regarding the elemental source/s of CL activation and quenching. Literature reports (e.g., Mariano, 1989; Remond et al., 1992; Hanchar and Rudnick, 1995; Corfu et al., 2003), generally attribute CL activation in zircon to REEs (particularly Dy – though Sm, Eu and Tb have also been hypothesized, e.g., Ohnenstetter et al., 1991). By contrast, CL quenching in zircon is generally attributed to U content or decay products thereof (Corfu et al., 2003). It can be said then, regardless of CL activation or quenching, CL signal is generally attributed to cations of large ionic radii (REE, U, etc) that are likely to occupy the Zr^{4+} dodecahedral site.

Experimental results, DFT simulations and Ti K-α XANES spectra show Ti occupies the zircon tetrahedral site, while the majority of elements responsible for CL signal occupy the dodecahedral site. This means that Ti-distribution and CL-activation can potentially be decoupled in zircon.

Indeed, synthetic zircons produced in this study (1300-U) have shown that Ti-distribution has little or no correlation to SEM-CL imagery. Several important conclusions can be drawn from this observation:

1) despite the high Ti content of zircons from this experiment (~0.57 wt% TiO_2), Ti appears to contribute little to the overall zircon SEM-CL signal,

2) synthetic zircons from experiment 1300-U indicate that Ti sector zoning is possible in zircon,

3) where parameters that control the incorporation of CL-activating elements (e.g., partitioning behaviour) and Ti (e.g., temperature, a_{SiO_2}, and a_{TiO_2}) are decoupled during zircon crystallization, SEM-CL imagery is an inappropriate petrographic tool for Ti-related investigations.

While the study of synthetic zircons can be used to demonstrate what is possible in nature, natural zircons represent the ultimate test. Analyses from "fir-tree" zoned zircons from Monviso show a doubling of Ti contents across SEM-CL domains (representing crystallization temperatures of 584 °C and 542 °C across the two domains, assuming a_{SiO_2} = 1). This example suggests that development of the "fir-tree" framework (as imaged in SEM-CL) correlates with the heterogeneous distribution of Ti. In short, Ti-distribution in Monviso samples appears to have a large crystallographic control (rather than just thermal).

LA-ICP-MS results from natural Northern Queensland zircons (NQ-1) show pronounced sector zoning for CL-activating and quenching elements (e.g., REE and U). REE contents across the two domains increase by between 70.8-81.8%, whereas Ti contents increase by ~9.5 % (Table 6.5). In this NQ-1 example, where SEM-CL domains appear to correlate to dramatic changes in REE, P, U, and Th, Ti-variation is far more subtle (with average calculated

crystallization temperatures across the two domains being 620 °C and 613 °C). Thus, sector zoning among NQ-1 samples is accompanied by little Ti-variation.

These examples demonstrate that Ti sector zoning can be present in both natural and synthetic zircon populations. It should be stressed that the zoned zircons presented here are examples in which sector zoning is most likely to be investigated. This is because Ti contents are sufficient for x-ray mapping and grain size is sufficient for LA-ICP-MS analyses.

It remains to be seen whether low-Ti zircons show Ti sector zoning in the absence of correlative SEM-CL. Therein lays one of the greatest challenges of zircon thermometry – determining the distribution of a trace element (e.g., Ti). Whereas SEM-CL operates at the micron scale, analytical techniques that may be used to measure zircon Ti content (particularly among zircons crystallized at temperatures <900 °C, where Ti exists at the sub-100 ppm levels) generally do not. Sector zoning is not the only concern with regard to correlation between SEM-CL and Ti-distribution. Secondary alteration, such as fluid alteration along cracks/fractures, may also work to locally modify zircon Ti content in a way that is not obvious from SEM-CL. Similarly, crystal deformation has potential to modify Ti concentration and distribution. Thus, it remains to be proven whether CL imaging is a good way to target Ti analyses for zircon thermometry.

Chapter 8

Conclusions

The various analytical and modelling techniques presented here can collectively be used to demonstrate that Ti-substitution in zircon predominantly occurs on the tetrahedral site and thus, equation 7.1 ($ZrSiO_4 + TiO_2 = Zr^{[4]}TiO_4 + SiO_2$) is the most appropriate substitution reaction for thermometry. In no way does this substitution mechanism invalidate the Ti-in-zircon hypotheses, but it does require an estimate for a_{SiO_2} (and although not directly addressed in this thesis, an estimate for a_{TiO_2}) at the time – and duration – of zircon growth.

Another issue concerning zircon thermometry is the relationship between SEM-CL/BSE and Ti distribution. If Ti sits on a different site from the elements that are responsible for the SEM-CL signal, which results presented here indicate, then such imaging techniques may not give an accurate picture of the Ti distribution and temperature history of the zircon grain.

This research also suggests that there is a notable pressure effect, over the 0.001-10 kbar pressure range, on zircon Ti content.

Broader application and future research

The experimental and analytical techniques used to fingerprint Ti site occupancy in zircon could be used to study trace element substitution in a broad range of minerals. The technique could be used to study the substitution of polyvalent elements within zircon (e.g., As, U, W, Mo, Cr, V, etc) as a function of mineral paragenesis and f_{O_2}. Equally important, the method is not solely restricted to the study of zircon, but can be applied to study trace element substitution in minerals that contain numerous cation sites or those that undergo complex/coupled substitutions.

Part 2

A new, large volume experimental technique: studies into the pelite-H_2O system at 25-35 kbar.

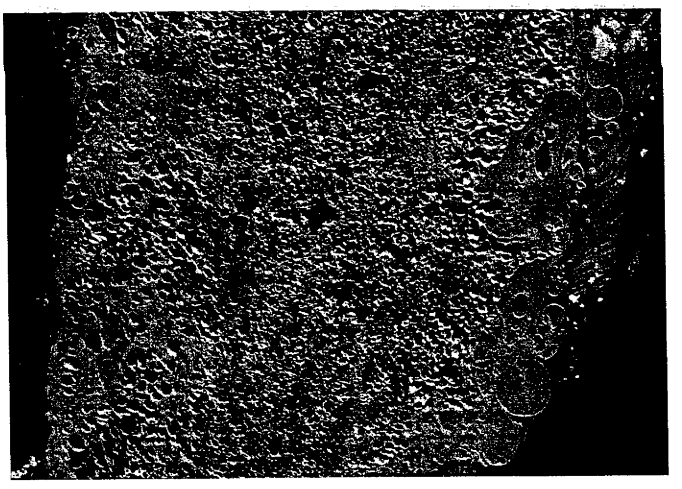

ABSTRACT

Previous research into the pelite-H_2O system at >20 kbar places the wet solidus at temperatures that vary by ~150 °C and the second critical end-point ($CP^2_{Pelite-H_2O}$) at conditions ranging from 35 kbar/700 °C (Bureau and Keppler, 1999) to 55 kbar/925 °C (Schmidt et al., 2004). The discrepancy between existing experimental studies is unfortunate, because accurate modeling and description of the pelite-H_2O system is crucial to understanding trace element recycling within the arc environment (particularly the LILE).

This work describes a new technique for studying silicate-H_2O systems at >20 kbar, with the pelite-H_2O system serving as a model. The technique is the first to employ the combined use of H-sensors (f_{H_2}) and oxygen buffers (f_{O_2}) in order to map out L-V relationships in a hydrous-silicate system. The basic premise behind this research is that if the f_{O_2} is fixed within an experiment (via a solid state buffer) and the f_{H_2} is sensed by an inert sensor capsule, the f_{H_2O} or a_{H_2O} can be calculated from the simple reaction:

$$f_{H_2} + \tfrac{1}{2} f_{O_2} = a_{H_2O}$$

Results from sliding H-sensor capsules, which employ a NiO-Ni-Pd assemblage, indicate that experiments at 35 kbar/900 °C the pelite-H2O system becomes supercritical, while experiments at 35 kbar/800 °C exist within the L+V miscibility gap. Furthermore, experiments at 35 kbar indicate that the wet solidus exists at temperatures between 750-800 °C, such that the wet solidus and critical curve are likely separated by ~100 °C. This brings into question the 55 kbar/925 °C second critical end-point of Schmidt et al. (2004), as it would require both the wet solidus and critical curve to show significant and unrealistic backbending.

Petrographic observations from this experimental study show that all quenched runs at supersolidus conditions contain silicate melt (L) + aqueous phase (V), even where sensors indicate supercriticality. Thus, passage through the L+V solvus (miscibility gap) during quench produces textures that obscure the true phase assemblage at experimental pressure and temperature. This brings into question the usefulness of textural interpretation when trying to determine supercriticality.

Chapter 9

Pelite-H_2O Introduction

9.1: Pelite-H_2O Introduction

Part 2 of this thesis presents a new experimental technique for studying silicate-H_2O systems at high pressures (e.g., >20 kbar). In order to test the new method, experiments were carried out within the pelite-H_2O system at various temperatures between 25 and 35 kbar. The earliest sections of Part 2 focus on the importance of the pelite-H_2O system, with regard to geochemical recycling within the subduction environment, as it pertains to understanding bulk chemical fractionation within the Earth. The early sections of the literature review provide the theoretical basis, as described by current models, of supercritical behaviour in silicate-H_2O systems in order to provide the reader with an up-to-date working model that is generally accepted by the broader Earth Science community. A significant body of the literature review is also devoted to highlighting problems and limitations regarding existing experimental studies within the pelite-H_2O system, which help explain why existing studies report such diverse results.

Later chapters of Part 2 discuss the thermodynamic and physical principles behind the new experimental technique, with several chapters devoted to describing how the technique was developed and various calibration methods used during testing.

The later chapters of Part 2 discuss results from pelite-H_2O experiments and how they provide new information regarding solid (S)-liquid (L)-vapour (V) relationships at high pressure. These results provide a new estimate of supercriticality in the system, while also permitting a re-evaluation of results presented in previous research.

Chapter 10

Literature Review

10.1: Literature Review: a general overview

The information presented in this review is organized into three research themes that directly relate to the aims of this, Part 2, of the thesis. The introductory section of this chapter (10.2) discusses mineral/rock-H_2O systems at high pressure conditions. This discussion focusses on theoretical constraints and how experimental techniques have been used to help decipher how pelite components may be introduced into the locus of partial melting beneath the active arc. Particular attention is paid to wet minimum melting temperatures and supercritical behaviour in hydrothermal silicate systems at high pressure and potential flaws in existing experimental datasets.

Intermediate sections of this chapter (10.3) focus on published phase and melting relations in pelite-H_2O systems. This section of the literature review highlights inconsistencies surrounding estimates of the pelite-H_2O solidus, critical curve and critical end point at high pressure.

The final sections of this literature review (10.4) focus on experimental techniques that involve the use of solid media oxygen buffers and sliding noble metal H-sensors. The various techniques discussed here provide the background information required to understand the experimental techniques developed during this research.

10.2: Mineral/rock-H_2O studies at high pressures

There have been numerous studies into rock-H_2O systems or mineral-H_2O systems at pressures >20 kbar. A variety of interchangeable (and sometimes misused) terms have been used to describe H_2O-bearing experiments within the literature. In order to provide a consistent terminology throughout this thesis, it is necessary to provide some working definitions. The term 'liquid' (L) refers to a silicate-dominated and H_2O-bearing liquid (melt), the term 'vapour' (V) refers to a H_2O-dominate (aqueous) and silicate-bearing vapour species (noting that the H_2O vapour has properties more akin to a liquid at high pressures) and the term 'solid' (S) refers to a single mineral or a mixture of solid minerals stable at a given P-T-*X*.

The wet solidus

The wet solidus is one of the most fundamental concepts in igneous petrology, playing a crucial role in the formation of new crust in both intracontinental and subduction settings. Phase relations in mineral/rock-H_2O systems show that the addition of water universally depresses the solidus among silicate systems (e.g., Yoder, 1958). Solidus depression via the addition of water has been confirmed via experimental studies in a number of silicate systems, including quartz (Kennedy et al., 1962); albite (Burnham and Davis, 1974); granodiorite (Robertson and Wyllie, 1971); gabbro (Lambert and Wyllie, 1972); peridotite (Kushiro et al., 1968; Mysen, 1973; Green, 1972) and pelite (Nichols et al., 1994; Johnson and Plank, 1999; Schmidt et al., 2004; Hermann and Spandler, 2008). The wet solidus marks the minimum temperature required to

produce silicate liquid (L) at a given pressure and is the locus in P-T-X space where solid, vapour and liquid coexist (defined as the S+V=L reaction).

While the addition of water appears to depress the minimum melting temperature of all silicate systems, the shape and P-T locus of the wet solidus appears to vary depending on the mineralogy/composition of the silicate-H_2O system and whether melting occurs via vapour-saturated or vapour-absent (dehydration) processes.

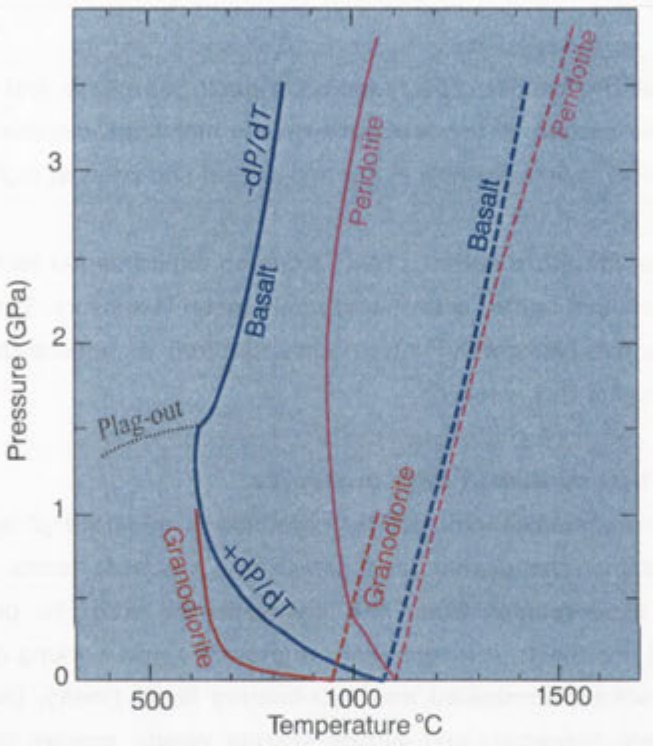

***Figure 10.1**: P-T projection of wet and dry solidi for various silicate-H_2O systems. Peridotite melting curves in pink (after Mysen, 1973), basalt melting curves in blue (after Lambert and Wyllie, 1972), and granodiorite solidi shown in red (after Robertson and Wyllie, 1971). Note the wet solidus inflection in the basalt-H_2O system at ~1.5 GPa, 670 °C corresponds to the breakdown reaction of plagioclase to jadeite plus quartz.*

Two important points can be made from previous research into the locus of various wet solidi. First, phase changes that occur among the solid mineral assemblage with increasing pressure can change the d*P*/d*T* slope of the wet solidus (provided that the transient solids are involved in the minimum melting reaction). A classic example is the wet solidus 'backbend' seen in the gabbro-H_2O system reported by Lambert and Wyllie (1972; Figure 7.1). The breakdown of plagioclase to form 'jadeite + quartz' is accompanied by an inflection (or backbending) in the gabbro or basalt wet solidus. Second, changes in the slope of a wet solidus with increasing pressure are generally thought to correspond to changes from low-pressure solidus minerals (such as the breakdown of amphibole or biotite) to high-pressure phases, like garnet, jadeitic pyroxenes, phengite or coesite (Boettcher and Wyllie, 1969; Lambert and Wyllie, 1972;

Millhollen and Wyllie, 1970; Merrill and Wyllie, 1972). Such phenomena were pointed out by Boettcher and Wyllie (1969), who suggested that changes in the wet solidus (particularly among complex mineralogical systems) may also result from dramatic negative volume changes (-d*V*) among solidus minerals with increasing pressure. Continuous mineralogical changes (e.g., solid-solutions) that occur in response to d*P*-d*T* may not cause abrupt changes in the rock-H_2O solubility relationships, but may cause subtle changes in relative density between the liquid and vapour phases. Ergo, a change in the density of the hydrous liquid (L) relative to the solid + vapour (S+V) could, theoretically, cause back-bending (or forward-bending) along the wet solidus. Such a scenario would be hard to monitor, as the phenomenon would not be associated with any obvious (i.e., discontinuous) change among the solids.

The albite-H_2O system: a working model of silicate-H_2O systems

The albite-H_2O system (Burnham and Davis, 1974) is commonly used as a model system for describing mineral-liquid-vapour relationships as they relate to the locus and termination of the wet solidus (Hack et al., 2007).

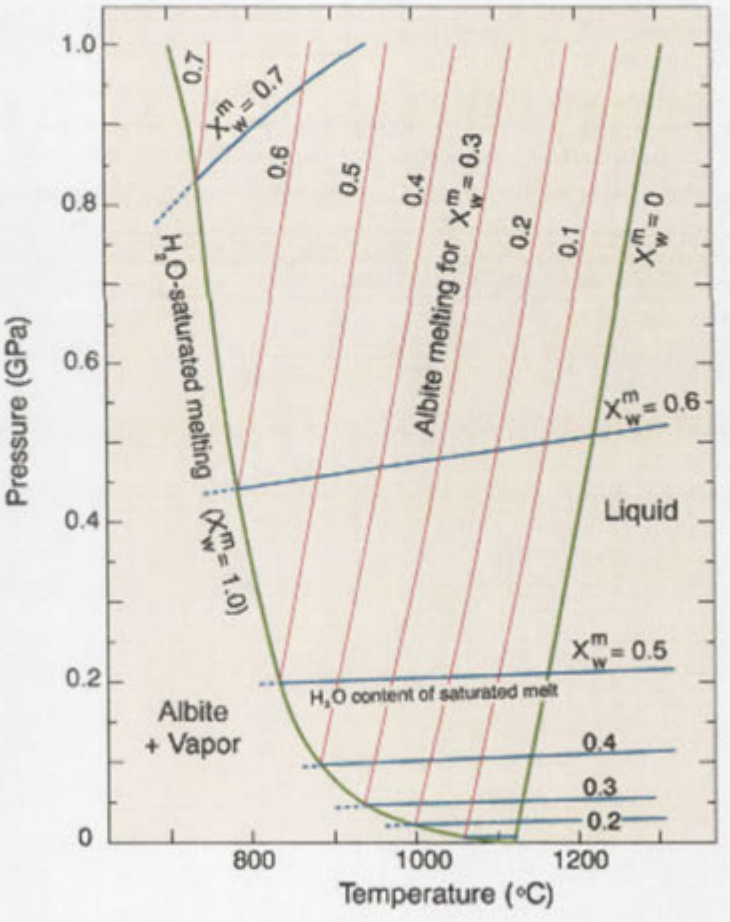

***Figure 10.2**: Model $NaAlSi_3O_8$-H_2O P-T projection of Burnham and Davis (1974). Blue curves represent solubility isopleths, where albite melt saturates at a fixed mole percent H_2O. Red curves represent melting isopleths, where albite melting occurs at a fixed mole percent H_2O. Green curves represent the locus of wet and dry solidi.*

As shown in Figure 10.2, the albite wet solidus is defined as the locus where melting and solubility isopleths at a fixed mole % H_2O meet. In other words, the wet solidus represents the minimum temperature (at a fixed pressure) required to melt albite in the presence of excess water. The importance of this phase diagram is not simply that it defines albite-H_2O minimum melting, but it also provides information on the topology of the liquid-vapour solvus through the inclusion of isopleths. The change in solubility isopleths reported by Burnham and Davis (1974, blue curves in Figure 10.2) shows changes in d*P*/d*T* indicating that there is a change in the shape of the L+V solvus with increasing pressure.

Later work by Paillat et al. (1992) combined experimental and thermodynamic considerations to construct a P-T-*X* model for the albite-H_2O system. As shown in Figure 10.3 the shape and position of the model L+V solvus changes dramatically with d*P*/d*T*. At low pressures (i.e., <0.5 GPa) $-dT/dX_w^m$ slopes (where *w* = H_2O and *m* = silicate liquid) are seen on the albite liquid (L) side of the L+V solvus, such that solubility isopleths predict +d*P*/d*T* slopes. At higher pressures (i.e., >1.0 GPa) the model system shows $+dT/dX_w^m$ slopes on the albite liquid (L) side of the L+V solvus, such that solubility isopleths predict -d*P*/d*T* slopes.

To demonstrate the importance of composition and solubility relationships, two hypothetical silicate-H_2O isobaric T-*X* sections are presented in Figure 10.4. There are several important features that are immediately obvious in this diagram, including the dry solidus (T_{DS}), wet solidus (T_{WS}) and the L=V solvus crest (critical point).

If the L=V solvus has $-dT/dX_w^m$ such that H_2O solubility decreases with increasing temperature in the silicate liquid (L) at isobaric conditions, then H_2O solubility isopleths (X_w^m) must have a +d*T*/d*P* slope (Hack et al., 2007).

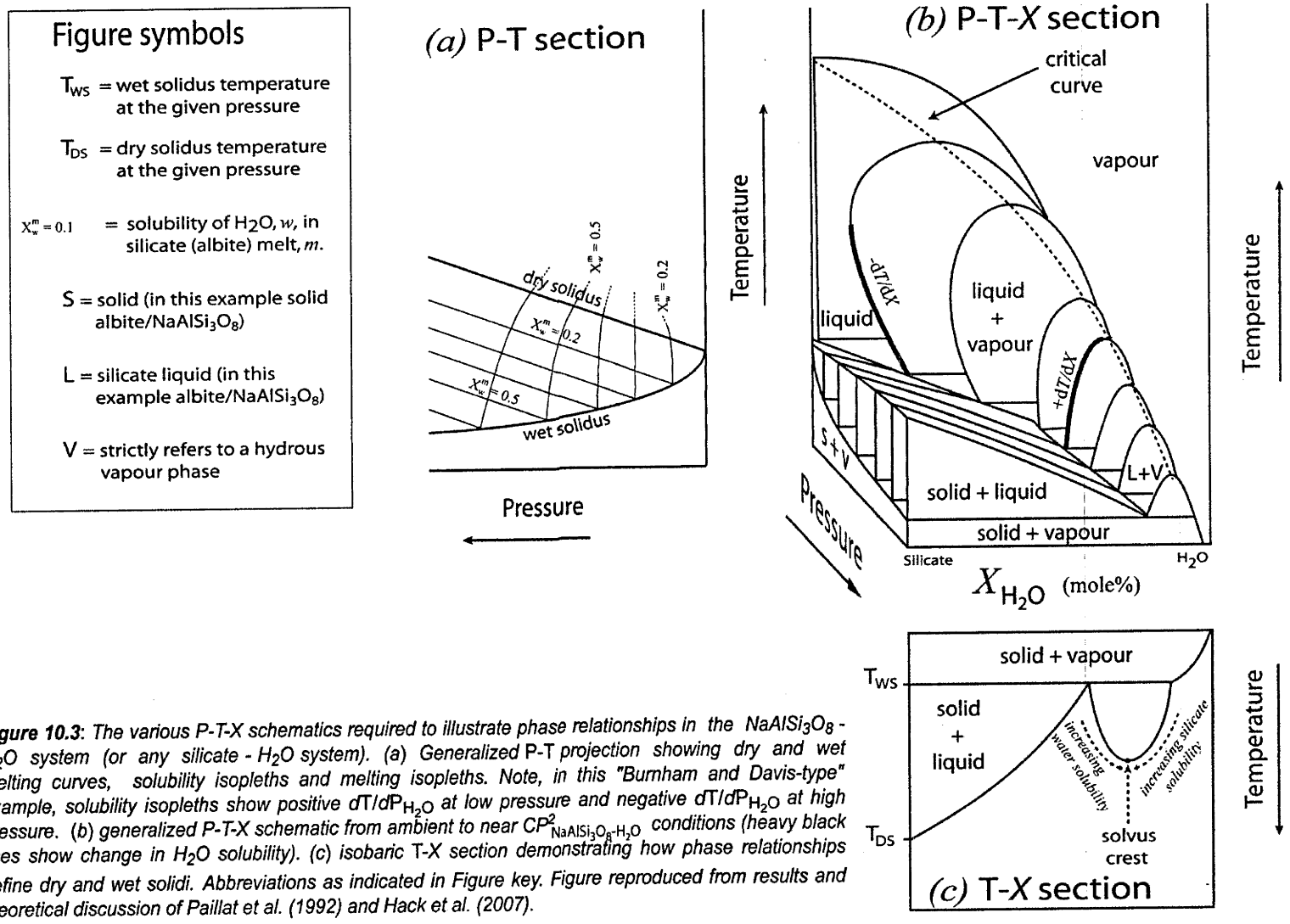

***Figure 10.3**: The various P-T-X schematics required to illustrate phase relationships in the $NaAlSi_3O_8$ - H_2O system (or any silicate - H_2O system). (a) Generalized P-T projection showing dry and wet melting curves, solubility isopleths and melting isopleths. Note, in this "Burnham and Davis-type" example, solubility isopleths show positive dT/dP_{H_2O} at low pressure and negative dT/dP_{H_2O} at high pressure. (b) generalized P-T-X schematic from ambient to near $CP^2_{NaAlSi_3O_8\text{-}H_2O}$ conditions (heavy black lines show change in H_2O solubility). (c) isobaric T-X section demonstrating how phase relationships define dry and wet solidi. Abbreviations as indicated in Figure key. Figure reproduced from results and theoretical discussion of Paillat et al. (1992) and Hack et al. (2007).*

If the L=V solvus shows $+\mathrm{d}T/\mathrm{d}X_w^m$ increasing H_2O solubility in the silicate melt with increasing temperature dictates water solubility isopleths of -d*T*/d*P* (see Figure 10.4).

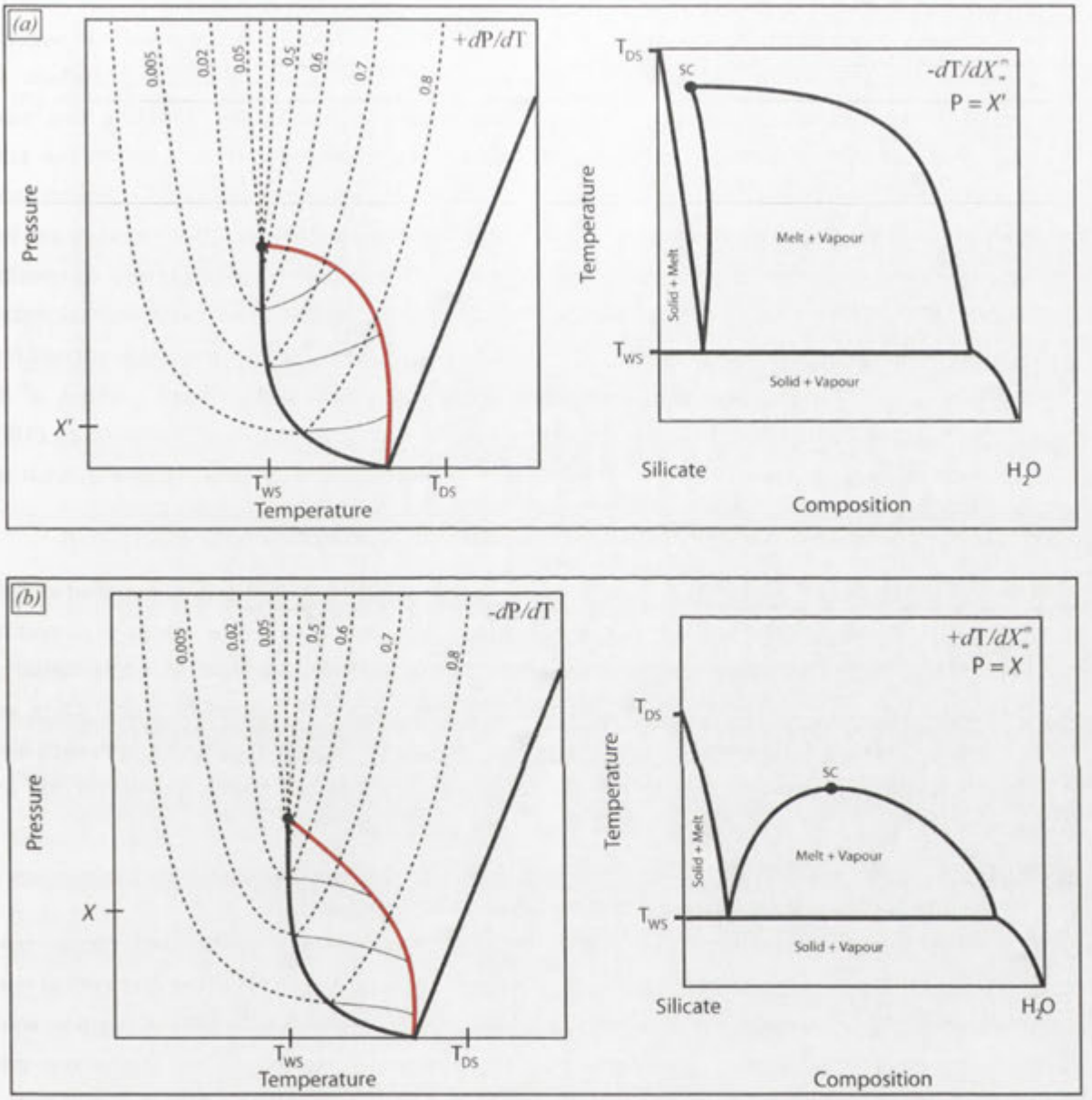

Figure 10.4: *Theoretical P-T-X relations in silicate-H_2O systems illustrating the relationship between T-X solvus topology and P-T projected solubility isopleths at sub-critical conditions. (a) 'jester-hat'-type solvus topology dictates decreasing water solubility in silicate melt with increasing temperature at isobaric conditions. (b) convex-down-type solvus topology dictates increasing water solubility in silicate melt with increasing temperature (at isobaric conditions). Dashed lines = X_w^m isopleths, red curve = critical curve. Abbreviations: T_{WS} = wet solidus temperature, T_{DS} = dry solidus temperature, SV = (L=V) solvus crest. Diagram based on discussions presented by Hack et al. (2007).*

The two hypothetical solvus topologies shown in Figure 10.4 demonstrate the importance of accurate characterization of the compositional axis (*X*), particularly the topology and termination

of the L+V solvus crest. A melt (L) that exists in a silicate-H_2O system with type-(*a*) topology in Figure 10.4 could resorb free H_2O during isobaric cooling, while a system with type-(*b*) topology would exsolve H_2O during isobaric cooling.

It is interesting to note that the model system of Paillat et al. (1992) indicates +d*T*/d*P* solubility isopleths at low pressure and -d*T*/d*P* at high pressure. Contrary to this model, Burnham and Davis (1974) predict d*T*/d*P*≈0 at < 0.2 GPa and +d*T*/d*P* at > 0.2 GPa. That the two model systems show inconsistent (almost opposite) trends with regard to H_2O solubility in the albite melt (L) is not unexpected, as many aspects of the albite-H_2O system were poorly constrained at the time of publication. The Paillat et al. (1992) and Burnham and Davis (1974) models are both based on datasets containing almost no information on the H_2O-rich vapour phase composition (making the vapour-side of the solvus unconstrained) and much of the experimental data is based on calculating the H_2O content of the albite liquid (L), based on textural observations from experiments (noting that representative photomicrographs show a significant amount of H_2O exsolved during quenching). It is also important to note that the majority of Paillat et al. (1992) experiments were carried out in an internally heated pressure vessel that has a slow quench rate (7 °C/s).

The work of Paillat et al. (1992) was an important contribution because it demonstrated that the compositional axis (*X*) and S-L-V relations are crucial to understanding how silicate-H_2O systems melt and evolve. The model diagram shown in Figure 10.3 shows that an albite liquid (L) dissolves increasing amounts of H_2O and the H_2O-rich vapour (V) dissolves more albite with increasing pressure. The mutual solubility of the liquid and vapour appears to approach unity with increasing pressure such that the critical curve (the locus of critical points on the L=V solvus in Figure 10.3) and wet solidus become more proximal.

The second critical end-point and the model albite-H_2O system

The model system of Paillat et al. (1992) suggests that the wet solidus and critical curve eventually intercept at pressures >1.25 GPa. The point where the solidus plane and critical curve intercept marks the initiation of a supercritical field (see Figure 10.5). The P-T-*X* position where the wet solidus and critical curve intercept is often referred to as the second critical end-point ($CP^2_{Rock-H_2O}$). At P-T conditions above the $CP^2_{albite-H_2O}$ (and anywhere above the L=V solvus) the albite-H_2O system is said to be supercritical, with the liquid (L) and vapour (V) showing complete miscibility. At supercritical conditions, albite no longer undergoes a discrete wet melting event but shows gradual changes from a solute-poor vapour (V) to a vapour-poor liquid (L) with increasing temperature (at isobaric conditions).

The work of Shen and Keppler (1997) was the earliest research to locate the $CP^2_{albite-H_2O}$ via direct observation in a hydrothermal diamond anvil cell (HDAC) fitted with an infrared

spectrometer. Fourier transform infrared (FT IR) analyses of the vapour and liquid were used to define the sovlus topology as a function of temperature at near-isobaric conditions (Figure 10.5). The critical curve for the albite-H_2O system was then constructed by linking L+V critical points determined from experiments carried out at different pressures. Convergence of the albite-H_2O critical curve and albite wet solidus indicates that the $CP^2_{albite-H_2O}$ exists at around 16 kbar and 700 °C (Shen and Keppler, 1997; Stadler et al., 2000).

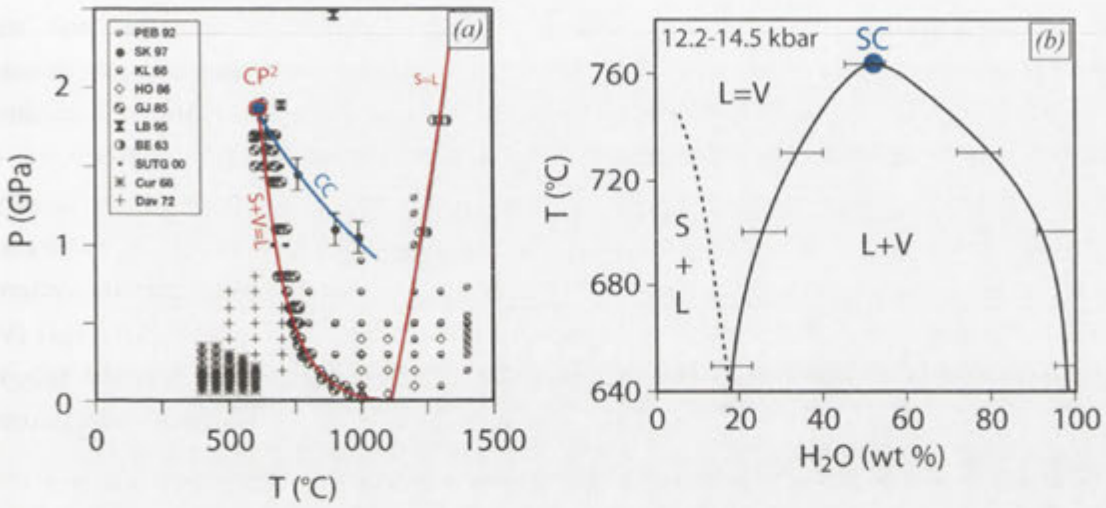

***Figure 10.5**: Experimentally determined phase relations in the albite-H_2O system. (a) Wet and dry solidus (red curves) and critical curve (blue curve) in P-T projection (for results and references see Hack et al., 2007). (b) Solvus topology of the albite-H_2O system determined by HDAC (modified after Shen and Keppler, 1997). Abbreviations: CC = critical curve, SC = solvus crest, CP^2 = second critical end-point, L = liquid, S = solid, V = vapour.*

Supercritical behavior in silicate-H_2O systems has potential to significantly influence chemical recycling in natural systems, such as subduction zones, by elements/compounds considered fluid-immobile at low pressures dissolving within the supercritical (L=V) phase. With regard to subduction systems, at supercritical conditions arguments regarding whether slab signatures are fluid- or melt-derived are likely unimportant (depending on how dramatically solubility isopleths change above the $CP^2_{Rock-H_2O}$). The importance of determining supercriticality is not merely focused on conditions near the wet solidus, but from a chemical recycling perspective, how solubility and activity relations change.

More complex systems: ternary systems and "rocks"

The albite-H_2O system is often used as a model for wet melting in natural rocks because the system is conceptually simple (containing only two components), has been studied over a range of P-T-*X* conditions, and has a working S-L-V phase diagram (Paillat et al., 1992; Shen and Keppler, 1997; Hack et al., 2007). Experimental work of Boettcher and Wyllie (1969b) in the ternary SiO_2-$NaAlSiO_4$-H_2O system and recent reviews by Hack et al. (2007) provide a theoretical framework on which more complex systems may be modeled.

Boettcher and Wyllie (1969b) used phase relations and interpretations of experimental run textures to locate the wet solidus and define the L+V miscibility gap (see Figures 10.6-10.8). In a review of existing data in the SiO_2-$NaAlSiO_4$-H_2O ternary system and L=V critical curves for system components, Hack et al., (2007) highlighted some notable inconsistencies between existing data and the work of Boettcher and Wyllie (1969b).

The wet solidi and critical curves of quartz-H_2O (Kennedy et al., 1962), albite-H_2O (Shen and Keppler, 1997), nepheline-H_2O and jadeite-H_2O (Bureau and Keppler, 1999) contradict the original quartz-albite wet solidus and L+V miscibility gap located by Boettcher and Wyllie (1969b) (see Figure 10.6*b*). The experimental results of Boettcher and Wyllie show the presence of a wet solidus up to 35 kbar and extensive miscibility at silica-undersaturated conditions (extending from pseudosections between albite-H_2O to nepheline-H_2O). Contrary to this estimate, critical curves for nepheline-H_2O, albite-H_2O and quartz-H_2O indicate supercriticality at <17 kbar at minimum melting temperatures (e.g., wet solidus – Figure 10.7). To elaborate on the argument of Hack et al. (2007), here we consider the SiO_2-$NaAlSi_2O_6$-H_2O ternary system at 17 kbar. The wet solidus is defined by the melting reaction albite (S) + quartz (S) + H_2O (V) = liquid (L). Results presented by Boettcher and Wyllie (1969b) indicate that only the SiO_2-H_2O system is supercritical such that the L+V miscibility gap exists at all silica-undersaturated conditions (Figure 10.8, plot *iv*).

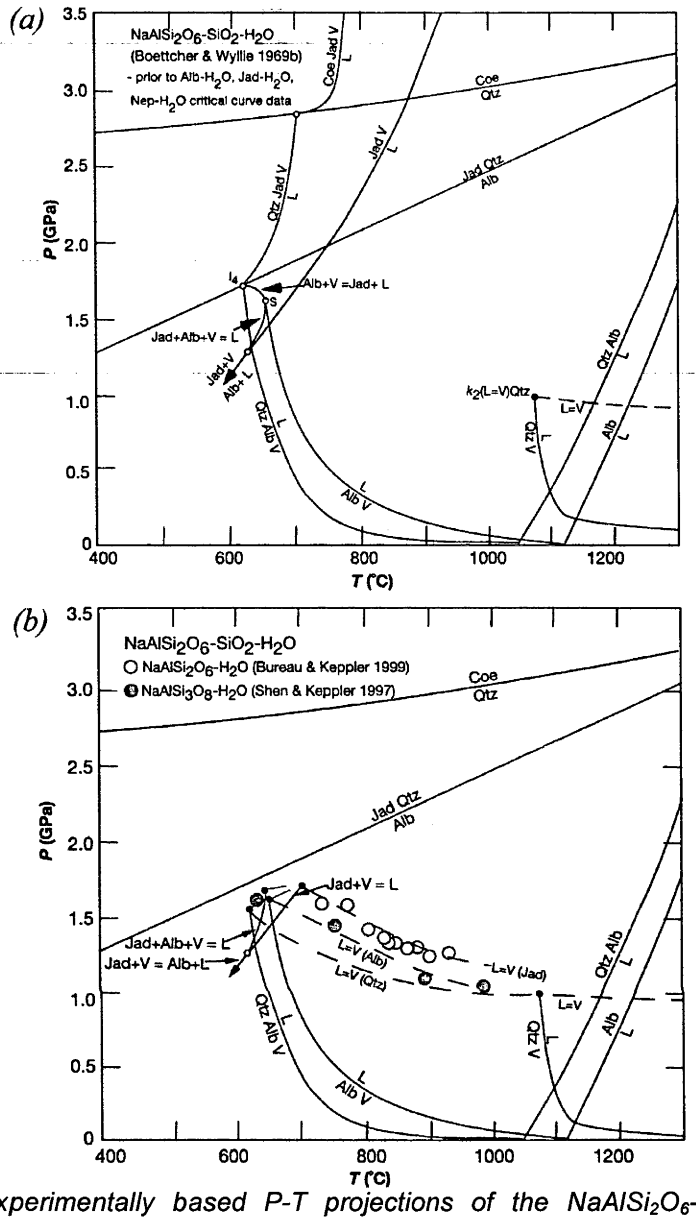

***Figure 10.6**: Experimentally based P-T projections of the $NaAlSi_2O_6$-SiO_2-H_2O system reported by: (a) Boettcher and Wyllie (1969b) showing wet solidi and no supercritical behavior (with the exception of the SiO_2-H_2O binary) up to 35 kbar. (b) interpretive projection of Hack et al. (2007) for wet melting relations where critical behaviour terminates the wet solidi for various components of the ternary system. Abbreviations include Alb = albite, Coe = coesite, Jad = jadeite, L = liquid, Qtz = quartz, V = vapour. Dashed lines represent critical curves reported by references listed. Figure modified after Hack et al. (2007) and Boettcher and Wyllie (1969).*

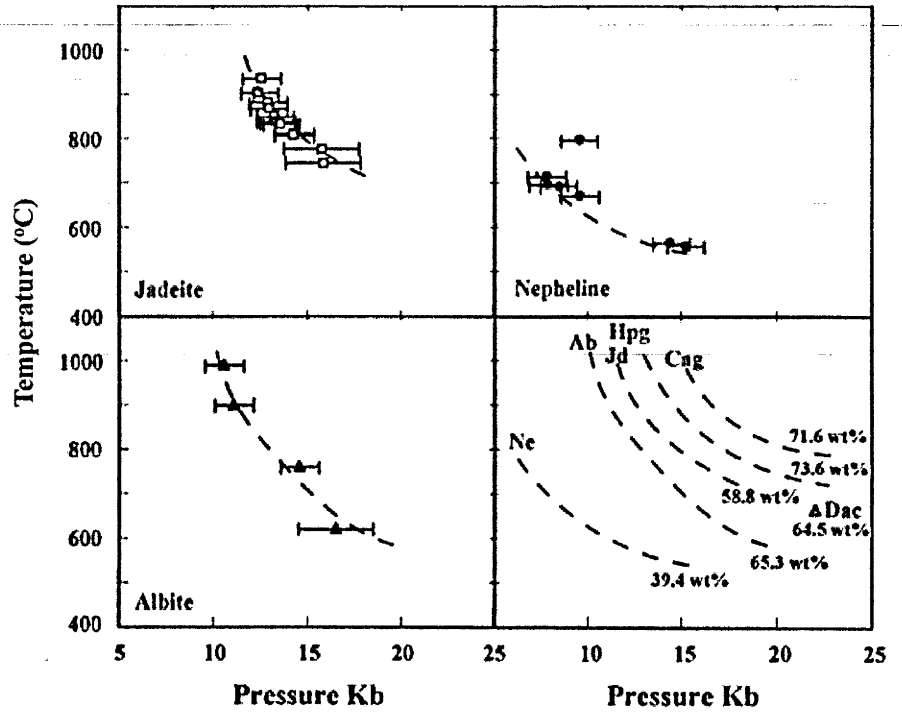

***Figure 10.7**: Experimentally determined critical curve P-T projections for various binary systems reported by Bureau and Keppler (1999). Bottom right figure contains critical curves reported with the wt% SiO_2 in the starting glass. Abbreviations include Ab = albite-H_2O, Cag = Ca-bearing granite-H_2O, Hpg = haplogranite-H_2O, Jd = jadeite, Ne = nepheline. Figure modified after Bureau and Keppler (1999).*

Critical curves for the albite-H_2O, quartz-H_2O and nepheline-H_2O binaries all intercept the albite-H_2O solidus at ~17 kbar (with the exception of jadeite, Figure 10.6*b* and 10.8). This means albite-H_2O, quartz-H_2O and nepheline-H_2O must be completely miscible at 17 kbar and the miscibility gap can only exist at conditions between (but not including) the albite-H_2O and nepheline-H_2O binaries (Figure 10.8). These theoretical discussions provide a new basis on which supercritical phenomena may be interpreted in natural (and complex) rock-H_2O systems (Shen and Keppler, 1997; Bureau and Keppler, 1999; Hack et al., 2007 and references therein). If the components involved in wet melting can be accurately defined and associated critical curves determined, it is possible to bracket a P-T-*X* region over which rock/mineral-H_2O miscibility can occur.

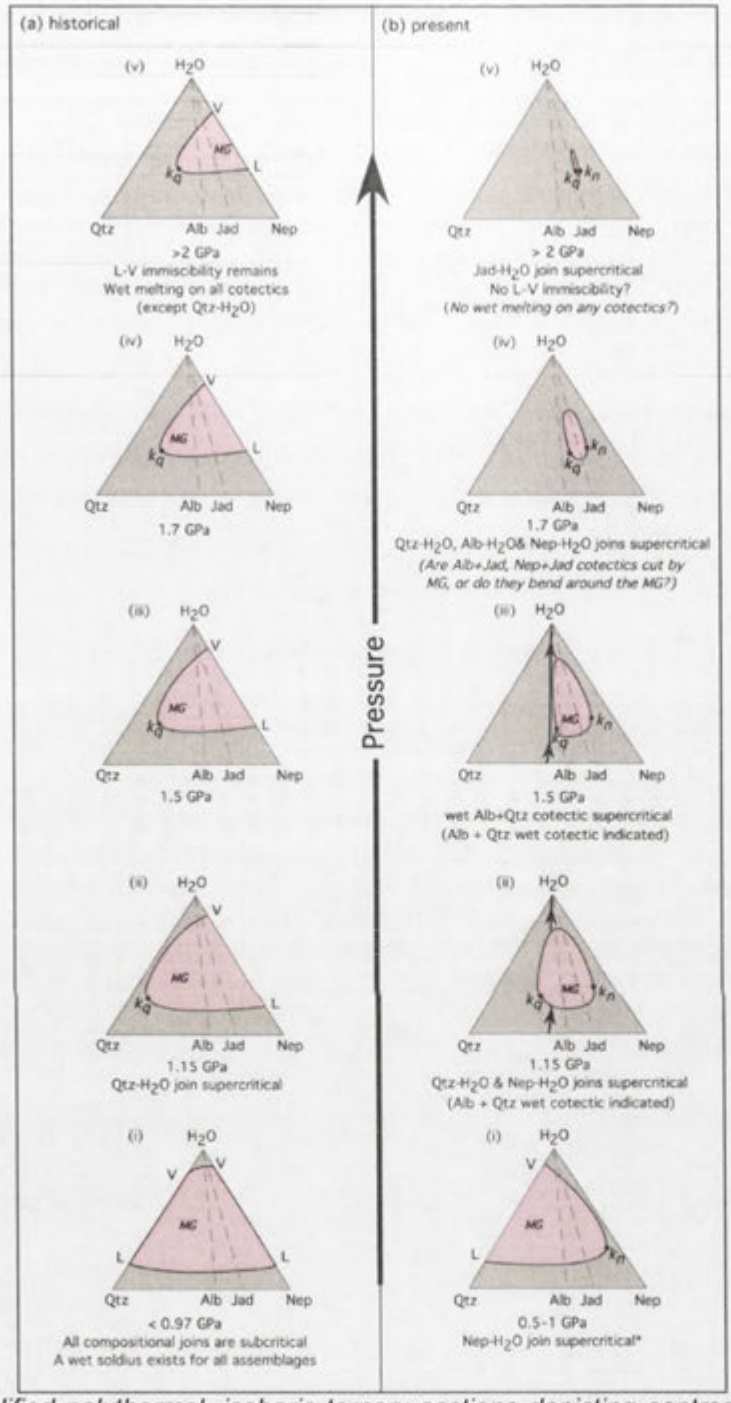

Figure 10.8: *Simplified polythermal, isobaric ternary sections depicting contrasting behavior in the $NaAlSiO_4$–SiO_2–H_2O system between (a) Boettcher and Wyllie (1969b) and, (b) Hack et al. (2007). Note that pressure (as labelled) increases up the diagram. (b) Hack et al. (2007) interpretation incorporates supercritical phenomena reported by Paillat et al. (1992), Shen and Keppler (1997), Bureau and Keppler (1999) and Stalder et al. (2000). Grey areas are polythermal regions in which a single solution is stable (with or without coexisting minerals) and pink areas are regions in which miscibility is expected. Binary Alb–H_2O and Jad–H_2O joins are shown as dashed lines. Abbreviations: MG = miscibility gap (L+V); V = vapor; L = liquid; kq and kn = different critical points in the ternary system and denote the maximum compositional extent of the MG at the P of interest; Qtz = quartz; Alb = Albite; Jad = Jadeite; Nep = Nepheline. Critical endpoints on wet solidi occur where k intersects the wet binary or ternary cotectic. Figure modified after Hack et al. (2007).*

10.3: Pelitic sediments and arc lavas: tracking geochemical cycles

An extensive body of literature demonstrates that several chemical components are recycled from subducting slabs into arc magmas (e.g., Plank and Langmuir, 1998 and references therein). The most obvious example for slab recycling is seen in the high H_2O-content of arc magmas, a chemical characteristic not seen in any other type of mantle-derived melt.

The importance of studying subduction factory inputs can be illustrated by comparing minor and trace element composition for mid-ocean ridge basalts (MORB) and primitive island arc basalts. Both magma types primarily involve mantle melting, yet a number of distinct geochemical variations are seen across the two populations (Figure 10.9). Arc magmas (aside from having higher H_2O contents) exist at higher oxygen fugacity (Figure 10.10), show enrichments in large-ion lithophile elements (LILE) and light rare earth elements (LREE), and depletions in high field strength elements (HFSE) compared to MORB (e.g., Tatsumi and Eggins, 1995).

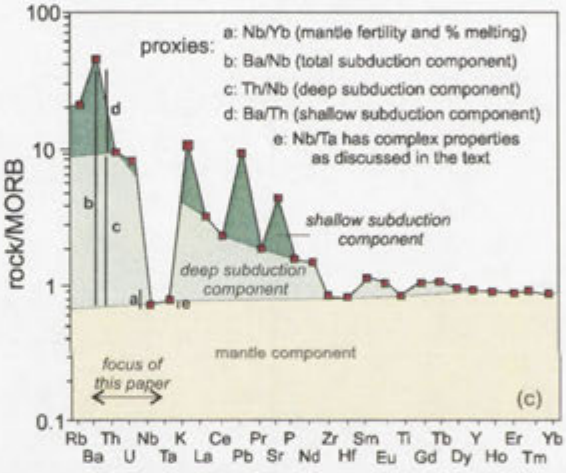

***Figure 10.9**: Extended trace element spidergram for Mariana arc basalts as reported by Pearce et al. (2005). Geochemical trends are separated into different model components (asthenosphere, deep subduction, and shallow subduction) on the basis of geochemical proxies for each component. Figure taken from Pearce et al., 2005).*

In order to constrain chemical recycling from slab to arc, various studies have focused on the composition of slab components (system inputs) relative to arc magmas (system outputs) from individual subduction systems. Upper portions of subducting slabs have been described and analyzed by ocean floor sample suites (e.g., Hole et al., 1984; Lin, 1992; Plank and Langmuir, 1998), while outputs have been characterized by the study of glasses and rocks from primitive island arc settings (e.g., Tatsumi and Eggins, 1995). Of the various lithologies that comprise a subducting slab and overlying mantle wedge, pelagic sediments (pelites) show the highest concentration of, and are considered the dominant host of, a number of incompatible elements (particularly LILE; Plank and Langmuir, 1998; Tenthorey and Hermann, 2004). This observation indicates that recycling of pelagic slab components into the locus of partial melting within the

rmantle wedge gives rise to a number of geochemical signatures characteristic of island arc rmagmas (e.g., Hawkesworth et al., 1993).

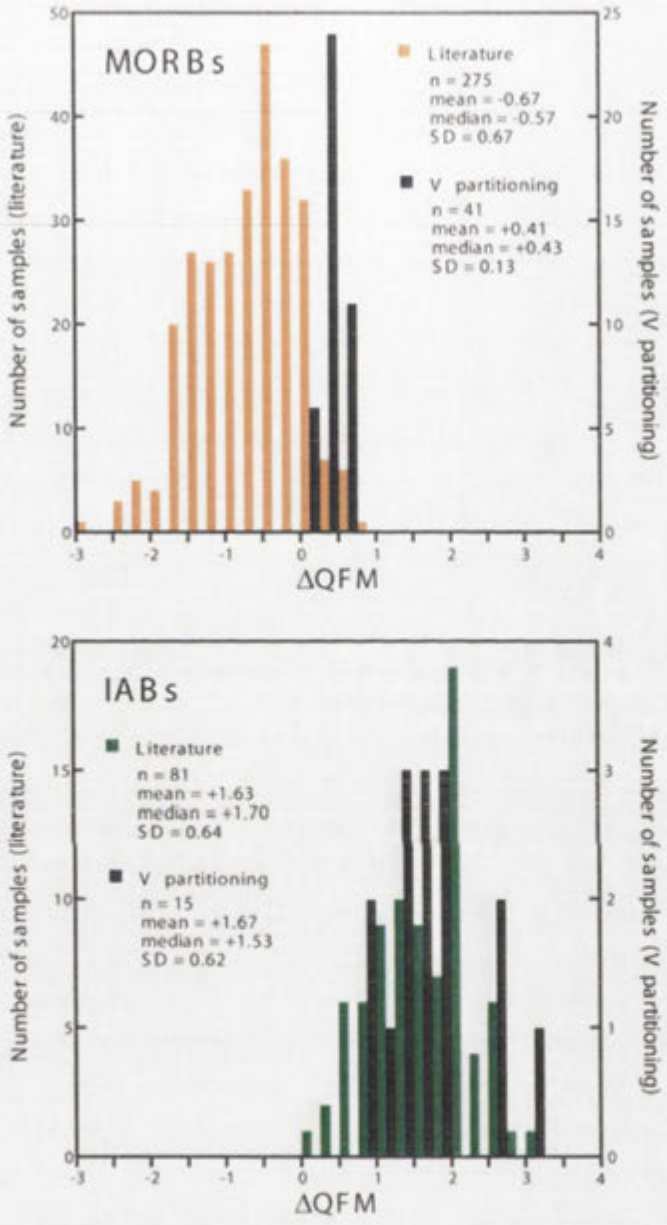

***Figure 10.10**: Comparison of oxygen fugacity estimates made from MORB and island arc basalts reported in the literature (after Mallman and O'Neill, 2007).*

Minor and trace element studies of drill core and dredge samples from subducting slabs provide further evidence for this hypothesis, with individual slab-arc systems showing correlative incompatible element/isotope ratios (e.g., Th/Rb, K/Na, Ba/Na, etc) for sediments and IABs (e.g., Plank and Langmuir, 1993, 1998; Peate et al., 1997). Further evidence for the introduction of sedimentary components into the locus of melting stems from the presence of

cosmogenic ^{10}Be and elevated radiogenic Pb in IABs relative to MORB (Armstrong, 1971; Kay et al., 1978; Woodhead and Fraser, 1985; Tera et al., 1986; Morris et al., 1990).

While it is generally accepted that slabs are recycled into the locus of partial melting, the mass transfer process is poorly understood. In other words, intermediate stages of the subduction factory are the least constrained and are the most controversial. This is largely because few known natural pelites have attained subduction pressures and temperatures without significant overprint or at relevant H_2O activities (though potential examples have been hypothesized – e.g., Hermann et al., 2006); there is no direct means of accessing the mantle wedge environment, and hydrothermal pelitic experiments at high pressure (subduction) conditions show conflicting results.

The controversy regarding pelite recycling focuses on whether primitive arc lavas contain contributions from melt-derived, fluid-derived or supercritical (i.e., L=V) components. In order to discuss the various models of chemical recycling from slab (pelite) to arc, the following section presents previous experimental pelite-H_2O research relevant to subduction.

Experimentally determined pelite wet solidi and subduction P-T paths

A number of experimental studies have constrained the locus of the pelite wet solidus at conditions <15 kbar (examples include: Huang and Wyllie, 1973, 1974; Huang et al., 1973; Le Breton and Thompson, 1988; Gardien et al., 1995). The large body of experimental research at low pressure demonstrates that minimum melting for pelites at <15 kbar is related to muscovite dehydration melting (in the presence of other co-existing phases) to form S-type granites. In short, phase relations and locus of the pelite-H_2O solidus at <15 kbar are well-constrained and documented for a range of pelitic starting compositions.

H_2O-saturated melting and phase relationships in the pelite-H_2O system at >20 kbar have been reported by several authors (Nichols et al., 1994; Johnson and Plank, 1999; Schmidt et al., 2004; Hermann and Spandler, 2008), with the locus of wet solidi (Figure 10.11) and mineral assemblages showing many inconsistencies. The wet solidus of Johnson and Plank (1999) is at particular odds with other studies, as it exists at significantly higher temperatures than other experiments (ΔT >100 °C at 20-40 kbar). Another important experimental observation is that haplogranite and Ca-granite critical curves of Bureau and Keppler (1999) intersect pelite wet solidi at 30-40 kbar (dashed red curves in Figure 10.11). Given that experimental studies show hydrous pelitic melts are granitic over a broad range of P-T-X conditions (Schmidt et al., 2004; Hermann and Spandler, 2007), comparison of granitic critical curves and pelite wet solidi can be used to provide an estimate of the $CP^2_{Pelite-H_2O}$ at 30-40 kbar and 650-800 °C. Contrary to this estimate, experimental work of Schmidt et al. (2004) reports the presence of a wet solidus extending to 55 kbar and 925 °C, almost double the pressure range of the pelite wet solidus of Bureau and Keppler (1999).

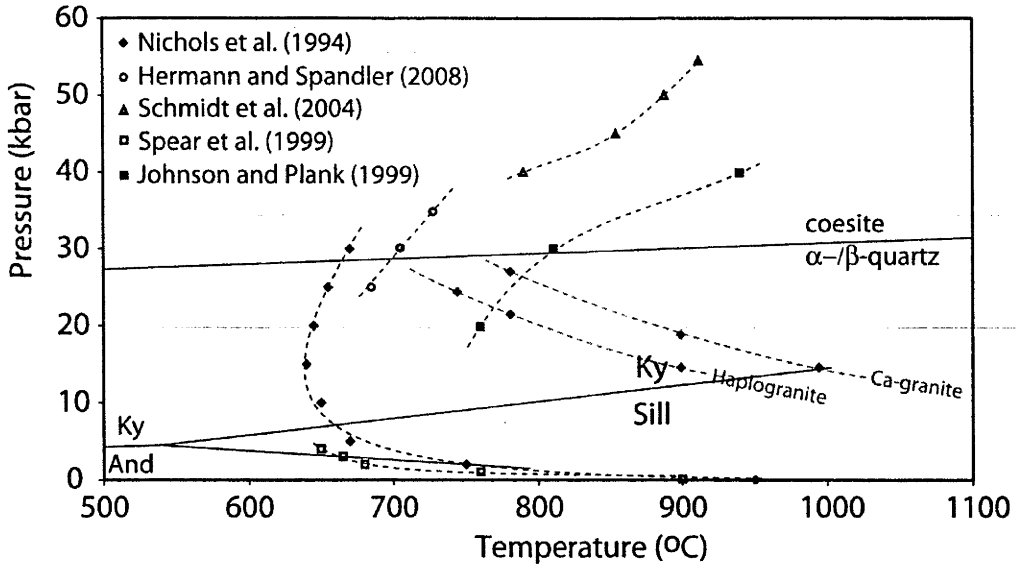

***Figure 10.11**: Experimentally determined pelite-H_2O wet solidus from existing literature. Experimental studies and wet solidii locus shown in black symbols and dashed black lines (references reported in the Figure). Dashed red lines represent haplogranite and Ca-granite L=V critical curves determined by Bureau and Keppler (1999). The Al_2SiO_5 phase diagram (and polymorphs therein) and quartz-coesite transition are shown for reference.*

Given the importance of pelite recycling during subduction, there are many questions regarding the pelite wet solidus at high pressures. In particular, "why do high pressure experiments produce such diverse results?" and "why are $CP^2_{Pelite-H_2O}$ estimates so different?'.

By comparing the experimentally determined pelite wet solidi (Figure 10.11) to various numerical and analogue models of top-slab temperatures reported in the literature (Figure 10.12), ignoring the results of Johnson and Plank (1999 – for reasons explained in later sections of this chapter) and potential supercritical behaviour, it is possible to assess potential element transfer processes from subducting pelites into the overlying mantle wedge. Where the P-T path predicted by top slab temperatures follow paths (*a*), (*b*) and (*c*) in Figure 10.4, elemental transfer should occur in the H_2O-rich vapour phase. Where subduction occurs along a path similar to curves (*d*) and (*e*) elemental transport can occur in a H_2O-rich vapour and/or a silicate liquid.

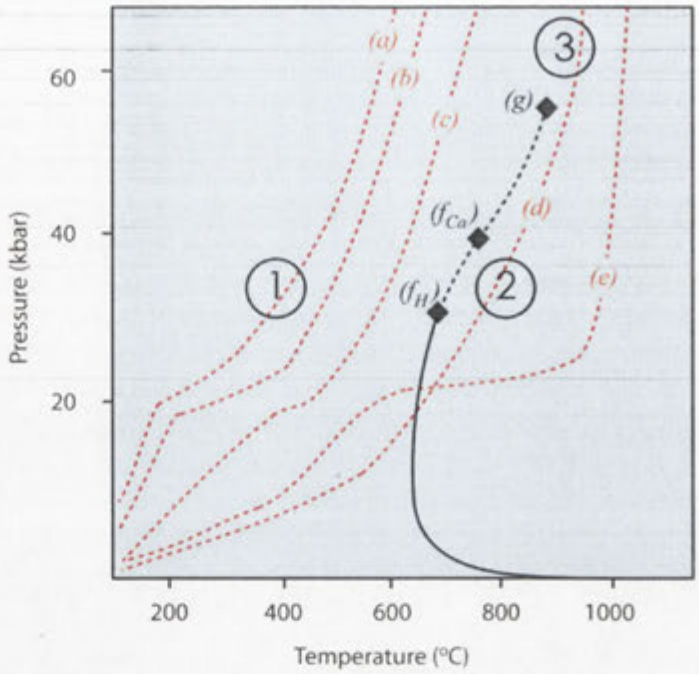

***Figure 10.12**: Top slab P-T paths from numerical and analogue models (dashed red lines) compared to the pelite wet solidus (black curve, see Figure 10.3). Black dashed curve represents estimates of the pelite wet solidus above minimum critical point estimates of Bureau and Keppler (1999). Red curves (a), (b) and (c) represent numerical models from Peacock et al. (1994) for slabs at 27° dip/(10 cm/year)/50 Myr old crust, 27° dip/(10 cm/year)/20 Myr old crust, and 27° dip/(3 cm/year)/20 Myr old crust respectively. Curve (d) represents a scaled analogue model from Kincaid and Griffiths (2004) at 49° dip/(3.5 cm/year). Curve (e) represents a numerical model of van Keken et al. (2002) enhanced coupling with the mantle wedge at 60° dip/(4.5 cm/year)/10 Myr old crust. Diamond symbols (f_H) and (f_{Ca}) are pelite-H_2O second critical end-points based on haplogranite and Ca-granite results of Bureau and Keppler (1999). Diamond symbol (g) is the pelite-H_2O second critical end-point of Schmidt et al. (2004). Region 1 = P-T field where elemental transfer occurs in an aqueous fluid, 2 = P-T field where elemental transfer occurs via fluid-present melting, and 3 = P-T field of possible supercritical behaviour for pelite-H_2O system.*

The great unknowns in this hypothetical model are whether pelitic systems are super- or subcritical ($CP^2_{Pelite-H_2O}$) at subduction pressures and temperatures.

Problems and limitations of previous pelite-H_2O experiments

As demonstrated in early sections of this literature review, all piston cylinder and multi-anvil studies into the pelite-H_2O system at >20 kbar (with the possible exception of Spandler et al., 2007) use some form of textural observation in order to interpret primary and secondary quench products. Major phase relations appear to be consistent among experimental studies at high pressures and generally consist of variable proportions of coesite, garnet, clinopyroxene, phengite, kyanite and rutile.

The work of Johnson and Plank (1999) appears to be the singular exception among experimental studies reported within the literature. This work contained a number of unique phases, including plagioclase, amphibole, magnetite and ilmenite (and notable absence of rutile). Johnson and

Plank (1999) suggest that differing mineralogy may stem from their experiments equilibrating at higher oxygen fugacity. This conclusion was based on the presence of more oxidized Fe-Ti oxides than reported from other experiments and, in association with the different mineral assemblage, was used to explain higher solidus temperatures. The potential influence of oxygen fugacity on the phase and melting relations is important to note, as all existing literature on the pelite-H_2O system at >20 kbar is reported from experiments where f_{O_2} is unconstrained (Nichols et al., 1994), is estimated from starting $Fe^{3+}/\Sigma Fe$ (Schmidt et al., 2004) or is based on an estimate of f_{O_2} imposed by the cell assembly (Hermann and Spandler, 2008). The various estimates of f_{O_2} from hydrothermal pelitic experiments reported in the literature are entirely anecdotal, lacking any definitive evidence or calculation. Many processes, including: reaction with the capsule, H-diffusion, f_{O_2} imposed by the cell assembly, and disequilibrium, have the potential to influence the f_{O_2} within an experimental charge. Where existing literature suggests that f_{O_2} may play an important role in pelite minimum melting, no experiment can be said to have an accurate or robust estimate of the f_{O_2}. The lack of experimental work at defined and varied f_{O_2} is surprising, as primitive arc lavas are known to exist at higher f_{O_2} than MORB (Figure 10.10) and appear to be unique among mantle-derived melts. The study of pelites at defined and different f_{O_2} may yet prove a fruitful avenue of investigation into how elemental recycling occurs during subduction and determining how accurately current experimental models mimic natural systems.

Another troubling aspect of previous research into the pelite-H_2O system is that literature reports often interpret run products differently, such that phase stability is not internally consistent. The earliest work into the pelite-H_2O system at >20 kbar was reported by Nichols et al. (1994), who used capsule position (relative to the hotspot) and crystal habit to distinguish primary from quench phases. Position within the capsule was considered a determinative factor of growth history on the assumption that dense primary phases (i.e., those existing at experimental P-T) will settle through the liquid or vapour during experiments, while irregular growth textures, including rosettes or atolls of skeletal/fine-grained phases, develop during experimental quench. On the basis of textural observations Nichols et al. (1994) calculated the pelite-H_2O solidus and liquidus, while concluding that many super-liquidus experiments contained a large amount of quench garnet, mica and kyanite (± rutile).

Johnson and Plank (1999) indicate that phase and melt textures seen in their experimental runs are different to those of Nichols et al. (1994) and the production of secondary phases on quench is minimal to absent. Ignoring the apparent high f_{O_2} of Johnson and Plank (1999) experiments, the described runs contain among the highest H_2O content (13-14 wt%) reported from any

pelite-H_2O experiment at >20 kbar. Thus, their experiments should be the most likely to produce large volumes of melt at a given P-T and the most likely to produce crystal settling (such that petrographic observations should be comparable to Nichols et al., 1994). Johnson and Plank (1999) also use the presence of vesicles to indicate that the system equilibrated within the L+V miscibility gap, and the presence of phases within vesicles to demonstrate phase stability at experimental conditions. This textural interpretation is particularly important in terms of interpreting results, as it assumes that a super-$CP^2_{Pelite-H_2O}$ or supercritical experiment does not produce vesicles on quench and that the vapour phase cannot crystallize solid phases on quench. If a supercriticial experiment cannot quench to vapour bubbles and phases (± glass), this begs the question 'are supercritical experiments texturally different to subcritical experiments upon quench'? If so, how? If not, why? This seems to be a question that is largely ignored within the literature, with the possible exception of Schmidt et al. (2004) who use phase stability (as determined by textural observations) to define the termination point of the wet solidus.

It is worth noting that while this review largely criticizes observations made by Johnson and Plank (1999), a number of the phases seen in vesicles they reported do appear to be primary (showing embayment into the melt and/or likely being too large to be considered "fluid" quench). This does not require that all vesicle-hosted phases are primary, nor does it automatically exclude vesicle hosted phases.

Schmidt et al. (2004) arguably represents the most extensive use of textural observations from high pressure experimental runs in order to determine the $CP^2_{Pelite-H_2O}$. The basic premise of their research is that termination of the pelite wet solidus (and miscibility gap) can be determined by phengite/glass textures and mass balance calculations. The work of Schmidt et al. (2004) used the gradual disappearance of phengite and the inability to quench to glass to infer that the $CP^2_{Pelite-H_2O}$ occurs at 55 kbar and 925 °C. Implicit to the interpretations of Schmidt et al. (2004) is the assumption that primary phases can be distinguished from secondary quench products (at pressures up to 75 kbar) and that vapour saturated melting can be determined from runs of low H_2O content (2.1 wt % - i.e., runs clearly in the S+L field).

The use of textural observations to determine the $CP^2_{Rock-H_2O}$ by Schmidt et al. (2004) should be considered in terms of previous research into supercriticality. If textural observations (as suggested by Schmidt et al., 2004) can be used to determine supercritical behaviour, the continuous disappearance of a phase in a simple binary system – e.g., albite-H_2O or quartz-H_2O - should be straight-forward and easily determined (provided the mineral melts congruently). Contrary to the interpretation of Schmidt et al. (2004), a large body of research on the simple SiO_2-H_2O system (including 31 articles cited by Hack et al., 2007) demonstrates a long-lived

controversy about whether supercritical behaviour can be determined on the basis of textural, compositional, thermodynamic and/or spectroscopic measurements. The back-bending wet solidus of Schmidt et al. (2004) relies heavily on the ability to determine primary phases, particularly phengite and glass, despite only 6 phengite and 6 glass analyses reported from 17 experiments (with individual phases described as too small and unstable for quantitative analyses). Arguments against the $CP^2_{Pelite-H_2O}$ determined by Schmidt et al. (2004) have been presented by Hermann et al. (2006), who suggest that the back-bending wet solidus could correspond to a solubility isopleth. It should be noted that the wet solidus and $CP^2_{Pelite-H_2O}$ estimated by Schmidt et al. (2004) may be correct, but there are three key assumptions with the estimates:

1) The disappearance of phengite, virtually the only major stable hydrous mineral considered at experimental pressures, can be used to mark supercritical behavior in the pelite-H_2O system. This interpretation, at low H_2O contents (<2.1 wt%) suggests that the pelite wet solidus is largely defined by the phengite dehydration melting reaction and that this reaction (extrapolated to H_2O-saturated conditions) is representative of minimum melting in subduction zones.
2) the wet solidus can be determined by the disappearance of the phase involved in the wet solidus reaction with the highest stability (greatest critical curve), assuming that there is no external water source for pelites (e.g., altered oceanic crust).
3) the continuous disappearance of phengite to a "melt phase" can be determined on the basis of experimental quench textures at a constant and low H_2O content. In other words, a discontinuous supercritical species and continuous H_2O-rich species can be determined on the basis of textural interpretations, such that primary and quench phengite (where analyses are not possible) can be distinguished.

Much of the discussion presented by Schmidt et al. (2004) is based on mass balance calculations/considerations, making textural observations focal to interpretations. It should also be noted that their experimental study contained the lowest H_2O content of all pelite experiments (2.1 wt%), with starting compositions designed to correspond to dehydration melting (such that pelite phase and melting relations do not include the introduction of H_2O from an external source).

The Nichols et al. (1994) supersolidus experiments contain 8 or 28 wt% H_2O in the starting compositions, while the experiments of Schmidt et al. (2004) contain 2.1 wt% H_2O, those of Hermann and Spandler contain 2.0-6.8 wt% H_2O, and those of Johnson and Plank contain 13-14 wt%. Thus, the majority of experiments carried out in the pelite-H_2O system are run at low starting H_2O content and show little to no variation in pelite:H_2O at experimental P-T conditions.

The work of Spandler et al. (2007), which utilized high pressure fluid inclusions, represents a new means of determining fluid compositions at subduction conditions. It should be noted that quartz stability is highly limited at high pressures and on the basis of constraints presented by Hack et al. (2007), the maximum pressure reported by Spandler et al. (2007) likely lies at conditions below the wet solidus.

The haplogranite and Ca-granite critical curves reported by Bureau and Keppler (1999), which indicate the $CP^2_{Pelite-H_2O}$ exists at between 30-40 kbar (Figure 10.11), also merit some discussion. The HDAC method is one of the most robust techniques for determining supercriticality by virtue of the fact that miscibility is directly observed. In other words, there is almost no doubting pelite-H_2O supercriticality within the HDAC when a single phase is observed. This being the case, the HDAC method of Bureau and Keppler (1999) has three major limitations. Firstly the technique is largely observational, such that mineral/melt/vapour species cannot be sampled and analyzed for comparison with other studies (other than H_2O content as determined by FTIR). The representative photomicrographs reported by Bureau and Keppler (1999) show virtually no crystalline phases (with the exception of starting glass in sub-solidus runs) at any condition. While this may be related to limited optics over the cell, the presence of solid phases would help demonstrate equilibrium at experimental conditions.

The second concern with the HDAC technique is the ability to calibrate experimental pressure accurately, with the use of H_2O as an internal pressure medium being of particular concern. Pressure uncertainty is dependent on how well the pure H_2O equation of state (EOS – the physical properties of the vapour at pressure and temperature) represents the H_2O-rich vapour species at experimental conditions. The more silicate material that dissolves within the vapour phase, particularly with increasing pressure, the greater the likelihood measured H_2O density differs from pure H_2O. In other words, the use of pure H_2O isochores to calibrate pressure in experiments with increasing pressure, where the H_2O-rich vapour phase clearly contains considerable silicate material, is questionable. More importantly, as silicate-solubility increases in the vapour phase with increasing pressure, calibrated pressure (based on pure H_2O density) is likely to increasingly underestimate experimental pressure.

The third concern with the HDAC technique described by Bureau and Keppler (1999) is that the critical curves from individual silicate-H_2O systems are reported from experiments run at a single and constant silicate:H_2O. Unless the starting composition has exactly the same composition as that of the solvus crest at the experimental pressures, the reported supercriticality will only correspond to when the starting composition intercepts the solvus rather than defining the true silicate-H_2O solvus crest (which defines the critical curve).

Inspection of various results from the pelite-H_2O system reported in the literature (Figure 10.11) shows a number of inconsistencies. This literature review highlights the need for new research

into the system, where the development of a new experimental technique that does not rely on subjective and uncalibrated textural interpretations.

10.4: Oxygen buffer techniques in hydrothermal experiments

Oxygen buffer and hydrogen-sensor techniques in high pressure experiments allow the study of redox-dependent/-influenced reactions in experimental apparatus not equipped with gas mixing lines (e.g., piston cylinder, mult-anvil, HDAC, etc). The following discussion outlines how oxygen buffer techniques were developed and how they function in experiments.

Oxygen buffer techniques

The use of metal-metal oxide (MMO) and mineral reaction buffers (e.g., $2SiO_2 + 2Fe = Fe_2SiO_4$) to fix f_{O_2} in high pressure hydrothermal experiments was established by Eugster (1957), who determined the stability of ferruginous biotite (annite) as a function of P-T-f_{O_2}. Since the work of Eugster, a great number of solid media oxygen buffers have been developed and calibrated for use in high pressure experimental apparatus (Figure 10.13).

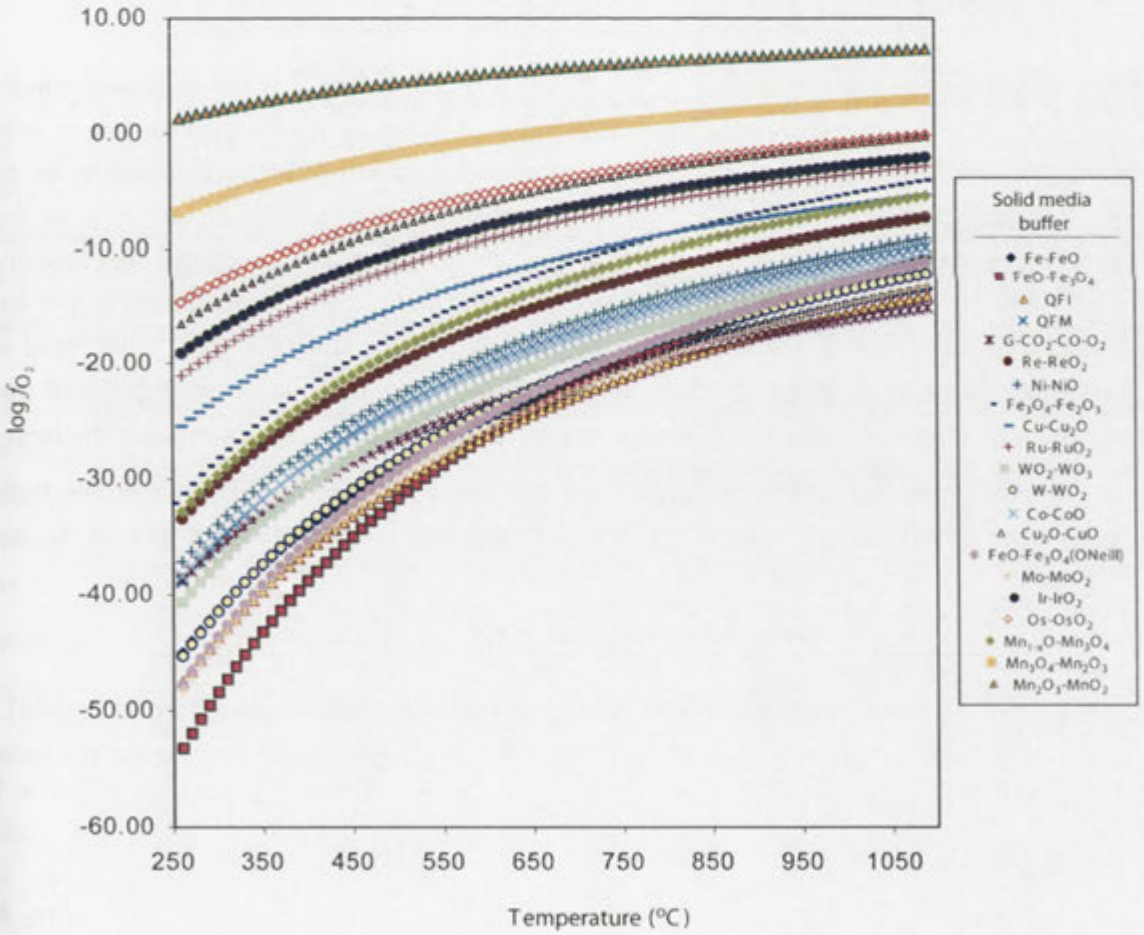

***Figure 10.13**: Temperature-f_{O_2} curves at 1 atm for various solid media oxygen buffers. Data based on Myers and Eugster (1983), O'Neill (1986, 1987, 1988), Chou (1987a, 1987b), Cygan and Chou (1987), O'Neill and Pownceby (1993), Pownceby and O'Neill (1994), O'Neill and Nell (1997).*

The experimental setup for a high pressure oxygen buffered experiment is fairly straightforward and is often referred to as the 'double-capsule' or 'capsule-in-capsule technique'. The inner capsule consists of the mineral assemblage under investigation (charge solids) and H_2O. The sealed (welded) inner capsule is generally constructed from thin-walled (<0.2 mm thick) inert metal tubing, typically Pt or Ag-Pd alloys (though very thin walled Ag has been used), and acts as a semi-permeable hydrogen membrane. The inner capsule, including the metal tubing and sample material, needs to be malleable in order to transmit pressure set by the cell assembly without disrupting chemical separation between the inner capsule and outer capsule components.

The inner capsule is placed in the larger outer capsule that also contains a solid media oxygen buffer (Figure 10.13) and H_2O. The outer capsule, as well as the inner counterpart, accurately transmits pressure and behaves inertly with regard to the buffering assembly. The outer capsule metal must not alloy with or modify the chemical potential of the solid media oxygen buffer, otherwise the buffer may be significantly displaced in order for the solid media oxygen buffer to function properly.

Arguably the most important role of the outer capsule is that it must minimize outward hydrogen loss via diffusion. This capsule is typically composed of Ag or Au because hydrogen diffusion through these metals is the slowest known (Table 10.1). The use of thick-walled Ag or Au will not eradicate hydrogen permeation out of the outer capsule, but if hydrogen loss (or oxygen production) does not cause complete oxidation of the solid MMO buffer, the oxygen fugacity in a high pressure hydrothermal piston cylinder experiment will be fixed. The success of the oxygen buffer technique is dependent on the appropriate selection of capsule materials and solid media oxygen buffers. If the inner capsule permeates H_2 too slowly, the experiment will require prolonged equilibration times. Similarly, if H_2 permeates the outer capsule too fast the large f_{H_2} gradient between cell and outer capsule will significantly reduce the lifespan of the buffering assembly, such that the experiment will be effectively unbuffered with regard to oxygen fugacity.

Permeation rates

Hydrogen permeation rates through various metal capsules were studied by Chou (1986). The permeation rate is related to the permeability constant k (here shown as *P*) using the following reaction:

$$\frac{\mathrm{d}M}{\mathrm{d}t} = -\frac{2\pi P l}{\ln(r_e / r_i)}[(f^i_{\mathrm{H_2}})^{1/2} - (f^e_{\mathrm{H_2}})^{1/2}] \qquad \textbf{(eq. 10.1)}$$

where, $\frac{dM}{dt}$ = permeation rate, l = capsule length, r_e / r_i = outer and inner radii of the capsule, $(f^i_{H_2})$ = hydrogen fugacity in the inner capsule and $(f^e_{H_2})$ = hydrogen fugacity in the outer capsule.

Permeability constants for Au, Pt, Ag, and Ag-Pd reported by Chou (1986) are shown in Table 10.1 and indicate that hydrogen permeation rates vary considerably as a function of temperature and type of metal.

Table 10.1: Hydrogen permeability constants through metals at 2 kbar (values reported in k x 10^{11} (g/cm.sec.bar$^{1/2}$)

Metal	Temperature		
	450 °C	600 °C	750 °C
$Ag_{70}Pd_{30}$	5.41	29.97	91.98
$Ag_{80}Pd_{20}$	0.58	4.02	19.67
Pt	0.34	3	14.48
Ag	0.057	0.206	2.28
Au	0.001	0.056	1.05

As can be seen from the permeability constants of the various metals/alloys at the given temperature, a system containing an inner $Ag_{70}Pd_{30}$ alloy capsule will approach osmotic equilibrium much faster than one utilizing a Pt or Ag inner capsule. It can also be seen that Au and Ag are the most resistant materials to hydrogen permeation and are thereby ideal for use as outer capsule material.

The importance of oxygen buffers

Oxygen fugacity is an intensive parameter that has potential to control phase stability or mineral assemblages that involve polyvalent elements. Oxygen buffers are regularly required to accurately model natural Earth systems via experimentation, particularly as different systems are thought to exist at very different f_{O_2} (e.g., core, mantle, continental arc, mid-ocean ridge settings). In short, the success of an oxygen buffered experiment is heavily dependent on equilibration with the buffer assemblage and the intrinsic f_{O_2} imposed by the apparatus.

If the buffer assemblage is present after completion of an experiment – as demonstrated by XRD, EPMA or other petrographic methods – the oxygen fugacity the system equilibrated at can be defined. There are, however, a number of conditions at which this assumption may be incorrect. If any of the buffer phases alloy with the capsule material, changes in phase activity will significantly change the calculated oxygen fugacity. If the buffer becomes isolated or "armored" by a reactant layer, the buffer reaction may prove ineffective. Finally, slow kinetics

associated with solid media oxygen buffers may also influence the successful use of a solid media buffer, as the buffer must equilibrate with all other polyvalent elements and the intrinsic f_{O_2} of the starting material.

Further development of oxygen buffers and hydrogen sensors

High pressure experiments involving the study of redox reactions have evolved to the following two approaches, involving:

1) Imposing a specific, and defined, f_{H_2} on the system by means of a solid media oxygen buffer technique (Figure 10.13).
2) Measuring, or more specifically sensing, the f_{H_2} via calculation of f_{O_2} in the sample-H_2O system by means of an inert hydrogen sensor held within a buffered or unbuffered hydrothermal experiment.

The hydrogen sensor technique was first developed by Chou and Eugster (1976), who adapted Ag-AgCl acid-base buffers (e.g., Frantz and Eugster, 1973) to measure f_{H_2} in hydrothermal experimental systems.

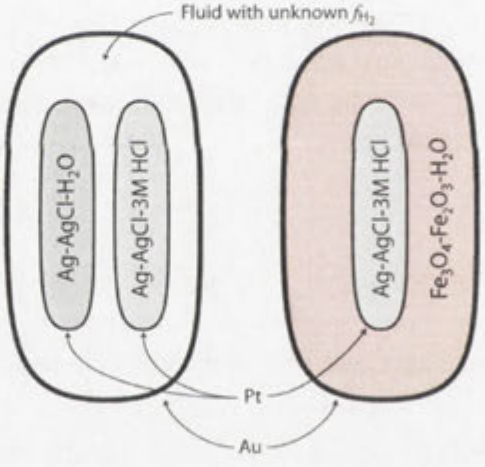

***Figure 10.14**: Simplified experimental arrangements for hydrogen sensors described by Chou and Cygan (1990) for: (i) experiments where hydrogen sensor is used to determine f_{O_2} in an experiment with unconstrained hydrogen fugacity (left-hand image), and (ii) hydrothermal experiments where hydrogen fugacity is fixed by an oxygen buffer held within the outer capsule (right-hand image).*

The earliest hydrogen sensors (shown in Figure 10.14) required the addition and accurate analysis of Ag-bearing solutions within inner Pt-capsules. The double capsule technique developed by Chou and Eugster (1976) involved one capsule containing a solution of H_2O + Ag + AgCl and another capsule containing a solution consisting of HCl + Ag + AgCl. After the two

solutions were exposed to a defined f_{H_2} imposed by an oxygen buffer (right-hand image in Figure 10.14), or was measured at the given P and T over sufficient time to allow f_{H_2} to equilibrate with a system of unknown hydrogen fugacity (left-hand image in Figure 10.14), the final solution could be used to determine hydrogen and oxygen fugacity within the experiment.

Since the original work of Chou and Eugster, the hydrogen sensor technique has seen many uses, including the calibration of oxygen buffers (Chou, 1978), determination of H_2O activity in brines (Chou and Williams, 1977), measurement of hydrogen permeation rates through platinum (Chou et al., 1978), and to study the stability of various mineral solid solutions.

The original hydrogen sensor technique suffers from a number of uncertainties and technical difficulties. These problems include uncertainty surrounding the HCl dissociation constant as a function of P and T, a particular problem at elevated P-T conditions relevant to this research. It should be stressed that the original technique remains to be tested at pressures >8 kbar and temperatures > 800 °C. Fluid extraction and analysis also represents a technical challenge, as any fluid evaporation that occurs during capsule piercing or during electrode analysis may introduce uncertainty.

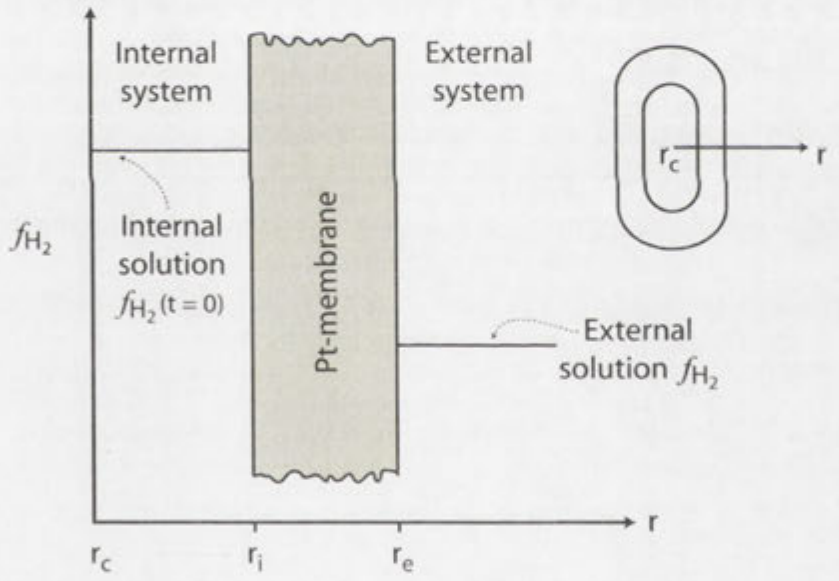

***Figure 10.15**: Schematic diagram of thickness of the Pt-membrane versus the starting f_{H_2} gradient between internal and external solutions that can influence how fast the system achieves equilibrium.*

The H-sensor technique of Chou and Eugster (1976) has been successfully applied to the study of numerous hydrothermal experimental systems, but the technique has not been tested at conditions necessary for this research. This being the case, a number of important observations can be drawn from the original H-sensor technique. Arguably the most important observation is

that thin Pt- or AgPd-membranes can be used to permeate hydrogen through a capsule wall in order for the two capsules to "communicate" hydrogen fugacity via H-permeation. Another important observation is that the inner sensor capsule should be an inert participant within the experiment, such that it does not modify phase relations/compositions in the large capsule but merely senses hydrogen fugacity within it.

10.5: Sliding metal-metal oxide (MMO) sensors

Sliding MMO redox sensors were originally described by Taylor et al. (1992), who described a technique involving the use of isobarically divariant oxide or alloy solid solutions to sense μ_{O_2} or μ_{H_2} in a double capsule experimental arrangement. The sensor is based on the addition of an inert oxide or noble metal to displace the buffer equilibrium (e.g., MMO buffer reactions described in Figure 10.13) to a different and broader range of μ_{O_2} or μ_{H_2} than the end-member buffer MMO reaction. The μ_{O_2} or μ_{H_2} can be calculated from the oxide or alloy solution composition after experiments by SEM or EPMA of oxide solid-solution or metal alloy and requires no estimate of experimental hydrothermal solution (e.g., Chou and Eugster, 1976). In other words, unlike the H-sensors of Chou and Eugster (1976), sliding sensors provide a simple means to study μ_{O_2} and μ_{H_2} over a very broad range high P-T conditions in a hydrothermal experiment.

Redox concepts

The sliding MMO redox sensor technique is based on previously calibrated metal-metal oxide (MMO) buffer equilibria (see Figure 10.13). A general reaction can be written for such equilibria, whereby:

$$xM + y/2(O_2) = M_xO_y \qquad \textbf{(eq. 10.2)}$$

At a given P and T the equilibrium constant for equation 10.2 can be expressed:

$$\log K_{(P,T)} = [\log(a_{MxOy}) - x\log(a_M) + (y/2 \cdot \log(f_{O_2})] \qquad \textbf{(eq. 10.3)}$$

where, M = the metallic element, x and y = the stoichiometric coefficients, $K_{(P,T)}$ = the equilibrium constant at the given P and T, a = the activity of the given species and f_{O_2} = the oxygen fugacity.

Where phases described in equation 10.2 are pure, the activity of the metal (a_M) and metal oxide (a_{MxOy}) are unity, such that:

$$\log K_{(P,T)} = -(y/2) \cdot \log(f_{O_2}) \qquad \textbf{(eq. 10.4)}$$

Equation 10.4 is the basis for calculating f_{O_2} for the various solid-solid buffer equilibria at a specified P-T (Eugster, 1957, see Figure 10.13).

If the activity of the metal component is lowered via dilution with a suitable metal component (i.e., so long as the two metal phases show a continuous and ideal solid-solution series – e.g., a binary alloy) the end-member buffer equilibria is diplaced to higher f_{O_2} at any given temperature and pressure:

$$\log(f_{O_2}) = -2[\log K_{(P,T)} - \log(a_{Mx})] \qquad \textbf{(eq. 10.5)}$$

The effect of adding metal dilutants (or metal oxide components) to the end-member buffer equilibria are shown in the mole fraction of the reactive component (X) curves plotted against f_{O_2} in Figure 10.16. This figure also demonstrates that the working range of a given sliding sensor is restricted to a narrow f_{O_2} range (~4-7 log units) and alloy/oxide solid-solutions have very small compositional variations as the system approaches an f_{O_2} of the end-member MMO buffer.

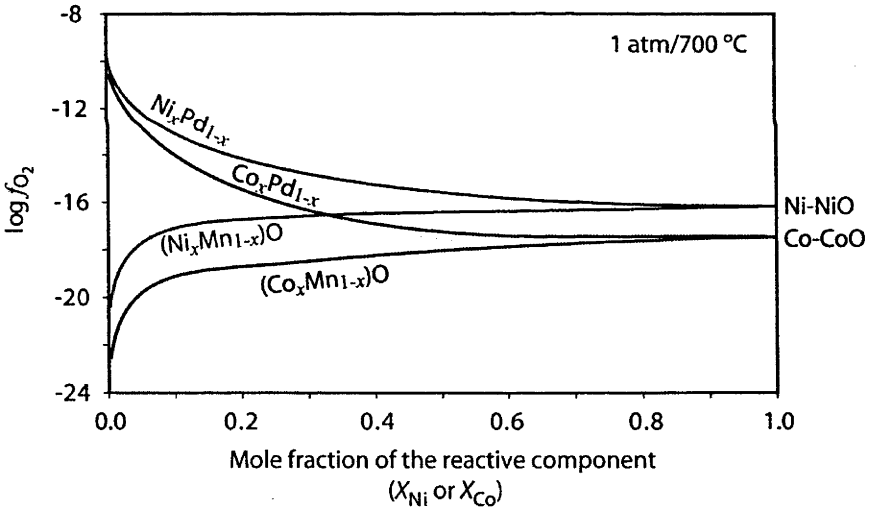

***Figure 10.16**: Binary alloy systems at 1 atmosphere (atm) and 700 °C (image modified after Taylor et al., 1992).*

The many advantages of the sliding sensor technique include: the system is self-adjusting to ambient conditions within an experiment (i.e., experiments do not require a fixed f_{O_2}); the technique involves small masses of reactants within a sensor capsule, and; providing that all reaction components are equilibrated and present within the capsule post-run, the technique can be employed over a broad range of P-T conditions (Huebner, 1971).

Criteria for the MMO sliding sensor

Experimental investigations of the sliding sensor technique have shown that a $\Delta(f_{O_2})$ across the walls of a sensor capsule can be influenced by: (1) the survival and effectiveness of the external oxygen buffer; (2) the thickness and permeation rate through the H-membrane, and; (3) the intrinsic f_{O_2} (or f_{H_2}) imposed by the experimental apparatus. In order for metal or metal-oxide components to successfully sense hydrogen or oxygen fugacity, systems must satisfy a number of conditions:

1) A continuous solid-solution series must form at the required pressures and temperatures.
2) The activity-composition relations must be known for the alloy or oxide solution at the temperature range of interest.
3) The oxide phase and metal phases must be mutually insoluble.

10.6: Relating oxygen buffers and sliding sensors

As discussed in the introduction of this chapter, oxygen buffers and sliding MMO sensors are introduced here because they are the theoretical basis for the technique developed herein. An experimental MMO oxygen buffer defines oxygen fugacity (f_{O_2}) within an experiment (so long as the buffering assemblage is present throughout the experiment duration) and provides a fixed f_{O_2} at experimental conditions (see red curves in Figure 10.17). By comparison, sliding MMO sensors can be used over a range of f_{H_2} (a_{H_2}) or f_{O_2} (a_{O_2}), as long as the system is defined by the presence of buffering phases, in an equilibrated hydrothermal experiment unbuffered with regard to f_{O_2} or f_{H_2}.

As shown in Figure 10.17, the working range of sliding MMO sensors extend simple MMO buffers to a much broader range of f_{O_2} conditions. With regard to this research, the most important observation is that coupling of sliding H-sesnors and MMO oxygen buffers can only be made where the two exist at similar oxygen fugacity. Therefore, the NiPd H-sensor could not be used in an experiment at QFM, as the NiO in the sensor will no longer be stable. This example demonstrates that in order to combine MMO oxygen buffers with sliding H-sensors it is necessary to choose two buffered systems that operate over similar f_{O_2}. It is similarly important to note that in a metal alloy H-sensor (i.e., where the dilutent is a metal), as f_{H_2} increases, the mole fraction of reactive component in the alloy increases dramatically as the end-member MMO of the sensor is approached (i.e., steepening of alloy compositions in Figure

10.17). This steepening means that care must be taken when interpreting results because there is not a linear trend between Ni:Pd and f_{H_2}.

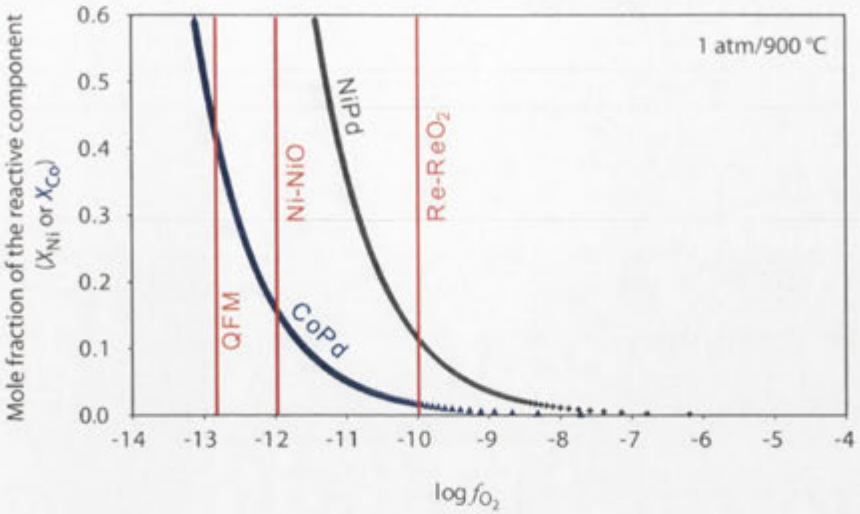

***Figure 10.17**: Working range of the NiO-Ni-Pd (shown in black) and CoO-Co-Pd (shown in blue) H-sensors relative to some MMO oxygen buffers (shown in red) at 1 atmosphere/900 °C.*

Taylor et al. (1992) hypothesized that the H-sensor technique could be used to study mixing properties of supercritical vapour species (i.e., at conditions around the $CP^{1}_{Silicate-H_2O}$). This original hypothesis assumes that f_{H_2O} (a_{H_2O}) can be calculated from a hydrothermal system at a constant temperature, pressure and f_{H_2} (imposed by the cell assembly), by comparing H-sensor results from a pure H_2O run with a H_2O-CO_2 run. This hypothesis assumes that changes in the f_{O_2}, caused by vapour dilution (f_{H_2O}) with CO_2, follows:

$$\log f_{H_2O} = \log f_{H_2} + \frac{1}{2}\log f_{H_2O} - \log K_{(T,P)} \qquad \textbf{(eq. 10.1)}$$

10.7: Summary

The details of this literature review are presented in order to highlight the extreme variability of supercriticality estimates for the pelite-H_2O, while also discussing the limitations of experimental techniques employed in previous studies of the system. While such studies provide a great deal of information regarding sediment melting during subduction, there are a variety of problems that stem from assumptions associated with existing techniques.

Later sections of this chapter (10.4-10.6) introduce concepts relevant to the technique designed in this research. These concepts include the use of oxygen buffers and inert H-sensors (that can be used to monitor f_{H_2} or f_{O_2}).

Chapter 11

Experimental Design

The experimental technique developed here was designed to address the research aims outlined in Chapter 10 and to be applicable to rock-H_2O systems over a wide range of P-T conditions. The introductory sections of this chapter concentrate on the end-loaded piston cylinder apparatus. This is followed by a discussion on how pressure and temperature are measured within experiments (including theoretical considerations, experimental tests and calibrations). The final sections of this chapter describe the new experimental technique and various tests that were carried out on the assembly.

11.1: Experimental rationale

The temperature and pressure range required to address research aims represents the most basic aspect of any experimental design in this field of research. As shown in Figure 11.1 (reproduced from Chapter 10), the desired P-T range for this research is 25-40 kbar and 650-900 °C. The working range of existing experimental techniques (Figure 11.2) shows that the end-loaded piston cylinder technique (Boyd and England, 1960) is the most suited to this work.

The piston cylinder apparatus

The end-loaded piston cylinder apparatus (designed by Boyd and England, 1960) consists of numerous components that all serve specific purposes. Detailed description and discussion of the apparatus is beyond the scope of this thesis and such information can be found in a number of publications (Boyd and England, 1960; Johannes et al., 1971; Mirwald et al., 1975; Boettcher et al., 1981).

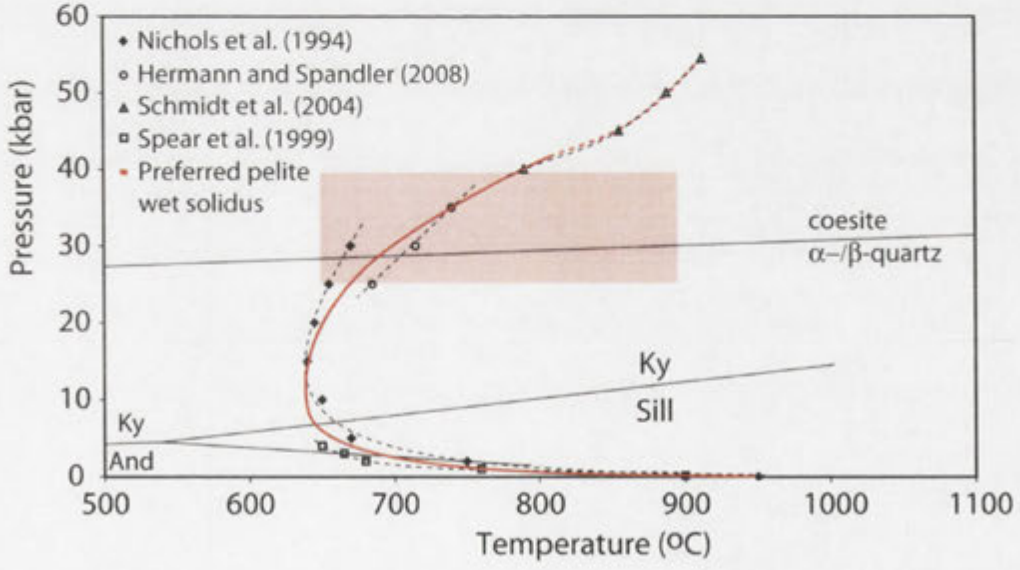

***Figure 11.1**: Experimentally determined pelite-H_2O wet solidus. Various experimental studies and wet solidi shown in black symbols and dashed black lines; solid red line represents preferred wet solidus as indicated by various experimental studies; light red rectangle represents the region about the solidus where notable back-bending begins and divergence exists among different experimental studies. The Al_2SiO_5 phase diagram (and polymorphs therein) and quartz-coesite transition are shown for reference.*

The basic manner in which the piston cylinder works is that a piston presses into a reinforced cylinder that contains the experimental medium. The pressure vessel, which contains the reinforced cylinder (and in turn, the experimental medium), is end-loaded within the apparatus and held in place by 150-200 tons load applied by means of a hydraulic ram. Experimental pressure is obtained by forcing the piston into the cylinder (see Figure 11.3), by means of another hydraulic ram system, such that it compresses solid media of known and calibrated properties. Temperature is applied to the experiment by passing high current through a resistive furnace (tube) held within the pressure vessel (i.e., the experiment is internally heated).

Pressure and temperature

Pressure exerted on an experiment is calculated by multiplying the amount of hydraulic ram applied to the piston (sometimes known as the Boyd pressure - P_B) by the cross-sectional area of the piston (P_P). As such, the P_B:P_P relationship dictates that smaller pistons (in terms of cross-sectional area) obtain higher pressures at a fixed hydraulic ram (see Figure 11.4). Precision of pressure during a piston cylinder experiment, generally attributed to friction decay (Hack and Mavrogenes, 2006), is in the order of 1-3 %.

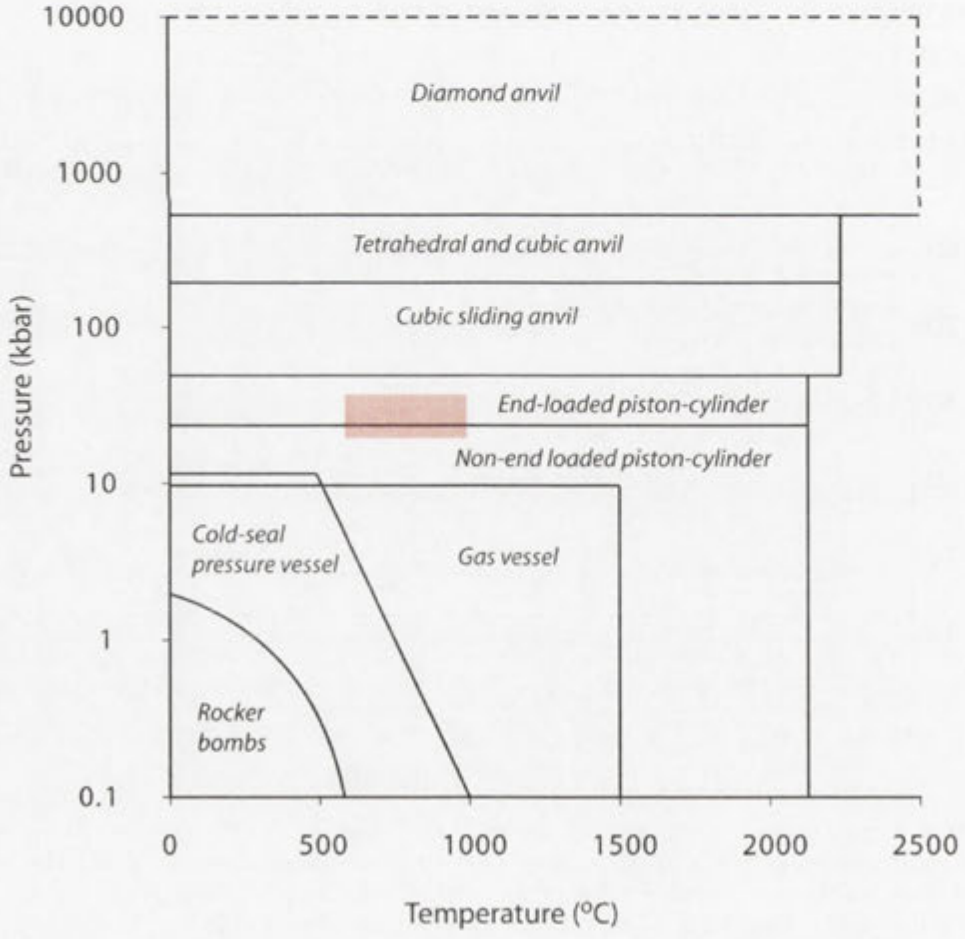

***Figure 11.2**: P-T range of various experimental apparatuses (figure modified after Holloway and Wood, 1988). The shaded red regions corresponds to the P-T region of interest to this study.*

The experimental technique developed during this research was designed for a 1/2" assembly (i.e., a 1/2" diameter piston and associated cylinder), which represents the smallest diameter (i.e., cross-sectional area) piston currently available at the RSES.

As demonstrated in Figure 11.3, the upper pressure limit of an experiment is dependent on the amount of main ram (instruments with higher main ram can safely achieve higher boyd ram pressures), P_B:P_P (a piston of smaller cross-sectional area can attain higher experimental pressure than a piston with a large cross-sectional area at a given P_B), and the type of solid media used within experiments (variations in bulk compressibility and thermal expansion require different calibrations). This is to say that pressure calibrations vary depending on the area and type of solid material used in a given assemblage.

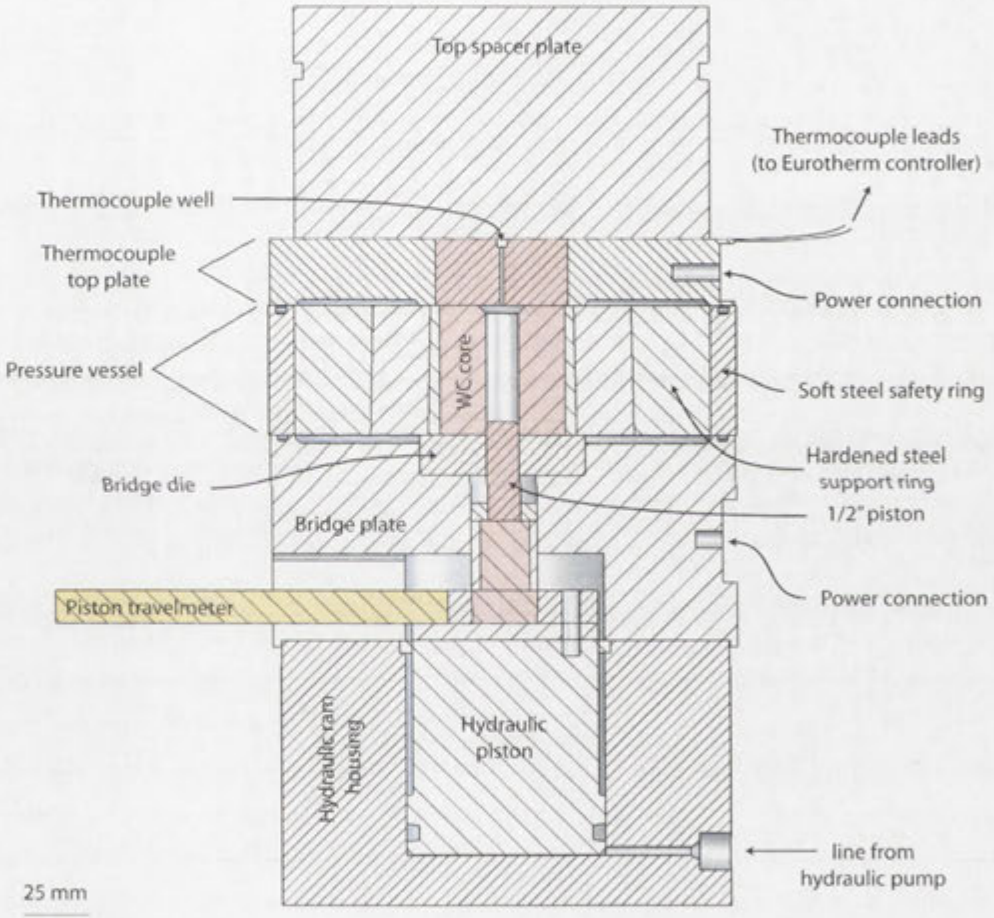

***Figure 11.3**: Cross-sectional schematic of the piston cylinder apparatus. Tungsten carbide parts are shown in purple hues, brass parts are shown in golden hues, voids are shown in grey hues and all other parts are made from various types of steel.*

Temperature is generated within an experiment by passing high current through a graphite tube furnace (see Figures 11.7 and 11.8). Experimental temperature is monitored with a type B thermocouple ($Pt_{70}Rh_{30}/Pt_{94}Rh_6$) held within a MgO-lined well in the top of the Ag capsule (see Figures 11.7 and 11.8). This thermocouple is suited for use at temperatures between 50 and 1,800 °C, with negligible drift or pressure effect expected at 650-900 °C (Presnall et al., 1973).

11.2: Experimental design

The technique developed here was designed to have a large starting volume, have the capacity to run at high H_2O content, and the capability to run at high pressures in a piston cylinder apparatus. Large capsule volume (i.e., an inner diameter >2 mm) and high water contents (i.e., >30 wt%) can be difficult using conventional metal (Pt, AgPd, Au, etc) capsules and welding techniques[1]. The basic problem with capsule welding is conductance of heat through the capsule from the weld pool. To obtain an effective seal the weld pool has to reach a temperature above the melting point of the capsule metal (e.g., Pt = 1,768 °C, Au = 1,064 °C). In other words, the physical properties that make metal capsules useful in geochemistry research (high melting point and thermal conductivity) also create large problems in hydrothermal experiments. A typical metal capsule (Pt, AgPd, Au, etc) conducts enough heat to volatilize free H_2O during welding.

One technique used to overcome H_2O loss during welding is to use hydrous minerals (e.g., mica, amiphibole, brucite, silicic acid, etc) as a water source during experiments. The addition of such compounds may not completely remove volatile loss via dehydration reactions during welding, but it does significantly reduce the risk.

In short, while capsule welding only requires a matter of seconds to create an effective seal, thermal conduction can generate temperatures >> 100 °C within the capsule and volatilize any free H_2O (i.e., unbound to a hydrous mineral). It should be noted that hydrothermal pelite/greywacke experiments presented in the literature never report experiments at water contents >30 wt% (Nichols et al.,1994 - 8-28 %; Johnson and Plank, 1999 - 13-14 wt%; Schmidt et al., 2004 - 2.1 wt%; Hermann and Spandler, 2008 - 2-7 wt%).

To circumvent the welding problem, Hack and Mavrogenes (2006) designed a cold-seal experimental technique involving 15.0 mm and 9.0 mm outer diameter capsules (Cu, Ag or Au). The large outer diameter of Hack et al. (2006) cold-seal capsules make them only suited to a 5/8"or 3/4" pressure vessel, which has maximum pressures of ~20 kbar and ~15 kbar (in a 150/200 ton main ram piston cylinder apparatus). In order to attain desired pressure conditions for the pelite-H_2O system (see Figure 11.3), the working conditions must be extended to higher pressures (up to ~40 kbar). In other words the capsule has to be scaled to fit into a 1/2" pressure vessel.

[1] Noting that various techniques have been used to limit volatilization on weld, yet such techniques do not completely eradicate thermal heat conducted during welding in all cases.

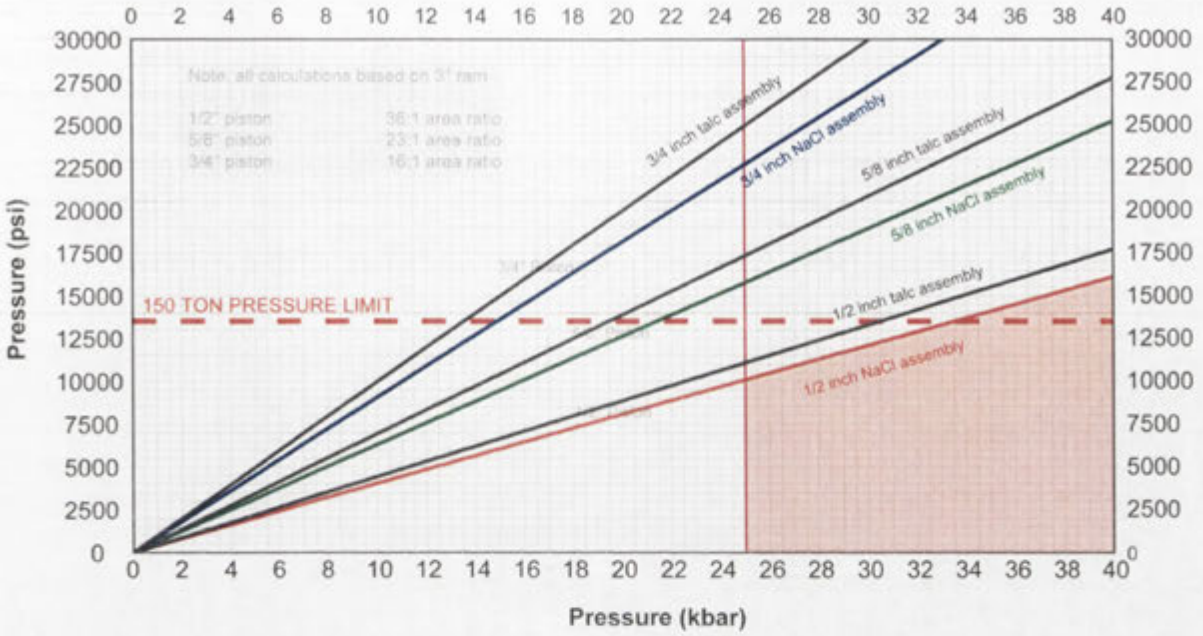

***Figure 11.4**: Experimental pressure calibration calculated for talc (10% friction) and NaCl (incompressible and "frictionless") assemblages at different piston cross-sectional areas.*

The 6 mm Ag capsule

In order to attain pressures > 20 kbar, a 6 mm Ag capsule was designed to run in a 1/2" pressure vessel (it is worth noting that other metals could be used). The design involves a capsule that is essentially a scaled-down and revised version of the Ø 15 mm capsule of Hack and Mavrogenes (2006) design. The capsule consists of a thick-walled (1 mm) Ag body that is open at the top, with a 0.65 mm (width) ledge along the top wall of the capsule (see Figure 11.5). The capsule lid is a dual indented Ag disc that is designed to slot within the ledged capsule wall. The upper indentation on the capsule lid is designed such that the swaged outer capsule wall can fold over the lid disc to form an effective cold-seal. The capsule lid also has a 1.8 mm deep thermocouple well that contains a lining of pressed MgO powder.

Capsule and lid components are swaged together with a brass tool (Figure 11.6), which consists of a basal die, an aligning tool and an indented piston tool (designed to roll the capsule wall lip inward and over the capsule lid). The circular indentation on the upper swaging piston has a diameter proportional to the capsule and a depth proportional to the depth of the capsule lid. Visual inspection of the capsule after swage ensures the quality of swage and alignment of capsule components (noting that misaligned capsules were discarded).

The capsule design, as shown in Figure 11.5, has an outer diameter of 6.3 mm. This dimension is used because preliminary tests of the capsule showed bulging and imperfections (very small "pinches" where the swage piston and die meet) around the lid of the capsule upon swage. The design was enlarged by 0.3 mm in order to account for bulging, such that the sealed capsule can be machined back to 6.0 mm after swaging. Capsule thickness (after

swage and lathe machining) is 1.0 mm along the capsule wall, 1.6-3.6 mm at the capsule bottom/top, with the inner dimensions of the capsule showing a volume of 120.65 mm^3.

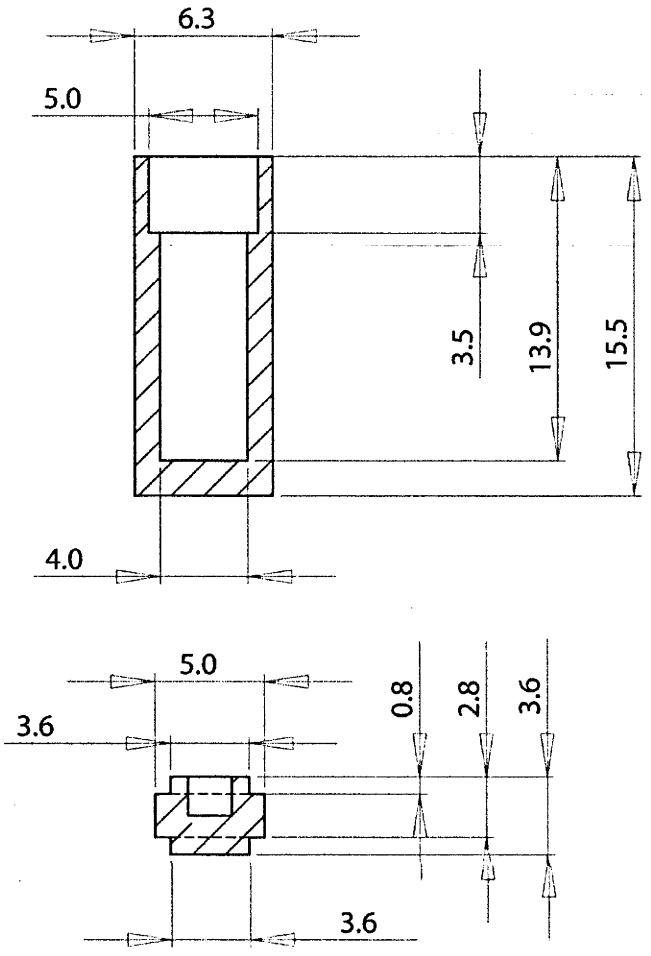

***Figure 11.5**: Front cross-sectional view of the un-swaged Ag capsule, with all dimensions reported in millimeters. Solid lines represent edges as viewed in section, while dashed lines represent edges at depth (i.e., not exposed at the field of view).*

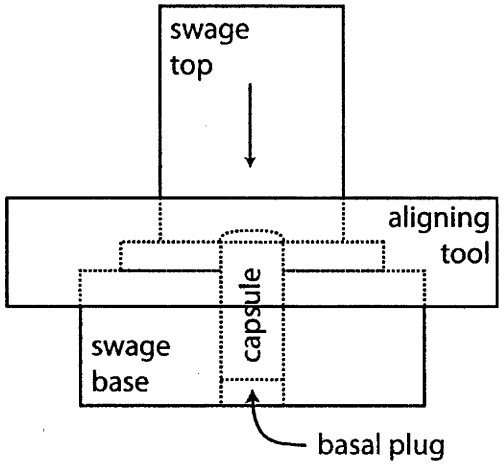

***Figure 11.6**: Schematic of the brass swaging tool (not to scale). It should be noted that the swage top tool has a circular indentation of a depth and diameter proportional to the lip thickness and outer diameter of the capsule and lid. Arrow indicates the direction of hydraulic pressure used to apply pressure to the swage piston in order to cold-seal the capsule.*

The capsule design shown in Figure 11.5 is not specific to Ag, but could be equally applicable to any number of metals. This being the case, it should be noted that the use of Ag has a number of advantages. The thermal conductivity of Ag (the highest among regularly used capsule materials) makes the use of large capsules, particularly with regard to length (or height), possible without introducing significant thermal gradients. The cost of Ag (even in a fluctuating market) is remarkably cheap compared to other metals commonly used as capsule (Pt, Pd, Au, etc) and the metal is easily machined or manipulated (such that it can be swaged). Another advantage of using Ag is that the metal shows low H-diffusion rates compared to Pt or Ag-Pd alloys, and insignificant Fe-loss, making it ideal for f_{O_2} -buffered hydrothermal experiments.

General assembly

The general experimental assemblage used in this research is shown in Figures 11.5 and 11.6. Every component of the experimental assembly, with the exception of the hardened steel plug and pyrophyllite mitre ring, are machined from raw components on a lathe or cold pressed in the laboratory.

The thick outer NaCl sleeve (Ø = 12.60 mm, wall thickness = 2.075 mm) is cold-pressed in a carbide vessel with a hardened steel piston-sleeve tool and dehydrated at 400 °C for 24 hours. The graphite tube furnace (Ø = 8.0 mm, wall thickness = 0.5 mm) is machined from graphite tubing. Visual inspection of the graphite furnace is used to check for cracks, flaking or other forms of imperfection (e.g., bulging or surface irregularities). Pyrophyllite spacers are machined from ~10 mm rods pre-fired at 50 °C/hour until reaching 850 °C, at which temperature the rods are fired for 12 hours. The upper semi-fired pyrophyllite spacer contains an MgO-lining (Ø = 1.8 mm, thickness = 3.1 mm). The MgO-lining acts as a soft lining around the mullite thermocouple tube and was included in the assembly because preliminary tests (unlined pyrophyllite) occasionally saw shearing of the thermocouple at high pressure. The talc sleeve (Ø = 7.3 mm, wall thickness = 0.65 mm) insulates the Ag capsule from the graphite furnace and is machined from natural talc. The talc component is the most difficult to machine without cracking or causing surface imperfection. In order to ensure complete insulation between capsule and furnace, slow lathe rates and visual inspection are crucial to the success of an experiment.

11.3: Experimental tests

A number of techniques were used to test this assembly design. Given the uniquely large capsule, and correspondingly small insulators and spacers, significant effort was made to independently determine the internal pressure and temperature within the 6 mm Ag capsule. It should be noted that all experiments (including test and subsequent studies) incorporated the piston-in method. In addition to pressure and temperature tests, efforts were made to determine H-diffusion and friction decay (which helps determine pressure precision) within experiments.

Pressure (friction) effects

The pressure exerted on the experimental charge (capsule) in a piston cylinder experiment is calculated from the relationship between the amount of Boyd ram and the cross-sectional area of the piston. The 1/2" cell assembly designed here (as in all such experiments) makes use of, and is constructed from, various solid media – Ag, talc, hardened pyrophyllite, MgO and NaCl. As each of these components exhibits different thermal (conductivity) and physical (compressibility, hardness and shear strength) properties, the cell assembly must experience some pressure heterogeneity. Of greatest concern to the success of the experiment is what pressure the capsule experiences and how closely this approximates the ideal P_B:P_P pressure estimate (Figure 11.4). Pressure uncertainty, or error, in an experiment is generally attributed to variable compressibility of cell components and shearing of different components against shared walls (commonly referred to as 'friction effects').

NaCl dominated assemblages appear to show the lowest pressure uncertainty (or friction effects) among piston cylinder cell assemblies, with uncertainty estimates ranging from ±1 % in a 1" NaCl assembly (Boettcher et al., 1981) to 1.7% in a 1/2" NaCl assembly (McDade et al., 2002). For this reason, NaCl-dominated assemblies are commonly referred to as "low-friction" or "incompressible" cells. While it is tempting to assume a similar "low-friction" pressure correction for the 1/2" assembly designed here, given it has a thick NaCl outer sleeve, the cell shows a number of unique components that merit pressure tests. The combination of large volume Ag capsule (Ø = 6 mm, length = 14.75 mm), thin talc insulator sleeve and hardened pyrophyllite spacers (see Figures 11.7 and 11.8) have never been studied or used before. It is also worth noting that a great deal of previous research into friction/pressure corrections is based on short-duration (i.e., <24 hours), high temperature runs (i.e., ≥ 1,000 °C). The experiments carried out during this research, by comparison, involve temperatures ranging from 650-900 °C and long run times (120-216 hours).

The unique cell assembly and run conditions of this experimental design require pressure testing in order to justify pressure and associated error estimates.

In order to determine pressure exerted on the 6 mm Ag capsule, three forms of tests were carried out. The first involved synthetic fluid inclusions, the second involved phase transition studies and the third involved monitoring piston travel during experiments.

Synthetic fluid inclusions

The synthetic fluid inclusions technique involves addition of shocked, inclusion-free (Brazilian) quartz and H_2O into the 6 mm Ag capsule (similar techniques are reported by Sterner and Bodnar, 1983; Bodnar and Sterner, 1985; Brodholt and Wood, 1994; Hack and Mavrogenes, 2006; Spandler et al., 2007). The basic concept behind this test is that temperature within an experiment is fixed (and accurately known), and inclusions form along annealed cracks at conditions representative of the experiment (greater details surrounding the technique are presented by Hack and Mavrogenes, 2006).

Experimental pressure is estimated from theoretical calibrations of an "incompressible" NaCl assemblage (see Figure 11.4) and temperature is controlled by a Type B thermocouple held within a well atop the Ag capsule (Figure 11.5). An experiment carried out at 20 kbar/800 °C for 120 hours showed abundant fluid inclusions in quartz, occurring along annealed cracks in the host grains. Fluid inclusions from this experiment were homogenized, by means of a heating stage, and used to calculate an appropriate isochore (details of the technique are outlined by Hack and Mavrogenes, 2006). By applying an appropriate equation of state (in this case, Brodholt and Wood, 1993), the homogenization temperature (T_h) can be used to estimate pressure (which assumes experimental temperature is accurately known). The homogenization temperatures seen in synthetic fluid inclusions correspond to the 1.0555 isochore, indicating an equilibration pressure of 20.025 kbar at 800 °C.

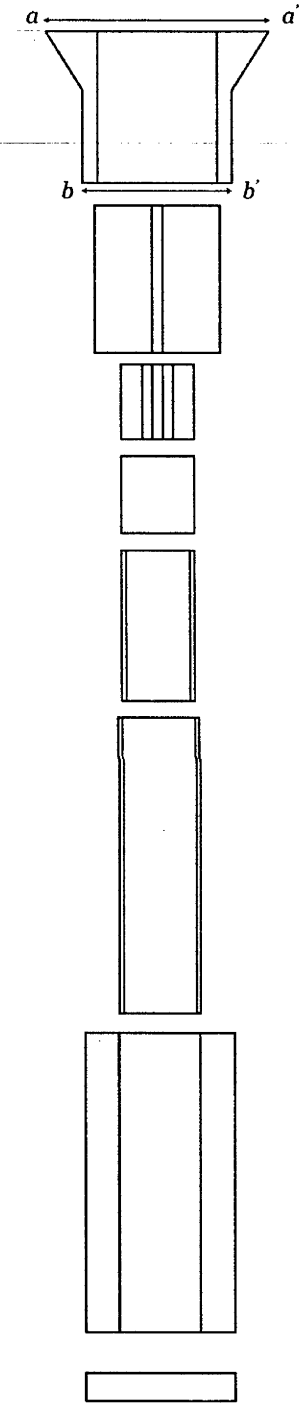

Material	Dimensions of part
Pyrophyllite mitre ring	$Ø_{a-a'}$ = 19.40 mm $Ø_{b-b'}$ = 12.45 mm Θ = 11.10 mm *h* = 12.65 mm
Hardened steel plug	Ø = 11.10 mm Θ = 1.60 mm *h* = 12.75 mm
MgO-lined pyrophyllite* top plug	$Ø_{Py}$ = 11.10 mm, $Ø_{MgO}$ = 3.10 mm $Θ_{Py}$ = 3.10 mm, $Θ_{MgO}$ = 1.60 mm *h* = 7.90 mm
Pyrophyllite* base plug	Ø = 11.10 mm Θ = 1.60 mm *h* = 7.90 mm
Talc sleeve	Ø = 7.30 mm Θ = 6.00 mm *h* = 14.40 mm
Graphite furnace	Ø = 8.30 mm Θ = 7.30 mm *h* = 32.00 mm
NaCl outer sleeve	Ø = 12.45 mm Θ = 8.30 mm *h* = 32.00 mm
Graphite disc	Ø = 12.45 mm *h* = 1.30 mm

***Figure 11.7**: Schematics of the 1/2" assembly. Symbols include: Ø = outer diameter, Θ = inner diameter, h = height, Py = pyrophyllite, * = pyrophyllite pre-fired prior to experiments, and MgO = pressed magnesia rod.*

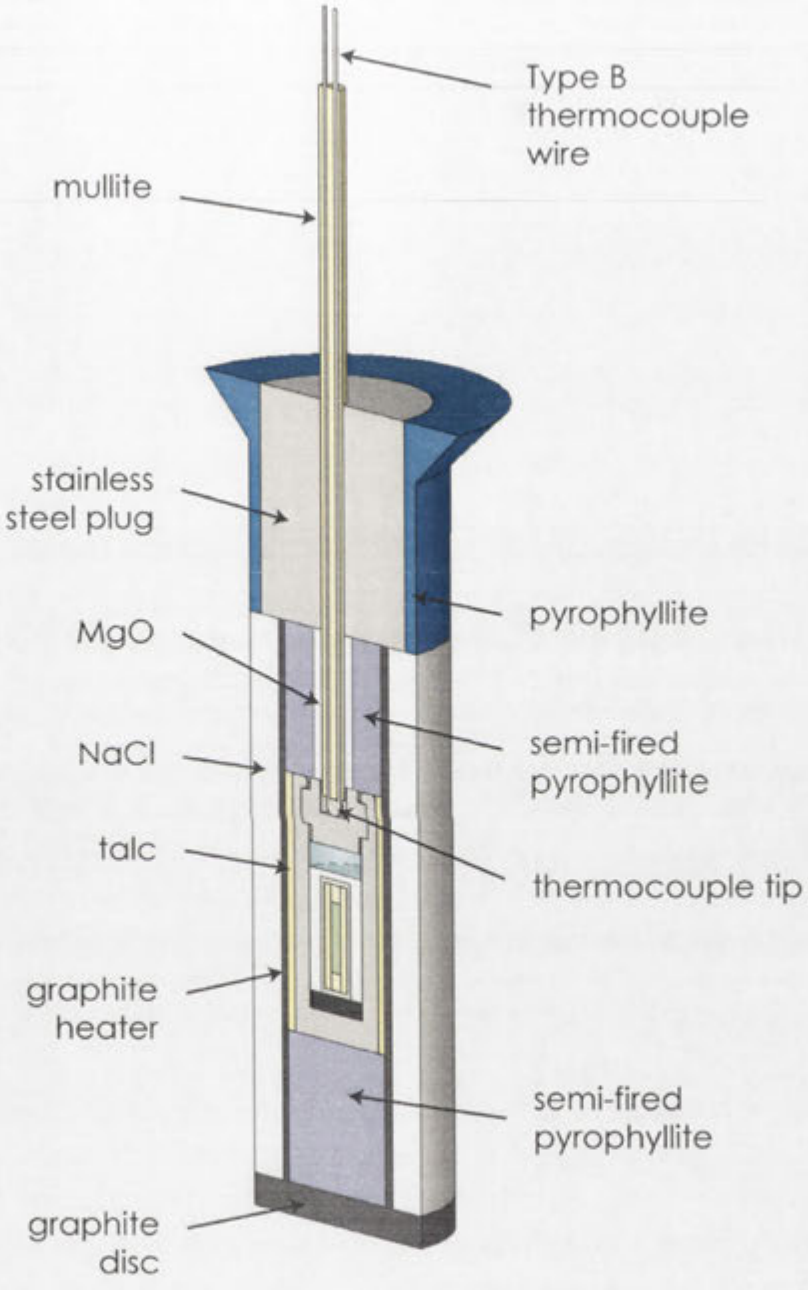

***Figure 11.8**: 3-dimensional cross-section of the 1/2" assembly produced with CAD software. The Ag capsule is found in the centre of the cell and contains pelite-type experimental components.*

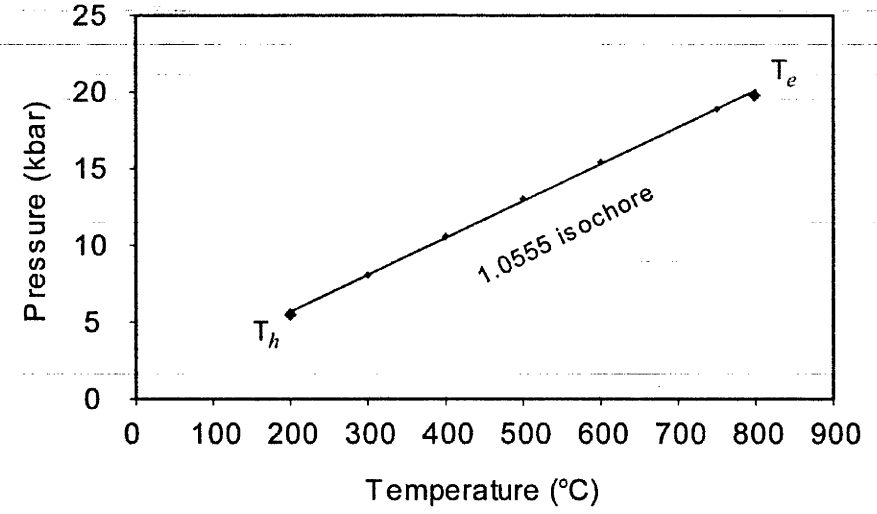

***Figure 11.9**: Representative heating experiment of 20 kbar/800 °C synthetic fluid inclusions. T_h = homogenization temperature and T_e = experimental temperature (as determined by thermocouple readings).*

The second method used to determine pressure within the capsule involves the quartz-coesite transition. This transition has been well studied and calibrated (Akaogi et al., 1984; Bohlen and Boettcher, 1982; Bose and Ganguly, 1995), with the univariant reaction occurring at P-T conditions located directly within the experimental range of pelite-H_2O studies presented here (Figure 11.1).

Six experiments containing 10 wt% de-ionized H_2O and 90% SiO_2 powder (Aldrich, 99.99 % purity) were run at different P-T conditions for 136.3-216 hours (Table 11.1). X-ray diffraction (XRD) analyses of run products determine the dominant silica phase within experiments and these results can be directly compared with previous experimental research into the phase transition (Bose and Ganguly, 1995). XRD analyses from all six experiments indicate that runs consist of a single silica species (at the limit of XRD detection, other species would account for <1%).

All results shown in Figure 11.10 are consistent with data from Bose and Ganguly (1995). Experiments C-2427 and C-2429 provide the greatest constraint on pressure uncertainty, with these experiments falling 0.005 and 1.150 kbar from the reaction loci. As all experiments are consistent with the work of Bose and Ganguly (1995), and experiments C-2427 and C-2429 show the closest bracket about the calibrated reaction curve, pressure estimates from the cell assembly can be reported with a maximum error of 1.15 kbar.

Table 11.1

Experiment #	Time (hours)	Pressure (kbar)	Temperature (°C)	Mineralogy
C-2427	136.3	29.0	750	Quartz
C-2429*	168.0	30.5	800	Coesite
C-2458	144.0	32.0	850	Coesite
C-2563	216.0	32.0	700	Coesite
C-2564	216.0	31.0	750	Coesite
C-2565	168.0	31.0	650	Coesite

* = leaked experiment

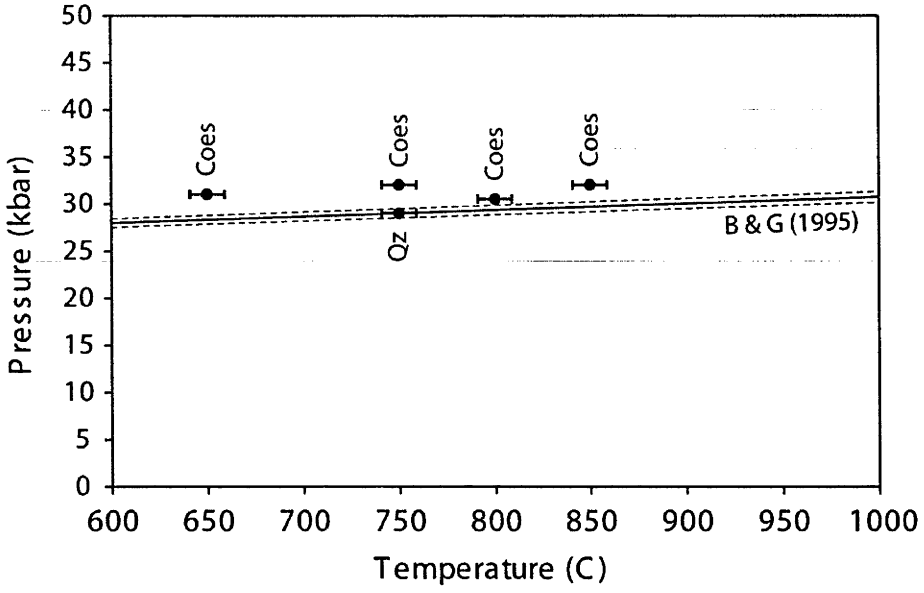

***Figure 11.10**: Silica species from experiments at different pressure-temperature conditions. Temperature error bars represent the highest thermal gradient seen in any test experiment (see proceeding sections). B & G = quartz-coesite calibration of Bose and Ganguly (1995), dashed lines represent uncertainties reported in the original calibration. Pressure uncertainty – be it uncertainties reported for NaCl cells (Boettcher et al., 1981; McDade et al., 2002) or variation in measured Boyd pressure – are less than symbol size.*

Piston travel (friction decay)

The piston-cylinder apparatus used in this experimental study is equipped with a brass plate (travelmeter - highlighted in yellow hues in Figure 11.3) fused to the tungsten carbide-hardened steel plug directly screwed to the hydraulic piston. As the 1/2" piston moves, the amount of displacement is measured by a digital indicator (with a 0.01 mm resolution) attached to the travelmeter. Once the cell assembly has reached experimental pressure and temperature, movement of the piston can be monitored over the duration of a run.

Assuming compression of tungsten carbide and steel components is negligible compared to the cell assembly components at experimental conditions, movement on the travelmeter can be used to monitor friction decay as a function of temperature and time. It should be noted that all Ø 6 mm Ag-capsule experiments are carried out using the piston-in mode, which assumes that Boyd pressure (nominal) approximates internal (capsule) pressure.

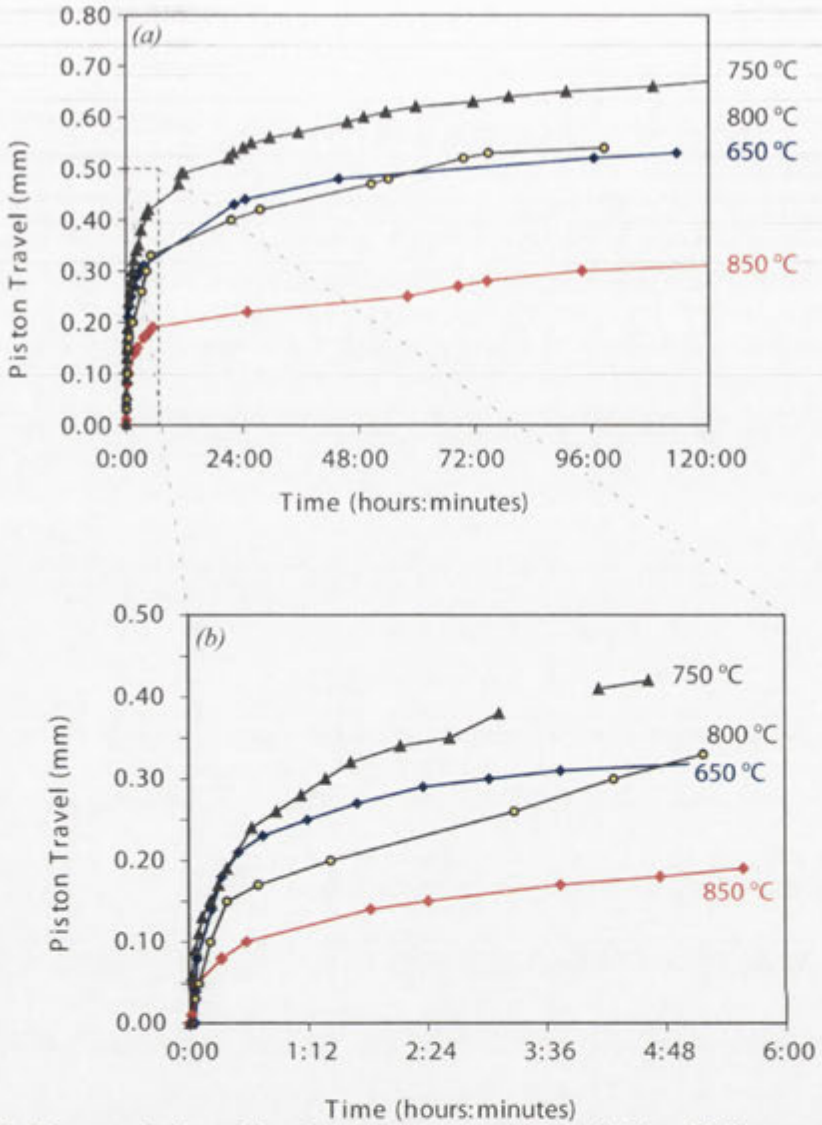

***Figure 11.11**: Representative piston travel measurements made from 35 kbar experiments as a function of time. Measurements are made from the travelmeter described in Figure 11.3 and time "zero" refers to the initial attainment of experimental pressure and temperature. (a) piston travel from four experiments, with equilibration temperature indicated, measured over 5 days. (b) piston travel in the first six hours of the same experiments shown in (a).*

Figure 11.11 shows piston travel from experiments at temperatures from 650-850 °C (all at 35 kbar or Boyd pressure of 14101 P.S.I.). Friction decay can be considered complete when all cell assembly components are fully equilibrated at experimental conditions (such that shearing, compression and composition of solid media cease to change). In a piston-in experiment the "frictionless" cell assembly is manifest as ceased piston travel or a plateau in piston travel measurements. Figure 11.11 indicates that all experiments at >650 °C show limited piston movement after 24 hours, suggesting that most of the friction has been lost from the 1/2" cell assembly and accurate pressure estimates are best made after this period of time. Interestingly, the time required to reach a plateau in piston movement (or for friction to leave the cell assembly) appears to be independent of temperature. In other words, regardless of temperature (from 650- 800 °C), all experiments appear to show similar friction decay windows as a function of time.

The greatest variation among experiments is the amount of piston travel (see Figure 11.11). Such variations most likely results from the minor imperfections found on the surface of the cell components or variations in their thickness (which, in turn, relate to the quality of lathe machining). These imperfections and minor variations among cell components from different experiments demonstrate the importance of treating each cell assembly as unique (with regard to friction), despite the fact that each shows the same dimensions (within 0.01 mm).

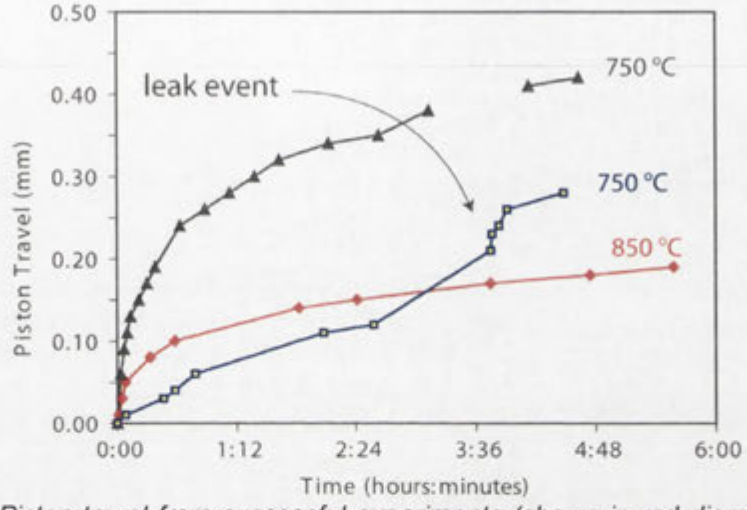

***Figure 11.12**: Piston travel from successful experiments (shown in red diamonds and black triangles) and leaked experiment (open blue squares).*

Another advantage of monitoring piston travel during an experiment is that it can be used to monitor capsule behaviour, particularly leakage events in hydrothermal experiments. When a capsule containing H_2O at the wt %-scale experiences fluid loss, partial or wholesale, fluid escape results in rapid volume change and associated shortening of the capsule. As demonstrated in Figure 11.12, capsule leaks are seen by rapid and unusual positive piston movements during experiments (which can later be confirmed by capsule mass and petrography). As most high pressure and low temperature (<900 °C) hydrothermal melting experiments require several days to equilibrate, piston travel can be used to identify experiment failure and dramatically reduce time wasted on failed experiments.

Thermal gradient tests

Two temperature calibration experiments were carried out in order to measure the thermal gradient within the 6 mm Ag capsule and to determine how this relates to thermocouple position. All calibration experiments involved the standard cell assembly described in Figures 11.7 and 11.8, with the only difference being that capsules contained semi-fired pyrophyllite (rather than pelite-H_2O starting material) and a 1.65 mm diameter thermocouple hole was drilled into the lid of the Ag-capsule. Each calibration experiment was carried out with 3 thermocouples, held in a four-bore mullite tube, positioned within or about the Ag-capsule. Experiments were held at initial starting conditions (10-12 kbar and ~600-700 °C) for 6 hours before ramping to 35 kbar and initiation of thermal gradient tests. Every incremental temperature increase was based on the basal thermocouple (the most reliable and consistent position – $^{2,3}T/C_1$) with the cell given 30 minutes to thermally equilibrate before temperature readings.

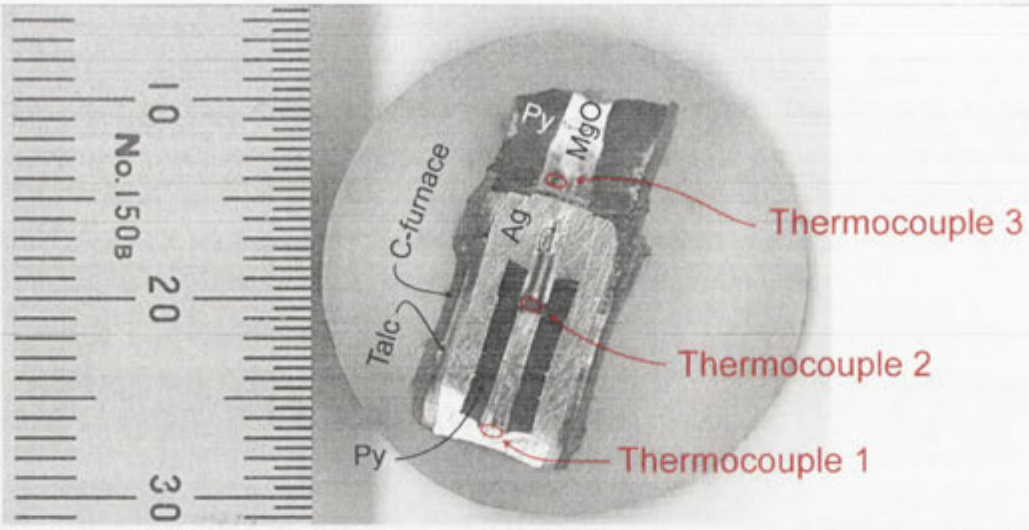

***Figure 11.13**: Representative photomicrograph of thermal gradient experiment, from run D-1077. Ruler is shown for scale (with major units shown in millimeters), abbreviations include: Py = pre-fired pyrophyllite (fired at 850 °C), Ag = silver capsule, MgO = pressed magnesia tubing, C-furnace = graphite furnace. Thermocouple positions as indicated.*

All calibration experiments were mounted in EPO-FIX resin post-run and thermocouple position (height) referenced to the base of the capsule (see Figure 11.14). Measured temperature variations are shown in Table 11.2 and Figure 11.14.

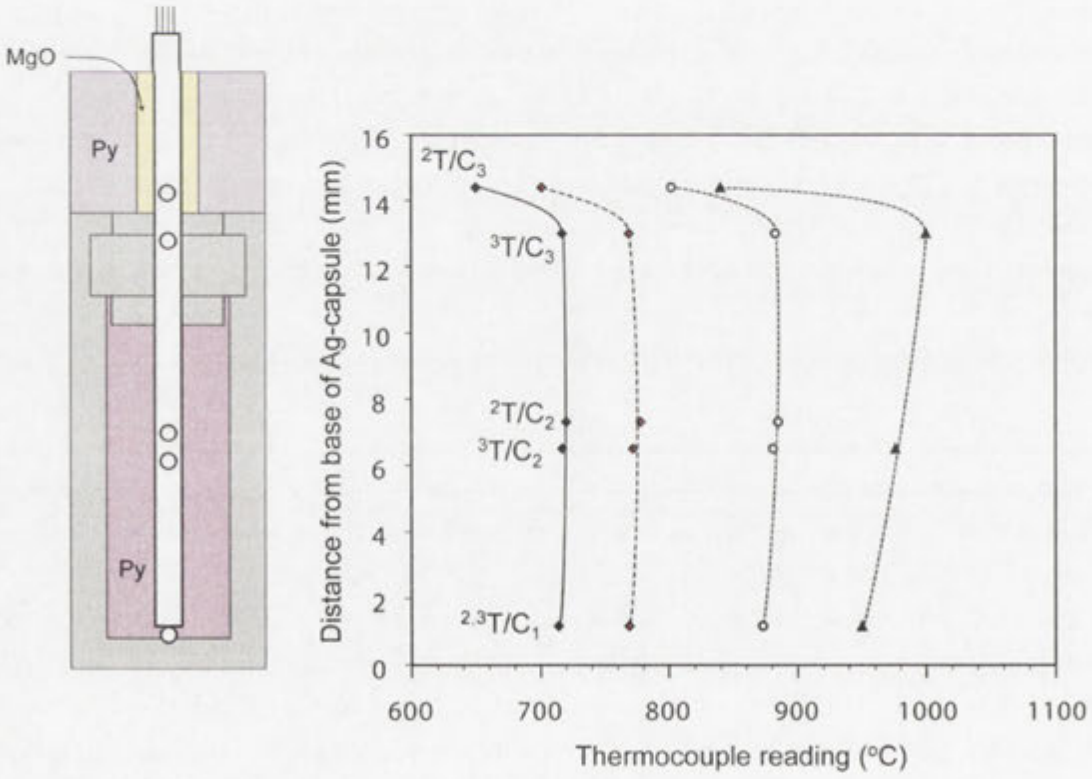

***Figure 11.14**: Temperature gradient measured from two experiments in the Ø 6 mm Ag capsule at different temperatures. Thermocouple positions indicated by circles. All measurements are made at 35 kbar.*

Experiments run at 700-800 °C show small thermal variation within the capsule, with maximum temperature difference being 0.8-1.5% or 6-9 °C (see Table 11.1). Profiles shown in Figure 11.14 demonstrate that experiments run at <800 °C have a hotspot located around the centre of the capsule. The observed thermal gradient within the capsules held at temperatures >800 °C is significantly larger than in low temperature runs. The maximum temperature difference for $^{2,3}T_1$ = 873 °C (see Table 11.1) is 1.4% or 12 °C, and for $^{2,3}T_1$ = 950 °C the difference is 5.1% or 50 °C.

Increasing thermal gradient with temperature is also accompanied by hotspot position drifting towards the top of the capsule (see Figure 11.14). Off-centre hotspots have been reported within the literature (Pickering et al., 1998) and have been attributed to different thermal conductivities of the steel top plug and tungsten carbide piston (see Table 11.2) as well as deformation in the cell during experiments. The thermal models and experiments of Pickering et al. (1998) indicate that the longer the cell assembly, particularly the graphite furnace, the further the hotspot is displaced upward from the tungsten carbide piston. Such phenomena could be used to explain why high temperature runs show hotspot shift to higher positions in the capsule. Another likely influence on hotspot position and capsule thermal gradient is related to capsule deformation during experiments. Runs at 35 kbar show increasing capsule deformation at temperatures >900 °C, with the top of the capsule bulging about the lid. This bulging is likely related to the silver capsule becoming more ductile as it approaches the silver melting temperature. Such bulging does not appear to disrupt the effectiveness of the graphite furnace or promote contact between capsule and furnace, but does cause variations from the ideal capsule-insulator-furnace geometry. These observations indicate that all capsules should be visually inspected post-run (to assess the potential influence capsule deformation may have on temperature estimates) and that silver capsules should not be run at temperatures within ~200 °C of the silver melting curve.

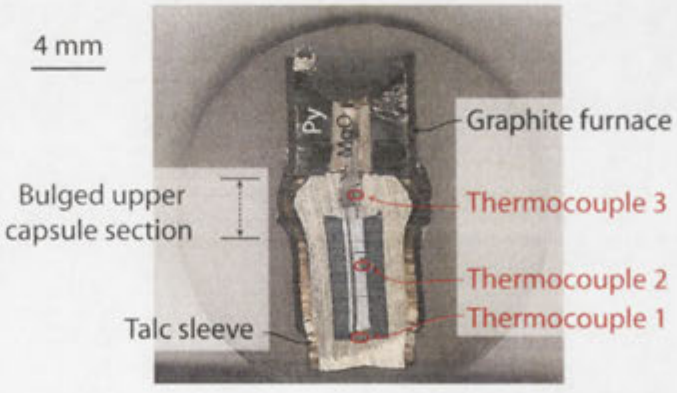

***Figure 11.15**: Deformed capsule from experiment D-1079 that was held at a maximum pressure and temperature of 35 kbar and 1,000 °C. Scale as indicated.*

Results from thermal gradient tests can be used to apply temperature uncertainties to experiments carried out using the same cell assembly, but it must be noted that these tests represent the most extreme case. The semi-fired pyrophyllite lining used to hold the 4-bore thermocouple rod within the silver capsule is a very effective thermal insulator (see Table 11.2). This means that thermocouples at the base and top of the capsule (in close proximity

to silver) are less influenced by thermal insulation. Thus such an assembly is likely to result in a greater thermal gradient than would be expected in a conventional experiment. The drilled out capsule lid also provides a means for heat to escape from the capsule because the top of the capsule has an incomplete silver seal. Hence, the thermal gradient experiments should be considered an upper limit to thermal gradients within the described cell assembly. The presence of free H_2O (which can circulate and convect heat) and the presence of a Pt sensor capsule (thermal conductor) means that temperature uncertainty in the experimental charge is likely lower than that determined in thermal gradient tests.

Chapter 12

Analytical Techniques

The various analytical techniques used in this research involved a significant number of analyses (>1,000 individual measurements or >2,000 hours) in order to determine major element composition of experimental run products (including mineral species, metal alloys and various forms of glass/fluid quench). The techniques employed include Scanning Electron Microscopy (SEM-EDS), electron probe microanalysis (EPMA-WDS), Laser Ablation-Inductively Coupled Plasma-mass spectrometry (LA-ICP-MS), x-ray diffraction analyses (XRD) and optical microscopy. The analytical methods discussed in this chapter are intended to present the reader with information on how results were obtained, while limiting details about efforts made to monitor statistical variations and precision associated with all experiments.

12.1: Scanning Electron Microscopy (EDS)

Phase identification and experimental petrography were determined by scanning electron microscopy (SEM). Quantitative major element analysis of experimental run products was obtained by energy dispersive x-ray spectroscopy (EDS) on a JEOL JSM6400, a Hitachi 4300 SE/N (Schottky Field Emission SEM) and a Zeiss UltraPlus analytical Field Emission SEM. All instruments are housed at the Research School of Biological Sciences, ANU. The JEOL instrument was primarily used for analyses of phases of sufficient size for conventional SEM operating conditions, while FESEM instruments were primarily used to image and analyze individual experimental phases that require higher spatial resolution and lower beam current (to limit excitation induced by the incident electron beam).

Beam conditions for JEOL analyses were set at an accelerating voltage of 15 kV and a beam current of 1 nA. Mineral analyses incorporated a focused beam, with spectra collected over a 120 second counting period and beam current checked after every 5 "unknown" analyses. Glass spectra[1], which involved quantification of an alkali-bearing and potentially volatile sample medium, were collected with a scanning beam (ranging from 10x10 to 200x200 μm in size). The majority of broad beam glass analyses from experiments also involved incremental analyses obtained at different spatial resolutions to assess potential volatile loss and the influence of spectral signal from the epoxy resin. Spectrum acquisition times for glass analyses were monitored at 20 second intervals over a 120 second counting period. Time series analyses (see Figure 12.1) show that alkali (K_2O or Na_2O) loss never exceeded 6 % in ≥10x10 μm scanning beam between 60 and 120 second counting periods (with larger beam sizes showing lower variation). Time series analyses also demonstrated that a minimum counting time of 60 seconds was required for sufficient spectral resolution (counting statistics) for cations at the 0.1-1.0 wt% oxide concentrations.

[1] The only glass analyses not carried out at this resolution were from experiments C-3155 and C-3119, which showed very thin glass pools (with vapour bubbles) located along grain boundaries making broad beam analyses impossible.

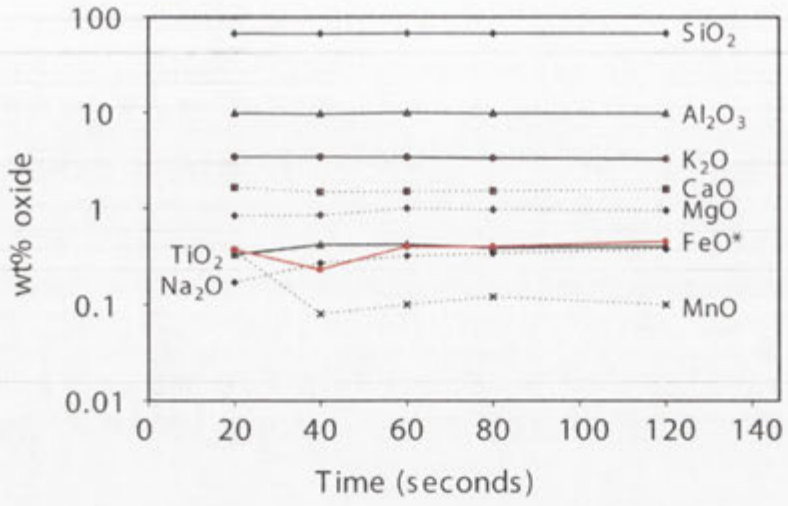

***Figure 12.1**: Representative time series analysis from experiment C-3130 at 10x10 µm defocused beam (analyses are shown in Table 12.1). Analytical totals are low (83.51-84.47) because the glass is vesicular (see Results) and must also contain significant amounts of H_2O.*

Glass analyses from low degree partial melting experiments (i.e., low H_2O-content experiments) proved the most difficult to analyse, as these experiments required very small beam size (with a "semi-scanned" incident beam set at 2x2-5x5 µm over glass pools away from co-existing phases). In low degree melt experiments (e.g., experiments C-3119 and C-3155) glass analyses where monitored with the closest mineral species about the incident electron beam for potential spectra and for anomalous compositions (i.e., where elemental ratios show influence by rutile – Ti, garnet – Fe, Al and Mg, phengite – K and Al, coesite – Si, etc). Any analysis containing unrealistic or anomalous totals (i.e., higher totals or individually higher cation concentrations relative to the general analytical population) were discarded.

Table 12.1: Time series analyses from EDS raster beam analyses from experiment D-1017

Time (sec)	20	40	60	80	120
Na_2O	0.17	0.27	0.32	0.34	0.38
MgO	0.84	0.85	1	0.97	0.95
Al_2O_3	9.86	9.73	9.96	9.83	9.83
SiO_2	67.01	66.98	67.34	67.37	67.21
K_2O	3.46	3.46	3.43	3.36	3.28
CaO	1.65	1.49	1.5	1.52	1.58
TiO_2	0.33	0.42	0.42	0.39	0.4
MnO	0.36	0.08	0.1	0.12	0.1
FeO*	0.37	0.23	0.4	0.4	0.45
Total	84.05	83.51	84.47	84.3	84.18

All EDS standards used in this research where ANU Electron Microscopy Unit in-house standards that are well documented, calibrated and regularly used. These standards include albite (Na and Al), MgO (Mg), sanidine (K and Si), rutile (Ti), hematite (Fe), diopside (Ca), Cr_2O_3 (Cr) and pure Mn (Mn). All spectra were processed with LINK ISIS-SEMIQUANT, employing full ZAF (2 or 3 iterations).

12.2: Electron Probe Microanalysis (EPMA-WDS)

All sensor capsule analyses were carried out using electron microprobe analytical techniques (EPMA) on a Cameca SX100 instrument in the wavelength dispersive (WDS) mode. All spectra were collected using a beam current of 40 nA, an accelerating voltage of 15 KeV, and a ~1x1 μm focused beam. Si counts were collected on a TAP spectrometer and calibrated against quartz or olivine. Ni, Pt and Re were all collected on a LLIF spectrometer calibrated against respective metal standards. Zr counts were collected on a LPET spectrometer and calibrated against a synthetic zirconia standard. Pd counts were collected on a PET spectrometer and calibrated against a Pd metal standard.

The Ni and Pd concentrations of alloys synthesized in this research are all at the wt%-scale and several orders of magnitude above the WDS detection limit. Care was taken to avoid problems from stray electrons by ensuring that the incident beam was focused away from the zirconia sleeve.

Ni K-α and Pd L-α x-ray maps were recorded for experiments showing the greatest compositional variation in this study. Analytical polygons were designed to incorporate a section over the entire alloy, zirconia sleeve and capsule wall about the centre of the capsule. Column conditions for such maps were set at 15 KeV and 200 nA, with each analysis (pixel) incorporating a 0.5 second dwell time and separated by a 2 μm step.

12.3: X-ray diffraction (XRD)

X-ray diffraction analyses were carried out on a Siemens D501 Diffractometer, using Bragg-Brentano geometry and a Cu radiation source. The use of XRD was not employed for all experiments, but focused on determining mineralogy within high H_2O-content experiments (where EDS analyses are insufficient) and the presence of Re-ReO_2 where the buffer could not be confirmed by SEM techniques.

Data analysis was carried out in DiffracPlusEva 10.0, with peak search/match performed against the International Centre for Diffraction Data (ICDD) powder diffraction file (PDF-2) database.

12.4: Laser ablation inductively coupled mass spectrometry (LA-ICP-MS)

LA-ICP-MS analyses were carried out using an Agilent 7500S (RF power = 1300 W; ablation cell gas flow = 0.3 l/m He+ 0.02 l/m H_2; auxiliary gas flow = 1.0 l/m Ar; laser energy = 50-55 mJ), coupled to an ANU HelEX laser ablation system, which employs a 193 nm wavelength EXCIMER laser (110 (ArF) COMPex, Lambda Physik). Data acquisition was performed with 20 seconds of background measurement, followed by 40 seconds of sample ablation. To minimise the potential for oxide production, the LA-ICP-MS was calibrated to low oxide production rates (ThO^+/Th^+ typically <0.4%). All samples and standards were analysed in batches of ~10 with NIST SRM 612 (used for external calibration) analysed at the beginning and end of each batch to allow corrections to be made for instrument drift. CaO was used for internal calibration of data. Reference material BCR-2G was analysed with each

batch of samples to monitor data quality (i.e., precision and accuracy). Analyses used an 80 µm diameter laser spot, a repetition rate of 5 Hz and an analytical routine incorporating 42 masses (elements). Data reduction was performed using an 'in-house' data reduction program, following the method described in Longerich et al. (1996).

LA-ICP-MS analysis was only used to analyze glasses as this was the only quench species of sufficient size for analysis. LA-ICP-MS results from experiments C-3127, C-3130, C-3150, C-3157, D-1010 and D-1022 are reported in Appendix 3. These represent the experiments containing glass pool of sufficient size for ablation. Replicate analyses (n=18) of BCR-2G were typically within 5% of preferred values on the GEOREM website (Jochum et al., 2005) and show ≤5% RSD, demonstrating high levels of accuracy and precision.

Chapter 13

Experimental Technique

Pelite-H_2O experiments in this study involved a number of components that all contribute to each individual experiment. As described in the previous chapter, the experimental technique employs a capsule in capsule arrangement in order to impose an oxygen fugacity and passively monitor hydrogen fugacity. The earlier sections of this chapter focus on construction of the H-sensor capsule, with later sections discussing the outer capsule and pelite starting material.

13.1: The inner H-sensor capsule

The H-sensor capsule consists of an Ø 2.3 mm Pt capsule constructed from Pt tubing that is cleaned, crimped and welded shut at both ends. A zirconia sleeve (see Figure 13.1), sealed at both ends with pressed zirconia powder, lines the inner wall of the Pt capsule and acts as a fluid permeable membrane separating Pt-capsule and H-sensor material (preventing alloying between sensor alloys and the capsule wall). The zirconia tubing contains a Ni-NiO-Pd powder mixture that is gently tamped into the centre of the sleeve with a drill bit and sealed at both ends with zirconia powder. A few drops of de-ionized H_2O were added to the final 'Pt-zirconia-Ni-NiO-Pd' mixture with a microlitre syringe to ensure H-diffusion between outer and inner capsules. The final mixture is weighed prior to and post-weld to ensure that the small amount of H_2O added to the capsule is not lost during the final capsule weld.

A number of Ni-NiO-Pd mixes were used during experiments, including Ni-Pd mixes ranging from 5-35 wt % Pd. Starting mixes were made from high purity reagents of Ni (Goodfellow – 99.6+ % purity), Pd (Goodfellow – 99.99 % purity) and NiO (synthesized from Ni metal in a gas mixing furnace) ground under acetone in an agate mortar and stored for use in a desiccator. The amount of NiO added to the starting mix was, by weight, 4-8 times higher than the sum of metal components (Ni and Pd).

Initial test experiments of the sensor capsule were carried out with layers of varying Ni:Pd separated by thin layers of packed zirconia powder. This type of experiment was designed to bracket or 'pseudo-reverse' experiments by approaching the equilibrium alloy composition from Ni- and Pd-rich end-members. This layered approach ultimately proved unsuccessful as deformation during experiments generally resulted in separated layers breaking through the zirconia powder and forming a single Ni-NiO-Pd alloy. For this reason, sensor capsules were run with a single Ni-NiO-Pd mix.

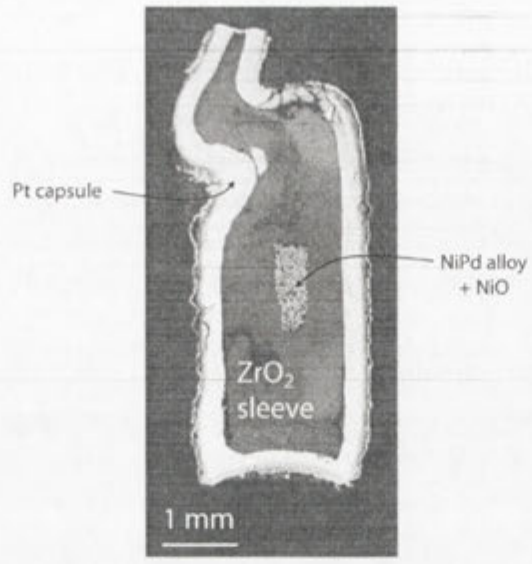

***Figure 13.1**: H-sensor from layered Ni-Pd test experiment. Note that the final assembly (after 5 days at 35 kbar/800 °C) consists of a single alloy-NiO assembly located within the centre of the capsule.*

After each experiment, sensor capsules were separated from the opened Ø 6.0 mm Ag capsules and mounted in EPO-FIX resin. The sample mount was carefully ground down until the thin outer wall of the Pt capsule was completely exposed, and was subsequently pierced with a fine WC tipped engraving tool to ensure that the capsule still contained H_2O (confirmed by bubbling from the hole). The pierced capsule was sliced open with a stainless steel scalpel and the Pt tubing folded out to expose the inner zirconia tubing. The opened capsule then underwent a series of successive epoxy impregnation-polishing sequences (between 3 and 6 re-impregnations) in order to limit plucking from the highly friable zirconia sleeve during polishing.

Once the centre of the sensor capsule was exposed, optical microscopy was used to confirm the presence of NiO (bright green), Ni-Pd alloys (metallic lustre) and possible contaminants/leaks (Ni-olivine and zircon are commonly produced in leaked capsules). The polished sample was then C-coated and studied by both SEM (for petrography) and EPMA (for phase analysis).

13.2: Ag-capsule and starting material

All thick-walled outer Ø 6 mm Ag capsules (with design tests described in the previous chapter) were cleaned and inspected prior to experiments. The first component added to the Ag capsule was 11-50 mg of Re-ReO_2 powder pressed in the bottom of the capsule with a Ø 3.9 mm stainless steel tool. Re-ReO_2 mixes were made from reagent grade powders of Re (Goodfellow – 99.99 % purity) and ReO_2 (Aldrich – 99.9 % purity) ground together under acetone in an agate mortar and checked by XRD for possible contamination. Re-ReO_2 mixes for experiments are shown in Table 13.1 and demonstrate that experiments typically contained more ReO_2 than Re metal.

Table 13.1: Re-ReO_2 starting composition for experiments

Run #	ReO_2 (mg)	Re^0 (mg)	Total Re-ReO_2 (mg)
C-3119	22.2	26.1	48.3
C-3121	13.9	16.2	30.1
C-3127	13.2	15.5	28.7
C-3128	12.9	15.2	28.1
C-3130	12.9	15.2	28.1
C-3150	6.6	5.2	11.8
D-1010	6.4	8.2	14.6
C-3155	5.0	6.3	11.3
D-1011	8.5	3.6	12.1
C-3157	8.4	3.6	12.0
C-3274	24.3	3.8	28.1
C-3275	23.8	3.7	27.5
D-1066	24.1	3.7	27.8
D-1069	24.0	3.7	27.7
D-1016	8.6	3.7	12.3
D-1017	9.0	3.8	12.8
D-1022	10.6	12.4	23.0
D-1025	13.4	5.8	19.2
D-1071	25.5	3.9	29.4

The H-sensor capsule was then placed into the Ag capsule in order to ensure that the sensor was not damaged during swaging.

The final two components added to the Ag capsule were pelite powder and deionized H_2O (added by microlitre microsyringe). The pelite starting material is particularly important to the success and applicability of experiments to natural systems and merits detailed discussion here and in Appendix 1.

Pelite starting material

Pelite starting material used in this work (pelite 1008) is a natural sample collected by Carl Spandler from the southern Pam Peninsula, in the New Caledonian ophiolite sequence (Figure 13.2). This sample was described by Spandler et al. (2003) as strongly foliated, coarse-grained and dominated by quartz (46.5 modal %) and phengite (37 modal %). Other phases in the sample include idoblastic garnet (6 modal %) and hornblende (8.5 modal %), while accessory phases include apatite, rutile, zircon and epidote. Detailed phase equilibria studies of the pelite (including garnet-clinopyroxene, garnet-phengite and garnet-amphibole thermometry) demonstrate the lithology equilibrated at a maximum metamorphic condition of 16-19 kbar/550-620 °C (Carson et al., 1999; Spandler, 2003).

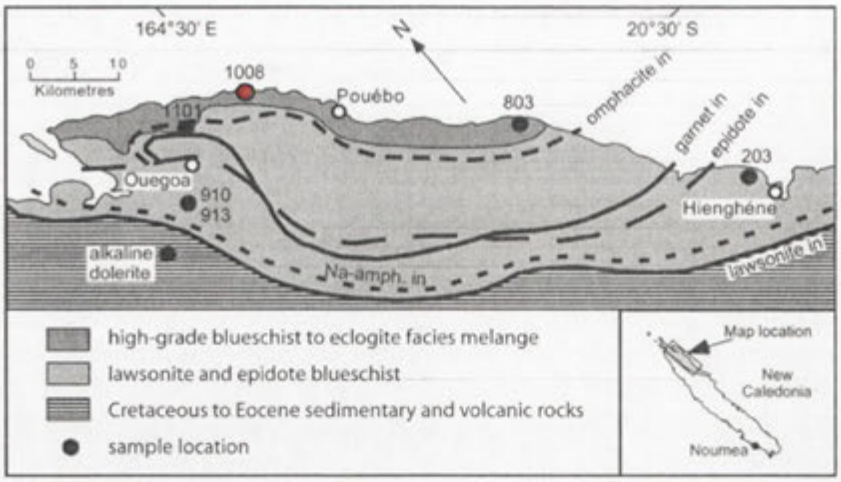

***Figure 13.2**: Simplified geological map of the Pam Peninsula, New Caledonia. Pelite 1008 sample locality shown in red (image modified after Spandler et al., 2003).*

Pelite sample 1008 was chosen as a starting material because the texture, mineralogy and bulk chemistry of this lithology is well known (Spandler et al., 2003), and it has a major and trace element composition remarkably similar to the global subducting sediment (GLOSS – see Table 13.1 and Figures 13.3 and 13.4) estimates of Plank and Langmuir (1998), making experimental studies/results directly applicable to pelitic sediments within the subduction zone environment.

Five grams of milled pelite 1008 powder were prepared for experimental runs by melting (homogenizing) the powder in a box furnace at 1,400 °C for successive 90 minute intervals (Figure 13.3). Samples were held in a shallow Pt-crucible, rapid quenched in H_2O and small glass chips separated after every 90 minute melting period for epoxy mounts and x-ray diffraction (XRD) analyses. After three homogenization runs in the box furnace (i.e., 270 hours at 1,400 °C), XRD analyses and SEM observations showed the starting material contained glass and <8 modal % SiO_2 (tridymite).

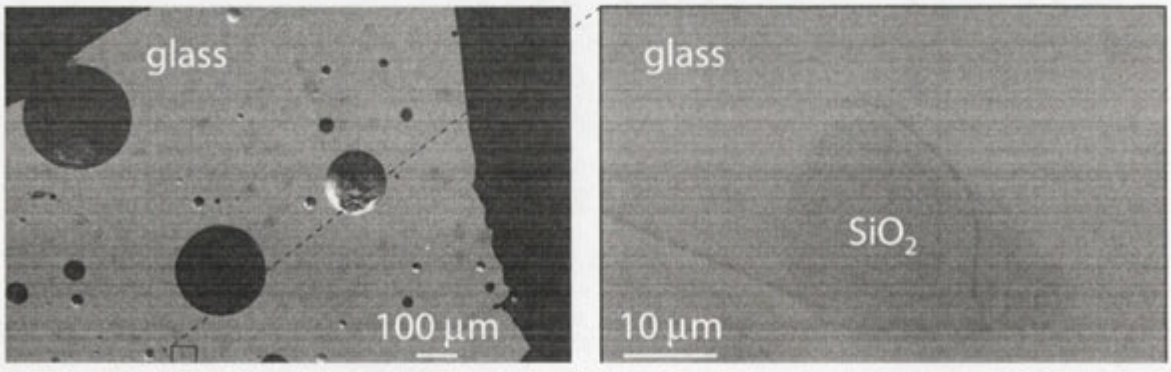

***Figure 13.3**: Representative BSE images of pelite 1008-1 glass chips after 90 hours at 1,400 °C in the box furnace.*

The final pelite homogenization run (1008-4) incorporated the minor addition of Na_2O and CaO in order to bring experimental starting compositions closer to GLOSS estimates (Table 13.2 and Figure 13.4). The final pelite 1008-4 mix was fused at 1,500 °C in a gas mixing

furnace for 90 minutes at 95% CO_2:5% CO in order to fix sample f_{O_2} at conditions near the Ni-NiO buffer. Major and minor element analytical details and variations for pelite 1008-4 are provided in Appendix 1.

The final homogenization run resulted in more dissolution of SiO_2, with petrography (and XRD) indicating that trydimite represents ≤3 modal % of pelite 1008-4.

Table 13.2: Major element concentration of GLOSS and pelite 1008

	GLOSS (P & L)	an-GLOSS (P & L)	1008 (SHAM)	1008-4	(σ)
SiO_2	58.57	65.31	71.75	69.44	(0.56)
TiO_2	0.62	0.69	0.54	0.57	(0.09)
Al_2O_3	11.91	13.28	12.59	12.66	(0.35)
FeO*	5.21	5.81	4.13	3.63	(0.21)
MnO	0.32	0.36	0.11	0.14	(0.02)
MgO	2.48	2.77	2.31	1.66	(0.25)
CaO	5.95	6.63	1.75	3.20	(0.21)
Na_2O	2.43	2.71	0.61	2.74	(0.07)
K_2O	2.04	2.27	3.87	4.01	(0.12)
P_2O_5	0.19	0.21	0.13	0.17	(0.03)
CO_2	3.01	-	-	-	-
H_2O	7.29	-	-	-	-

GLOSS = global subducting sediment, P & L = Plank and Langmuir (1997), an-GLOSS = global subducting sediment recalculated to volatile-free, 1008 = XRF fused disc bulk rock analyses, SHAM = Spandler et al. (2003), 1008-4 = pelite starting material with standard deviation reported from 9 SEM-EDS analyses.

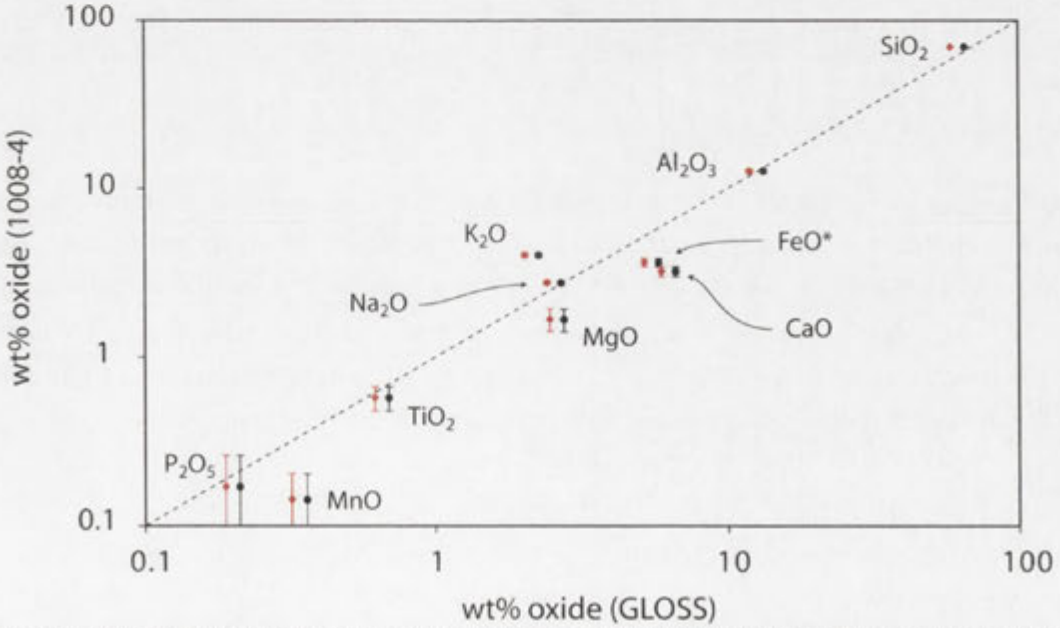

***Figure 13.4**: Major element comparison of pelite 1008-4 and GLOSS (Plank and Langmuir, 1998). Black datum points represent bulk composition of pelite 1008-4 as determined by broad-beam EDS analyses and red points indicate composition with the addition of 6 wt% SiO_2. Error bars represent 2σ from multiple glass analyses.*

A number of minor and trace elements show small deviations between pelite 1008-4 and GLOSS, most notably - Ca, Ba, Sr, Cr and Co. As demonstrated by the notable compositional variation among natural sediments used to estimate GLOSS (which include variation in the amount of terrigenous and carbonate material, the biological component, the presence of Mn-nodules, etc), variation between pelite 1008-4 and GLOSS is not unexpected. The most important point regarding the composition of pelite 1008-4 is that it is a natural rock highly analogous to sedimentary components entering the subduction environment and has a composition (in terms of major, minor and most trace elements) that is similar to and broadly applicable to natural systems.

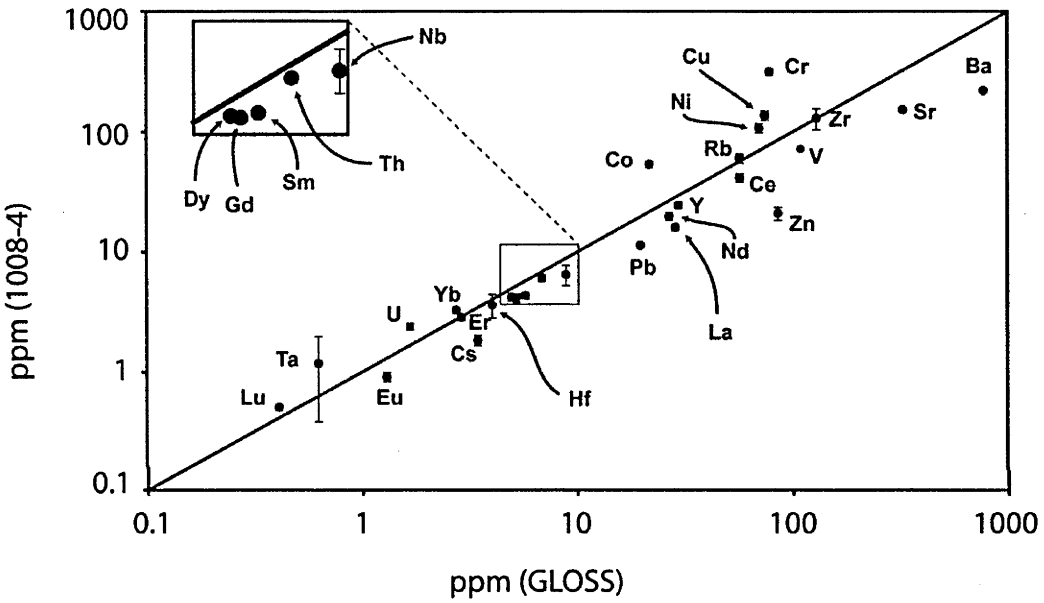

***Figure 13.5**: Minor and trace element comparison of pelite 1008-4 and GLOSS (Plank and Langmuir (1998) without the addition of 6 wt% SiO_2 (the data shift in trace element compositions is so minor that it is almost negligible at the scale of the figure). Error bars are shown as σ from multiple LA-ICP-MS glass analyses (see Appendix 1).*

Comparison of the pelite 1008-4 starting composition and other pelite mixtures reported within the literature (natural and synthetic) are shown in Figure 13. 6. As can be seen, with the possible exception of Johnson and Plank (1999), all starting compositions fall in a very restricted compositional space. Thus, experiments presented here can be directly compared to other forms of experimental research in the pelite-H_2O system and can also be used to hypothesize about processes that occur within subduction zone environments.

Table 13.3: Minor and trace element concentrations of GLOSS and pelite 1008

	GLOSS (P & L)	an-GLOSS (P & L)	1008 (SHAM)	1008-4	(σ)
Sc	13.1	14.6	13.7	N/A	N/A
V	110	122.7	83.6	72.4	(1.7)
Cr	78.9	88	19	315.4	(19)
Co	21.9	24.4	12.1	54.0	(3.2)
Ni	70.5	78.6	26.5	107.7	(9.5)
Cu	75	83.6	6	136.6	(12.2)
Zn	86.4	96.3	15	21.1	(2.6)
Rb	57.2	63.8	55.0	60.3	(5.3)
Cs	3.48	3.88	1.60	1.84	(0.18)
Sr	327	364	159.1	152.8	(4.9)
Ba	776	865	240.0	221.3	(3.7)
Y	29.8	33.2	31.7	24.7	(1.5)
Zr	130	145	182.1	130.2	(26.0)
Hf	4.06	4.53	4.75	3.63	(0.81)
Nb	8.94	9.97	7.20	6.51	(1.26)
Ta	0.63	0.7	0.47	1.18	(0.80)
La	28.8	32.1	18.5	16.2	(1.0)
Ce	57.3	63.9	42.2	41.6	(3.3)
Nd	27	30.1	21.6	19.8	(1.4)
Sm	5.78	6.45	5.03	4.35	(0.28)
Eu	1.31	1.46	1.03	0.91	(0.08)
Gd	5.26	5.87	4.76	4.15	(0.33)
Dy	4.99	5.56	5.03	4.24	(0.31)
Er	2.92	3.26	3.28	2.87	(0.17)
Yb	2.76	3.08	3.79	3.28	(0.21)
Lu	0.41	0.46	0.61	0.51	(0.03)
Pb	19.9	22.2	9.34	11.4	(0.3)
Th	6.91	7.71	6.72	6.09	(0.38)
U	1.68	1.87	2.37	2.39	(0.15)

P & L = Plank and Langmuir (1998), GLOSS = volatile-bearing estimate, an-GLOSS = recalculated to volatile-free estimate, SHAM = bulk XRF analyses reported by Spandler et al. (2003) and pelite 1008-4 analyses are detailed in Appendix 1.

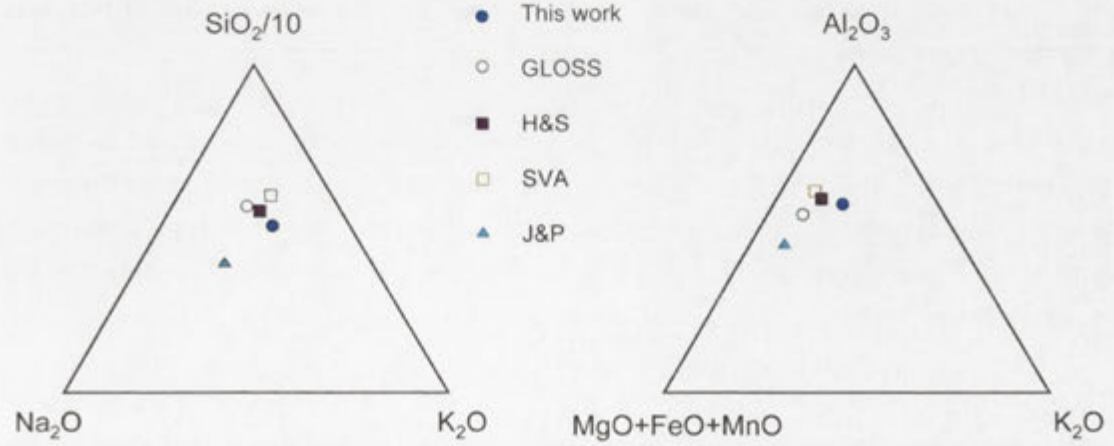

***Figure 13.6**: Ternary projection of pelite 1008-4 experimental starting material compared to GLOSS (Plank and Langmuir, 1998), H&S = Hermann and Spandler (2008), SVA = Schmidt et al. (2004), J&P = Johnson and Plank (1999).*

13.3: The final assembly and starting mixtures

The various components added to the Ø 6.0 mm Ag capsule are shown in the general schematic in Figure 13.7. It is worth noting that the pelite powder is not pressed in the capsule (so as not to damage the H-sensor capsule) and acts as a porous medium that the H_2O percolates through when added by microsyringe (such that there is no pool of water as indicated in Figure 13.7).

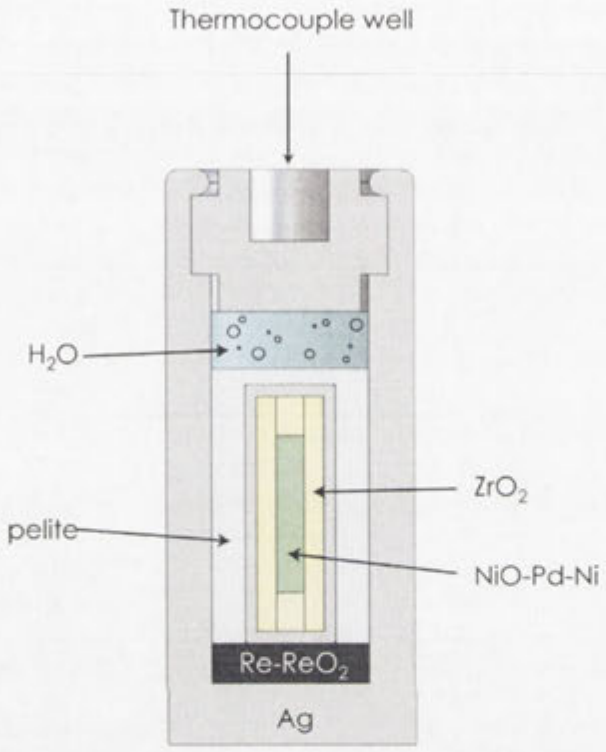

***Figure 13.7**: General schematic of the final Ø 6.0 mm Ag capsule after swaging.*

The starting compositions of 19 experiments are shown in Table 13.4. As indicated, all experiments were carried out with the addition of minor amounts of SiO_2 (ranging from 3.54-7.36 wt% and at a near constant pelite:SiO_2) in an effort to use coesite as a potential fluid inclusion host. Unfortunately, coesite was among the earliest phases to dissolve within the melt, but in order to keep experiments internally consistent the same amount of SiO_2 was added to all experiments.

Once experimental components were added to the Ag capsule, attention was paid to ensure that no starting material was present along the lid-step atop the capsule or along the initial 0.8 mm of the capsule wall where the Ag lid resides. The final step in capsule preparation was to swage-seal the capsule by applying 3,000 P.S.I. to the swaging tool described in the previous chapter.

All piston-cylinder experiments used the piston-in method and a temperature ramp-rate of 50 °C/minute. Pressure was applied synchronously with temperature such that experiments ramped to pressure and temperature along a single isochore (with H_2O-density calculated from EOS estimates of Brodholt and Wood, 1993). The pressure range of experiments (25-

35 kbar – see Table 13.4) often required the addition of 2-7 kbar prior to the application of current to the graphite furnace. The "cold" application of Boyd pressure at the start of experiments has the added advantage of applying load to the capsule, essentially reinforcing the swaged seal and likely contributes to the success of the technique.

Figure 13.8 shows the P-T-*X* conditions of all experiments relative to the preferred pelite wet solidus (see Chapter 10). As shown in Figure 13.8, experiments were designed to correspond to P-T conditions situated near the hypothesized backbend in the wet solidus while also incorporating H_2O-contents that range from rock-dominated to fluid-dominated compositions.

Table 13.4: Experimental pelite-H_2O starting mixes (by weight) and run conditions

Run #	Pressure (kbar)	Temperature (°C)	pelite (mg)	pelite (wt%)	SiO_2 (mg)	SiO_2 (wt%)	Total (pelite+SiO_2 in wt%)	H_2O (mg)	H_2O (wt%)
C-3119	35	900	56.0	85.68	3.4	5.14	90.82	6.0	9.18
C-3121	35	900	98.3	71.36	8.5	6.20	77.56	30.9	22.44
C-3127	35	900	49.2	43.95	7.2	6.43	50.37	55.6	49.63
C-3128	35	700	36.7	43.41	3.3	3.93	47.34	44.5	52.66
C-3130	35	800	66.8	71.44	5.1	5.45	76.90	21.6	23.10
C-3150	35	900	75.8	59.95	6.0	4.77	64.72	44.6	35.28
D-1010	25	900	81.0	64.37	9.3	7.36	71.72	35.6	28.28
C-3155	35	800	87.2	83.60	6.9	6.62	90.22	10.2	9.78
D-1011	25	900	86.9	83.33	7.0	6.70	90.03	10.4	9.97
C-3157	35	900	87.2	71.94	7.0	5.78	77.72	27.0	22.28
C-3274	35	750	72.8	71.93	5.2	5.14	77.08	23.2	22.92
C-3275	35	750	71.9	87.97	5.1	6.28	94.25	4.7	5.75
D-1066	35	750	51.0	47.72	3.8	3.54	51.26	52.1	48.74
D-1069	35	750	64.5	81.05	4.8	6.01	87.06	10.3	12.94
D-1016	25	900	66.4	53.17	5.3	4.23	57.41	53.2	42.59
D-1017	25	900	65.4	60.87	5.3	4.96	65.83	36.7	34.17
D-1022	25	900	39.2	45.43	3.4	3.88	49.31	13.8	50.69
D-1025	25	900	71.4	88.15	5.2	6.42	94.57	4.4	5.43
D-1071	35	800	67.1	88.17	5.0	6.57	94.74	4.0	5.26

Note: all experiments were run for between 168-216 hours.

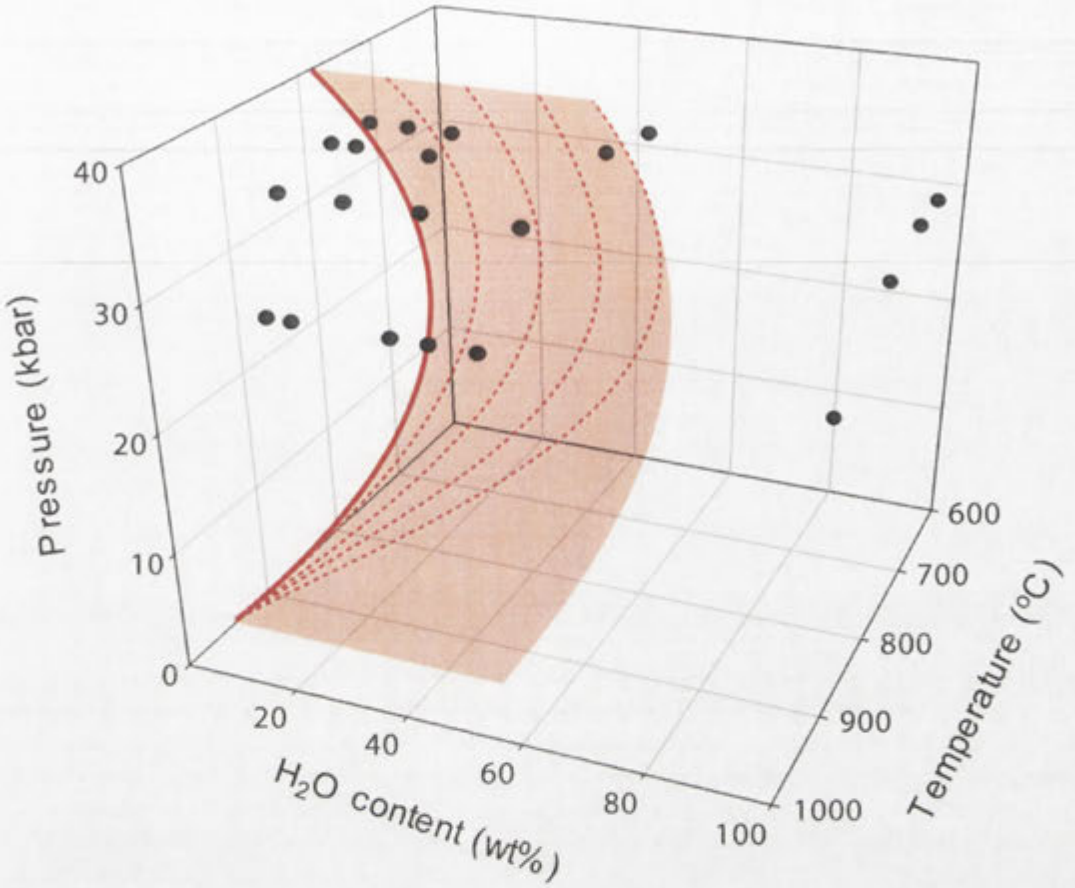

***Figure 13.8**: P-T-X locus (relative to H_2O-content) of individual pelite experiments (represented by black circles). Solid red line represents the model pelite wet solidus (see Figures 10.11 and 10.12) as would be projected in P-T space. Dashed lines are purely schematic and presented in order to demonstrate that the position of the univarient melting curve is largely unconstrained in compositional space, but must fall somewhere along the lightly-shaded red surface. It should also be noted that experimental conditions all plot at P-T conditions situated about back-bending observed in the wet solidus.*

13.4: Summary

The experimental technique designed in this research involves a large-volume and thick-walled Ag capsule that can be run in a ½" pressure vessel. As described in Chapter 11, the thick wall of the capsule limits H-diffusion into (or out of) the experiment, while capsule swaging allows experiments to be carried out at very high H_2O contents (>50 wt%). A small Pt capsule is placed within the Ag capsule and functions as an inert sliding H-sensor during pelite-H_2O experiments.

The silicate starting material consists of a homogeneous glass obtained from a natural New Caledonian pelite (1008-4). This glass was fused at an oxygen fugacity ~Ni-NiO in a 1 atmosphere furnace and then milled to a fine powder for experimentation.

Components of the ½" cell assembly include a thick NaCl pressure medium, semi-fired pyrophyllite spacers and a thin talc insulator.

Chapter 14

Results

In order to produce results from pelite-H_2O experiments, a number of analytical and petrographic techniques are required to describe mineral paragenesis and report mineral/melt/alloy compositions. Initial sections of this chapter focus on petrography seen in quenched pelite-H_2O experiments. No textural interpretation is used to distinguish primary and secondary quench products, with reported results simply describing and presenting observed run products. Later sections of this chapter detail the composition of run products, including glass and phase analyses. Final sections of this chapter focus on Ni and Pd analyses and statistical variations seen in alloys from sliding H-sensor capsules.

14.1: General summary of experimental run products

Experimental run products and phase relations examined by optical and electron microscopy (FE-SEM/SEM) are summarized in Table 14.1 and shown graphically in Figure 14.1 (for 35 kbar runs). Experiments show an extremely diverse range of quench textures and mineralogy depending on the starting P-T-*X* conditions. Starting H_2O content and amount of glass present in experiments appears to have the greatest influence on quench texture, with experiments containing >30 wt% H_2O producing increasingly porous assembly and displaying a diverse range of vapour bubbles, vapour bubble-hosted phases (amorphous and crystalline) and glass. Representative photomicrographs from individual experiments are shown in Figures 14.2-14.6 and discussed in detail below.

Major and minor phase summary

The dominant mineral phases seen in experiments are consistent across 25 and 35 kbar experiments, consisting of variable mixtures of phengite, SiO_2 (quartz/coesite), garnet, rutile, melt and vapour bubbles. The only notable mineralogical difference between 25 and 35 kbar experimental populations, excluding phase stability limits, is the presence of kyanite in experiments with low starting H_2O contents at 25 kbar.

Considerable effort was made to identify accessory phases in experiments (e.g., zircon, monazite, allanite, apatite, etc), yet very few are seen. Experiments C-3119 and D-1071 are the only runs to definitively show the presence of zircon ± apatite, with all other experiments containing phases too small for phase identification (noting that experiments without glass show the presence of rare P-rich and Zr-rich phases that are too small for phase identification) or a complete lack of element signatures to constrain the existence of accessory phases within run products. It is possible that accessory phases are present in experiments, but are so rare that they cannot be identified by spectroscopic or diffraction analyses.

Table 14.1: Experimental run products

Run #	Pressure (kbar)	Temperature (°C)	H_2O (wt%)	Run products
C-3119	35	900	9.18	Coes, Phen, Glass, V, Grnt, Ap, Rt, Zirc
C-3157	35	900	22.28	Glass, V, Coes, Grnt, Ky, Rt
C-3121	35	900	22.44	Glass, V, Ky, Rt + NaCl + $AgCl_2$
C-3150	35	900	35.28	Glass, V, Grnt, Rt, Ky[1], Mica[2]
C-3127	35	900	49.63	Glass, V, Grnt, Mica[2], Rt
	35	900	100.00*	V
D-1071	35	800	5.26	Phen, Coes, Grnt, Glass, Rt, V, Zirc, Ca-phase[3]
C-3155	35	800	9.78	Phen, Coes, Grnt, Glass, V, Rt
C-3130	35	800	23.10	Melt, V, Grnt, Rt
	35	800	100.00*	V
C-3275	35	750	5.75	Coes, Phen, Grnt, V, Rt
D-1069	35	750	12.94	Coes, Phen, Grnt, V, Rt
C-3274	35	750	22.92	Coes, Phen, V, Grnt, Rt
D-1066	35	750	48.74	V, Phen, Coes, Grnt, Rt
	35	700	100.00	V
C-3128	35	700	52.66	Coes, Phen, V, Grnt, Rt
C-2576*	32	800	49.51	Glass, V, Grnt, Rt, Mica[2]
D-1010	25	900	28.28	Glass, V, Rt, Mica[2]
D-1011	25	900	9.97	Glass, V, Qtz, Grnt, Rt
D-1016	25	900	42.59	Glass, V, Rt, Mica[2]
D-1017	25	900	34.17	Glass, V, Rt, Grnt. Mica[2]
D-1022	25	900	50.69	Glass, V, Grnt, Rt, Mica[2]
D-1025	25	900	5.43	Glass, V, Qtz, Grnt, Ky, Rt
D-1026	25	900	100.00*	V

[1]A single, small kyanite grain was observed within a vapour bubble from experiment C-3150. The phase is reported, but it is unclear whether it is experiment related or introduced from the polishing pad.
[2]Vapour bubble-hosted micas are abundant in 35 kbar experiments. As discussed in section 14.3, these quench phases qualitatively indicate compositions and crystal structures analogous to phengite (white mica).
*sensor capsule failure (such that Ni-Pd results are unreliable)
Abbreviations: Phen = phengite, Coes = coesite, V = vapour bubbles, Grnt = garnet, Ap = apatite, Rt = rutile, Zirc = zircon, Ky = kyanite, Mica = unidentified white mica.

In terms of major phases, phengite, quartz/coesite ± kyanite rapidly disappear with increasing proportions of glass (i.e., with increases in starting H_2O contents in glass-bearing runs) at 25-35 kbar. Rutile and garnet are the only omnipresent phases reported from experiments in this research, with the phases being stable at all studied P-T-*X* conditions.

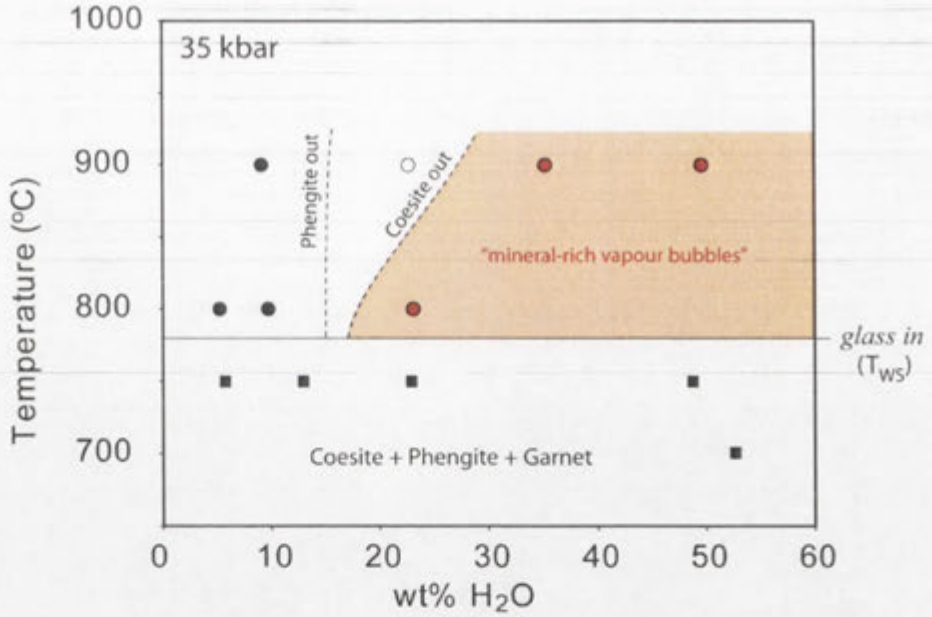

***Figure 14.1**: T-X stability fields and wet solidus at 35 kbar. Black squares represent glass-free runs consisting of coesite-phengite-garnet. Black circles represent glass-present experiments with coesite-phengite-garnet-glass assembly. Open circle represents an experiment with coesite-garnet-glass assembly. Red circles represent glass-present experiments with a garnet-rutile assembly. Shaded red field corresponds to the P-T-X over which experiments contain vapour bubbles with notable mineral and amorphous material. The "glass in" curve represents the temperature at which glass first appears (what would be traditionally interpreted as the wet solidus – T_{WS}).*

One of the most interesting observations from this research, albeit the most difficult to quantify or describe, is the complex array of vapour bubble populations in experiments and varying amounts of amorphous and crystalline material within vapour bubbles (see Figures 14.2-14.6).

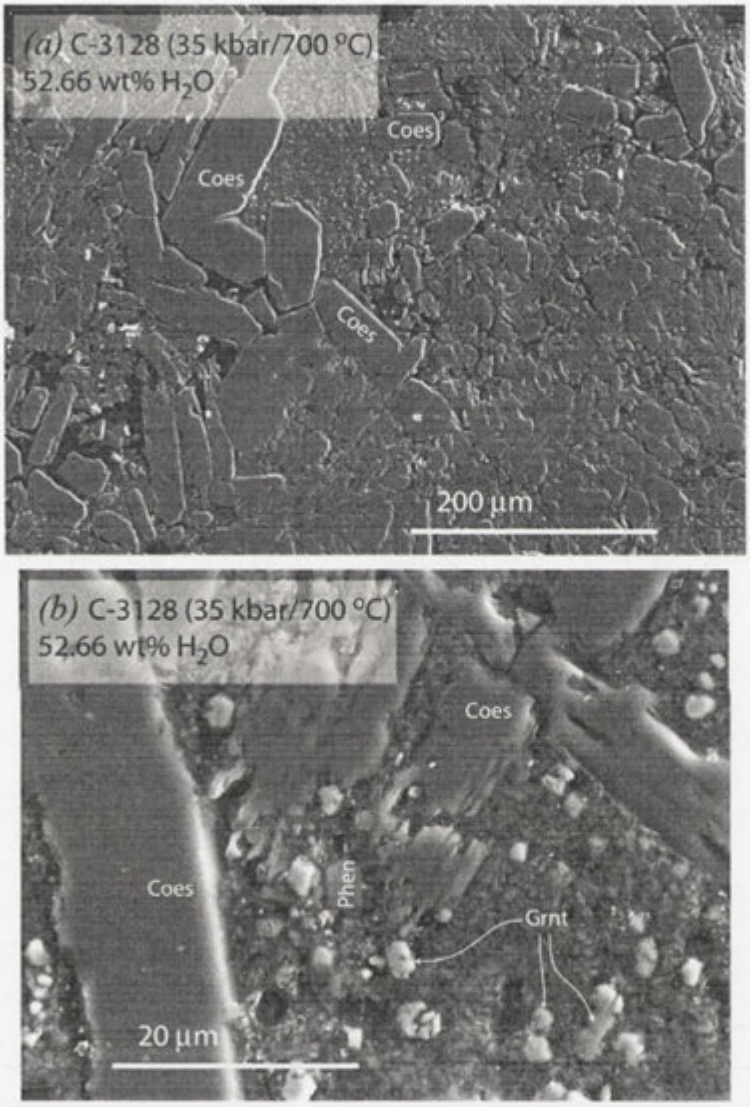

***Figure 14.2**: FE-SEM secondary electron (SE) photomicrograph of experiment C-3128. Coesite (Coes) grains are shown as large, elongate and well-defined grains. The experimental "groundmass" is highly porous and is dominated by very-fine-grained, euhedral phengite (Phen) and garnet (Grnt).*

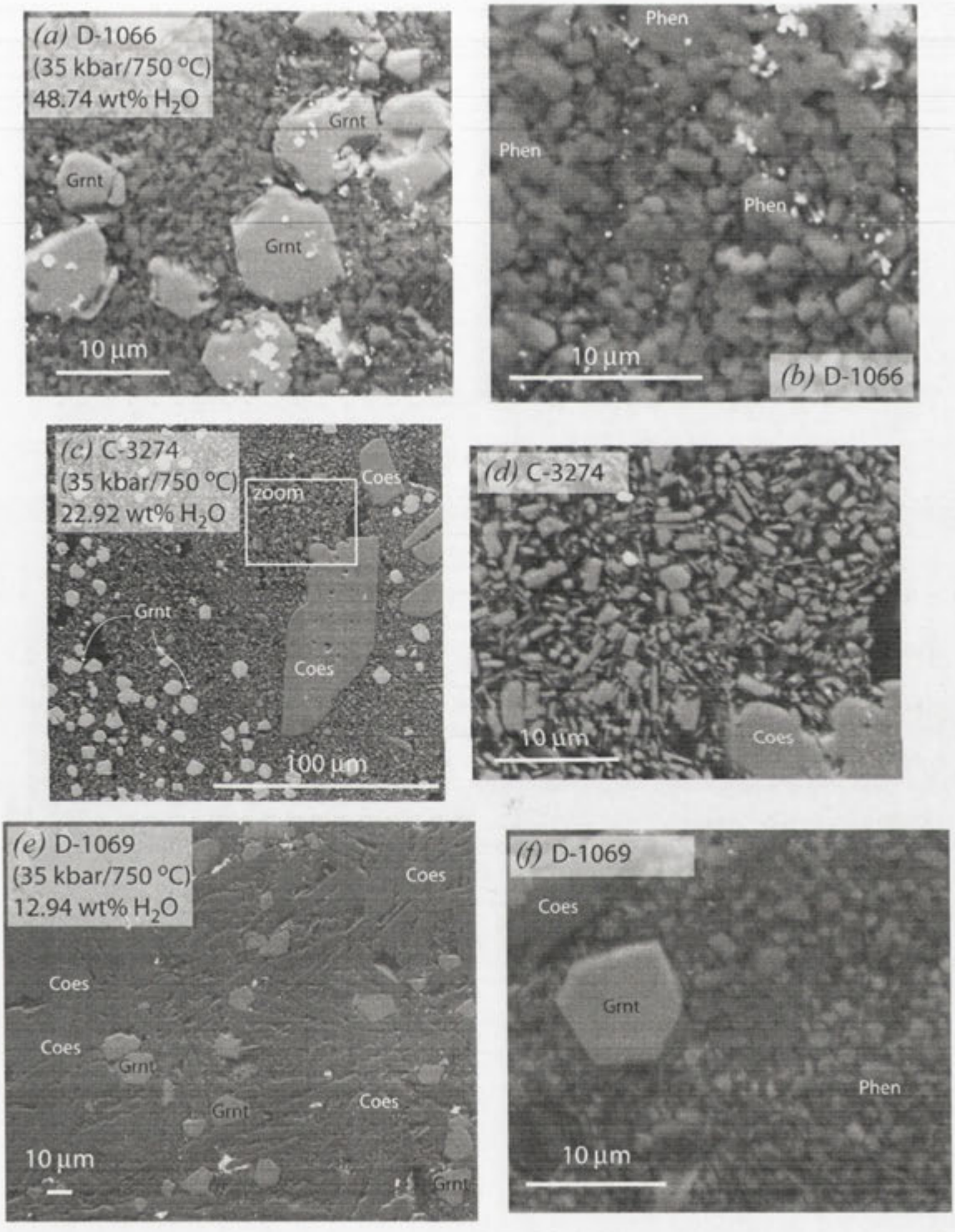

***Figure 14.3**: SEM SE photomicrographs of 750 °C/35 kbar experiments at variable H_2O contents. Experimental groundmass is highly porous and phengite + garnet dominated. Abbreviations as in previous Figure. Bright white inclusions in Figures (a) and (b) correspond to entrained inclusions of Re-ReO_2. Abbreviations as in previous Figures.*

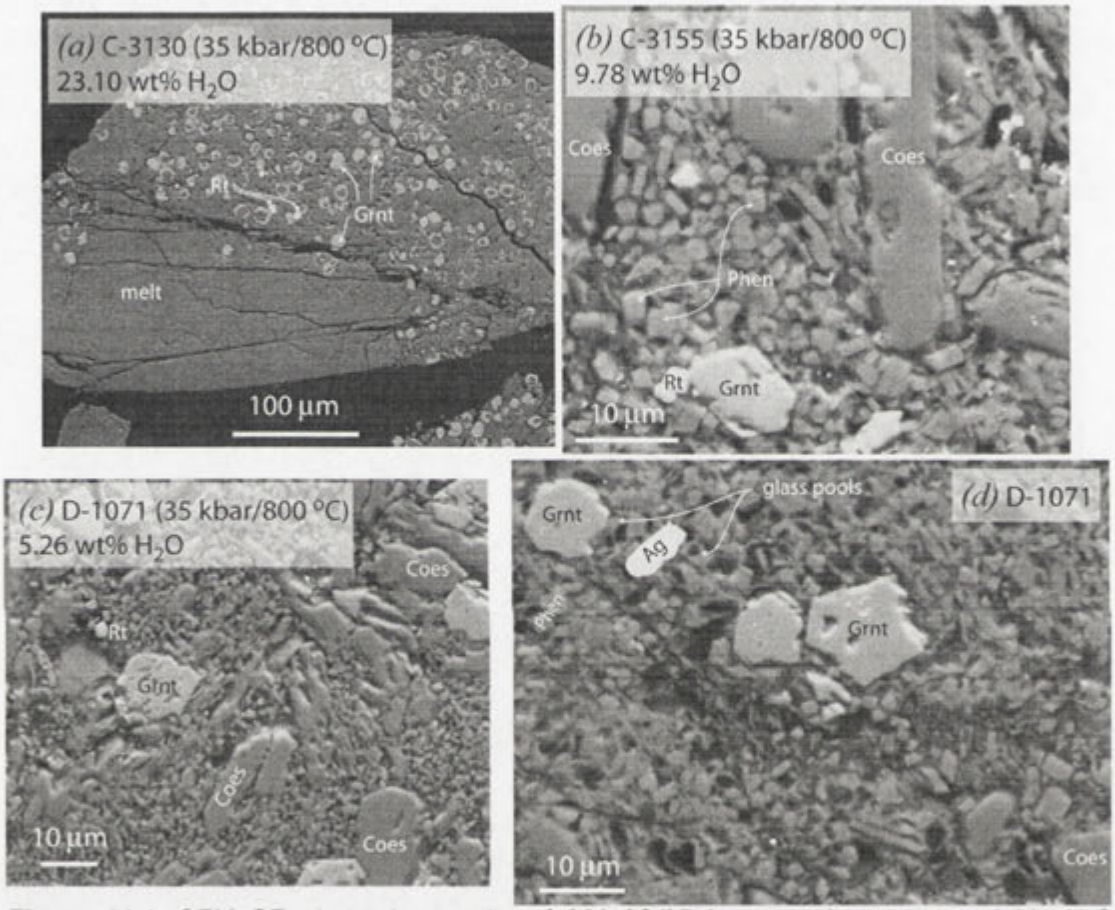

***Figure 14.4**: SEM SE photomicrographs of 800 °C/35 kar experiments at variable H_2O content. Low H_2O content runs (e.g., Figures 14.4.b-d) show the development of very small glass pools with abundant vapour bubbles. Ag = silver, all other abbreviations as in previous Figures.*

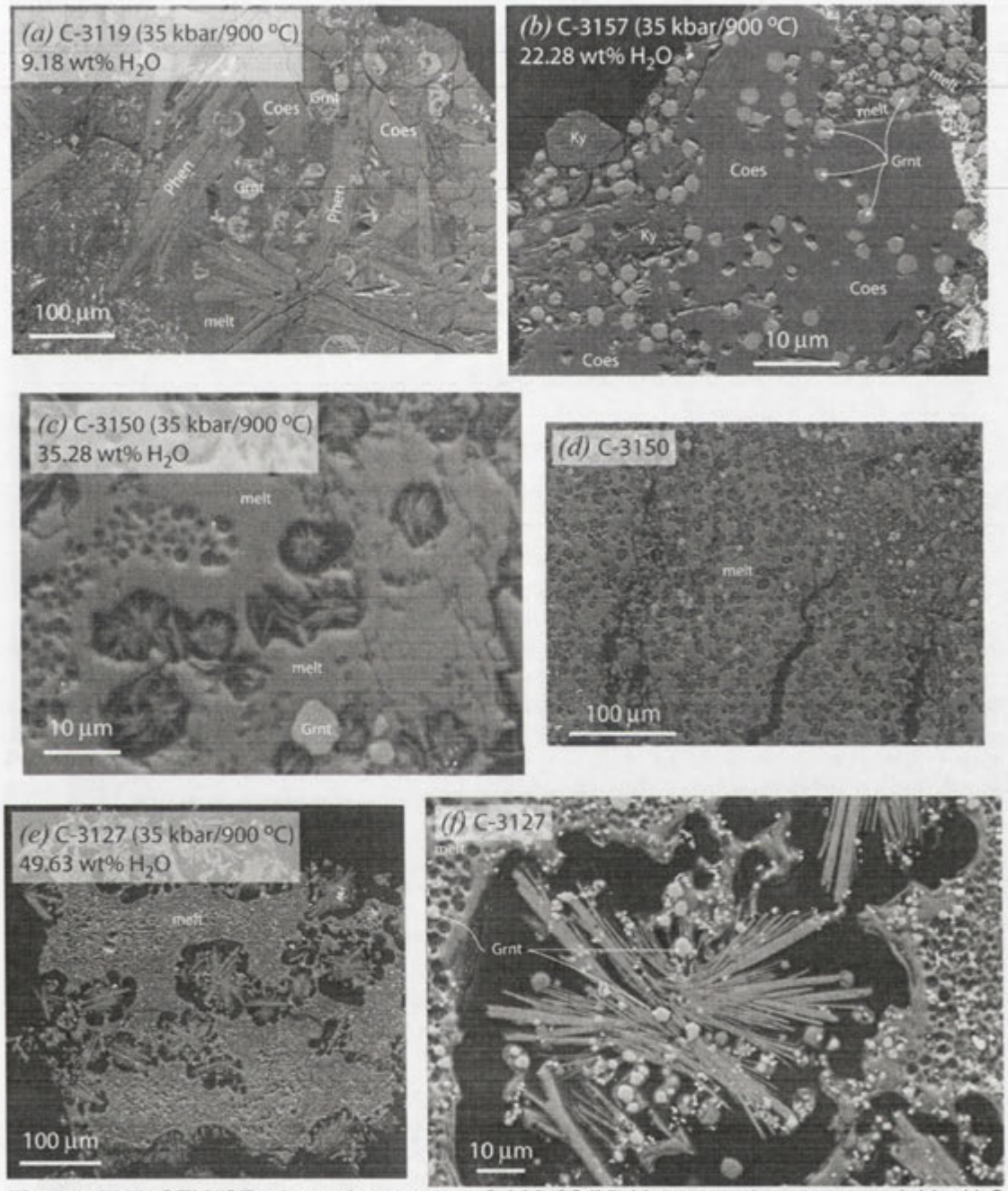

***Figure 14.5**: SEM SE photomicrographs of 900 °C/35 kbar experiments at variable H_2O content. All runs show the development of large glass pools with abundant vapour bubbles. Figures (c)-(f) show the presence of different vapour bubble populations – small and phase-free bubbles and large phase-present bubbles. Ag = silver, all other abbreviations as in previous Figures.*

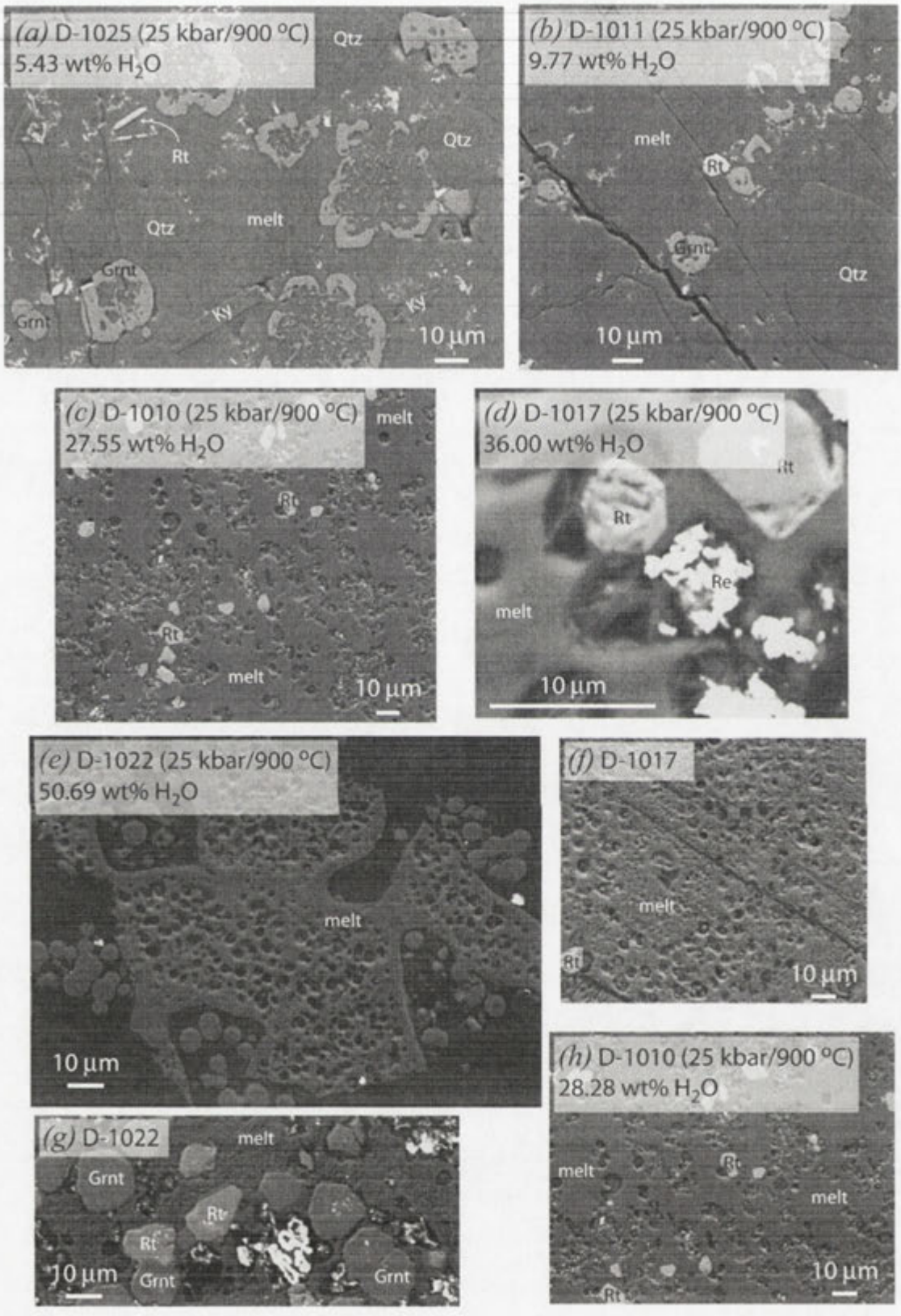

***Figure 14.6**: SEM SE photomicrographs of 900 °C/25 kbar experiments at variable H_2O content. All runs show the development of large glass pools, while run D-1025 (a) is the only run to lack vapour bubbles. Figures (c)-(f) show the presence of large and small vapour bubble populations, with the former containing a range of solid material. Re = Re-ReO_2 buffer (also shown as bright species in Figures g and e), all other abbreviations as in previous Figures.*

14.2: Textures: Oxygen buffer, solid phases, glass and vapour bubbles

Re-ReO_2 buffer

Electron microscopy was used to confirm the presence and distribution of the Re-ReO_2 solid media f_{O_2} buffer in experiments. Petrographic observations show that the majority of the oxygen buffer assembly is retained at the base of the capsule (where the powder was pressed – Figure 14.7) with only small amounts of Re and ReO_2 seen in the bulk of the experimental charge. Electron microscopy was also used to demonstrate the presence of both buffer species, Re and ReO_2, with the two phases readily distinguished by atomic density (Z) contrast (Figure 14.7*b*). Analyses from Re-ReO2 indicate that very little Fe has alloyed with Re, a result consistent with the low temperature of experiments.

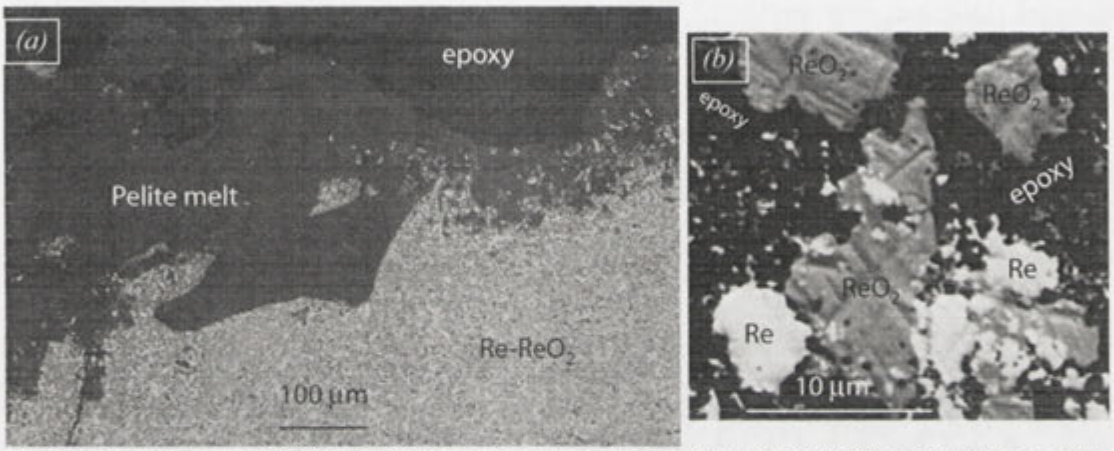

***Figure 14.7**: Representative SEM SE photomicrograph of Re-ReO_2 buffer assemblage from experiment D-1017. Figure (a) shows the spatial separation of the buffer from the bulk experimental system, while (b) shows the presence of both buffering species.*

Glass and vapour bubbles

Glass is observed in all experiments equilibrated at ≥800 °C and shows vapour bubbles in all but one run (D-1025). The textural relationship between glass-bubbles shows notable and complex variation with changing P-T-*X*. Experiments starting with <25 wt% H_2O generally show a single population of vapour bubbles (≤10 µm in diameter) that are largely free of crystalline or amorphous phases. At higher starting H_2O contents vapour bubbles become more complex, often showing multiple vapour bubble populations. Experiments with high H_2O starting content show vapour bubbles that can be broadly separated into two groups: the first consisting of small (≤10 µm in diameter) and phase-free bubbles, and; the second being larger bubbles (generally >>10 µm in diameter) containing a range of amorphous and crystalline phases (Figure 14.8). Large vapour-bubbles seen in experiments at 25 kbar appear to be dominated by amorphous spheres or colloids ("quench roe", Newton and Manning 2008) , while also containing occasional very-fine-grained needles. Large vapour bubbles at 35 kbar are dominated by radial and very-fine-grained needles, while containing small amounts of amorphous colloids.

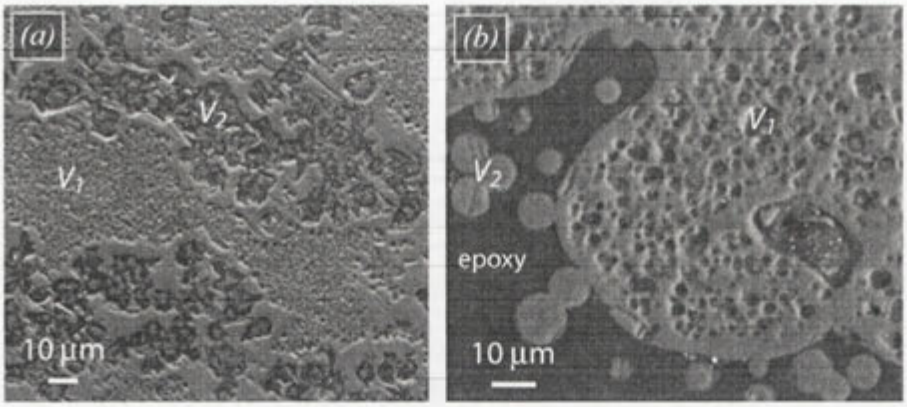

***Figure 14.8**: Representative photomicrographs of vapour bubble-glass relationships from experiment (a) C-3150 and (b) D-1022. Small phase-free vapour bubbles are shown in glass-rich domains (V_1) and large, phase-rich vapour bubbles are shown in epoxy-rich domains (V_2). 35 kbar experiments (a) tend to show large vapour bubbles rich in crystalline and micaceous phases, while 25 kbar experiments (b) tend to show amorphous colloidal phases.*

Garnet and rutile

Garnet and rutile are the only phases present in all experiments over the pressure-temperature range of this study. Rutiles are always seen as small (generally <20 µm along the long axis) idiomorphic and euhedral grains. As shown in Figure 14.9, rutile crystal habit ranges from long, elongate prisms to more typical short, stubby prisms.

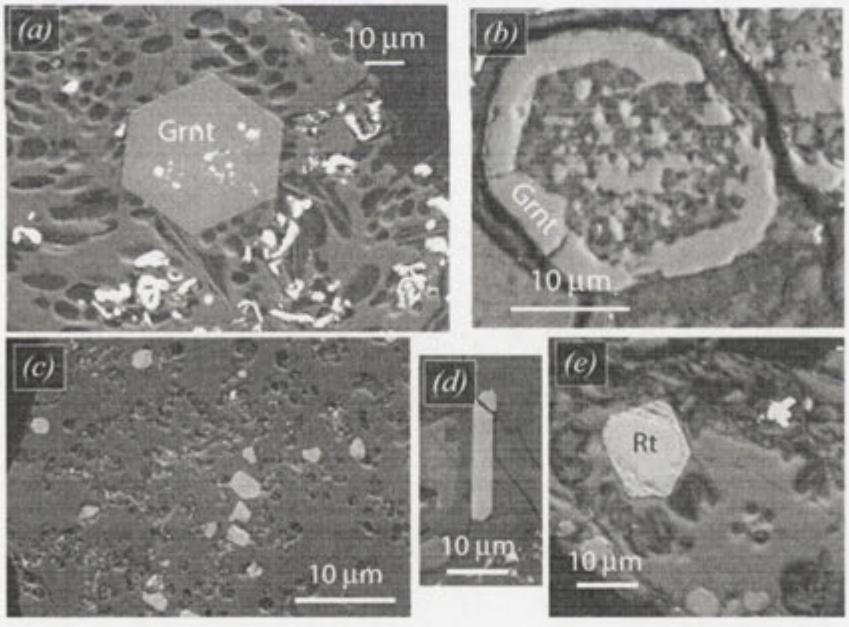

***Figure 14.9:** Photomicrographs of garnet (a-b) and rutile (c-e) textures from experiments. Garnets display textures ranging from euhedral (a) to skeletal (b). Abbreviations as in previous Figures.*

Quartz and Coesite

Quartz and coesite are only present in glass-free and glass-poor experiments, with the two SiO_2 polymorphs showing similar textures. In glass-absent experiments, quartz/coesite form rosettes of elongate (up to 300 µm in length) and euhedral crystal clusters (Figure 14.10*a*). These crystals often contain numerous fluid inclusions and are a dominant phase within

experiments. At low glass contents (Figure 14.10*b*) both SiO_2 species show euhedral crystal habits and often contains mineral and rare melt inclusions. With increasing glass-content, SiO_2 species become smaller, increasingly round and contain more inclusions (Figure 14.10*c*).

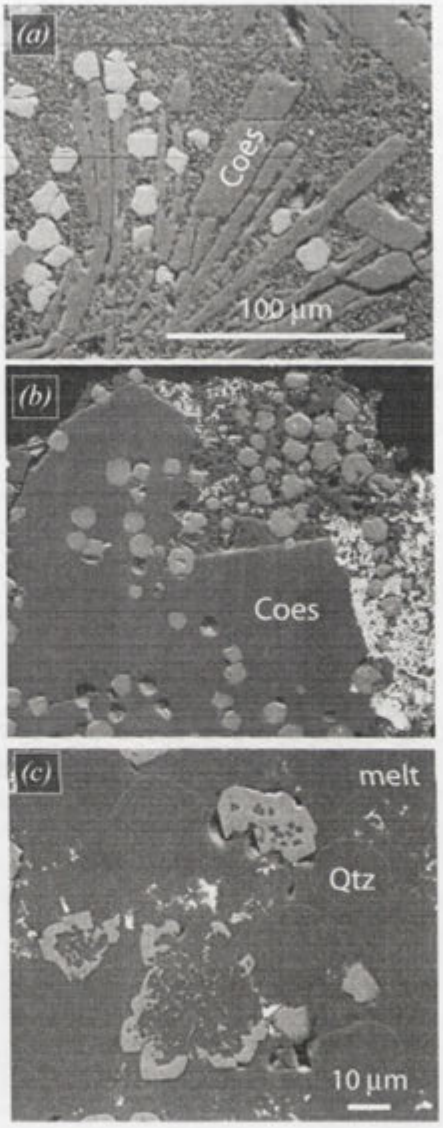

***Figure 14.10**: Representative photomicrographs of quartz and coesite textures from experiments C-3274 (a), C-3157 (b) and D-1025 (c). Abbreviations as in previous Figures.*

Phengite

Phengite is typically found as very small (< 10 µm) euhedral grains that form the bulk of the experimental matrix in glass-absent runs. Petrographic observations of phengite indicate that the mineral regularly displays sheet-like crystal habit and hexagonal symmetry. While phengite is the dominant mineral in glass-absent experiments, the phase rapidly disappears with the appearance of glass.

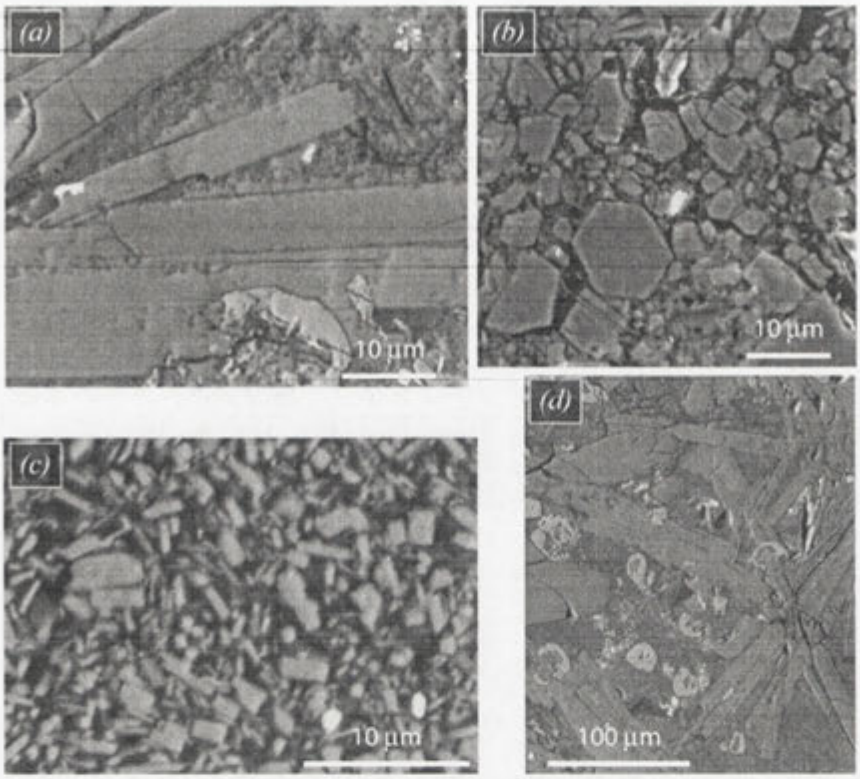

***Figure 14.11**: Representative photomicrographs of phengite-dominated domains from experiments C-3119 (a and d), D-1066 (b) and C-3274(c). Phengite is the dominant and largest grain shown in all images..*

14.3: Major element EDS results from the pelite-H_2O system

Analytical results reported from this research primarily focus on phases that show major and minor element solid-solutions. This does not mean that some experimental run products were ignored and not analyzed. Rather, data on mineral or amorphous species reported here show variability that merits discussion. In this regard, a number of phases analysed during this research show no major or minor element variation worthy of discussion (e.g., quartz/coesite, kyanite and rutile).

Glass composition

Glass analyses are reported in Tables 14.2 and 14.3, with all totals normalized to anhydrous conditions in order to account for the presence of H_2O and small (i.e., <10 µm) vapour bubbles incorporated in glass analyses. It should be noted that all normalized, scanning (raster) beam analyses are reported from domains absent of Re-species (which will predominately influence Fe totals) and free of large (phase-rich) vapour bubbles.

Glass compositions show a number of consistent trends across experiments, with all glasses showing highly silicic compositions (>76 wt% SiO_2). At a given pressure and temperature (≥800 °C) experiments with the lowest amount of glass (or starting H_2O content) show the highest Na_2O, K_2O, Al_2O_3 and CaO contents. Experiments with the largest amount of glass (or highest starting H_2O content) at a given pressure and temperature show the lowest Na_2O and K_2O content and highest FeO content.

Figure 14.12 shows the composition of experimental glasses in terms of total alkali versus silica bulk composition (TAS plot, after Le Bas, 1986), and indicates that melts are highly silicic and essentially rhyolitic/granitic in composition. With increasing glass and H_2O content in experiments at isobaric conditions, glasses clearly show increases in SiO_2 and decreases in Na_2O+K_2O.

Cation ratios reported from glass analyses show broadly consistent trends (Figure 14.13), though these trends do not directly correlate to the starting H_2O content or amount of glass in experiments.

Table 14.2: 25 kbar glass compositions normalized to anhydrous

	D-1025	σ	D-1011	σ	D-1010	σ	D-1017	σ	D-1022	σ
Na_2O	0.82	0.08	0.36	0.06	0.61	0.07	0.75	0.18	0.35	0.05
MgO	1.12	0.06	1.59	0.09	1.85	0.37	1.21	0.34	1.38	0.34
Al_2O_3	13.31	0.19	12.97	0.08	12.07	0.27	11.90	0.16	12.26	0.24
SiO_2	76.24	0.19	78.62	0.47	78.60	0.47	78.50	0.74	79.70	0.65
P_2O_5	0.23	0.12	0.14	0.10	0.33	0.11	0.22	0.09	0.19	0.09
K_2O	5.64	0.13	3.49	0.50	3.70	0.12	4.48	0.41	2.92	0.21
CaO	1.91	0.11	1.82	0.08	1.62	0.09	1.83	0.14	1.71	0.11
TiO_2	0.30	0.06	0.33	0.08	0.35	0.06	0.31	0.06	0.33	0.06
MnO	0.06	0.09	0.04	0.10	0.09	0.08	0.18	0.09	0.14	0.08
FeO*	0.35	0.17	0.63	0.15	0.70	0.13	0.66	0.28	0.83	0.33
n	15		7		10		10		15	
Raw Total	85.38	0.55	83.69	0.35	81.31	3.41	80.16	4.27	81.62	2.41
P (kbar)	25		25		25		25		25	
T (°C)	900		900		900		900		900	
H_2O (wt%)	5.43		9.77		27.55		36		50.69	

n = number of analyses
FeO* = total iron calculated on ferrous basis.
Raw Total = analytical totals from un-normalized scanning (raster) EDS.

Table 14.3: 35 kbar glass compositions normalized to anhydrous

	C-3119	σ	C-3157	σ	C-3150	σ	C-3127	σ	C-3155	σ	C-3130	σ
Na_2O	1.61	0.29	0.69	0.05	0.88	0.11	0.66	0.10	3.02	0.46	0.49	0.09
MgO	0.16	0.19	1.51	0.08	0.72	0.13	0.39	0.23	0.09	0.03	1.65	0.31
Al_2O_3	12.10	0.24	11.43	0.11	11.17	0.14	9.67	0.57	11.24	0.71	11.71	0.30
SiO_2	76.85	0.76	78.78	0.13	79.60	0.54	83.46	0.95	79.07	1.50	79.19	0.50
P_2O_5	Bdl	-	0.16	0.07	0.13	0.13	bdl	-	0.16	0.18	bdl	-
K_2O	5.05	0.46	4.31	0.07	4.61	0.30	2.83	0.28	3.58	0.36	3.91	0.15
CaO	3.35	0.13	1.63	0.08	2.09	0.19	1.97	0.31	2.59	0.33	1.81	0.07
TiO_2	0.28	0.05	0.42	0.08	0.32	0.12	0.23	0.11	0.11	0.13	0.33	0.08
MnO	0.11	0.08	0.04	0.06	0.11	0.07	0.05	0.05	0.07	0.07	0.17	0.07
FeO*	0.50	0.32	1.02	0.17	0.29	0.15	0.61	0.31	0.08	0.10	0.73	0.16
n	15		10		11		14		7		16	
Raw Total	77.36	5.15	82.05	2.12	83.16	1.82	82.10	3.08	71.97	6.93	83.03	0.98
P (kbar)	35		35		35		35		35		35	
T (°C)	900		900		900		900		800		800	
H_2O (wt%)	9.18		22.28		35.28		49.63		9.78		23.1	

n = number of analyses
FeO* = total iron calculated on ferrous basis.
Raw Total = analytical totals from un-normalized scanning (raster) EDS.

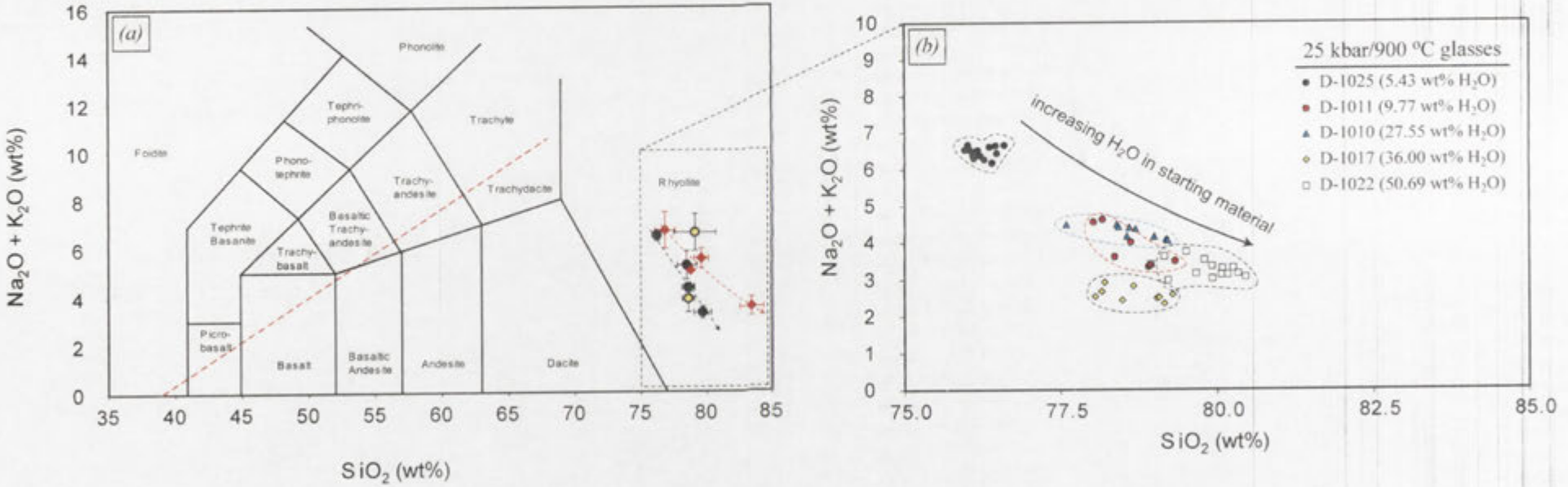

***Figure 14.12**: Glass analyses from experiments plotted in the total alkali-silica (TAS) diagram of Le Bas (1986). Figure (a) shows average glass analyses (with error reported in standard deviations) for 25 kbar/900 °C experiments (black circles), 35 kar/800 °C experiments (yellow-filled black circles) and 35 kbar/900 °C experiments (red filled diamonds).*

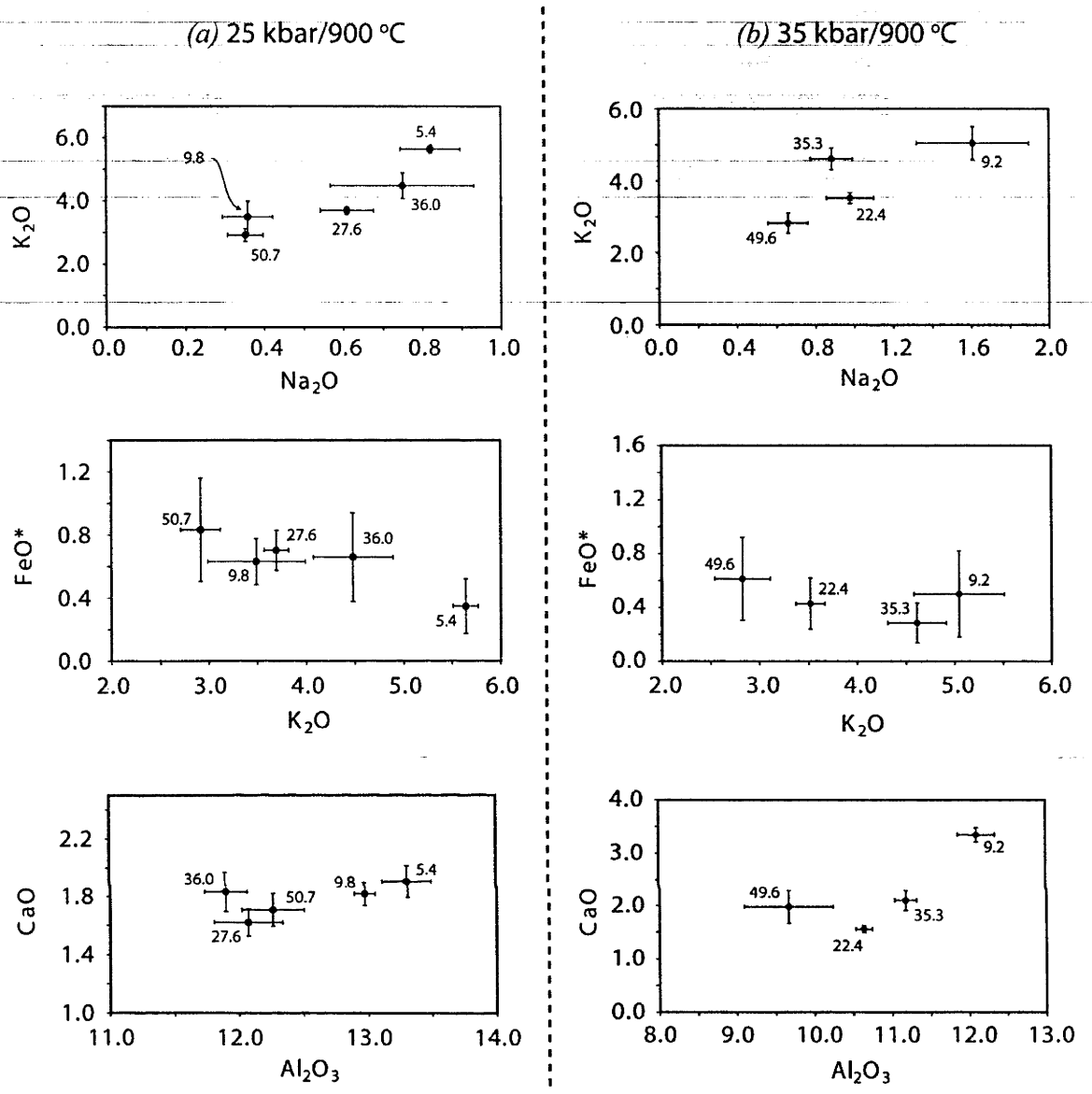

***Figure 14.13**: Major element co-variation diagrams from scanning (raster) beam glass analyses from (a) 25 kbar/900 °C experiments and (b) 35 kbar/900 °C experiments. Errors are reported in standard deviations, while values attached to analyses report starting H_2O content.*

Large vapour bubble analyses

Many attempts were made to analyse amorphous and crystalline phases from vapour bubble species, including XRD, SEM and EPMA techniques. However, no quantitative or determinative estimate of bulk composition or mineralogy was obtained from any large vapour bubble-hosted species. This is largely because large vapour bubble-hosted phases are highly volatile under the electron beam, are too fine-grained for quantitative SEM analysis (showing very low totals) and are not of significant concentration or lack crystalline structures for XRD determination.

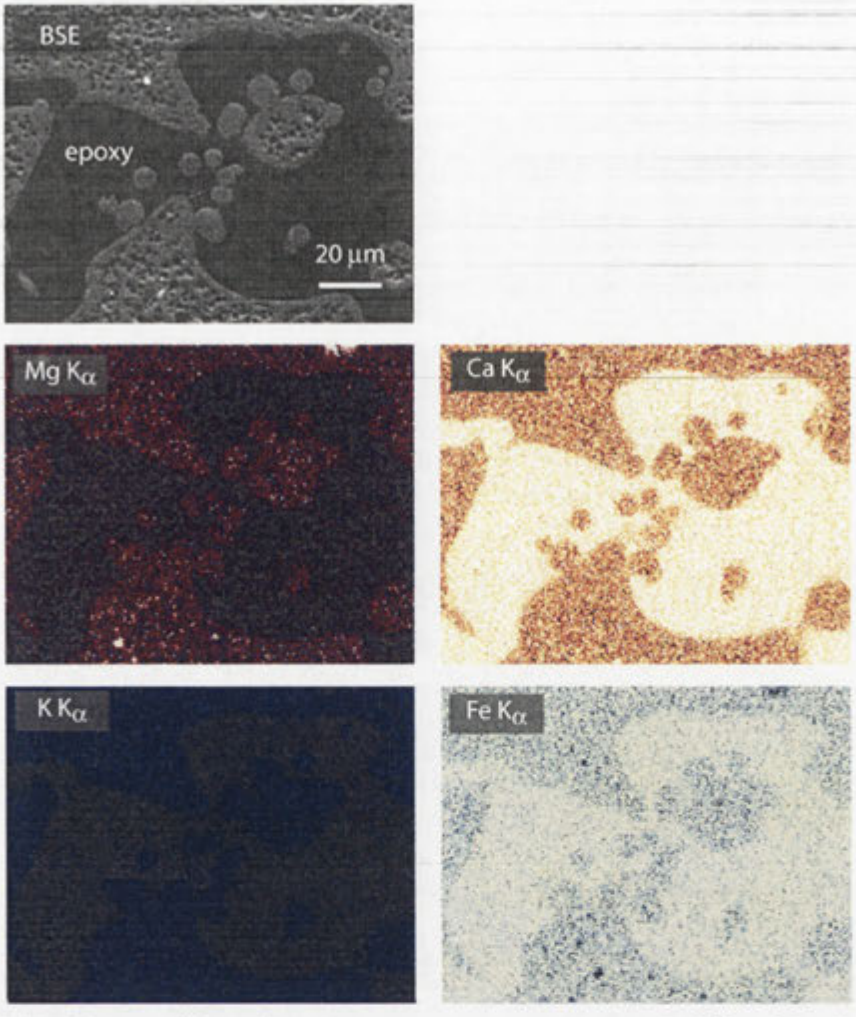

***Figure 14.14**: Energy dispersive x-ray maps over a vapour-bubble rich domain from experiment D-1022 (25 kbar). Selected elements and x-ray absorption lines as indicated. Greyscale image represents an electron back-scatter image (BSE).*

Low current (10 nA) x-ray maps collected over large vapour bubbles from 35 kbar/900 °C indicate that the amorphous, colloidal material has a composition similar to the silicate glass (Figure 14.14).

X-ray maps collected over large vapour bubbles from 35 kbar/900 °C at >20 wt% H_2O show that very-fine-grained and crystalline needles consist of a single K- and Mg-rich aluminosilicate species (Figure 14.15). Qualitative comparison of x-ray counts from these needles relative to the silicate glass, combined with crystal habit, indicates the crystalline phase has a composition similar to phengite. This phengite phase (referred to as Mica[2] in Table 14.1) is solely contained within large vapour bubbles, while other minerals (including garnet and rutile) can be found within both glass and large vapour bubbles.

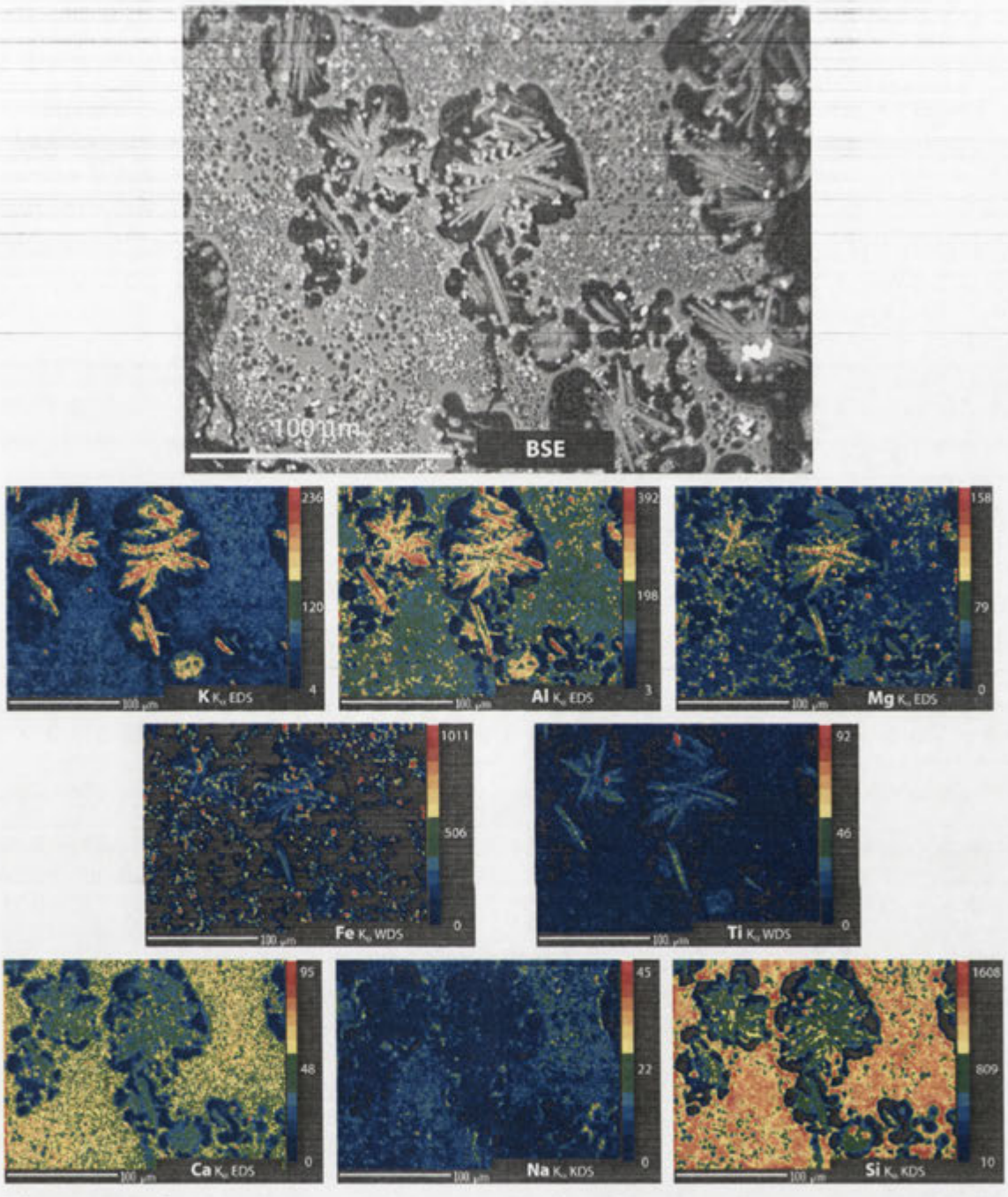

***Figure 14.15**: Combined energy and wave-length dispersive x-ray maps over a vapour-bubble rich domain from experiment C-3127 (35 kbar). Selected elements, x-ray absorption lines and analytical method as indicated. Colour scale and numerical values indicate counts/second/pixel. Greyscale image represents an electron back-scatter image (BSE). Note that the distribution of garnet and rutile can be discerned from bright red domains in Fe x-ray and Ti x-ray maps respectively.*

Garnet

Although garnet is present in all experiments from this research, the mineral shows some notable chemical variation. For the purpose of discussing changes in garnet composition within experimental series, analyses from 35 kbar runs are shown in Table 14.4, with all individual analyses shown in Figure 14.6 (noting that garnet analyses from 25 kbar and 35 kbar/<800 °C experiments are reported in Appendix 2). No obvious garnet core-to-rim zonation was observed from SEM observations (including electron images and x-ray maps),

though analytical variations seen in Figure 14.16 cannot rule out the possibility (at very low statistical variation). Garnet compositions are remarkably constant in glass-free experiments at 35 kbar (i.e., < 800 °C), regardless of starting H_2O content (ranging from 6-53 wt% H_2O). At 800 °C, the appearance of glass does not significantly change garnet chemistry relative to glass-free compositions (at 700-750 °C) until large amounts of glass are present (i.e., >23 wt% H_2O in the starting material for experiment C-3130). Experiment C-3130 shows the first appearance of large amounts of glass at 35 kbar/800 °C, with garnets showing a dramatic decrease in CaO content (or grossular component).

All 35 kbar/900 °C experiments contain garnets with similar compositions to experiment C-3130, showing low CaO or grossular contents. Increasing H_2O starting content in these experiments is broadly accompanied by increasing FeO (almandine) and MnO (spessartine) content (Table 14.4 and Figure 14.15).

Table 14.4: 35 kbar/900 °C garnet analyses

	D-1025	σ	C-3119	σ	C-3157	σ	C-3150	σ	C-3127	σ
MgO	14.42	1.71	9.92	1.59	11.33	0.82	11.73	1.41	10.39	0.16
Al_2O_3	21.80	0.44	20.44	0.49	20.85	0.25	21.01	0.37	21.06	0.34
SiO_2	40.12	0.89	38.39	0.84	39.09	0.47	38.96	0.61	39.13	0.21
CaO	4.67	0.76	6.48	1.56	3.59	0.52	2.98	0.78	1.46	0.26
TiO_2	0.75	0.26	1.08	0.22	1.31	0.36	1.07	0.26	0.31	0.26
MnO	0.72	0.26	1.32	0.44	1.65	0.12	1.89	0.27	1.34	0.07
FeO*	15.41	2.05	19.88	2.25	20.53	1.34	21.20	2.16	25.63	0.19
Total	98.88	0.44	98.75	1.00	98.36	0.49	98.84	0.23	99.32	0.28
n	12		12		10		20		10	
P (kbar)	35		35		35		35		35	
T (°C)	900		900		900		900		900	
H_2O (wt%)	5.43		9.18		22.28		35.28		49.63	

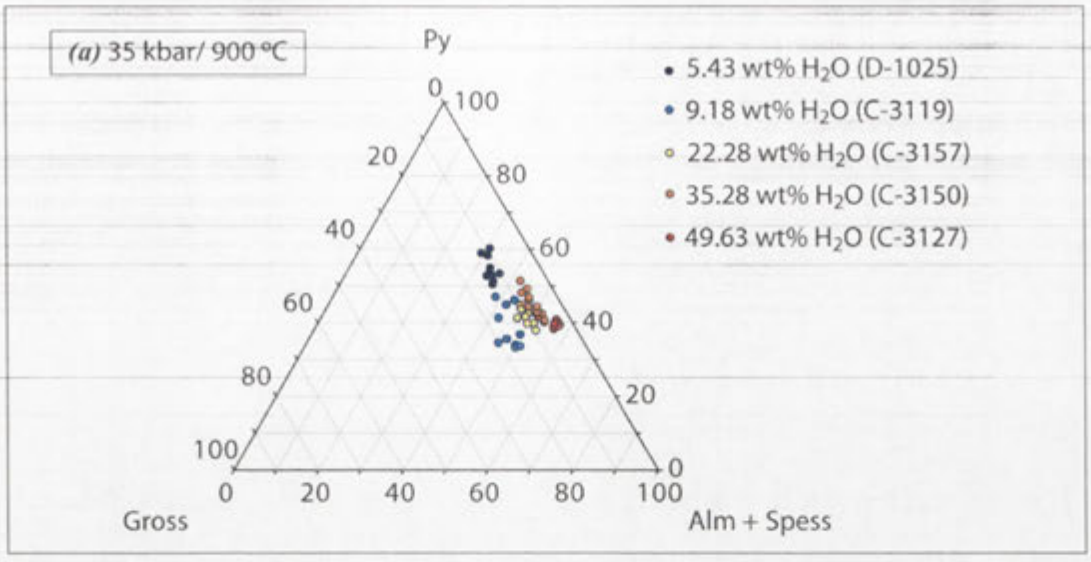

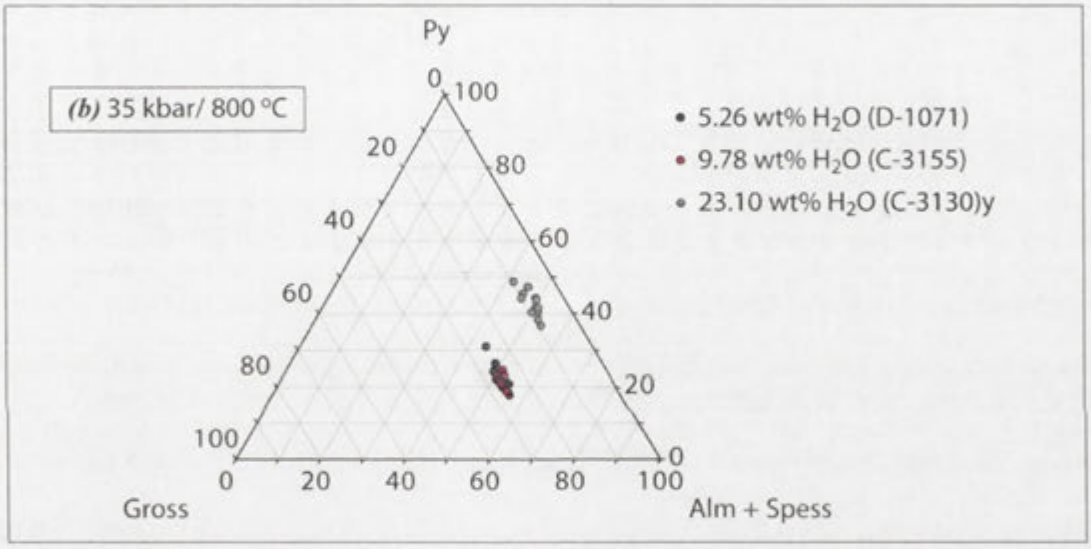

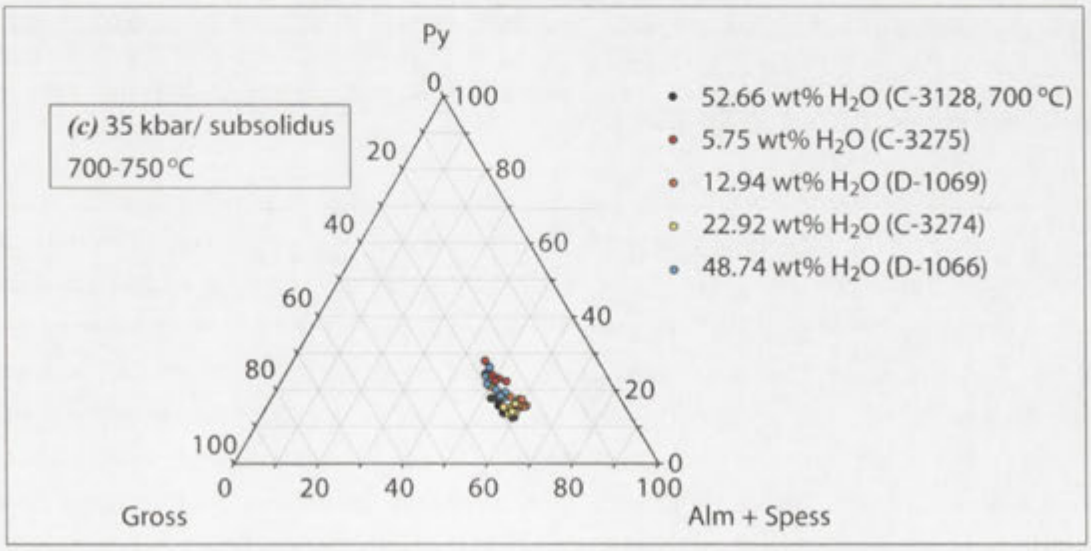

***Figure 14.16**: Garnet analyses projected into garnet ternary diagrams. Abbreviations include: Py = pyrope, Gross = grossular, Alm = almandine and Spess = spessartine, Experiment pressure, temperature and starting H_2O content as indicated.*

Phengite

Synthetic phengite compositions are reported from all experiments (Table 14.5) except runs C-3274 and D-1071, which contained grains too small for EDS analyses. Phengites from 35 kbar experiments show Si-contents between 3.46-3.53 atoms per formula unit (pfu), while TiO_2 content systematically increases from 0.36 to 0.92 with increasing temperature (Figure 14.7). The Na_2O content of synthetic phengites are characteristically low, indicating that the paragonite component exists at close to the EDS detection limit.

Table 14.5: Phengite composition

	C-3128	σ	C-3119	σ	C-3155	σ	D-1066	σ	D-1069	σ
Na_2O	0.25	0.18	0.03	0.05	0.54	0.28	0.19	0.06	0.34	0.06
MgO	4.34	1.2	4.79	0.71	4.36	0.13	3.97	0.17	3.68	0.25
Al_2O_3	21.83	1.1	23.49	0.94	23.89	0.84	23.34	0.65	22.32	1.25
SiO_2	47.85	2.4	51.45	0.70	50.38	0.71	49.21	1.31	46.66	2.44
K_2O	7.42	0.88	9.08	0.29	9.81	0.55	9.93	0.42	9.24	0.53
CaO	0.24	0.11	0.10	0.03	0.09	0.15	0.04	0.04	0.04	0.06
TiO_2	0.4	0.23	0.92	0.15	0.81	0.11	0.36	0.06	0.43	0.08
FeO*	2.68	0.58	0.85	0.26	1.24	0.42	1.75	0.25	1.85	0.27
Total	85.01	3.12	90.60	0.64	91.35	1.41	88.89	2.52	84.75	4.61
n	7		9		10		11		11	
P (kbar)	35		35		35		35		35	
T (°C)	700		900		800		750		750	
H_2O (wt%)	52.66		9.18		9.78		48.74		12.94	
Si (pfu)	3.48	0.02	3.53	0.03	3.47	0.02	3.48	0.01	3.46	0.02
ΣA	0.80	0.04	0.81	0.03	0.95	0.04	0.93	0.02	0.93	0.01
ΣR	2.10	0.03	2.06	0.01	2.04	0.02	2.07	0.01	2.07	0.02

ΣA and ΣR = cation sum for the *A*-site (interlayer site) and *R*-site (octahedral site) in experimental micas based on 12 oxygens.
pfu = (atoms) per formula unit

Ti- and Si-content of phengites produced in this research are compared to results of Hermann and Spandler (2008) in Figure 14.17. Variations in Ti-content appear to show trends broadly consistent with Hermann and Spandler (2008), albeit at lower solubilities. Si-contents (in pfu) of 35 kbar experiments are characteristically high (>3.4 pfu) and are similar to high pressure (i.e., 20-40 kbar) phengites reported elsewhere (Massonne and Schreyer, 1987; Massonne and Szpurzka, 1997; Hermann, 2002b; Schmidt et al., 2004; Hermann and Spandler, 2008). Minor deviations among synthetic phengites reported here and elsewhere (Figure 14.17) – including Na_2O, TiO_2, Al_2O_3 and SiO_2 content – at analogous conditions is not unexpected. Given that elemental substitutions in phengite are complex (e.g., coupled) and different experiments in the pelite-H_2O system show different mineral-buffered assemblages (particularly in relation to the presence of kyanite, clinopyroxene and

biotite), it is unsurprising that some variation exists among all experiments in the pelite-H_2O system.

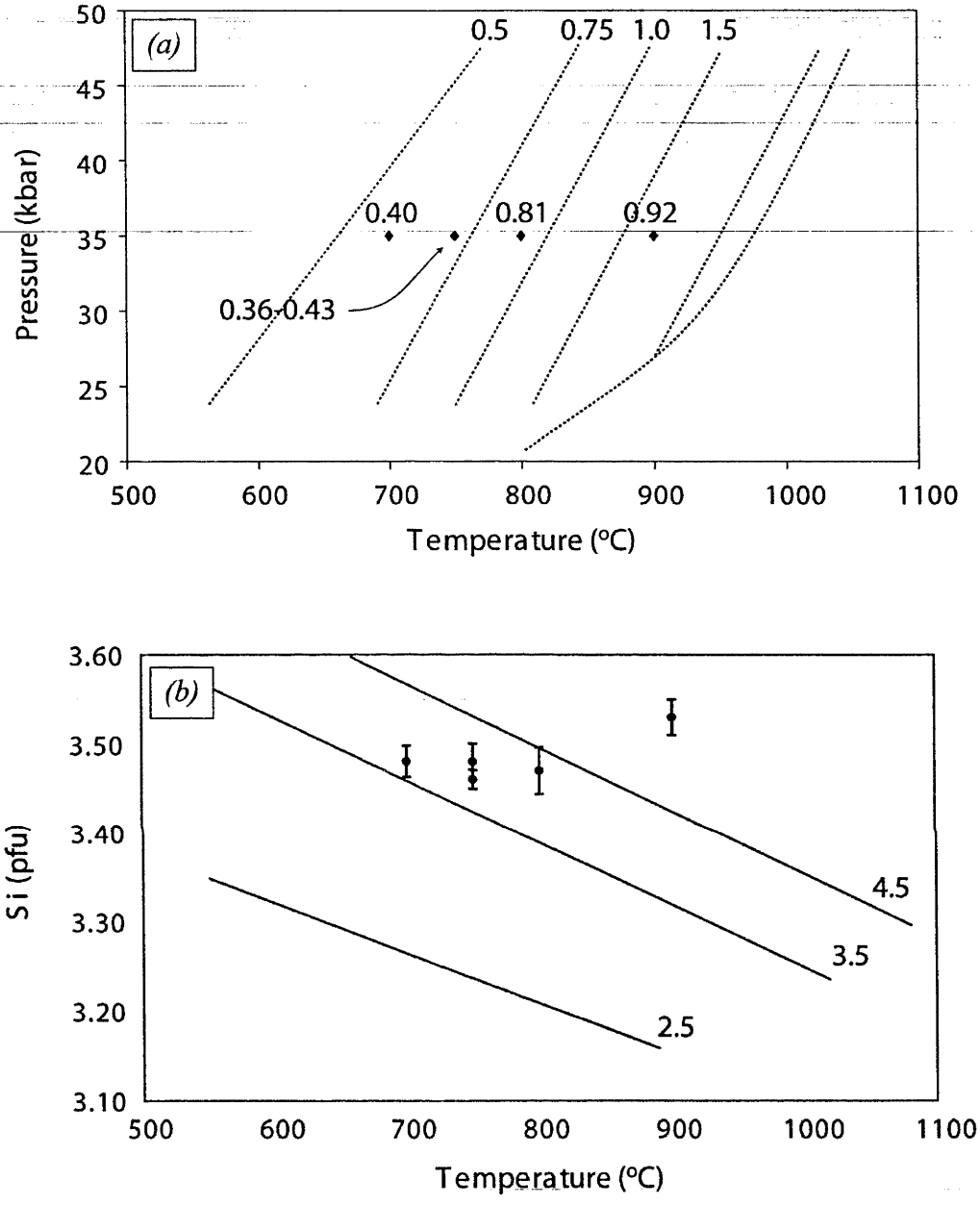

***Figure 14.17**: 35 kbar phengite compositions plotted relative to (a) TiO_2 isopleths and (b) Si-content results of Hermann and Spandler (2008).*

14.4: H-sensors: WDS results and experimental observations

Results reported from H-sensors involved both optical and WDS microscopy. Much like the larger 6 mm Ag capsules, the presence of H_2O within sensors was confirmed by the appearance of bubbles during capsule piercing. Optical microscopy was also used to demonstrate the presence of NiO, a phase that can be easily identified by its emerald green colour (Figure 14.18). While the presence of NiO sounds straightforward, the constrast in hardness and grain-size between alloy and NiO makes polishing problematic. H-sensors often required 3-5 series of impregnations in order to prevent plucking during polishing.

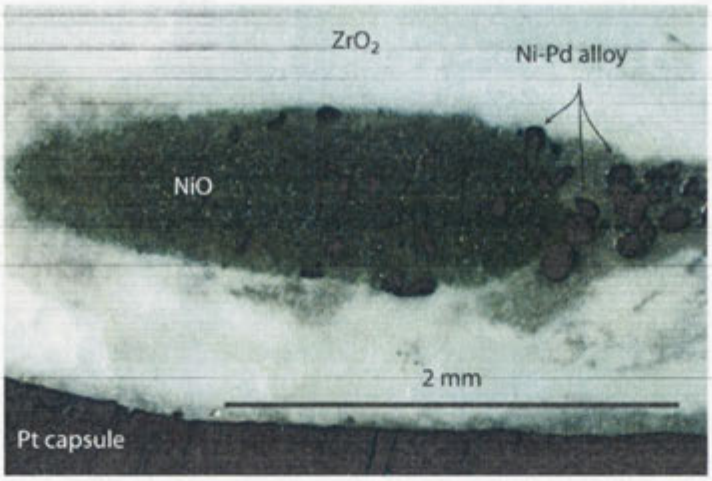

***Figure 14.18**: Representative optical photomicrograph from experiment D-1017 showing NiO (green) and Ni-Pd alloy (dark, round blebs), zirconia tubing (white) and Pt-capsule.*

Other means of determining the success of H-sensors include the presence of foreign phases within the sensor (i.e., those not present in the sensor starting material), the position of the metal alloy relative to the wall (interior rim) of the Pt-capsule, and, sensor capsule shape. As shown in Figure 14.19, leaked experiments often contain foreign phases like Ni-olivine (deep blue in colour) and zircon. Capsules that show significant deformation during runs can show the migration of the alloy towards the rim of the Pt-capsule, permitting alloying with the capsule and showing significant Ni/Pd variation depending on proximity to the capsule wall.

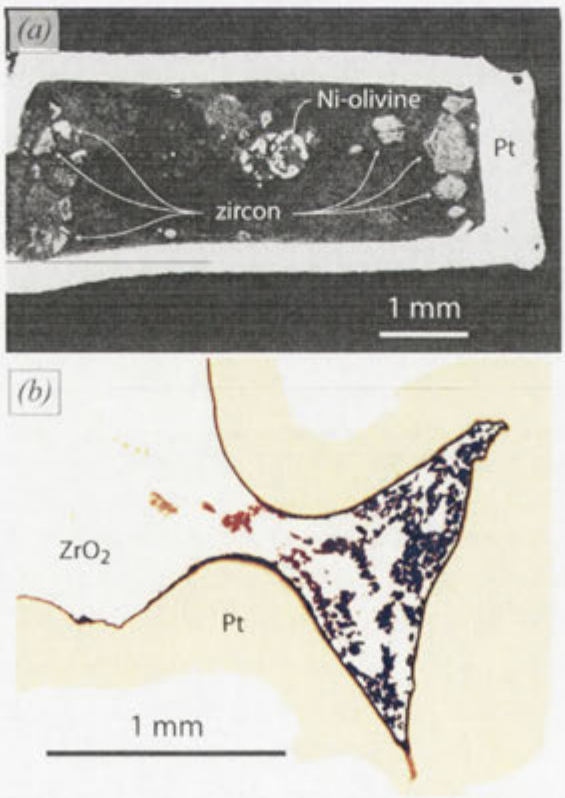

***Figure 14.19**: Failed sensors from (a) showing the presence of Ni-olivine and zircon, and, (b) H-sensor showing alloy migration to the top of the capsule and large Ni/Pd gradients as the alloy approaches the rim of the capsule.*

Alloy analyses are reported in Table 14.6 and demonstrate that successful experiments report low statistical variation, with 2σ being within 1.4 and 14.8 % of the mean (with an average 2σ within 9.1 % of the mean). As indicated by Figure 14.20, much of the statistical variation in Ni- and Pd-content within experiments appears to correspond to height of the alloy within the sensor capsule.

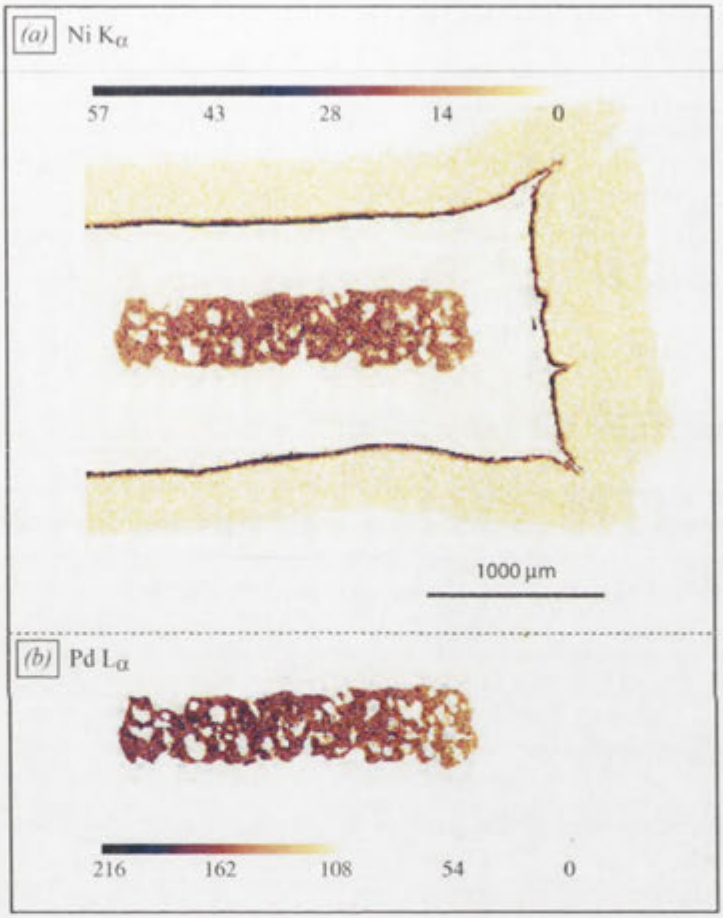

***Figure 14.20**.: X-ray maps of (a) Ni and (b) Pd from experiment C-3119. Optical microscopy demonstrates the presence of small amounts of NiO in pores within the alloy.*

Table 14.6

Run #	P (kbar)	T (°C)	H_2O (wt%)	Ni (wt%)	Σ	Pd (wt%)	σ	X_{Ni}	error‡	*n*	Comments
C-3119	35	900	9.18	7.14	0.53	92.48	0.46	0.123	0.011	37	
C-3157	35	900	22.28	14.27	0.50	86.81	0.55	0.230	0.012	20	
C-3121	35	900	22.44	16.52	0.38	83.43	0.43	0.264	0.010	30	Failed pelite†
C-3150	35	900	35.28	47.45	2.40	52.55	2.66	0.621	0.031	42	NiO absent
C-3127	35	900	49.63	26.33	0.71	71.23	0.50	0.403	0.019	37	
D-1071	35	800	5.26	32.45	3.08	67.74	2.90	0.464	0.094	75	
C-3155	35	800	9.78	16.69	0.72	84.65	0.63	0.263	0.017	17	NiO absent
C-3130	35	800	23.1	11.45	0.76	88.13	0.79	0.191	0.017	36	
D-1089	35	800	100*	11.45	0.71	90.27	0.44	0.187	0.011	32	
C-3275	35	750	5.75	15.19	0.52	87.22	0.52	0.240	0.012	20	
D-1069	35	750	12.94	22.87	1.58	78.39	1.40	0.346	0.042	60	ReO_2 and NiO absent
C-3274	35	750	22.92	29.67	1.33	72.29	1.31	0.426	0.041	70	ReO_2 and NiO absent
D-1066	35	750	48.74	15.86	0.54	85.07	0.57	0.253	0.013	83	
C-3128	35	700	52.66	16.96	0.77	83.38	0.78	0.269	0.019	32	
C-3362	35	700	100*	13.10	0.27	88.02	0.68	0.213	0.004	32	
D-1025	25	900	5.43	30.42	1.67	70.58	1.69	0.438	0.055	36	NiO absent
D-1011	25	900	9.97	29.71	0.80	70.26	1.89	0.429	0.022	32	NiO absent
D-1010	25	900	28.28	17.06	1.26	83.72	1.23	0.269626	0.031	33	
D-1017	25	900	34.17	13.49	1.65	86.95	1.26	0.219214	0.036	33	
D-1016	25	900	42.59	17.79	1.18	83.42	1.17	0.278663	0.029	36	
D-1022	25	900	50.69	13.25	3.60	87.19	3.61	0.214728	0.074	15	
D-1026	25	900	100*	58.84	0.39	42.00	0.42	0.717	0.003	28	Deformed capsule

†Large amounts of NaCl and AgCl present in the pelite experiment, *H-sensor leaks as determined by the presence of Ni-olivine and/or zircon.

X_{Ni} ($X_{Ni}^{NiPdalloy}$) = Ni content of alloys as calculated by $\frac{(NiM/PdM)}{1+(NiM/PdM)}$

error‡ = represents the standard deviation of X_{Ni} from all analyses of a given experiment

Figure 14.21 shows the NiPd alloy compositions from equilibrated experiments at 35 kbar/900 °C and a f_{O_2} defined by Re-ReO_2. The observed Ni and Pd contents in H sensors demonstrate that compositional changes occur along the binary solid solution of the model NiPd alloy (e.g., Massalski, 1986).

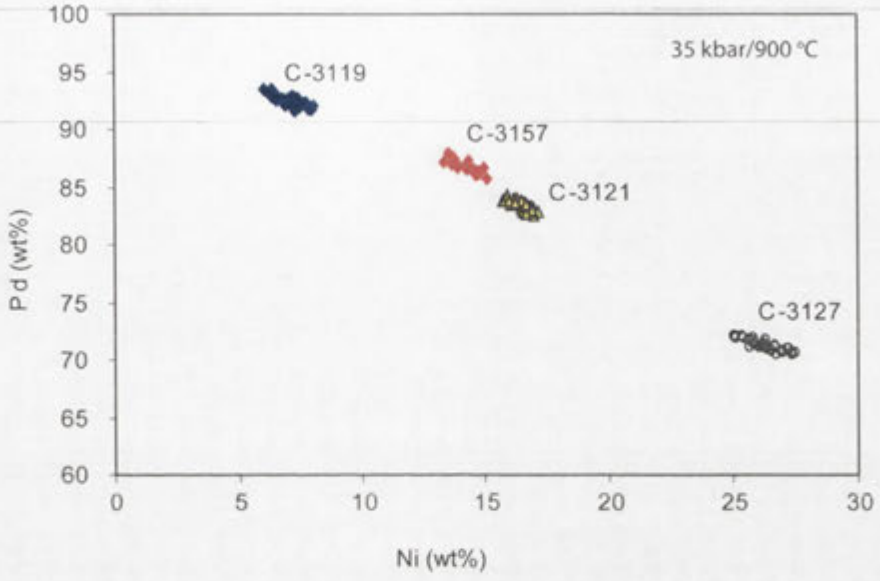

***Figure 14.21**: NiPd results from 35 kbar/900 °C experiments containing Re-ReO_2 solid media oxygen buffer assemblage in the large Ag-capsule and NiO + Ni-Pd assemblage in the small H-sensor capsule post-run.*

H-sensor results are reported from all experiments, including runs that lack a f_{O_2} buffer (Re-ReO_2) and/or NiO within the sensor capsule (such that the sliding sensor results are unconstrained and irrelevant – shown in red in Figures 14.22-14.24). In this manner, reported analyses indicate how failed experiments can be monitored and differentiated.

H-sensor NiPd alloy compositions from the two most extensive (i.e., involving a broad pelite:H_2O at a constant P-T), equilibrated and buffered experiments are shown in Figure 14.22. Results from 35 kbar/900 °C indicate that an increase in starting H_2O content in experiments (at a constant f_{O_2}) is accompanied by a systematic increase in Ni content in the alloy (or increasing f_{H_2}). By comparison, experiments at 25 kbar/900 °C show a near-linear Ni/Pd compositions as a function of starting pelite:H_2O.

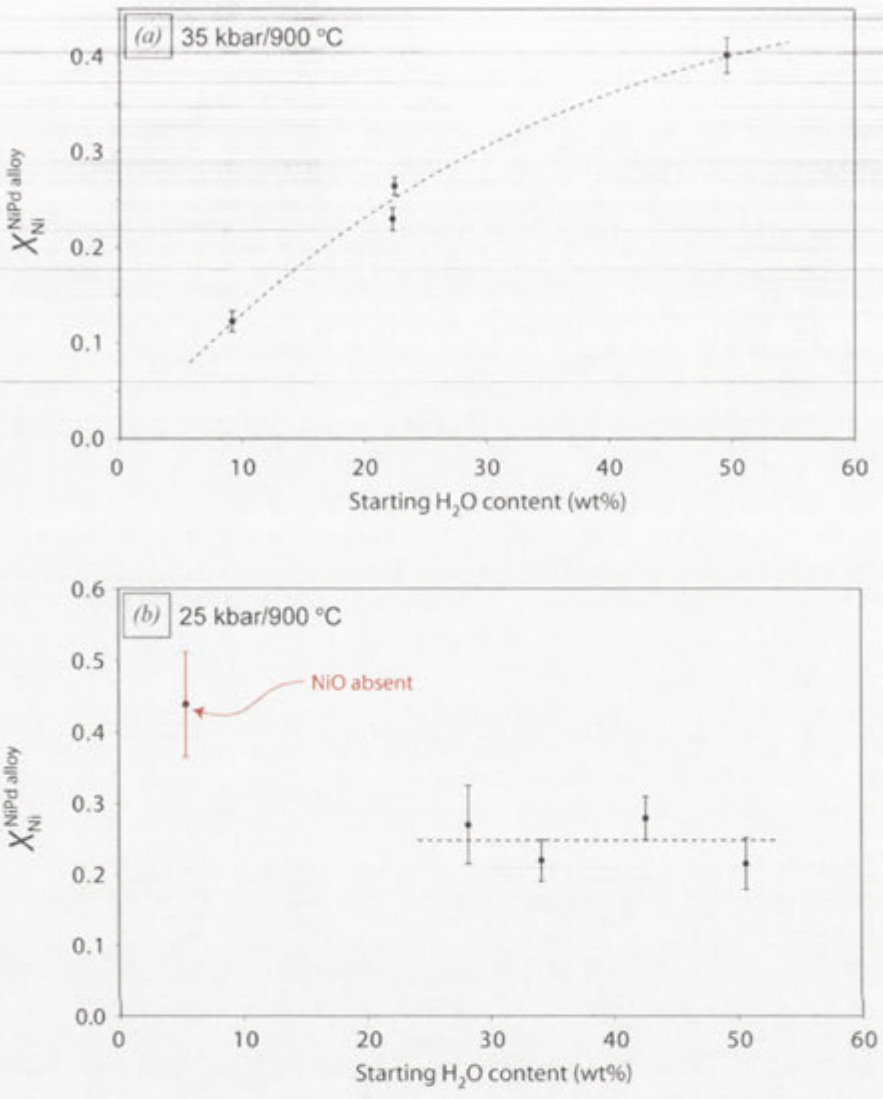

***Figure 14.22**: H-sensor alloy compositions from experiments at (a) 35 kbar/900 °C and, (b) 25 kbar/900 °C. Black symbols represent experiment containing a buffered Re-ReO_2 and NiO + Ni-Pd assemblage. Red symbols represent experiments lacking NiO in the sensor capsule.* $X_{Ni}^{NiPdalloy}$ *represents* X_{Ni} *shown in Table 14.6.*

H-sensor results at 35 kbar/800 °C show only limited success (Figure 14.23), with only two pelite-H_2O experiments, D-1071 and C-3130, showing the presence of NiO and Re-ReO_2 within the experiment. The Ni content of the D-1071 H-sensor shows notable statistical variation around the mean and exists at significantly higher values than all other experiments at the same condition (including the pure H_2O experiment, run D-1089). There is something anomalous with this experiment, and it is difficult to conclude whether results from this experiment indicate equilibrium conditions.

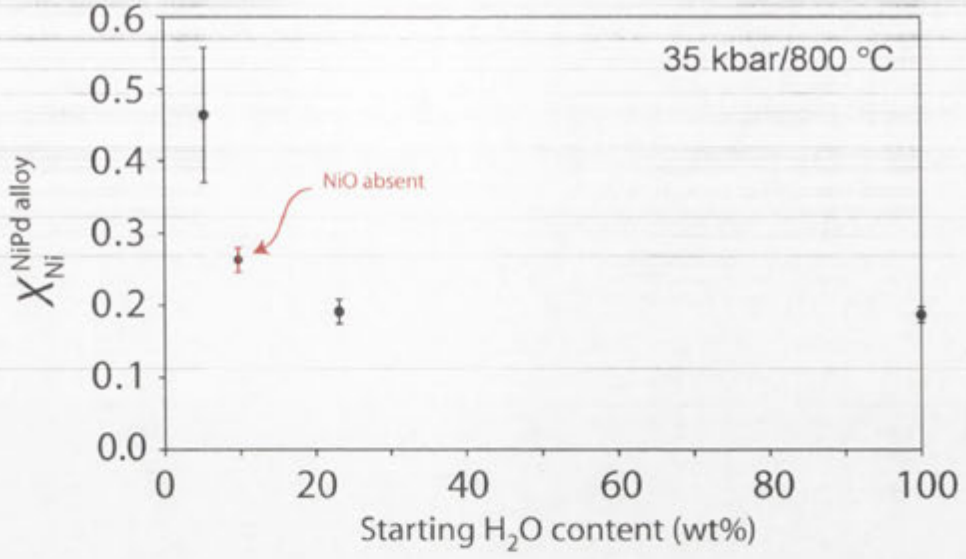

***Figure 14.23**: H-sensor alloy compositions from experiments at 35 kbar/800 °C. Red symbols represent failed sensors.*

H-sensor results from glass-free experiments at 35 kbar/700-750 °C, show remarkably constant Ni contents (with the exception of two failed sensors).

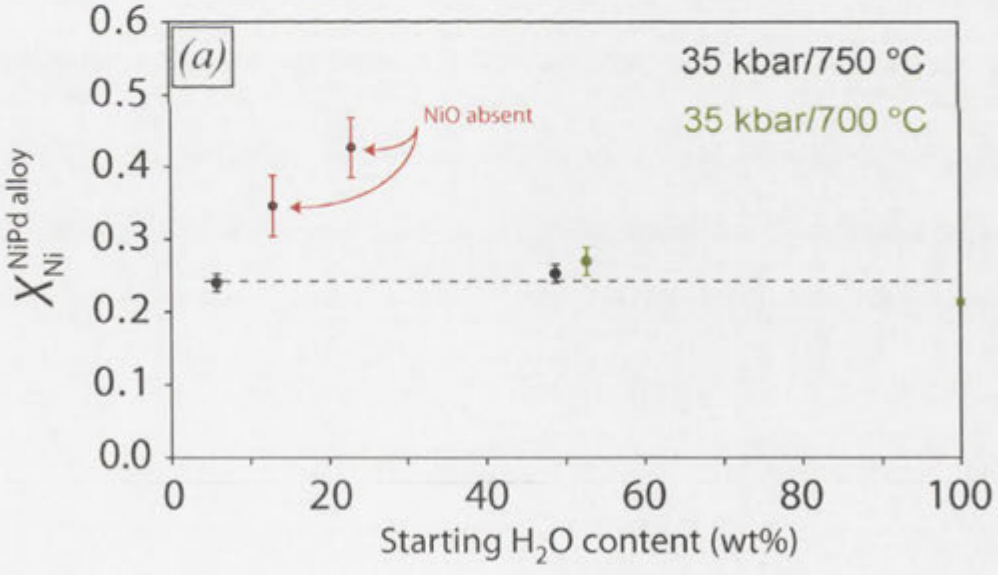

***Figure 14.24**: H-sensor alloy compositions from glass-absent experiments at 35 kbar/700-750 °C. Red symbols represent failed sensors.*

Chapter 15

Discussion

Most of this chapter is focused on using results to provide new estimates of the wet solidus and second critical end-point for the pelite-H_2O system at high pressure (i.e., >20 kbar) as determined by the technique developed in this research. These discussions focus on how textural interpretation of quench products and L-V relationships are related or misleading, and the crucial role experimental quench products play in interpreting run products.

Later sections of this chapter focus on the usefulness of the technique itself. Such discussion centres on how the method provides new avenues of study, providing estimates of a_{H_2O}, while also highlighting the limitations experienced during this study.

15.1: The wet solidus, melting reaction and starting H_2O content

As discussed in the literature review, H_2O solubility in silicate (pelite) melts increases dramatically as a function of pressure (particularly at >20 kbar). This dictates that experiments aimed at determining the wet solidus and run at constant starting H_2O content result in decreasing melt fractions with increasing pressure. Confirming the presence of glass on the basis of textural observations in experiments that contain very small amounts of excess H_2O, such as Schmidt et al. (2004 – 0.4-0.9 wt% H_2O), becomes increasingly difficult as the melt fraction becomes smaller and harder to detect.

The ability to vary pelite:H_2O in the experimental charge described in this research, rather than using hydrous minerals as a constant starting H_2O content (e.g., Nichols et al., 1994; Schmidt et al., 2004, etc), makes constraining the wet solidus far easier to determine on the basis of textural observations (i.e., the higher the H_2O content the larger the volume of melt produced during wet melting). While it is possible to vary pelite:H_2O by changing the modal proportions of hydrous starting minerals, such a technique becomes increasingly complicated when trying to maintain a constant (pelite) starting composition. The use of hydrous minerals also has an upper H_2O limit, which is based on the stability and H_2O content of the various hydrous phases being used. In short, the experimental technique developed in this research is far simpler and has a broader compositional range (in terms of X_{H_2O}) than conventional welded capsule, piston cylinder techniques.

The 35 kbar experiments from this research can be used to make some textural interpretations, and limitation therein, of the pelite wet solidus. The lack of glass in experiments at 700-750 °C, despite starting H_2O contents ranging from 5-50 wt%, and the first appearance of glass at 35 kbar and 800 °C (with starting H_2O contents ranging from 5-23 wt%) indicates that the wet solidus is located at temperatures between 750-800 °C. Observations made from experiments containing large amounts of excess H_2O (50 wt%) at 750 °C and small amounts of excess H_2O (5 wt%) at 800 °C, suggest that a discrete melting event (wet solidus) occurs at 35 kbar.

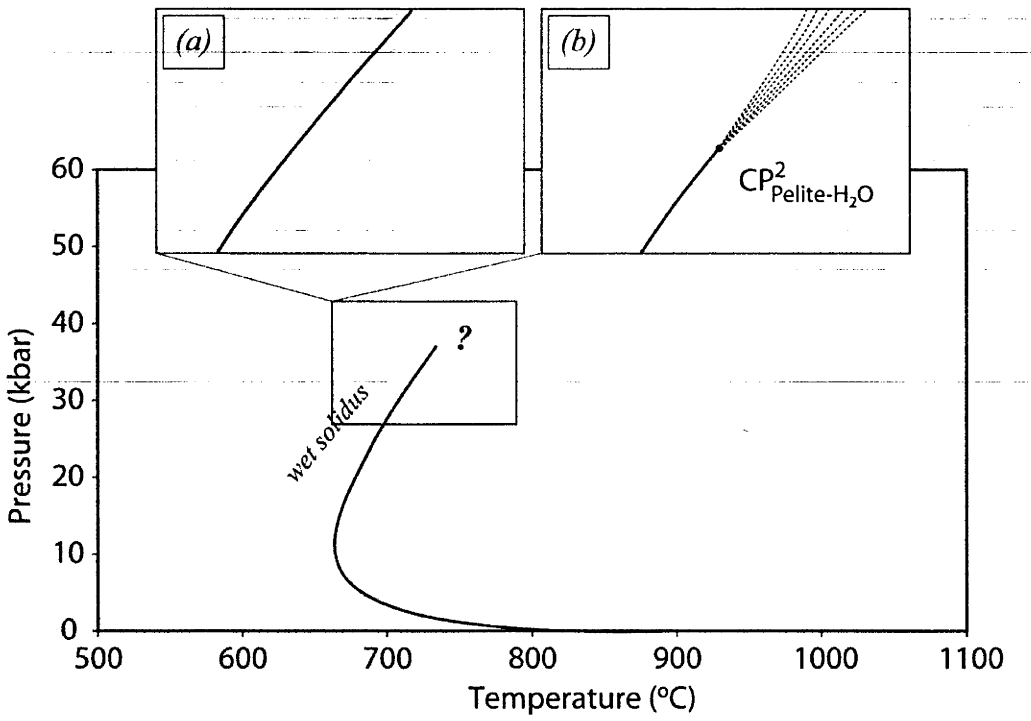

Figure 15.1: The pelite wet solidus as indicated by 35 kbar experiments in this study and previous research (see Figure 9.11). Projection *(a)* shows the existence of a wet solidus to higher pressure, and *(b)* predicts supercrticallity at ~35 kbar with closely spaced solubility isopleths as a function of d*P*-d*T*. It should be noted that projections (a) and (b) likely result in very similar experimental quench products and would be difficult to distinguish on the basis of textures.

It could be argued that the pelite-H_2O system is supercritical at these conditions and the loci of solubility isopleths are so proximal (i.e., smaller than the 50 °C intervals of experiments) that quench products still indicate the presence of a wet solidus (Figure 15.1). This scenario seems unlikely, as the gradual breakdown of phengite would likely produce residual kyanite according to the reaction:

$$\text{Phengite} + H_2O = \text{Garnet} + \text{Kyanite} + \text{'K-Si vapour'} \qquad (\textbf{\textit{eq. 15.1}})$$

where the 'K-Si vapour' represents a potassic- and silicic-bearing H_2O vapour species.

The lack of kyanite and abundance of phengite at 35 kbar/750 °C, particularly in runs containing 50 wt% H_2O, indicates that the vapour phase is solute-poor and a discrete melting event occurs at this pressure.

Given that there is no direct evidence within the literature that can be used to distinguish quench products from sub- and supercritical experiments (without making some fundamental assumptions) both scenarios presented in Figure 15.1 are possible.

The 750-800 °C temperature estimate for the wet solidus is consistent with Hermann and Spandler (2008) and low pressure extrapolations of estimates made by Schmidt et al. (2004).

The melting reaction and phase stability

The mineralogy observed in pelite experiments presented in this research and elsewhere are generally consistent (excluding Johnson and Plank, 1999) at 35 kbar, with the absence of a Ca-rich phase in this work (e.g., clinopyroxene) being the only notable difference. Subsolidus experiments (e.g., 700-750 °C) at 35 kbar are dominated by phengite and quartz/coesite, with the two phases rapidly disappearing with increasing temperature and the appearance of glass. This suggests that the melting reaction for the pelite-H_2O experiments in this research is likely:

$$\text{Phengite} + SiO_2\ (\text{quartz/coesite}) + H_2O = \text{Melt} + \text{Garnet} \qquad (\textbf{\textit{eq. 15.2}})$$

The brief appearance of kyanite following the dissolution of phengite at 35 kbar/900 °C/22.3 wt% H_2O (Figure 15.2) and 25 kbar/900 °C/5.4 wt% H_2O suggests that the melting reaction at ≥25 kbar involves the breakdown of phengite (in the presence of coesite) to produce kyanite and melt, such that:

$$\text{Phengite} + \text{Coesite} + H_2O = \text{Kyanite} + \text{Melt} + \text{Garnet} \qquad (\textbf{\textit{eq. 15.3}})$$

The presence of kyanite after the disappearance of phengite (C-3157 and D-1025) indicates that kyanite is only present at conditions above the wet solidus and is rapidly dissolved within the melt with increasing melt fraction.

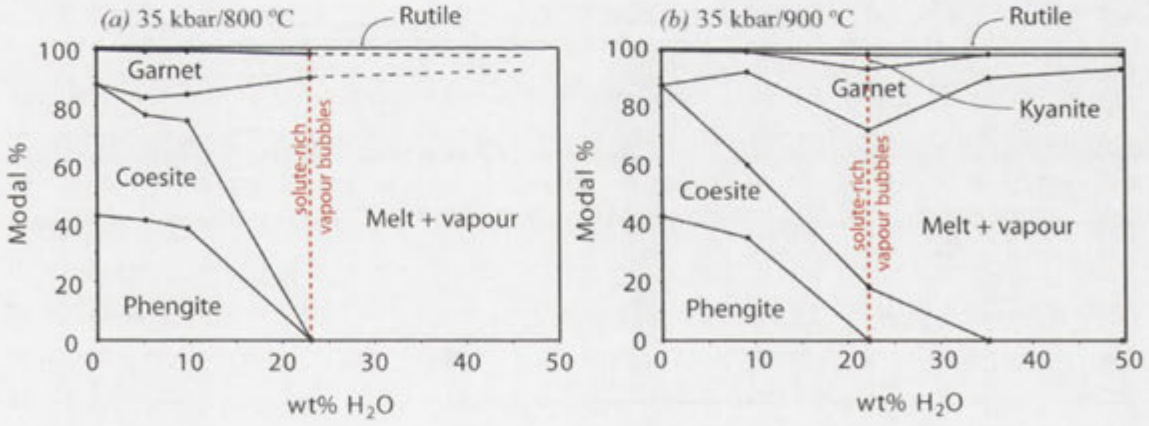

***Figure 15.2**: Modal proportions (volume percent) estimates of (a) 35 kbar/800 °C, and (b) 35 kbar/900 °C runs, based on SEM observations, plotted against starting H_2O content of experiments. Anhydrous estimates represent an average from subsolidus experiments at 35°kbar/750 °C, with the vapour phase (which shows negligible influence on the proportions of solid phases) ignored. Melt + vapour = the estimated proportions of silicate glass and associated vapour bubbles. Dashed red curve indicates the first appearance of solute-bearing, large vapour bubbles within experiments.*

Phase stability

As the glass starting material contains only one solid phase (SiO_2), crystal seeds and remnant phases are not important when considering textural and phase relationships from experiments (a potential problem with existing works in the pelite-H_2O system). At conditions where quartz/coesite is present, the phase shows large, (semi-) euhedral grains

that contain an array of fluid, mineral and melt inclusions. These observations can be collectively used to conclude that SiO_2 is a primary and buffering phase.

Synthetic phengite (excluding vapour bubble-hosted mica) and garnet reported from experiments merit some discussion regarding phase stability and equilibrium. Both phases are notoriously hard to nucleate at sufficient size for analyses (e.g., Schmidt et al., 2004), while garnet is known to show irregular/skeletal textures within experiments (Nichols et al., 1994).

The high Si (pfu) and TiO_2 (wt%) content of synthetic phengites from glass-free and glass-bearing experiments show compositions consistent with previous experimental studies into white micas at high pressure conditions, indicating that the phase is primary. The high Ti content of phengite is particularly noteworthy, as silicate melts in this research all show low TiO_2 (due to the presence of rutile).

Garnet is present in all experiments and is considered a buffering phase over the studied P-T-*X* range. Petrographic observations made from garnets in experiments containing low melt fractions (D-1025 and C-3119) show textures similar to those reported by Nichols et al. (1994), with irregular and disrupted cores surrounded by a rim of crystalline garnet (see Figure 14.9*b*). The remarkably similar composition of synthetic garnets showing skeletal habit to those displaying euhedral habits (at higher melt fractions and the same P-T) suggests that the phase is primary. The skeletal texture seen in low melt fraction experiments is likely related to nucleation, rather than equilibrium processes.

One of the most intriguing observations from these experiments is the presence of phengite in large vapour bubbles (particularly in 35 kbar/900 °C experiments). The reappearance of phengite, a mineral species that defines the minimum melting reaction and rapidly dissolves with increasing melt fraction, complicates textural interpretation of results (here and elsewhere). One way in which these textures may be interpreted is via comparison with 25 kbar experiments, which show large vapour bubbles containing increasing amounts of amorphous and colloidal silicate material as a function of starting H_2O content (at a constant temperature). This suggests that as starting composition approaches the vapour (H_2O) side of the miscibility gap (solvus), the amount of vapour-dissolved solute increases. If the same textural interpretation is applied for 35 kbar experiments, the increasing amount of phengite in large vapour bubbles as a function of starting H_2O content (at 35 kbar/900 °C) represents an increasing amount of solute dissolved within the vapour phase. Using this interpretation, large vapour bubble-hosted phengite can be considered a quench product at pressures ≥35 kbar.

15.2: Textural interpretation of the L-V solvus

The textural diversity observed from experiments in this research serves as an example of the complexity associated with interpretations made from petrographic observations in hydrothermal experiments at high pressure. Textural interpretation includes the stability of

solid phases (minerals), a variety of quench species (e.g., glass, white mica and amorphous silicates) and vapour bubble populations.

If textural interpretation is used to map out or determine whether an experiment within the L=V solvus (or miscibility gap), the presence of two distinct vapour bubble populations, one consisting of a small solute-poor population and the other consisting of a large, solute-rich populations, suggests that all 25 and 35 kbar experiments exist at conditions below the critical curve and second critical end point ($CP^{2}_{Pelite-H_2O}$). This interpretation (as suggested by Johnson and Plank, 1999) assumes that small vapour bubbles represent the H_2O dissolved in the liquid (at experimental P-T) that cannot be quenched, while large vapour bubbles and associated amorphous silicates + mica represent the solutes dissolved within the vapour (at experimental P-T).

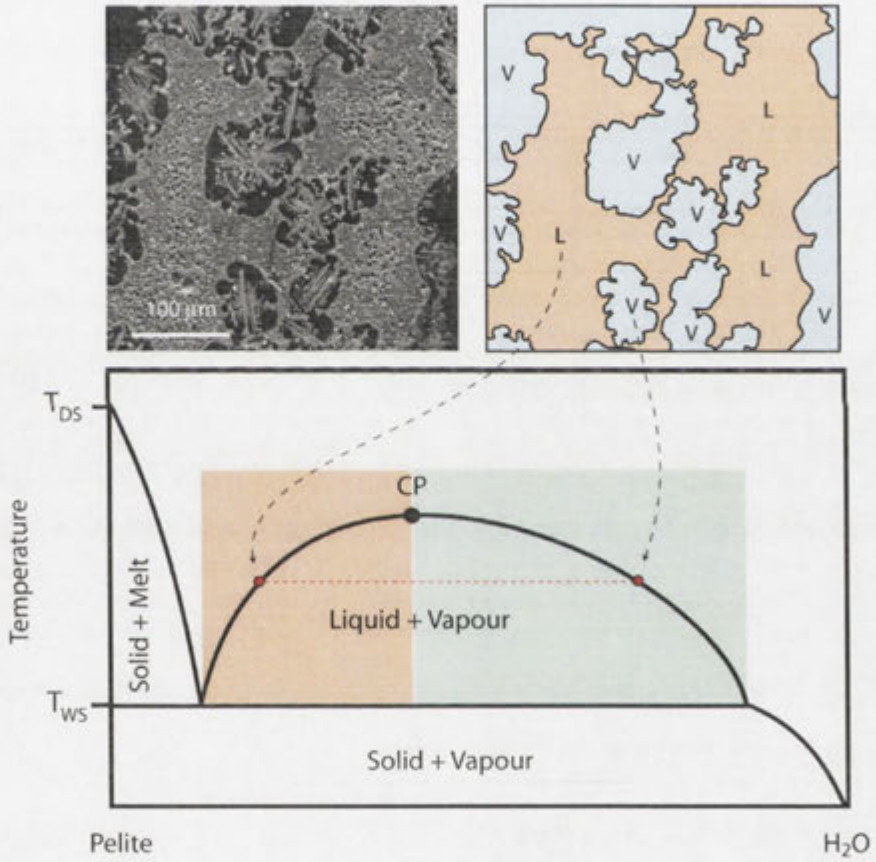

***Figure 15.3**: Textural observations from experiment C-3127. Upper left image shows SEM-BSE backscatter electron image, while upper right image uses petrography to describe liquid (silicate melt, shown in red) and vapour (shown in blue) domains. Textures in this experiment could be used to describe an assemblage that exists within a L+V (two-phase) field as shown in the lower image (theoretical pseudo-binary projection).*

To demonstrate this point, observations from the experiment of the highest pressure, temperature and starting H_2O content (C-3127, 35 kbar/900 °C/50 wt% H_2O) – which is the most likely run from this research to exist at supercritical conditions, are used as an example. Textures from this experiment show two distinct domains (Figure 15.3): the first is dominated by silicate melt and small vapour bubble (see light red hues in Figure 15.3) and

the second is dominated by mica- and amorphous silicate-rich material in large vapour bubbles (see light blue hues in Figure 15.3). These textures show petrographic observations that would be expected from an experiment run within the pelite-H_2O miscibility gap (or pseudo-solvus), namely a solute-rich vapour phase and a H_2O-rich silicate melt.

On the basis of textural observations shown in Figure 15.3, it could readily be assumed that the pelite-H_2O system is subcritical, such that a miscibility gap still exists at 35 kbar/900 °C.

15.3: H-sensors

The original technique

The combined use of oxygen buffers and H-sensors is an entirely new concept in the study of silicate-H_2O systems at high pressure conditions (i.e., systems relevant to subduction zones). This being the case, the original publication describing the H-sensor technique (Taylor et al., 1992) hypothesized that the method could be used to study mixing properties of supercritical vapour species (i.e., at conditions around the $CP^{1}_{Silicate-H_2O}$). This original hypothesis suggests that f_{H_2O} (or a_{H_2O}) can be calculated by comparing H-sensor results from a pure H_2O run to others containing mixtures of H_2O-CO_2 (or some other hydrothermal diluent), provided that experiments are run at constant conditions. The original hypothesis states that changes in f_{H_2O} can be monitored by shifts in f_{O_2} by:

$$\log a_{H_2O} = \log a_{H_2} + \frac{1}{2}\log a_{H_2O} - \log K_{(T,P)} \qquad \textbf{(eq. 15.4)}$$

The technique described by Taylor et al. (1992) was focused on vapour properties in an experiment containing H_2O (or, as hypothesized for supercriticality studies, another vapour species – CO_2) in the outer capsule, such that it needed buffering for f_{O_2} if silicates were added. With these considerations in mind, and in order to adapt that technique to study f_{H_2}, f_{O_2} and f_{H_2O} in systems containing silicate/s (minerals and melt), the experimental technique involves some simple modifications.

Explaining the technique used here

The greatest difference between the research presented here and Taylor et al. (1992) is the involvement of an inert oxygen buffer, in this study Re-ReO_2, to fix f_{O_2} within the outer Ag capsule (Figure 15.4). Both species of this MMO buffer are highly insoluble in hydrous silicate melts, solute-rich vapours and mineral phases present within experiments, such that they buffer f_{O_2} without significantly modifying phase stability or composition. Similarly, Re does not alloy with either the Ag or Pt capsule, so that the buffer or capsule is not lost during runs. These properties, combined with the fact that Re-ReO_2 likely approximates f_{O_2} within subduction slabs (NNO+2), makes the solid media buffer ideal for experimentation.

The inner H-sensor is a passive participant in experiments, and simply monitors the f_{H_2} imposed by the pelite-H_2O system in the outer capsule (Figure 15.4). The NiO-Ni-Pd mix of the H-sensor self-adjusts during experiments as H-diffusion through the thin Pt wall attains an equilibrated f_{H_2} between inner and outer capsules.

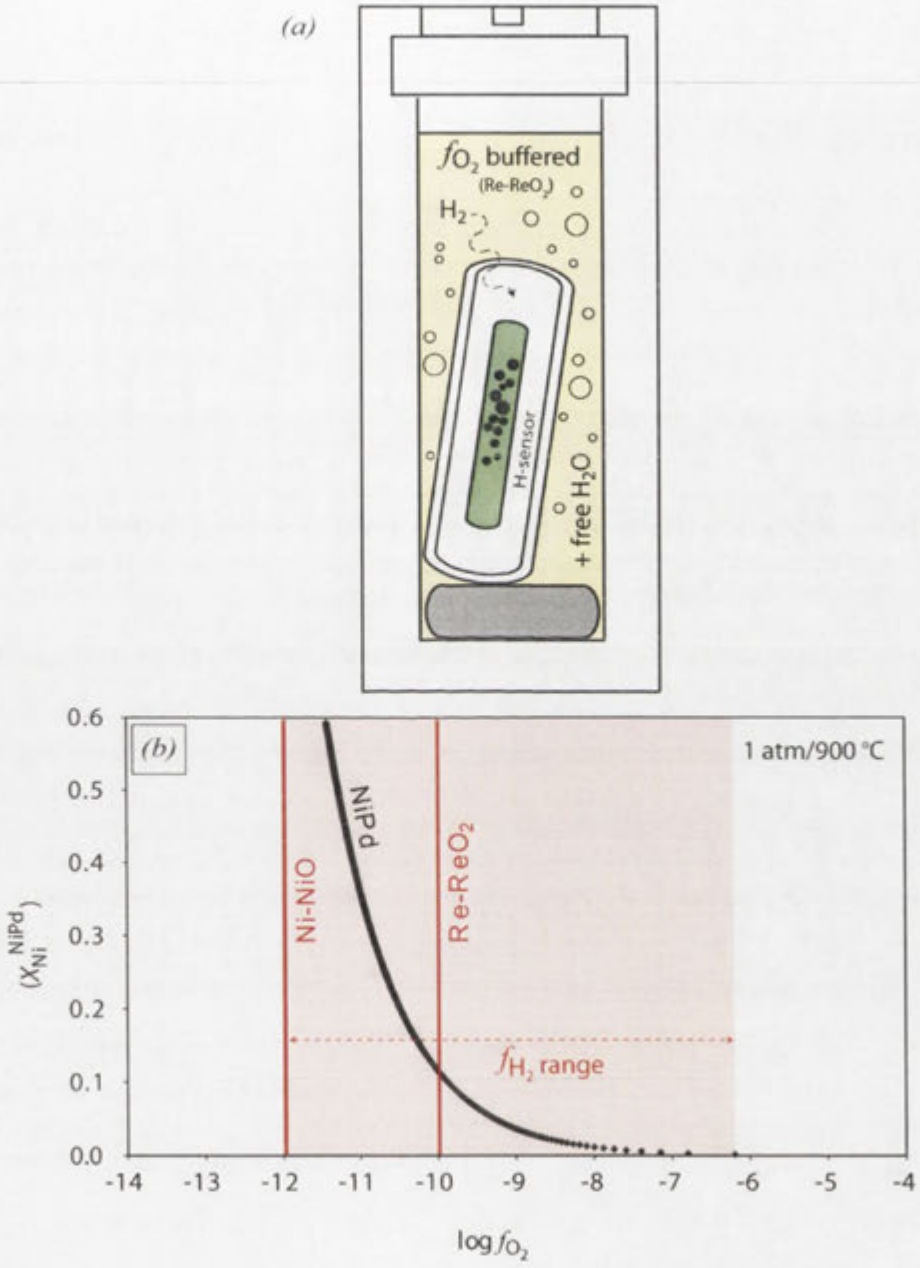

***Figure 15.4**: (a) General schematic of the pelite-H_2O experimental arrangement. Yellow shaded region represents the outer capsule where the pelite-H_2O system has a f_{O_2} buffered by Re-ReO_2. The inner H-sensor (as marked) measures f_{H_2} via H-diffusion through the Pt capsule. (b) MMO f_{O_2} buffers relevant to this experimental technique compared to the working range of the NiO-Ni-Pd H-sensor (shaded red region). It should be noted that as the H-sensor contains no external source of H_2O, decreasing f_{O_2} represents increasing f_{H_2} within the sensor (as imposed by the pelite-H_2O system in the outer Ag capsule).*

If T, P and f_{O_2} are all fixed within an experimental series (i.e., where the only variable is silicate:H_2O), then measured changes in f_{H_2} can be used to monitor changes in f_{H_2O} (or a_{H_2O}) by the reaction:

$$H_2O = H_2 + \frac{1}{2}O_2 \qquad \textbf{(eq. 15.5)}$$

Shifts in the H-sensor alloy with Δf_{H_2} can be considered according to the reaction:

$$Ni \text{ (in NiPd alloy)} + H_2O = NiO + H_2 \qquad \textbf{(eq. 15.6)}$$

Equation 15.6 can be used to demonstrate two important points regarding how the experimental technique can be used to study silicate-H_2O systems. Firstly, if the Ni content of the NiPd alloy (H-sensor) is constant with varying H_2O content among pelite experiments at constant P-T-f_{O_2}, then f_{H_2} and a_{H_2O} must also be constant. Secondly, if the Ni content of the NiPd alloy increases with starting H_2O content among experiments at a constant P-T-f_{O_2}, the f_{H_2} and a_{H_2O} must be increasing. It should be noted that H-sensor results can only be directly compared among experiments at a constant set of P-T conditions (as there will be a pressure and temperature effect on the oxygen buffer and sliding H-sensor).

The ability to monitor changes in the f_{H_2}, and measure relative shifts in a_{H_2O}, make it possible to map out the L-V solvus for the pelite-H_2O system. As shown schematically in Figure 15.5, an experiment that exists within the pelite-H_2O miscibility gap (as projected in the pseudo-binary) must have a constant and defined a_{H_2O}. This is because the geometry of the phase diagram fixes composition of the liquid *(c)* and vapour *(d)*, and changing system composition within the solvus merely changes the proportions of liquid and vapour. Hence, starting composition (*X*) can vary anywhere along dashed red line *c-d* in Figure 15.5, and a_{H_2O} will remain constant. By contrast, a completely miscible or supercritical pelite-H_2O system (i.e., at P-T-*X* conditions above the miscibility gap or solvus), will show gradual increases in a_{H_2O} as starting H_2O increases (i.e., as the supercritical species becomes more "vapour-like" or as $X_{H_2O}^{Pelite-H_2O}$ increases). This is to say that as starting compositions change along the dashed red line *a-b* in Figure 15.5, there will be a gradual change in a_{H_2O}.

Using this theoretical framework (Figure 15.5) it is possible to interpret H-sensor results from pelite-H_2O experiments run at different P-T conditions.

Chapter 16

Conclusions

Results presented in this thesis indicate that supercriticality in the pelite-H_2O system occurs at 40-45 kbar/800-850 °C. Equally important, textural observations from supercritical runs are remarkably similar to those at subcritical conditions (in terms of minerals and vapour bubbles). Experiments also record a reappearance of phengite (white mica) with increases in starting H_2O content at constant P-T (in supersolidus runs at 35 kbar). These observations and results bring into question the use of textural observations to determine supercriticality, particularly where the presence of phengite in experiments is used as a monitor (e.g., Schmidt et al., 2004).

The combined use of H-sensors and phase analyses has constrained the minimum melting reaction and conditions where complete L-V miscibility occurs. Further experimentation in the pelite-H_2O system could provide additional information regarding silicate solubility in the vapour phase (e.g., providing accurate models of solubility isopleths). Hence, whereas the experiments presented here establish potential of the technique, additional runs could provide accurate models of the miscibility gap and solvus topology in the pseudo-binary pelite-H_2O system. The most important direction of future research is to carry out additional runs at 25 and 35 kbar, with particular focus on incomplete experimental series (e.g., 35 kbar/800 °C) and runs at intermediate temperatures (e.g., 850 °C).

As results presented here define supercriticality in the pelite-H_2O system at 40-45 kbar/800-850 °C, future studies should also focus on experiments at ≥40 kbar. Another avenue of future research, as indicated in Appendix 3, should include quantification of trace element systematics in the pelite-H_2O system at subduction conditions. Such studies would help explain the processes involved in trace element recycling from subducting sediment to primitive arc magmas.

16.1: Potential developments of the technique

The results presented here have largely focused on experiments at constant conditions to map out S-L-V relationships in the pelite-H_2O system. The same technique could be used to provide a quantitative estimate of a_{H_2O} in any number of systems pertinent to Earth science (e.g., basalt-H_2O, peridotite-H_2O, etc).

The basic premise of this technique is that two experiments run at constant P-T-f_{O_2}, but one run with an outer capsule containing Re-ReO_2 (the f_{O_2} buffer) + H_2O and another run containing Re-ReO_2 + H_2O + pelite, would to define a_{H_2O} by the following reaction:

$$\ln a_{H_2O} = \ln(a_{Ni}^{NiPdalloy})_{H_2O} - \ln(a_{Ni}^{NiPdalloy})_{Silicate-H_2O} \qquad \textbf{(eq. 15.7)}$$

A total of 12 pure H_2O (+ Re-ReO_2) runs were carried out in an attempt to quantify changes in a_{H_2O} from 25 and 35 kbar experiments. Of these runs, only 2 (35 kbar/700 °C and 35 kbar/800 °C) showed an equilibrated and buffered assemblage. Deformation of the Ag-

and H-sensor capsule at extremely high H_2O contents and temperatures >800 °C, often leads to shearing of the talc insulator or leakage from the capsule. Further work will be required to provide quantitative estimates of a_{H_2O}, particularly at 35 kbar/900 °C and 25 kbar/900 °C (i.e., at P-T conditions at which the most extensive experimental information is available). Furthermore, some redesigning of the capsule/cell assemblage may be required in order to carry out experiments that contain pure H_2O (+Re-ReO_2).

References

Akaogi, M. and Navrotsky, A. (1984) The Quartz Coesite Stishovite Transformations - New Calorimetric Measurements and Calculation of Phase-Diagrams. *Physics of the Earth and Planetary Interiors*, **36**: 124-134.

Amelin, Y., Lee, D.-C. and Halliday, A. N. (2000) Early Middle Archean Crustal Evolution Deduced from Lu-Hf and U-Pb Isotopic of Single Zircon Grains. *Geochimica et Cosmochimica Acta*, **64**: 4205-4225.

Anderson, A. T., Davis, A. M. and Lu, F. Q. (2000) Evolution of Bishop Tuff Rhyolitic Magma Based on Melt and Magnetite Inclusions and Zoned Phenocrysts. *Journal of Petrology*, **41**: 449-473.

Armstrong, R. L. (1971) Isotopic and Chemical Constraints on Models of Magma Genesis in Volcanic Arcs. *Earth and Planetary Science Letters*, **12**: 137–142.

Azough, F., Freer, R., Wang, C. L. and Lorimer, G. W. (1996) The Relationship Between the Microstructure and Microwave Dielectric Properties of Zirconium Titanate Ceramics. *Journal of Materials Science*, **31**: 2539-2549.

Baldwin, J. A., Brown, M. and Schmitz, M. D. (2007) First Application of Titanium-in-Zircon Thermometry to Ultrahigh-Temperature Metamorphism. *Geology*, **35**: 295-298.

Ballman, A. A. and Laudise, R. A. (1965) Crystallization and Solubility of Zircon and Phenacite in Certain Molten Salts. *Journal of the American Ceramic Society*, **48**: 130-133.

Bea, F., Montero, P., Gonzalez-Lodeiro, F. and Talavera, C. (2007) Zircon Inheritance Reveals Exceptionally Fast Crustal Magma Generation Processes in Central Iberia During the Cambro-Ordovician. *Journal of Petrology*, **48**: 2327-2339.

Bejan, A. (1993) Heat Transfer. Wiley, New York, 675 pp.

Berry, A. J., Walker, A. M., Hermann, J., O'Neill, H. S. C., Foran, G. F. and Gale, J. D. (2007) Titanium Substitution in Forsterite. *Chemical Geology*, **242**: 176-186.

Bianco, A., Paci, M. and Freer, R. (1998) Zirconium Titanate-from Polymeric Precursors to Bulk Ceramics. *Journal of the European Ceramics Society*, **18**: 1235-1243.

Bodnar, R. J. and Sterner, S. M. (1985) Synthetic fluid inclusions in natural quartz II. Application to PVT studies. *Geochimica et Cosmochimica Acta*, **49**: 1855–1859.

Boettcher, A. L., Windom, K. E., Bohlen, S. R. and Luth, R. W. (1981) Low Friction, Anhydrous, Low- to High-Temperature Furnace Sample Assembly for Piston-Cylinder Apparatus. *Review of Scientific Instruments*, **52**: 1903-1904.

Boettcher, A. L. and Wyllie, P. J. (1969) The System $CaO-SiO_2-CO_2-H_2O$. Second Critical End-Point on the Melting Curve. *Geochimica et Cosmochimica Acta*, **33**: 611-632.

Bohlen, S. R. and Boettcher, A. L. (1982) The Quartz-Coesite Transformation: A Precise Determination and the effects of other Components. *Journal of Geophysical Research*, **87**: 7073-7078.

Bordet, P., McHale, A., Santoro, A. and Roth, R. S. (1986) Powder Neutron-Diffraction Study of $ZrTiO_4$, $Zr_5Ti_7O_{24}$, and $Fe_nB_2O_6$. *Journal of Solid State Chemistry*, **64**: 30-46.

Bose, K. and Ganguly, J. (1995a) Experimental and Theoretical Studies of the Stabilities of Talc, Antigorite and Phase A at High Pressures with Applications to Subduction Processes. *Earth and Planetary Science Letters*, **136**: 109-121.

Bose, K. and Ganguly, J. (1995b) Quartz-Coesite Transition Revisited: Reversed Experimental Determination at 500-1200°C and Retrieved Thermochemical Properties. *American Mineralogist*, **80**: 231-238.

Boyd, F. R. and England, J. L. (1960) The Quartz-Coesite Transition. *Journal of Geophysical Research*, **65**: 749-756.

Brodholt, J. P. and Wood, B. J. (1993) Simulations of the Structure and Thermodynamic Properties of Water at High Pressures and Temperatures. *Journal of Geophysical Research*, **98**: 519-536.

Brodholt, J. P. and Wood, B. J. (1994) Measurements of the PIZ Properties of Water to 25 kbars and 1600°C from Fluid Inclusions in Corundum. *Geochemistry Geophysics and Geosystems*, **58**: 2143-2148.

Brown, F. H. and Duwez, P. (1954) The Zirconia-Titania System. *Journal of the American Ceramic Society*, **37**: 129-132.

Buhl, J. C. and Willgallis, A. (1989) Hydrothermal Synthesis of $(Zr_{0.33}\ Ti_{0.67})O_2$ - Srilankite in the System $ZrO_2-TiO_2-H_2O$-Naf, Kf. *Crystal Research and Technology*, **24**: 263-268.

Bureau, H. and Keppler, H. (1999) Complete Miscibility between Silicate Melts and Hydrous Fluids in the Upper Mantle: Experimental Evidence and Geochemical Implications. *Earth and Planetary Science Letters*, **165**: 187-196.

Burnham, C. W. and Davis, N. F. (1974) The Role of H_2O in Silicate Melts; II, Thermodynamic and Phase Relations in the System $NaAlSi_3O_8$ –H_2O to 10 Kilobars, 700 Degrees to 1100 Degrees C. *American Journal of Science*, **274**: 902-940.

Carson, C. J., Powell, R. and Clarke, G. L. (1999) Calculated Mineral Equilibria for Eclogites in CaO-Na_2O-FeO-MgO-Al_2O_3-SiO_2-H_2O; Application to the Pouebo Terrane, Pam Peninisula, New Calidonia. *Journal of Metamorphic Geology*, **17**: 9-24.

Carte, A. E. (1955) Thermal constants of pyrophyllite and their change on heating. *British Journal of Applied Physics*, **6**: 326-328.

Cherniak, D. J. and Watson, E. B. (2007) Ti Diffusion in Zircon. *Chemical Geology*, **242**: 470-483.

Chou, I. M. (1978) Calibration of Oxygen Buffers at Elevated-P and Elevated-T Using Hydrogen Fugacity Sensor. *American Mineralogist*, **63**: 690-703.

Chou, I. M. (1986) Permeability of Precious Metals to Hydrogen at 2 kb Total Pressure and Elevated Temperatures. *American Journal of Science*, **286**: 638-658.

Chou, I. M. (1987a) Calibration of the Graphite-Methane Buffer Using the Fh_2 Sensors at 2-Kbar Pressure. *American Mineralogist*, **72**: 76-81.

Chou, I. M. (1987b) Phase-Relations in the System NaCl-KCl-H_2O .3. Solubilities of Halite in Vapor-Saturated Liquids above 445-Degree-C and Redetermination of Phase-Equilibrium Properties in the System NaCl-H_2O to 1000-Degree-C and 1500 Bars. *Geochimica et Cosmochimica Acta*, **51**: 1965-1975.

Chou, I. M. and Eugster, H. P. (1976) Sensor for Hydrogen Fugacities at Elevated-P and Elevated-T and Applications. *Transactions-American Geophysical Union*, **57**: 340-340.

Chou, I. M., Eugster, H. P., Berens, P. and Weare, J. H. (1978) Diffusion of Hydrogen through Platinum Membranes at High-Pressures and Temperatures. *Geochimica et Cosmochimica Acta*, **42**: 281-288.

Chou, I. M. and Williams, R. J. (1977) Hydrogen Fugacity Sensor Measurements of Quartz-Fayalite-Magnetite and Hematite-Magnetite Buffer Reactions. *Transactions-American Geophysical Union*, **58**: 520-520.

Claiborne, L. L., Miller, C. F., Walker, B. A., Wooden, J. L., Mazdab, F. K. and Bea, F. (2006) Tracking Magmatic Processes Through Zr/Hf Ratios in Rocks and Hf and Ti Zoning in

Zircons: An example from the Spirit Mountain batholith, Nevada. *Mineralogical Magazine*, **70**: 517-543.

Cohan, L. H., Klement Jr, W. and Kennedy, G. C. (1966) Melting of Cu, Ag and Au at high pressures. *Physical Review Letters*, **145**: 519-525.

Corfu, F., Hanchar, J. M., Hoskin, P. W. O. and Kinny, P. (2003) Atlas of Zircon Textures. *Reviews in Mineralogy and Geochemistry*, **53**: 469-500.

Coughanour, L. W., Roth, R. S. and Deprosse, V. A. (1954) Phase Equilibrium Relations in the Systems Lime-Titania and Zirconia-Titania. *Journal of Research of the National Bureau of Standards*, **52**: 37-41.

Cygan, G. L. and Chao, I. M. (1987) Calibration of the WO_2-WO_3 buffer. *EOS*, **68**: 451.

Degeling, H. S. (2003) Zr Equilibria in Metamorphic Rocks. PhD Thesis, 231 pp.

Ellis, P. J. and Freeman, H. C. (1995) Xfit - an Interactive Exafs Analysis Program. *Journal Of Synchrotron Radiation*, **2**: 190-195.

Eugster, H. P. (1957) Heterogeneous Reactions Involving Oxidation and Reduction at High Pressures and Temperatures. *Journal of Chemical Physics*, **26**: 1760-1761.

Farges, F. (1997) Coordination of Ti^{4+} in Silicate Glasses: a High-Resolution XANES Spectroscopy Study of the Ti K Edge. *American Mineralogist*, **82**: 36-43.

Farges, F., Brown Jr., G. E. and Rehr, J. J. (1996a) Coordination Chemistry of Ti(IV) in Silicate Glasses and Melts: I. XAFS study of Titanium Coordination in Oxide Compounds. *Geochimica et Cosmochimica Acta*, **60**: 3023-3038.

Farges, F., Brown Jr., G. E. and Rehr, J. J. (1996b) Coordination Chemistry of Ti(IV) in Silicate Glasses and Melts: II. Glasses at Ambient Temperature and Pressure. *Geochimica et Cosmochimica Acta*, **60**: 3039-3053.

Farges, F., Brown Jr., G. E. and Rehr, J. J. (1997) Ti K-edge XANES Studies of Ti Coordination and Disorder in Model Compounds: Comparison Between Theory and Experiment. *Physical Review*, **B56**: 1809-1819.

Ferry, J. M. and Watson, E. B. (2007) New Thermodynamic Models and Revised Calibrations for the Ti-in-Zircon and Zr-in-Rutile Thermometers. *Contributions to Mineralogy and Petrology*, **154**: 429-437.

Finch, R. J. and Hanchar, J. M. (2003) Structure and Chemistry of Zircon and Zircon-Group Minerals. *Reviews in Mineralogy and Geochemistry*, **53**: 1-25.

Finch, R. J., Hanchar, J. M., Hoskin, P. W. O. and Burns, P. C. (2001) Rare-Earth Elements in Synthetic Zircon: Part 2. A Single-Crystal X-ray Study of Xenotime Substitution. *American Mineralogist*, **86**: 681-689.

Frantz, J. D. and Eugster, H. P. (1973) Acid-Base Buffer - Use of Ag + AgCl in Experimental Control of Solution Equilibria at Elevated Pressures and Temperatures. *American Journal of Science*, **273**: 268-286.

Fu, B., Page, F. Z., Cavosie, A. J., Fournell, J., Kita, N. T., Lackey, J. S., Wile, S. A. and Valley, J. W. (2008) Ti-in-Zircon Thermometry: Applications and Limitations. *Contributions to Mineralogy and Petrology*, **156**: 197-215.

Gale, J. D. (2006) A Periodic Density Functional Study of the Location of Titanium within TS-1. *Solid State Science*, **8**: 234-240.

Gardien, V., Thompson, A. B., Grujic, D. and Ulmer, P. (1995) Experimental Melting of Biotite Plus Plagioclase Plus Quartz Plus of Minus Muscovite Assemblages and Implications for Crustal Melting. *Journal of Geophysical Research*, **100**: 15581-15591.

Glikson, A. Y. (2006) Comment on "Zircon Thermometry Reveals Minimum Melting Conditions on Earliest Earth" I. *Science*, **311**: 779a.

Green, D. H. (1973) Experimental Melting Studies on a Model Upper Mantle Composition at High Pressure under Water-Saturated and Water-Undersaturated Conditions. *Earth and Planetary Science Letters*, **19**: 37-53.

Gummow, R. J. and Sigalas, I. (1988) The thermal conductivity of talc as a function of pressure and temperature. *International Journal of Thermophysics*, **9**: 1111-1120.

Hack, A. C. and Mavrogenes, J. A. (2006) A cold-Sealing Capsule Design for Synthesis of fluid Inclusions and other Hydrothermal Experiments in Piston-Cylinder Apparatus. *American Mineralogist*, **91**: 203-210.

Hack, A. C., Thompson, A. B. and Aerts, M. (2007) Phase Relations Involving Hydrous Silicate Melts, Aqueous Fluids, and Minerals. *mineralogical Society of America*, **65**: 129-185.

Hanchar, J. M., Finch, R. J., Hoskin, P. W. O., Watson, E. B., Cherniak, D. J. and Mariano, A. N. (2001) Rare Earth Elements in Synthetic Zircon: Part 1. Synthesis, and Rare Earth Element and Phosphorus Doping. *American Mineralogist*, **86**: 667-680.

Hanchar, J. M. and Miller, C. F. (1993) Zircon Zonation Patterns as Revealed by Cathodoluminescence and Backscattered Electron Images: Implications for Interpretation of complex Histories. *Chemical Geology*, **110**: 1-13.

Hanchar, J. M. and Rudnick, R. L. (1995) Revealing Hidden Structures: The Application of Cathodoluminescence and Back-Scattered Electron Imaging to Dating Sircons from Lower Crustal Xenoliths. *Lithos*, **36**: 289-303.

Hanchar, J. M. and Watson, E. B. (2003) Zircon Saturation Thermometry. *Zircon*, **53**: 89-112.

Harrison, T. M., Aikman, A. B., Holden, P., Walker, A. M., McFarlane, C., Rubatto, D. and Watson, E. B. (2005a) Testing the Ti-in-Zircon Thermometer, American Geophysical Union, Fall Meeting, San Fransisco, America.

Harrison, T. M., Blichert-Toft, J., Muller, W., Albarede, F., Holden, P. and Mojzsis, S. J. (2005b) Heterogeneous Hadean Hafnium: Evidence of Continental Crust at 4.4 to 4.5 Ga. *Science*, **310**: 1947-1950.

Harrison, T. M. and Schmitt, A. K. (2007) High Sensitivity Mapping of Ti Distributions in Hadean Zircons. *Earth and Planetary Science Letters*, **261**: 9-19.

Harrison, T. M., Schmitt, A. K., McCulloch, M. T. and Lovera, O. M. (2008) Early (>= 4.5 Ga) Formation of Terrestrial Crust: Lu-Hf, delta O-18, and Ti Thermometry Results for Hadean Zircons. *Earth and Planetary Science Letters*, **268**: 476-486.

Harrison, T. M., Watson, E. B. and Aikman, A. B. (2007) Temperature Spectra of Zircon Crystallization in Plutonic Rocks. *Geology*, **35**: 635-638.

Hawkesworth, C. J., Gallagher, K., Hergt, J. M. and McDermott, F. (1994) Destructive Plate Margin Magmatism: Geochemistry and Melt Generation. *Lithos*, **33**: 169-188.

Hayden, L. A. and Watson, E. B. (2007) Rutile saturation in Hydrous Siliceous Melts and its Bearing on Ti-Thermometry of Quartz and Zircon. *Earth and Planetary Science Letters*, **258**: 561-568.

Hermann, J. (2002) Experimental Constraints on Phase Relations on Subducted Continental Crust. *Contributions to Mineralogy and Petrology*, **143**: 219-235.

Hermann, J., O'Neill, H. S. C. and Berry, A. (2005) Titanium Solubility in Olivine in the System TiO2-MgO-SiO2: No Evidence for an Ultra-Deep Origin of Ti-bearing Olivine. *Contributions to Mineralogy and Petrology*, **148**: 746-760.

Hermann, J., Rubatto, D., Korsakov, A. and Shatsky, V. (2001) Multiple Zircon Growth During Fast Exhumation of Diamondiferous, Deeply Subducted Continental Crust (Kokchetav Massif Kazakhstan). *Contributions to Mineralogy and Petrology*, **141**: 66-82.

Hermann, J. and Spandler, C. (2008) Sediment Melts at Sub-arc Depths: an Experimental Study. *Journal of Petrology*, **49**: 717-740.

Hermann, J., Spandler, C., Hack, A. and Korsakov, A. V. (2006) Aqueous Fluids and Hydrous Melts in High-Pressure and Ultra-High Pressure Rocks: Implications for Element Transfer in Subduction Zones. *Lithos*, **92**: 399-417.

Hiess, J., Nutman, A. P., Bennett, V. C. and Holden, P. (2008) Ti-in-zircon Thermometry Applied to Constraining Archean Metamorphic and Igneous Systems. *Chemical Geology*, **247**: 323-338.

Hohenberg, P. and Kohn, W. (1964) Inhomogeneous Electron Gas. *Physical Review*, **136**: 864-871.

Holden, P., Aikman, A. B., Ireland, T. R. and Hiess, J. (2005) Does Ti Record the Crystallization Temperature of Zircon, American Geophysical Union, Fall Meeting, San Fransisco, America.

Hole, M. J., Saunders, A. D., Marriner, G. F. and Tarney, J. (1984) Subduction of Pelagic Sediments: Implications for the Origin of Ce-anomalous Basalts from the Mariana Islands. *Geological Societry of London*, **141**: 453-472.

Holland, T. J. B. and Powell, R. (1998) An Internally Consistent Thermodynamic Data set for Phases of Petrological Interest. *Journal of Metamorphic Geology*, **16**: 309-343.

Holloway, J. R. and Wood, B. J. (1988) Simulating the Earth: Experimental Geochemistry. Unwin-Hyman, New York, 196 pp.

Huang, W. L. and Wyllie, P. J. (1973) Melting Relations of Muscovite Granite to 35 kbar as a Model for Fusion of Metamorphosed Subducted Oceanic Sediments. *Contributions to Mineralogy and Petrology*, **24**: 1-14.

Huang, W. L. and Wyllie, P. J. (1975) Melting Reactions in the System $NaAlSi_3O_8$–$KAlSi_3O_8$–SiO_2 to 35 Kilobars, Dry and with Excess Water. *Journal of Geology*, **83**: 737–748.

Huebner, J. S. (1971) Buffering Techniques for Hydrostatic Systems at Elevated Pressures. In: G. C. Ulmer (Editor), Research Techniques for High Pressure and High Temperature. Springer-Verlag, pp. 123-177.

Jochum, K. P., Nohl, L., Herwig, K., Lammel, E., Stoll, B. and Hofmann, A. W. (2005) GeoReM: A new geochemical database for reference materials and isotopic standards. *Geostandards and Geoanalytical Research*, **29**: 333-338.

Johannes, W., Bell, P. M., Mao, H. K., Boettche.Al, Chipman, D. W., Hays, J. F., Newton, R. C. and Seifert, F. (1971) Interlaboratory Comparison of Piston-Cylinder Pressure Calibration Using Albite-Breakdown Reaction. *Contributions to Mineralogy and Petrology*, **32**: 24-38.

Johnson, M. C. and Plank, T. (1999) Dehydration and Melting Experiments Constrain the Fate of Subducted Sediments. *Geochemistry Geophysics and Geosystems*, **1**: 10.1029/1999GC000014.

Junquera, J., Paz, O., Sánchez-Portal, D. and Artacho, E. (2001) Numerical Atomic Orbitals for Linear-Scaling Calculations. *Physical Review B*, **64**: 235111, 1-9.

Kay, R. W., Sun, S.-S. and Hu, C.-N. (1978) Pb and Sr isotopes in Volcanic Rocks from the Aleutian Islands and Pribilof Islands, Alaska. *Geochimica et Cosmochimica Acta*, **42**: 263-273.

Kennedy, G. C., Wasserberg, G. J., Heard, H. C. and Newton, R. C. (1962) The Upper Three-Phase Region in the System SiO_2-H_2O. *American Journal of Science*, **260**: 501-521.

Kincaid, C. and Griffiths, R. W. (2004) Variability in Flow and Temperatures within Mantle Subduction Zones. *Geochemistry Geophysics and Geosystems*, **5**: 10.1029/2003GC000666.

Kohn, W. and Sham, L. J. (1965) Self-Consistent Equations Including Exchange and Correlation Effects. *Physical Review*, **140**: 1133-1138.

Kushiro, I., Syono, Y. and Akimoto, S. (1968) Melting of a Peridotite Nodule at High Pressures and High Water Pressures. *Journal of Geophysical Research*, **73**: 6023-6029.

Lambert, I. B. and Wyllie, P. J. (1972) Melting of Gabbro (quartz eclogite) with Excess Water to 35 Kilobars, with Geological Applications. *Journal of Geology*, **80**: 693-708.

Le Bas, M. J., Le Maitre, R. W., Strekeisen, A. and Zanettin, B. (1986) A Chemical Classification of Volcanic Rocks Based on the Total Alkali-Silica Diagram. *Journal of Petrology*, **27**: 745-750.

Le Breton , N. and Thompson, A. B. (1988) Fluid-absent (dehydration) Melting of Biotite in Metapelites in the Early Stages of Crustal Anatexis. *Contributions to Mineralogy and Petrology*, **99**: 226-237.

Lee, C.-T. and Rudnick, R. (1999) Compositionally Stratified Cratonic Lithosphere: Petrology and Geochemistry of Peridotite Xenoliths from the Labait Volcano, Tanzania. In: J. J. Gurney and S. R. richardson (Editors), Proceedings of seventh international kimberlite conference, Cape Town, pp. 503–521.

Levin, E. M., Robbins, C. R. and McMurdie, H. F. (1969) Phase Diagrams for Ceramists. The American Ceramic Society, Columbus, Ohio, 601 pp.

Lin, P.-N. (1992) Trace Element and Isotopic Characteristics of Western Pacific Pelagin Sediments: Implications for the Petrogenesis of Mariana Arc Magmas. *Geochimica et Cosmochimica Acta*, **56**: 1641-1654.

Longerich, H. P., Jackson, S. E. and Günther, D. (1996) Elemental fractionation in laser ablation-inductively coupled plasma-mass spectrometry: evidence for mass olad induced matrix effects in the ICP during ablation of silicate glass. *Journal of Analytical Atomic Spectrometry*, **11**: 899-904.

Maas, R., Kinny, P. D., Williams, I. S., Froude, D. O. and Compston, W. (1992) The Earths Oldest Known Crust - a Geochronological and Geochemical Study of 3900-4200 Ma Old Detrital Zircons from Mt Narryer and Jack Hills, Western-Australia. *Geochimica et Cosmochimica Acta*, **56**: 1281-1300.

Mallmann, G. and O'Neill, H. s. C. (2007) The effect of Oxygen Fugacity on the Partitioning of Re between Crystals and Silicate Melt during Mantle Melting. *Geochimica et Cosmochimica Acta*, **71**: 2837-2857.

Mariano, A. N. (1989) Cathodoluminescence Emission Spectra of Rare Earth Element Activators in Minerals. In: B. R. Lipin and G. A. McKay (Editors), Geochemistry and Mineralogy of Rare Earth Elements. Reviews in Mineralogy 21, Mineralogical Society of America, pp. 339-348.

Massalski, T. B. (1986) Binary Alloy Phase Diagrams. American Society of Metals, 1-2, 3589 pp.

Massonne, H.-J. and Szpurka, Z. (1997) Thermodynamic Properties of White Micas on the Basis of High-Pressure Experiments in the Systems K_2O-MgO-Al_2O_3-SiO_2-H_2O and K_2O-FeO-Al_2O_3-SiO_2-H_2O. *Lithos*, **41**: 229-250.

McDade, P., Wood, B. J. and Van Westrenen, W. (2002) Pressure corrections for a selection of piston-cylinder cell assemblies. *Mineralogical Magazine*, **66**: 1021-1028.

McDonough, W. F. and Frey, F. A. (1989) Rare Earth Elements in Upper Mantle Rocks. *Reviews in Mineralogy and Geochemistry*, **21**: 99-145.

McHale, A. and Roth, R. S. (1986) Low-Temperature Phase Relationships in the System ZrO_2-TiO_2. *Journal of the American Ceramic Society*, **69**: 827-832.

McHale, A. E. and Roth, R. S. (1983) Investigation of the Phase-Transition in $ZrTiO_4$ and $ZrTiO_4$-SnO_2 Solid-Solutions. *Journal of the American Ceramic Society*, **66**: C18-C20.

Médard, E., McCammon, C. A., Barr, J. A. and Grove, T. L. (2008) Oxygen Fugacity, Temperature Reproducibility, and H_2O Contents of Nominally Anhydrous Piston-Cylinder Experiments using Graphite Capsules. *American Mineralogist*, **93**: 1838-1844.

Merrill, R. B., Robertson, J. K. and Wyllie, P. J. (1970) Melting Reactions in the System $NaAlSi_3O_8$-$KAlSi_3O_8$-SiO_2-H_2O to 20 Kilobars Compared with Results for other Feldspar-Quartz-H_2O and Rock-H_2O Systems. *Journal of Geology*, **78**: 558-569.

Millhollen, G. L., Wyllie, P. J. and Burnham, C. W. (1971) Melting Relations of $NaAlSi_3O8$ to 30 kb in the Presence of H_2O:CO_2 = 50:50 Vapor. *American Journal of Science*, **271**: 473-480.

Mirwald, P. W., Getting, I. C. and Kennedy, G. C. (1975) Low-Friction Cell for Piston-Cylinder High-Pressure Apparatus. *Journal of Geophysical Research*, **80**: 1519-1529.

Morris, J. D. and Tera, F. (1989) ^{10}Be and ^{9}Be in Mineral Separates and Whole Rocks from Volcanic Arcs: Implications for Sedimen Subduction. *Geochimica et Cosmochimica Acta*, **53**: 3197–3206.

Myers, J. and Eugster, H. P. (1983) The System Fe-Si-O - Oxygen Buffer Calibrations to 1,500k. *Contributions to Mineralogy and Petrology*, **82**: 75-90.

Mysen, B. O. (1973) Melting in a Hydrous Mantle: Phase Relations of Mantle Peridotite with Controlled Water and Oxygen Fugacitie. Carnegie Instn. Washington, Year Book 72, 467-478 pp.

Newnham, R. E. (1967) Crystal Structure of $ZrTiO_4$. *Journal of the American Ceramic Society*, **50**: 216.

Newton, R. C. and Manning, C. E. (2008) Solubility of Corundum in the System Al2O3-SiO2-H2O-NaCl at 800°C and 10 kbar. *Chemical Geology*, **249**: 250-261.

Nichols, G. T., Wyllie, P. J. and Stern, C. R. (1994) Subduction Zone Melting of Pelagic Sediments Constrained by Melting Experiments. *Nature*, **371**: 785-788.

Noguchi, T. and Mizuno, M. (1968) Phase Changes in ZrO_2-TiO_2 System. *Bulletin of the Chemical Society of Japan*, **41**: 2895-2899.

Nutman, A. P. (2006) Comment of "Zircon Thermometer Reveals Minimum Melting Conditions on Earliest Earth" II. *Science*, **311**: 779b.

Nyman, H., Hyde, B. G. and Andersson, S. (1984) Zircon, Anhydrite, Scheelite and Some Related Structures Containing Bisdisphenoids. *Acta Crystallographica Section B-Structural Science*, **40**: 441-447.

O'Neill, H. S. and Nell, J. (1997) Gibbs Free Energies of Formation of RuO_2, IrO2, and OsO_2: A High-Temperature Electrochemical and Calorimetric Study. *Geochimica et Cosmochimica Acta*, **61**: 5279-5293.

O'Neill, H. S. C. (1986) Mo-MoO_2 (Mom) Oxygen Buffer and the Free-Energy of Formation of MoO_2. *American Mineralogist*, **71**: 1007-1010.

O'Neill, H. S. C. (1987a) Free energies of formation of NiO, CoO, Ni_2SiO_4, and $CoSiO_4$. *American Mineralogist*, **72**: 280-291.

O'Neill, H. S. C. (1987b) Quartz-Fayalite-Iron and Quartz-Fayalite-Magnetite Equilibria and the Free-Energy of Formation of Fayalite (Fe_2SiO_4) and Magnetite (Fe_3O_4). *American Mineralogist*, **72**: 67-75.

O'Neill, H. S. C. and Pownceby, M. I. (1993) Thermodynamic Data from Redox Reactions at High Temperatures. 1. An Experimental and Theoretical Assessment of the Electrochemical Method using Stabalized Zirconia Electrolytes, with Revised Values for the Fe-"FeO", Co-CoO, Ni-NiO and Cu-Cu_2O Oxygen Buffers, and New Data for the W-WO_2 Buffer. *Contributions to Mineralogy and Petrology*, **114**: 296-394.

O'Neill, H. S. C. and Mavrogenes, J. A. (2002) The Sulfide Capacity and the Sulfur Content at Sulfur Saturation of Silicate Melts at 1400°C and 1 bar. *Journal of Petrology*, **43**: 1049-1087.

Ohnenstetter, D., Cesbron, F., Remond, G., Caruba, R. and Claude, J.-M. (1991) Émissions de Cathodoluminescence de deux Populations de Zircons Naturels: Téntative d'interpretation. *Comptes Rendues de l´Academie des ScSciences. Serie II de la Terre et des planets*, **313**: 641-647.

Ono, A. (1972) Phase Transformation in the System ZrO_2-CeO_2. *433*, **7**: 66-76.

Paillat, O., Elphick, S. C. and Brown, W. L. (1992) The Solubility of Water in $NaAlSi_3O_8$ Melts: a Re-examination of Ab-H_2O Phase Relationships and Critical Behavior at High Pressures. *Contributions to Mineralogy and Petrology*, **112**: 490-500.

Palin, E. J., Walker, A. M. and Harrison, R. J. (2008) A Computational Study of Order-Disorder Phenomena in Mg_2TiO_4 Spinel (qandilite). *American Mineralogist*, **93**: 1363-1372.

Pawley, A. R. and Wood, B. J. (1995) The High Pressure Stability of Talc and 10 A Phase: Potential Storage Sites for H_2O in Subduction Zones. *American Mineralogist*, **80**: 998-1003.

Peacock, S. M., Rushmer, T. and Thompson, A. B. (1994) Partial Melting of Subducting Oceanic-Crust. *Earth and Planetary Science Letters*, **121**: 227-244.

Pearce, J. A., Stern, R. C., Bloomer, S. H. and Fryer, P. (2005) Geochemical Mapping of the Mariana Arc-Basin System: Implications for the Nature and Distribution of Subduction Components. *Geochemistry Geophysics and Geosystems*, **6, Q07006**(7): doi:10.1029/2004GC000895.

Peate, D. W., Pearce, J. A., Hawkesworth, C. J., Colley, H., Edwards, C. M. H. and Hirose, K. (1997) Geochemical Variations in Vanuatu Arc Lavas: The Role of Subducted Material and a Variable Mantle Wedge Composition. *Journal of Petrology*, **38**: 1331-1358.

Pena, P. and DeAza, S. (1976) The ZrO_2-SiO_2-TiO_2-system. *Boletin de la Sociedad Espanola de Articulo de Revision Ceramica y Vidrio*, **15**: 93-95.

Perdew, J. P., Burke, K. and Emzerhof, M. (1996) Generalized Gradient Approximation Made Simple. *Physical Review*, **77**: 3865-3868.

Pickering, J. M., Schwab, B. E. and Johnston, A. D. (1998) Off-center hot spots: Double thermocouple determination of the thermal gradient in a 1.27 cm (1/2 in.) CaF2 piston-cylinder furnace assembly. *American Mineralogist*, **83**: 228-235.

Plank, T. and Langmuir, C. H. (1993) Tracing Trace Elements from the Sediment Input to Volcanic Output at Subduction Zones. *Nature*, **362**: 739-742.

Plank, T. and Langmuir, C. H. (1998) The Chemical Composition of Subducting Sediment and its Consequences for the Crust and Mantle. *Chemical Geology*, **145**: 325-394.

Pownceby, M. I. and Oneill, H. S. C. (1994) Thermodynamic Data from Redox Reactions at High-Temperatures .4. Calibration of the Re-ReO_2 Oxygen Buffer from Emf and NiO+Ni-Pd Redox Sensor Measurements. *Contributions to Mineralogy and Petrology*, **118**: 130-137.

Presnall, D. C., Brenner, N. L. and O'Donnell, T. H. (1973) Drift of Pt/Pt10Rh and W3Re/W25Re thermocouples in single stage piston-cylinder apparatus. *American Mineralogist*, **58**: 771-777.

Ravel, B. and Newville, M. (2005) ATHENA, ARTEMIS, HEPHAESTUS: Data Analysis for X-Ray Absorption Spectroscopy using IFEFFIT. *Journal Of Synchrotron Radiation*, **12**: 537-541.

Rehr, J. J. and Ankudinov, A. L. (2005) Progress in the Theory and Interpretation of XANES. *Coordination Chemistry Reviews*, **249**: 131-140.

Remond, G., Cesbron, F., Chapoulie, R., Ohnenstetter, D., Roques-Carmes, C. and Schoverer, M. (1992) Cathodoluminescence Applied to the Microcharacterization of Mineral Materials: A Present Status in Experimentation and Interpretation. *Scanning Microscopy*, **6**: 23-68.

Rios, S., Malcherek, T., Salje, E. K. H. and Domeneghetti, C. (2000) Localized Defects in Radiation-Damaged Zircon. *Acta Crystallographica Section B-Structural Science*, **56**: 947-952.

Robertson, J. K. and Wyllie, P. J. (1971) Rock-Water Systems, with Special Reference to the Water-Deficient Region. *American Journal of Science*, **271**: 252-277.

Rubatto, D. and Hermann, J. (2003) Zircon Formation During Fluid Circulation in Eclogites (Monviso, Western Alps): Implications for Zr and Hf Budget in Subduction Zones. *Geochimica et Cosmochimica Acta*, **67**: 2173-2187.

Ryerson, F. J. and Watson, E. B. (1987) Rutile Saturation in Magmas - Implications for Ti-Nb-Ta Depletion in Island-Arc Basalts. *Earth and Planetary Science Letters*, **86**: 225-239.

Schmidt, M. W., Vielzeuf, D. and Auzanneau, E. (2004) Melting and Dissolution of Subducting Crust at High Pressures: The Key Role of White Mica. *Earth and Planetary Science Letters*, **228**: 65–84.

Shen, A. and Keppler, H. (1997) Direct Observation of Complete Miscibility in the Alibte-H_2O System. *Nature*, **385**: 710-712.

Shevchenko, A. V., Lopato, L. M., Maister, I. M. and Gorbunov, O. S. (1980) The TiO_2-ZrO_2 System. *Russian Journal of Inorganic Chemistry*, **25**: 1379–1381.

Slifka, A. J., Filla, B. J. and Phelps, J. M. (1998) Thermal Conductivity of Magnesium Oxide from Absolute, Steady-State Measurements. *Journal of Research of the National Institute of Standards and Technology*, **103**: 357-363.

Soler, J. M., Artacho, E., Gale, J. D., García, A., Junquera, J., Ordejón, P. and Sánchez-Portal, D. (2002) The Siesta Method for Ab Initio Order-N Materials Simulation. *Journal of Physics Condensed Matter*, **14**: 2745-2776.

Spandler, C., Hermann, J., Arculus, R. J. and Mavrogenes, J. (2003) Redistribution of Trace Elements During Prograde Metamorphism from Lawsonite Blueschist to Eclogite Facies; Implications for Deep Subduction-Zone Processes. *Contributions to Mineralogy and Petrology*, **146**: 205-222.

Spandler, C., Mavrogenes, J. and Hermann, J. (2007) Experimental Constraints on Element Mobility from Subducted Sediments using High-P Synthetic Fluid/melt Inclusion. *Chemical Geology*, **239**: 228-249.

Speer, J. S. (1982) Zircon. *American Mineralogical Society Reviews in Mineralogy*, **5**: 67-112.

Stadler, R., Ulmer, P., Thompson, A. B. and Gunther, D. (2000) Experimental Approach to Constrain Second Critical End Points in Fluid/Silicate Systems: Near-Solidus Fluids and Melts in the System Albite-H_2O. *American Mineralogist*, **85**: 68-77.

Sterner, S. M. and Bodnar, R. J. (1984) Synthetic Fluid Inclusions in Natural Quartz I. Compositional Types Synthesized and Applications to Experimental Geochemistry. *Geochimica et Cosmochimica Acta*, **48**: 2659–2668.

Sugai, T. and Hasegawa, S. (1968) Growth of Zirconium Titanate ($ZrTiO_4$) Single Crystals from Molten Salts. *Journal of the Japanese Ceramic Society*, **76**: 429.

Tatsumi, Y. and Eggins, S. M. (1995) Subduction Zone Magmatism. Blackwell, Cambridge, 211 pp.

Taylor, J. R., Wall, V. J. and Pownceby, M. I. (1992) The Calibration and Application of Accurate Redox Sensors. *American Mineralogist*, **77**: 284-295.

Tenthorey, E. and Hermann, J. (2004) Composition of Fluids During Serpentinite Breakdown in Subduction Zones: Evidence for Limited Boron Mobility. *Geology*, **32**: 865-868.

Tera, F., Brown, L., Morris, J., Sacks, I. S., Klein, J. and Middleton, R. (1986) Sediment Incorporation in Island-Arc Magmas: Inferences from ^{10}Be. *Geochimica et Cosmochimica Acta*, **50**: 535–550.

Tomkins, H. S., Powell, R. and Ellis, D. J. (2007) The Pressure Dependence of the Zirconium-in-Rutile Thermometer. *Journal of Metamorphic Geology*, **25**: 703-713.

Troitzsch, U., Christy, A. G. and Ellis, D. J. (2005) The Crystal Structure of Disordered $(Zr,Ti)O_2$ Solid Solution including Srilankite: Evolution towards Tetragonal ZrO_2 with Increasing Zr. *Physics and chemistry of minerals*, **32**: 504-514.

Troitzsch, U. and Ellis, D. J. (2004) High-PT Study of Solid Solutions in the System ZrO_2-TiO_2: the Stability of Srilankite. *European Journal of Mineralogy*, **16**: 577-584.

Troitzsch, U. and Ellis, D. J. (2005) The ZrO_2-TiO_2 Phase Diagram. *Journal of Materials Science*, **40**: 4571-4577.

Troullier, N. and Martins, J. L. (1991) Efficient Pseudopotentials of Plane-Wave Calculations. *Physical Review*, **B. 43**: 1993-2006.

Truckenbrodt, J., Ziegenbein, D. and Johannes, W. (1997) Redox Conditions in Piston-Cylinder Apparatus; The Different Behavior of Boron Nitride and Unfired Pyrophyllite Assemblies *American Mineralogist*, **82**: 337-344.

van Keken, P. E., Kiefer, B. and Peacock, S. M. (2002) High-Resolution Models of Subduction Zones: Implications for Mineral Dehydration Reactions and the Transport of Water into the Deep Mantle. *Geochemistry Geophysics and Geosystems*, **3**: 1056.

Walker, A. M., Hermann, J., Berry, A. J. and O'Neill, H. S. C. (2007) Three Water Sites in Upper Mantle Olivine and the Role of Titanium in the Water Weakening Mechanism. *Journal of Geophysical Research*, **112**: B05211.

Wark, D. A. and Watson, E. B. (2006) TitaniQ: a Titanium-in-Quartz Geothermometer. *Contributions to Mineralogy and Petrology*, **152**: 743-754.

Watson, E. B. and Harrison, T. M. (2005) Zircon Thermometer Reveals Minimum Melting Conditions on Earliest Earth. *Science*, **308**: 841-844.

Watson, E. B. and Liang, Y. (1995) A simple Model for Sector Zoning in Slowly Grown Crystals: Implications for Growth Rate and Lattice Diffusion, with Emphasis on Accessory Minerals in Crustal Rocks. *American Mineralogist*, **80**: 1179-1187.

Watson, E. B., Wark, D. A. and Thomas, J. B. (2006) Crystallization Thermometers for Zircon and Rutile. *Contributions to Mineralogy and Petrology*, **151**: 413-433.

Waychunas, G. A. (1987) Synchrotron Radiation XANES Spectroscopy of Ti in Minerals: Effects of Ti Bonding Distances, Ti Valence, and Site Geometry on Absorption Edge Structure. *American Mineralogist*, **72**: 89-101.

Willgallis, A. and Hartl, H. (1983) $(Zr_{0.33}Ti_{0.67})O_2$ - a Natural Zirconium-Titanium Oxide with an Alpha-PbO_2 Structure. *Zeitschrift Fur Kristallographie*, **164**: 59-66.

Woodhead, J. D. and Fraser, D. G. (1985) Pb, Sr and 10 Be Isotopic Studies of Volcanic Rocks from the Northern Mariana Islands. Implication for Magma Genesis and Crustal Recycling in the Western Pacific. *Geochimica et Cosmochimica Acta*, **49**: 1925–1930.

Yoder Jr, H. S. (1958) Effect of Water on the Melting of Silicates, Yearbook 57. Carnegie Institute of Washington, pp. 189-191.

Zack, T., Moraes, R. and Kronz, A. (2004) Temperature Dependence of Zr in Rutile: Empirical Calibration of a Rutile Thermometer. *Contributions to Mineralogy and Petrology*, **148**: 471-488.

Appendix 1

The Ti-in-zircon exchange reaction

This appendix presents theoretical arguments regarding the Ti-in-zircon substitution mechanism as it may be described by different types of reaction.

A.1: Previous research

As outlined in Chapters 3 and 7, previous research into the zircon thermometer recognized two potential substitution mechanisms for To-in-zircon. Watson et al. (2006) and Ferry and Watson (2007) described the two theoretical substitution mechanisms as:

$$\underset{\text{Zircon}}{ZrSiO_4} + \underset{\text{Rutile}}{TiO_2} = \underset{\text{Zircon}}{ZrTiO_4} + \underset{\text{Quartz}}{SiO_2} \qquad \textbf{(eq. A1)}$$

and,

$$\underset{\text{Rutile}}{TiO_2} + \underset{\text{Quartz}}{SiO_2} = \underset{\text{Zircon}}{TiSiO_4} \qquad \textbf{(eq. A2)}$$

Where, *equation A1* represents substitution on the tetrahedral or $^{[4]}$Si site and *equation A2* describes substitution on the dodecahedral or $^{[8]}$Zr site.

The interesting thing about these two reactions is that they are not equivalent or directly comparable in describing the substitution mechanism. *Equation A1* represents and exchange reaction, whereas *equation A2* represents a simple chemical reaction (i.e., not an exchange reaction). An exchange reaction for Ti on the dodecahedral site in zircon can be written as:

$$\underset{\text{Zircon}}{ZrSiO_4} + \underset{\text{Rutile}}{TiO_2} = \underset{\text{Zircon}}{TiSiO_4} + \underset{\text{Zirconia}}{ZrO_2} \qquad \textbf{(eq. A3)}$$

And a simple reaction for Ti on the tetrahedral site in zircon can also be written as:

$$\underset{\text{Zirconia}}{ZrO_2} + \underset{\text{Rutile}}{TiO_2} = \underset{\text{Zircon}}{ZrTiO_4} \qquad \textbf{(eq. A4)}$$

This raises the question, which equation more accurately describe the Ti substitution mechanism on the different site in zircon?

A.2: Substitution on the tetrahedral site

Comparison of equations for Ti substitution on the tetrahedral or $^{[4]}$Si site (*eq. A1* and *A4*) are similar in that decreases in titania activity result in decreasing Ti-in-zircon. This can be considered in terms of the equilibrium constant, where titania activity is consistently expressed as a denominator:

$$K(A1) = \frac{a_{ZrTiO_4}^{zircon} a_{SiO_2}}{a_{TiO_2}} \qquad \textbf{(eq. A5)}$$

$$K(A4) = \frac{a_{ZrTiO_4}^{zircon}}{a_{ZrO_2} a_{TiO_2}} \qquad \textbf{(eq. A6)}$$

Two fundamental differences exist between equations *A1* and *A4*, or equilibrium constant expressions *A5* and *A6*. The first is the presence of a zirconia activity term in equation *A6* (and *A4*). The importance of zirconia activity where Ti occupies the tetrahedral or $^{[4]}$Si site in zircon is limited and only influences zircon thermometry by influencing whether or not zircon crystallization occurs. In essence zirconia activity can influence zircon crystallization (and by extension zircon thermometry) if equation *A4* is considered the equivalent of the following reaction:

$$\underset{\text{Zirconia}}{ZrO_2} + \underset{\text{Quartz}}{SiO_2} = \underset{\text{Zircon}}{ZrSiO_4} \qquad \textbf{(eq. A7)}$$

The second manner in which equations *A5* and *A6* (or *A1* and *A4*) are different is that the former contains a silica activity term. As indicated in equation *A7* the crystallization of zircon is dependent on silica activity, but this does not necessitate a silica activity of unity for the crystallization of zircon. In fact the majority of experiments carried out in this research (and many natural rocks) contain no quartz, such that silica activity is less than unity. The importance of this observation or thermodynamic consideration is that there is a range, from zircon saturated to silica (quartz) saturated, over which silica activity may vary. If and where Ti occupies the tetrahedral or $^{[4]}$Si site, varying silica activity can influence Ti-in-zircon. Most importantly, the results presented in Chapter 6 and discussions in Chapter 7 demonstrate that silica activity influences Ti-in-zircon.

A.3: Substitution on the dodecahedral site

Comparison of equations for Ti substitution on the dodecahedral site or $^{[8]}$Zr site (*eq. A2* and *A3*) are similar in that decreases in titania activity result in decreasing Ti-in-zircon. This can be expressed in terms of the equilibrium constant, where titania activity is consistently expressed as a denominator:

$$K(A2) = \frac{a_{TiSiO_4}^{zircon}}{a_{TiO_2} a_{SiO_2}} \qquad \textbf{(eq. A8)}$$

$$K(A3) = \frac{a_{TiSiO_4}^{zircon} a_{ZrO_2}}{a_{TiO_2}} \qquad \textbf{(eq. A9)}$$

Similar to Ti substitution on the tetrahedral site, equations *A8* and *A9* show considerable variation depending on whether the substitution is represented by a normal or an exchange reaction. For the exchange reaction (equation *A8*), silica activity will only influence whether

or not zircon crystallizes (e.g. equation A7). The exchange reaction, by contrast, contains a zirconia term that should influence Ti-in-zircon. This is to say that the range of zirconia activities, from zircon- to zirconia-saturated conditions, will influence Ti-in-zircon. If Ti occupies the dodecahedral or $^{[8]}Zr$ site in zircon, then equations A3 and A9 should provide the most accurate thermodynamic calibrations for thermometry purposes. This being the case, as no experimental or model results indicated such substitution these points are largely semantic.

Appendix 2

Pelite 1008-4 analyses

This appendix contains analytical conditions and results for scanning electron microscopy energy dispersive spectra (SEM-EDS) and laser ablation inductively coupled plasma mass spectra (LA-ICP-MS) for pelite 1008-4 starting material.

A.2: SEM (EDS)

Quantitative analysis of pelite glass was obtained by EDS on carbon coated epoxy mounts imaged on a JEOL 6400 SEM (Electron Microscopy Unit, ANU). Operating conditions were set at 15 kV and 1 nA. A broad (defocused) beam was used during analyses and counting times were set to 90 seconds. The use of a low beam current and a defocused beam during analyses was employed in order to limit alkali loss.

EDS standards included albite (Na and Al), periclase (Mg), sanidine (K and Si), diopside (Ca), rutile (Ti), hematite (Fe), manganese metal (Mn) and apatite (P). All spectra were processed with LINK ISIS-SEMIQUANT software, employing full ZAF (3 iterations). The fit index was also monitored to ensure the quality of peak resolution in EDS during analyses (particularly for elements at low concentrations). Element totals were monitored at 15 second intervals during analyses and indicate very minimal alkali loss, with Na_2O content decreasing by <4 % as analytical live time increased from 30 to 90 seconds.

All elements analysed by SEM-EDS show concentrations, peak resolutions and fit indices (i.e., < 1.5) sufficient for major element analyses. The only concern with SEM analyses pertains to P_2O_5 and MnO, which show concentrations at the lower end of detection limits. Mn and P have absorption K-lines sufficiently removed from other elements to allow accurate peak resolution, while fit indices indicate sufficient counts exist to accurately resolve minor element spectra (with maximum fit index values of 1.5 and 1.3 respectively).

Table A.2: SEM-EDS results (in wt % oxide) from pelite 1008-4 glass chips

	Spot 1	Spot 2	Spot 3	Spot 4	Spot 5	Spot 6	Spot 7	Spot 8	Spot 9	**Mean**	(σ)
SiO_2	69.82	70.49	68.83	69.83	69.21	68.65	69.32	69.50	69.30	**69.44**	0.56
TiO_2	0.62	0.66	0.66	0.43	0.54	0.51	0.44	0.65	0.63	**0.57**	0.09
Al_2O_3	12.37	12.43	13.23	12.75	12.51	12.49	12.80	13.17	12.22	**12.66**	0.35
FeO*	3.87	3.44	3.88	3.81	3.65	3.54	3.62	3.58	3.26	**3.63**	0.21
MnO	0.14	0.09	0.15	0.14	0.13	0.12	0.17	0.14	0.15	**0.14**	0.02
MgO	1.80	1.49	1.79	1.40	2.06	1.71	1.40	1.38	1.94	**1.66**	0.25
CaO	3.15	2.96	3.48	3.14	3.10	3.62	3.00	3.17	3.21	**3.20**	0.21
Na_2O	2.61	2.76	2.79	2.84	2.82	2.73	2.74	2.67	2.72	**2.74**	0.07
K_2O	3.88	4.10	4.00	4.20	4.00	3.80	4.09	3.97	4.06	**4.01**	0.12
P_2O_5	0.22	0.18	0.15	0.17	0.18	0.22	0.19	0.16	0.21	**0.19**	0.03

FeO* = analyses calculated on ferrous iron (as the powder was fused at 95% CO_2:5% CO the sample should have equilibrated at an fO_2 well below the haematite-magnetite oxygen buffer)

High resolution electron backscatter (BSI) and secondary electron (SEI) images from pelite 1008-4 were also obtained using the JEOL 6400 SEM and ZIESS UltraPlus FESEM (ANU electron microscopy unit) in order to determine if pelite 1008-4 glass chips contained any phases/materials (other than SiO_2) that may stem from incomplete melting or sample contamination. 16 hours of slow-scan high-resolution SEM-imaging and x-ray mapping indicated that glass starting material was free of minerals, with the exception of SiO_2, and showed no detectable variations in major element distribution.

A.2: LA-ICP-MS

LA-ICP-MS analyses of pelite 1008-4 were carried out on an 7500S Agilent coupled to an ArF laser ablation system (193 nm wavelength, RSES, ANU). Glass analyses employed a laser aperture of 54 μm, a 5 Hz repetition rate, an energy of 90 mJ, a power of 0.45 watts. Data acquisition was performed with 30 seconds of background measurement, followed by 40 seconds of sample ablation. NIST SRM 612 was used for external calibration of data. Preferred values for NIST SRM 612 were obtained from the GeoReM website (Max-Planck-Institute database; http://georem.mpch-mainz.gwdg.de/).

^{27}Al was used for internal calibration of LA-ICP-MS data, with Al_2O_3 values for each spot determined independently by SEM-EDS. As shown in Figure A.1, LA-ICP-MS profiles show excellent peak-to-background resolution. Visual inspection of ablation profiles show that glass spectra are free of anomalous spikes or potential signal from trydimite.

NIST SRM 612 was analysed before and after five 1008-4 (pelite) analyses to allow corrections to be made for analytical drift. The full range of isotopes and analytical results are presented in Table A.2.

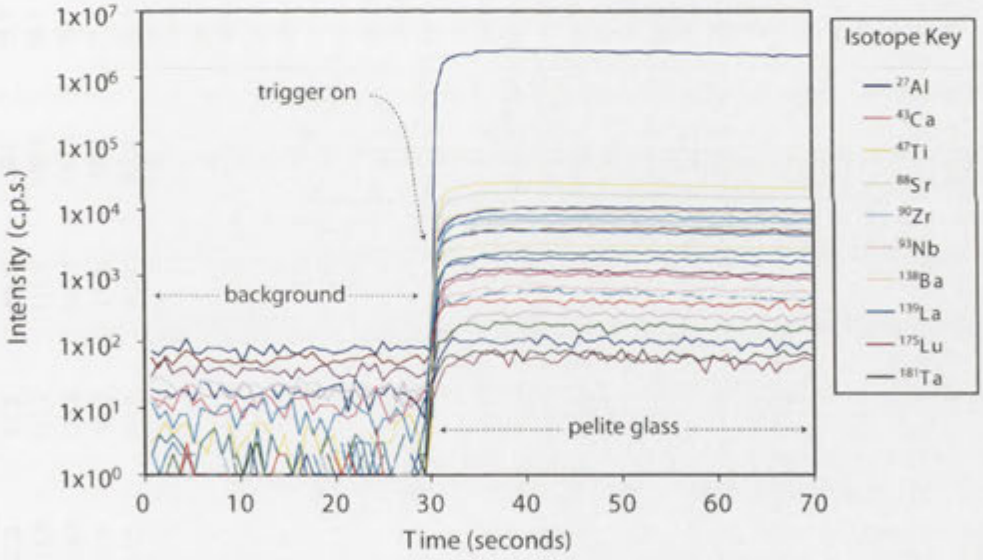

***Figure A.1**: Representative LA-ICP-MS profile from pelite 1008-4 analysis. Specific isotopes are not of particular importance in this diagram, but good peak-to-background ratios are clearly shown.*

Table A.2: LA-ICP-MS results (in ppm) from pelite 1008-4 glass

Isotope	Spot 1	Spot 2	Spot 3	Spot 4	Spot 5	Spot 6	Spot 7	Spot 8	Spot 9	Spot 10	**Mean**	(σ)
^{47}Ti	3105.1	3114.4	3276.7	3252.5	3111.6	3472.7	3168.4	3145.4	3401.9	3801.2	**3285.0**	221.4
^{51}V	74.7	71.3	71.4	74.4	71.3	74.9	71.2	70.1	71.6	72.6	**72.4**	1.7
^{53}Cr	756.1	305.9	184.4	412.1	118.2	358.0	77.9	121.2	407.2	412.8	**315.4**	203.7
^{59}Co	57.1	52.3	51.9	55.1	52.8	58.5	50.0	49.4	54.4	58.1	**54.0**	3.2
^{60}Ni	105.9	112.5	112.7	115.4	107.6	96.7	98.4	97.4	103.7	127.0	**107.7**	9.5
^{63}Cu	122.0	124.5	124.6	150.3	157.5	130.1	132.0	137.8	138.6	148.6	**136.6**	12.2
^{66}Zn	21.4	19.9	19.3	21.3	19.4	21.2	27.7	18.3	19.9	22.4	**21.1**	2.6
^{85}Rb	53.2	60.0	59.9	57.6	62.3	56.4	68.2	69.7	60.1	55.8	**60.3**	5.3
^{88}Sr	158.8	152.5	153.2	155.1	151.4	157.2	145.0	145.2	151.6	158.2	**152.8**	4.8
^{89}Y	26.2	24.8	25.4	25.4	23.7	26.3	22.7	22.2	24.0	26.1	**24.7**	1.5
^{90}Zr	123.3	120.1	133.5	118.7	112.1	153.2	104.5	124.7	194.3	117.9	**130.2**	26.0
^{93}Nb	5.97	5.57	6.46	6.36	5.60	7.34	5.49	5.72	6.97	9.64	**6.51**	1.26
^{133}Cs	1.59	1.83	1.84	1.76	1.93	1.74	2.10	2.16	1.84	1.65	**1.84**	0.18
^{138}Ba	224.8	220.6	221.1	223.6	221.7	224.0	215.7	215.2	219.8	226.4	**221.3**	3.7
^{139}La	17.1	15.6	16.3	16.7	15.7	17.9	15.0	14.7	15.7	16.8	**16.2**	1.0
^{140}Ce	43.2	39.8	41.8	41.4	40.8	49.7	40.1	37.5	39.4	42.2	**41.6**	3.3
^{141}Pr	4.87	4.46	4.61	4.74	4.46	5.14	4.21	4.18	4.43	4.85	**4.59**	0.30
^{146}Nd	20.8	19.3	20.1	20.1	19.5	23.0	18.8	17.7	18.9	20.3	**19.8**	1.4
^{147}Sm	4.44	4.25	4.40	4.33	4.18	5.00	4.09	3.93	4.36	4.48	**4.35**	0.28
^{153}Eu	0.97	0.89	0.97	0.93	0.87	0.94	0.79	0.85	0.81	1.06	**0.91**	0.08
^{157}Gd	4.44	4.10	4.11	4.29	3.90	4.62	3.69	3.72	4.08	4.59	**4.15**	0.33
^{159}Tb	0.67	0.62	0.64	0.65	0.60	0.71	0.59	0.57	0.63	0.64	**0.63**	0.04
^{163}Dy	4.52	4.23	4.34	4.45	4.11	4.69	3.72	3.77	4.17	4.37	**4.24**	0.31
^{165}Ho	0.95	0.89	0.94	0.94	0.82	0.97	0.81	0.80	0.89	0.95	**0.90**	0.06
^{166}Er	3.04	2.82	2.98	2.96	2.77	2.94	2.64	2.66	2.77	3.13	**2.87**	0.17
^{169}Tm	0.47	0.45	0.44	0.46	0.43	0.47	0.41	0.40	0.43	0.43	**0.44**	0.02
^{174}Yb	3.62	3.38	3.30	3.38	3.12	3.42	2.95	2.98	3.28	3.43	**3.28**	0.21
^{175}Lu	0.54	0.50	0.52	0.53	0.47	0.54	0.46	0.47	0.49	0.53	**0.51**	0.03
^{178}Hf	3.39	3.38	3.70	3.40	3.17	4.27	2.69	3.41	5.66	3.27	**3.63**	0.81
^{181}Ta	0.93	0.73	0.93	0.94	0.68	0.95	0.91	0.80	3.33	1.63	**1.18**	0.80
^{208}Pb	11.3	11.4	11.3	11.6	11.3	11.6	11.1	11.1	11.4	12.0	**11.4**	0.3
^{232}Th	6.06	5.83	6.13	6.19	5.77	6.86	5.62	5.72	6.37	6.37	**6.09**	0.38
^{238}U	2.46	2.34	2.37	2.45	2.24	2.72	2.28	2.22	2.32	2.55	**2.39**	0.15

Trace element results from LA-ICP-MS analyses presented in Table A.2 and Figures A.2 and A.3 demonstrate that experimental homogenization of the pelite starting powder via glass fusion was successful for the majority of elements. Elevated standard deviations (statistical variability where 2σ falls outside 20 % of the mean) are seen for Cr, Nb, Ta, Zr and Hf, meriting further discussion.

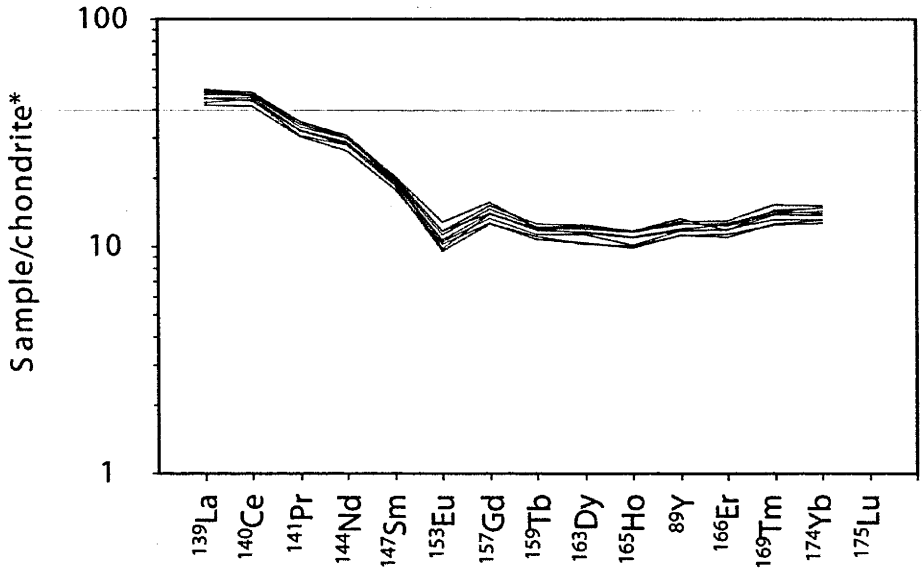

***Figure A.2**: C1 chondrite-normalized REE profile from ten pelite 1008-4 LA-ICP-MS analyses showing low statistical variation (isotopes as indicated). Chondrite values taken from MacDonough (1987).*

The Varying Cr contents among the ten analyses (Figure A.3.*a*) are likely related to contamination from stainless pliers used to pluck pelite glass from the Pt crucible. All LA-ICP-MS analyses from pelite 1008-4 show clean ^{53}Cr profiles, devoid of nugget-effects (spikes) or other forms of spectral irregularity (at the resolution of spectra). This statistical variation is interpreted to result from small shards from the pliers entering the starting material and having insufficient time to evenly diffuse (homogenize) while dissolving within the melt. It is worth noting that the measured Cr contents from pelite 1008-4 are all < 800 ppm (with 90 % of analyses showing <500 ppm) and are unlikely to significantly effect phase equilibria (as most Cr is likely to substitute within rutile at experimental conditions).

The LA-ICP-MS high field strength element (HFSE) results also show notable statistical variation in 2σ values about the mean – Nb (39 %), Ta (134 %), Zr (40 %) and Hf (45 %). Such variability were not unexpected, as the HFSE are present at low concentrations (1-130 ppm). This variation is most likely related to ionization efficiency related to the instrument, rather than representing true statistical distribution among the pelite 1008-4 glass.

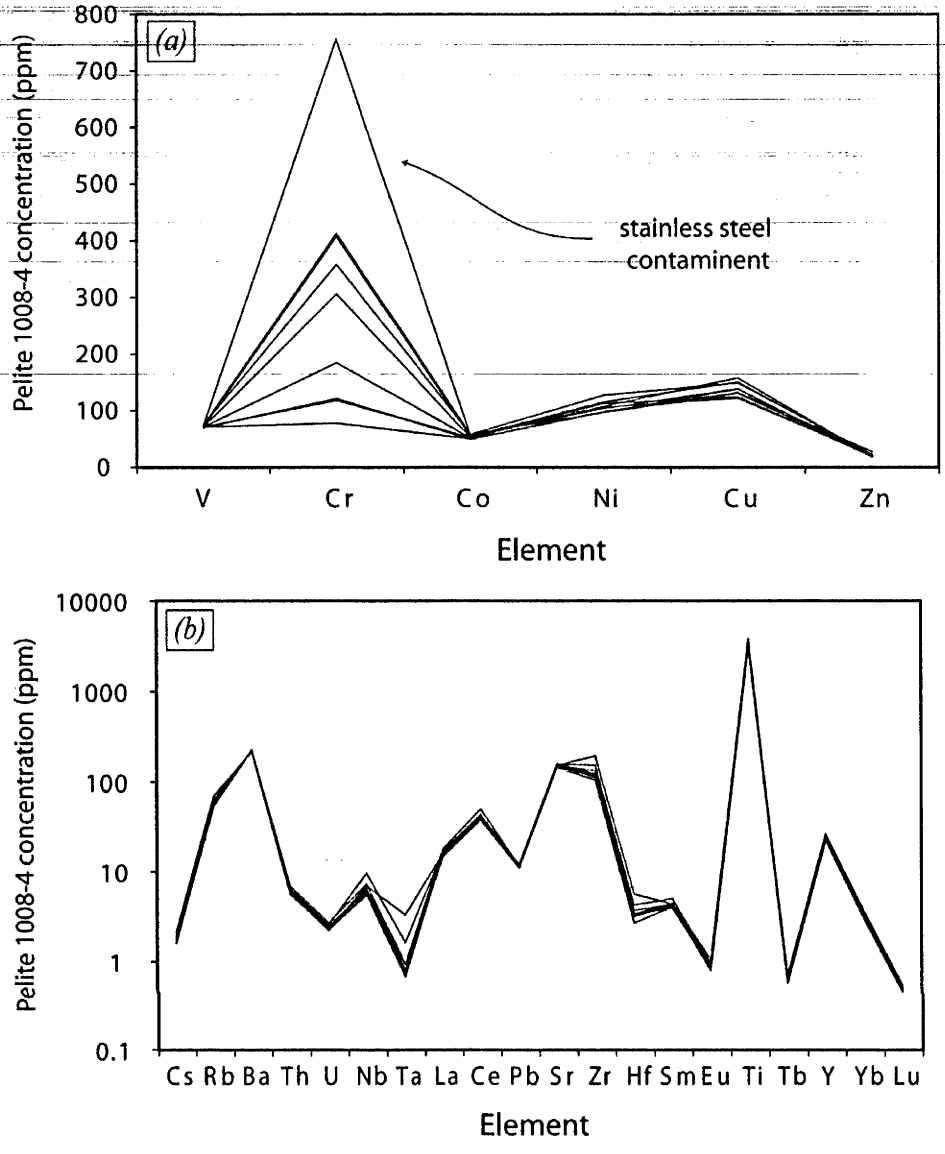

***Figure A.3**: Trace element histograms from ten LA-ICP-MS analyses from pelite 1008-4. (a) concentration of transition metals (note the highly variable Cr contents), (b) concentration of HFSE, LILE and selected REE.*

Appendix 3

Garnet analyses

Table A2.1: 35 kbar/900 °C garnet analyses

	D-1025	σ	C-3119	σ	C-3157	σ	C-3150	σ	C-3127	σ
MgO	14.42	1.71	9.92	1.59	11.33	0.82	11.73	1.41	10.39	0.16
Al_2O_3	21.80	0.44	20.44	0.49	20.85	0.25	21.01	0.37	21.06	0.34
SiO_2	40.12	0.89	38.39	0.84	39.09	0.47	38.96	0.61	39.13	0.21
CaO	4.67	0.76	6.48	1.56	3.59	0.52	2.98	0.78	1.46	0.26
TiO_2	0.75	0.26	1.08	0.22	1.31	0.36	1.07	0.26	0.31	0.26
MnO	0.72	0.26	1.32	0.44	1.65	0.12	1.89	0.27	1.34	0.07
FeO*	15.41	2.05	19.88	2.25	20.53	1.34	21.20	2.16	25.63	0.19
Total	98.88	0.44	98.75	1.00	98.36	0.49	98.84	0.23	99.32	0.28
n	12		12		10		20		10	
P (kbar)	35		35		35		35		35	
T (°C)	900		900		900		900		900	
H_2O (wt%)	5.43		9.18		22.28		35.28		49.63	

Table A2.2: 35 kbar/800 °C garnet analyses

	D-1071	σ	C-3155	σ	C-3130	σ
MgO	6.33	1.39	5.19	0.50	11.26	1.01
Al_2O_3	20.77	1.15	20.50	0.18	21.11	0.32
SiO_2	39.16	2.20	37.45	0.22	38.83	0.41
CaO	9.30	0.47	9.96	0.28	3.28	0.47
TiO_2	0.80	0.18	1.30	0.14	1.19	0.19
MnO	1.22	0.18	1.74	0.35	1.71	0.34
FeO*	21.40	1.91	23.07	0.40	22.27	1.42
Total	98.99	0.31	99.21	0.08	99.65	0.10
n	8		12		13	
P (kbar)	35		35		35	
T (°C)	800		800		800	
H_2O (wt%)	5.26		9.78		23.1	

Table A2.3: 35 kbar/700-750 °C garnet analyses

	C-3128	σ	C-3275	σ	D-1069	σ	C-3274	σ	D-1066	σ
MgO	3.93	0.66	6.64	0.76	3.97	0.26	3.85	0.63	5.49	0.87
Al_2O_3	21.06	0.42	21.39	0.53	19.74	0.09	19.96	0.30	20.38	0.33
SiO_2	38.22	0.58	38.91	0.49	36.56	0.23	36.70	0.39	37.97	0.66
CaO	10.23	0.24	9.29	0.30	9.14	0.28	9.79	0.41	10.63	0.40
TiO_2	0.95	0.15	0.50	0.24	1.14	0.09	1.29	0.10	0.93	0.19
MnO	1.72	0.46	0.98	0.33	2.41	0.23	2.09	0.40	1.60	0.22
FeO*	23.68	1.13	21.70	1.21	25.08	0.52	23.16	0.78	22.30	1.20
Total	99.80	0.08	99.39	0.56	98.04	0.44	98.83	0.59	99.68	0.51
n	11		7		9		8		9	
P (kbar)	35		35		35		35		35	
T (°C)	700		750		750		750		750	
H_2O (wt%)	52.66		5.75		12.94		22.92		48.74	

Appendix 4

LA-ICP-MS analyses of experimental glasses

The main reason for using a natural pelite starting material in this research was to permit trace elemental partitioning studies between liquid and solids in a system that has a trace element composition analogous to subducting sediments. LA-ICP-MS analyses in this Appendix report preliminary results from 25 and 35 kbar glasses in order to demonstrate potential areas that exists for future research.

Figure A3.1 shows the trace element concentration of pelite glasses normalized to the 1008-4 starting material. The reported values represent averages of 7 to 19 analyses from individual experiments, with visual inspection of the data used to remove analyses containing mixed signal from glass+minerals or statistical outliers.

One of the most notable observations from Figure A3.1 is that all glasses show distinct negative anomalies in Nb, Ta and Ti relative to starting material. This is not unexpected, as rutile is present in all experiments and buffers these elements in the glass (silicate liquid). The interesting observation from these analyses is that Nb and Ta concentrations of glasses at 35 kbar are consistently higher than 25 kbar glasses. Covariation of Nb-Ta (Figure A3.2) shows that glasses with the highest Ti have the highest Nb and Ta, suggesting that there is an increase in rutile solubility with increasing pressure.

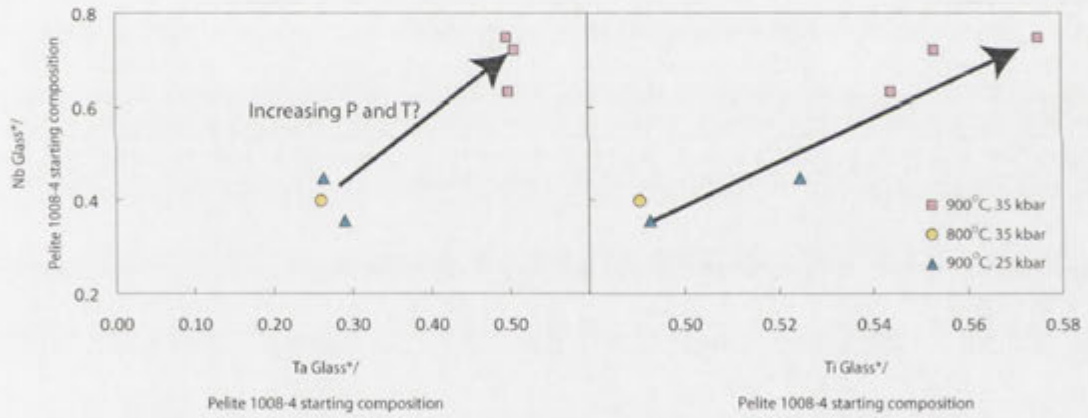

A3.2: Covariation diagrams of Nb-Ta and Nb-Ti from experimental glasses

Other important observations from glass analyses include: distinct changes in the LREE/HREE from 35 kbar/900 °C runs as starting H_2O increases (likely demonstrating changes in garnet composition with increasing melt fractions); Zr contents around unity, suggesting zircon has completely dissolved); Cs/Rb variations as a function of starting H_2O and pressure, correlations in Ba/La, depletions in highly to moderately siderophile elements (capsule alloying) and enrichments in Zn.

These few analyses demonstrate the many lines of investigation still possible with these experiments and in particular, how they can further be used to constrain processes involving pelite recyling.

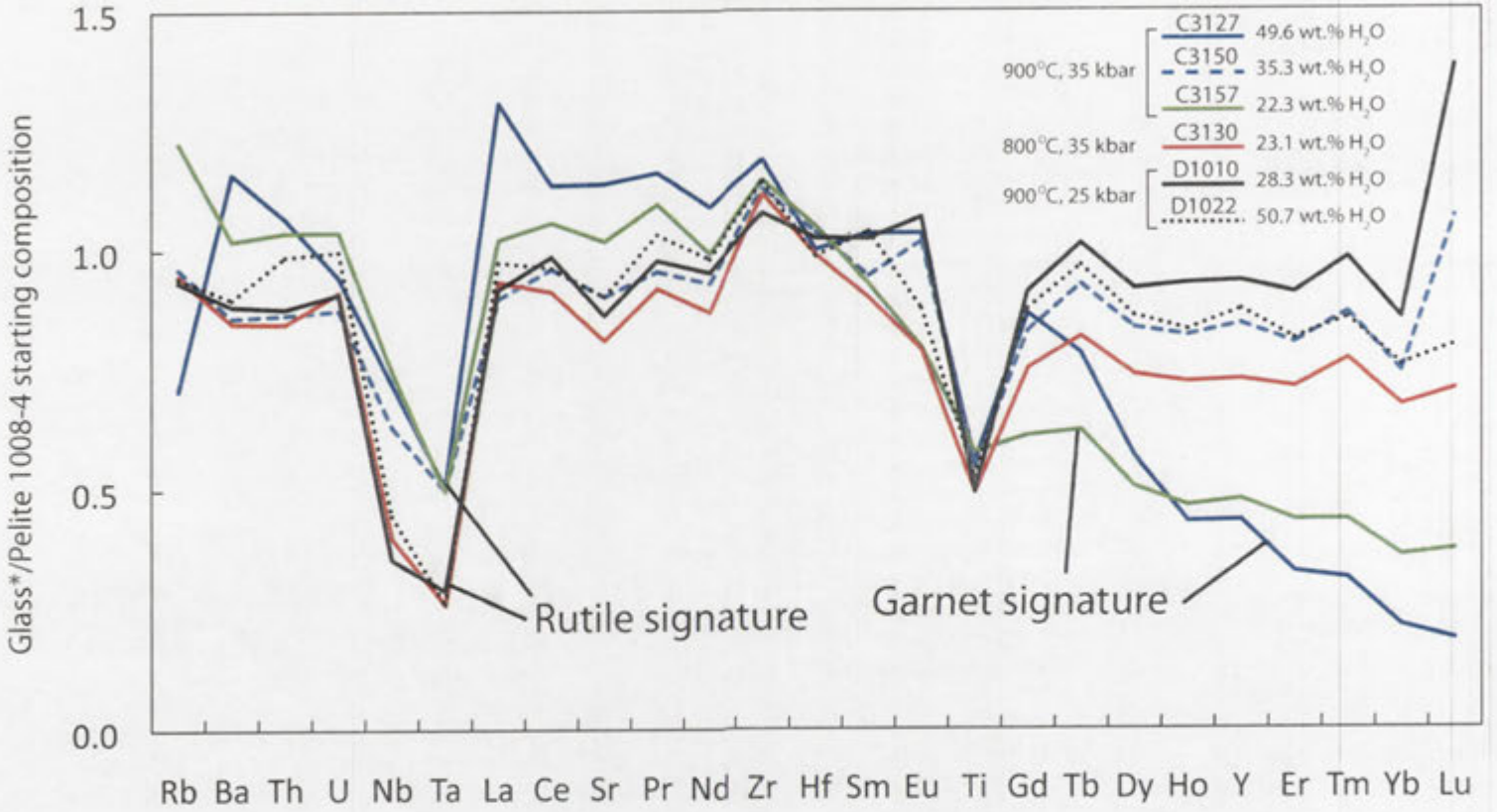

Figure A3.1: Trace element spidergram for pelitic glasses, normalized to Pelite 1008-4 starting material, as determined by LA-ICP-MS.